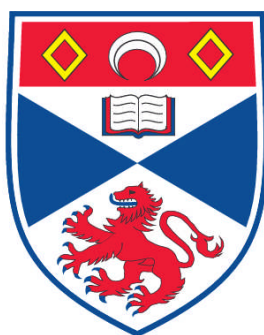# SYNTHESIS AND CHARACTERISATION OF ELECTRONICALLY ACTIVE SPECIES

Thushitha Mahenthirarajah

A Thesis Submitted for the Degree of PhD
at the
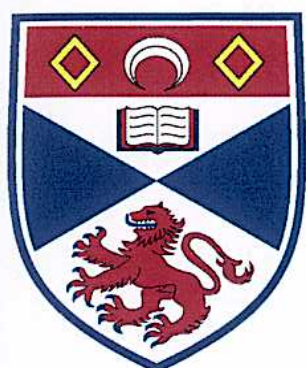## University of St. Andrews

2009

University
of
St Andrews

EaStCHEM

The Edinburgh and St Andrews
Research School of Chemistry

Synthesis and Characterisation of
Electronically Active Species

A thesis presented for the degree of

Doctor of Philosophy

in the Faculty of Science of the University of St Andrews

by Thushitha Mahenthirarajah

July 2009

Declaration

1. I, Thushitha Mahenthirarajah, hereby certify that this thesis, which is approximately 50,000 words in length, has been written by me, that it is the record of work carried out by me and that it has not been submitted in any previous application for a higher degree.

Date 08.07.09   Signature of candidate

2. I was admitted as a research student in February 2006 and as a candidate for the degree of PhD in February 2007; the higher study for which this is a record was carried out in theUniversity of St Andrews between 2006 and 2007.

Date 08.07.09   Signature of candidate

3. I hereby certify that the candidate has fulfilled the conditions of the Resolution and Regulations appropriate for the degree of Ph.D. in the University of St Andrews and that the candidate is qualified to submit this thesis in application for that degree.

Date 08.07.09   Signature of supervisor

4. In submitting this thesis to the University of St Andrews we understand that we are giving permission for it to be made available for use in accordance with the regulations of the University Library for the time being in force, subject to any copyright vested in the work not being affected thereby. We also understand that the title and the abstract will be published, and that a copy of the work may be made and supplied to any bona fide library or research worker, that my thesis will be electronically accessible for personal or research use unless exempt by award of an embargo as requested below, and that the library has the right to migrate my thesis into new electronic forms as required to ensure continued access to the thesis. We have obtained any third-party copyright permissions that may be required in order to allow such access and migration, or have requested the appropriate embargo below.

The following is an agreed request by candidate and supervisor regarding the electronic publication of this thesis:

Access to Printed copy and electronic publication of thesis through the University of St Andrews.

Access to all or part of printed copy but embargo of all or part of electronic publication of thesis for a period of 1 year on the following ground: publication would preclude publication.

Date 08.07.09   Signature of candidate

Signature of supervisor

Abstract

An exploration of some early transition metal (oxy) fluoride systems using solvothermal techniques has been carried out. 30 novel materials have been synthesised, which fall into three classes based on different metal centres; vanadium (21), molybdenum (5) and niobium (4). Some of these also contain secondary metal centres, namely copper (22) and zinc (1). Simultaneously, the relationship between the SHG values and the crystal structures of the hilgardites family members $Pb_2B_5O_9Cl$, $Pb_2B_5O_9Br$, $Sr_2B_5O_9Cl$ and $Ba_2B_5O_9Cl$ was investigated. In particular, the Pb–containing members of the hilgardite family of borate halides exhibit an abnormally large non–linear optical response, which was analysed based on neutron powder diffraction.

Using solvothermal synthesis in HF–containing media, 21 novel vanadium oxyfluorides containing interesting structural features, were synthesised at 160˚C using a range of organo-amine compounds as a ligand, template, linker or structure directing agent. The architectures of the crystal structures may be categorised into; four clusters including monomeric vanadium units, five clusters including vanadium dimers, eight 1–D chains, two 2–D layers and two 3–D networks. 'Composition–space' diagrams with three components were used to study the effect of stoichiometry changes of reactants and to map out the crystallisation fields.

The combination of early (Nb^{5+}, Mo^{6+}) and late (Cu^{2+}) transition metals with different organo-amines produced nine novel compounds incorporating monomers, chains and 2–D interpenetrated networks. The chains and layers were synthesised from a systematic series of reactions at 160˚C and can be subdivided into four pairs, the topologies of which are essentially unique to each ligand, containing in each case a Cu–based cationic species, but alternately either $[MoO_2F_4]^{2-}$ or $[NbOF_5]^{2-}$, in an isomorphous manner, as the anionic moiety. The overall structures of these materials reflect the influence of the organo–amine ligands.

The materials have been studied for their magnetic properties and characterised by thermogravimetric analysis, Rietveld refinement and elemental analysis where relevant.

Acknowledgements

Dedication

This thesis is dedicated to my God 'Arthi–Soodi–Pillaiyar', and my late grand parents, Mr and Mrs. C. S. Arumugampillai, and Dr. and Mrs. Subramaniam. It is also dedicated to my parents, Dr. and Mrs. S. Mahenthirarajah, my sisters Mrs. Najinii Varatharaj, to Mrs. Shangeetha Sivakumaran and to the late Mr. Aazeer, each of whom have been involved in making me the person I am today.

Thank you.

Table of Contents

CHAPTER ONE

Introduction

The work described in this thesis concerns the synthesis of novel borate materials and transition metal oxyfluorides and their characterisation. These materials were targeted in order to achieve combined properties from these two families, such as magnetic properties and non–linear optical (NLO) properties. It was anticipated that the combination of materials with unpaired spins and distorted building units, capable of multiple coordination modes in extended networks may produce materials with interesting magnetic interactions and NLO properties. The following chapter discusses transition metal oxyfluorides and their properties in relation to their distorted building units. Further, I describe the known vanadium oxyfluorides based on the local geometry and composition of the vanadium containing units, and the major roles of organic moieties and secondary metals in these systems. The final part of this chapter describes various fundamental building blocks of borate crystal structures, synthesis of borates and their potential properties.

1.1 Vanadium Oxides and Oxyfluorides

Over a period of years, there has been continuous interest in the rich and complex aqueous chemistry of vanadium. In particular, vanadium oxide based chemistry has been of great interest as it provides an interface between material science and coordination chemistry. Vanadium has a diversity of properties based on the variations of oxidation states, coordination sites, geometry and the chemical composition of vanadium and the incorporated secondary metal atoms, leading to crystal structures with various dimensions of packing such as clusters, chains, layers and 3–D networks.[1]

In recent years vanadium oxides and their derivatives have been much explored because of their potential applications in the field of electronics based on lithium–ion batteries.[2] The first vanadium containing crystal structure, VO_2, was introduced in 1926.[3] Later on,

components incorporating vanadium with alkali metals, alkaline earth metals and transition metals were also reported. The richness of this vanadium chemistry is enhanced by its variety of oxidation states and their reduction–oxidation properties, which will readily allow further addition and removal of ions. Further developments have been attained by defining vanadium containing building blocks prepared by solvothermal synthesis. During the past two decades organic cations have been extensively used as templates or structure directing agents in solvothermal synthesis (see section 1.1.3). The first well characterised vanadium oxide material incorporating an organic component, 2,2'–bipyridine, was reported by Jacobson et al in 1991.[4] The long history of vanadium chemistry has been changed dramatically after the introduction of organic components in the solvothermal reaction media leading to metal–organic hybrid structures. Nevertheless, these structures are mostly present in higher oxidation states (see Appendix–I) with less interest based on magnetic properties.

Zubieta and co–workers introduced transition metals into the system, which contribute significantly by increasing the dimensionality and having magnetic interactions, though the vanadium still exhibits the +5 oxidation state. The crystal structure of $[\{Cu_3(C_2H_3N_3)_2\}V_4O_{12}]$ exhibits a 3-D network built up from layers of copper complexes linked through vanadate chains containing corner–sharing vanadium tetrahedra present in the +5 oxidation state (see Figure 1.1). The magnetically active species, the copper complexes, exhibits "4+2" octahedral geometry and forms a trinuclear Cu^{2+} ring. The neighbouring four trinuclear rings are bridged by the triazolate ligand into a 2–D network. The magnetic data reveal long–range ferromagnetic ordering exists in the crystal structure.[5]

Interesting magnetic interactions with this combination are possible if unpaired spins are arranged into dimers, chains, layers or 3–D networks.

Using hydrofluoric acid as a mineraliser in solvothermal synthesis significantly contributes to expanding the range of magnetic structures, by forming vanadium oxyfluorides in lower oxidation states.
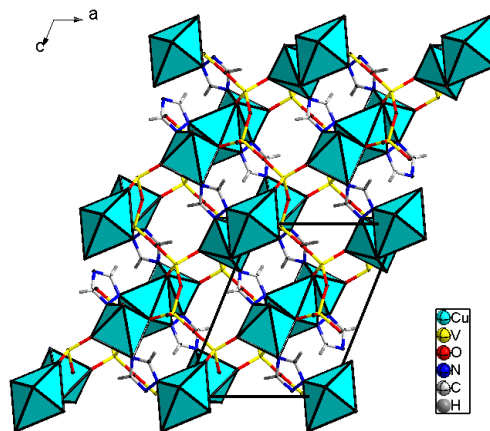
Figure 1.1 Organic–inorganic hybrid structure of [{$Cu_3(C_2H_3N_3)_2$}V_4O_{12}] viewed down the *b* axis.

Despite the challenges of designing the materials for the purpose of magnetic and NLO applications, solvothermal chemistry of vanadium oxyfluorides systems still remains relatively unexplored and uncharacterised. Recently Welk *et al.*[6] have reported the crystal structure of [$Cu(py)_4VOF_4$], (py = pyridine) synthesised under mild hydrothermal conditions (see section 1.1.2). This compound exhibits both magnetic interactions as well as NLO properties. The alignment of the V=O bonds in the distorted vanadium oxyfluoride anions destroys the centre of symmetry within the chain. The research group of Zubieta reported various vanadium oxyfluorides with organophosphonates and phosphate linkers. Poeppelmeier and co–workers have reported transition metal oxyfluorides including vanadium and comparison studies based on polyhedral distortions. Both groups have characterised NLO properties or magnetic interactions of these oxyfluoride systems (see section 1.1.2).

1.1.1 Properties and Crystal Structures

Magnetic Properties

The availability of unpaired electrons in the d orbitals of vanadium provides magnetism. The arrangement of unpaired spins, geometry of the metal centre, dimensionality of the

crystal structure and contacts between magnetically active centres are the key factors determining the magnitude and the type of magnetic interactions. However 'single ion anisotropy' and 'spin–orbit coupling' have a great influence on magnetism[7] of clusters. These factors are always excluded when fitting various models such as Bleaney–Bowers model[8], Heisenberg chain model[9] and Ising chain model[10]. The compound $[C_{12}H_{12}N_2]_{0.5}[VOF_3]$ exhibits a 'spin–ladder' like structure (see section 1.1.2). The crystal structure shows two possible magnetic interaction pathways such as along the rungs and legs of the ladder. The magnetic susceptibility data are fitted well with a spin ½ Heisenberg antiferromagnetic chain model rather than a Bleaney–Bowers model, which reveals the superexchange pathway is predominantly along the legs of the ladder.[11] The strength of exchange interactions is related to the distance between vanadium centres, number of vanadiums bridged by a particular ligand and the bridging angle.[7] Trinuclear V^{3+} units exhibit "sausages" of magnetic frustration created by the corner-sharing $[VF_6]$ monomers in the unusual 1–D crystal structure of $[C_4H_{12}N_2]_3[V_7F_{27}]$.[12] The magnetic interaction is reported as antiferromagnetic, with geometric frustration, according to the review by Ramirez[13], which defines a method to distinguish ferrimagnetism from geometrically frustrated magnets.

NLO Properties

A beautiful summary about the relationship between the crystal structures and optical properties in oxide materials has been given by Halasyamani and Poeppelmeier.[14] Except for the point group 432, all the other 20 non–centrosymmetric point groups exhibit NLO behaviour, as shown in Figure 1.2. Especially the d^0 transition metal oxides exhibit out–of–centre octahedral distortions, which have a strong inter-connection with symmetry dependent properties, *eg*. in $LiNbO_3$.[15,16] The *intra*–octahedral distortions of the d^0 transition metal centres occur when having the terminal oxide bond or connection to another d^0 transition metal centre. Similar environments are observed in early d^0 transition metal oxyfluorides (*eg*. V^{5+}, Nb^{5+}, Mo^{6+}) and the magnitudes of the distortion have been parameterised by Halasyamani.[17]

4
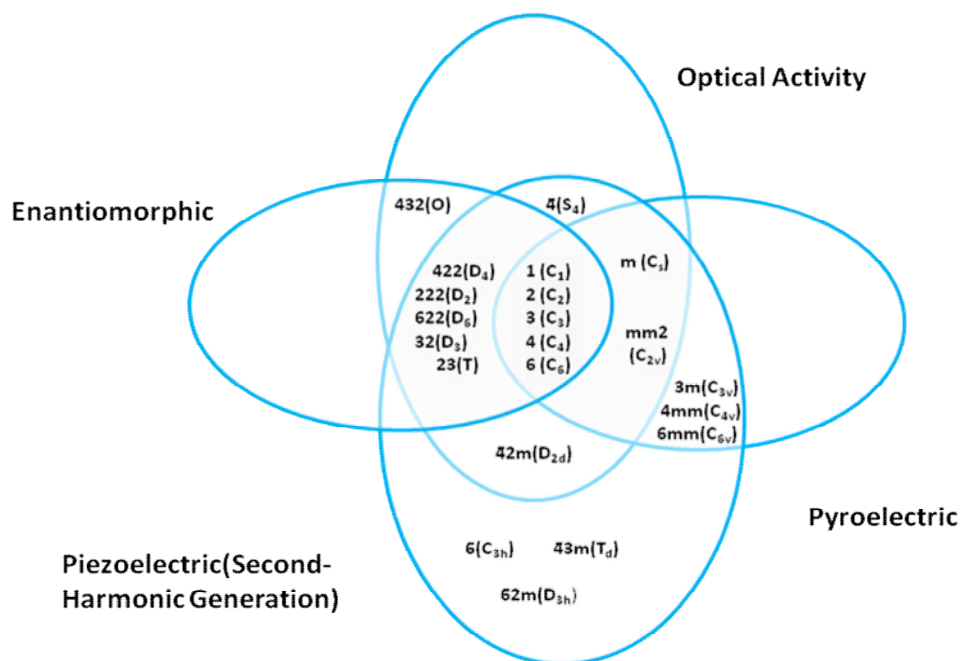
Figure 1.2 *Inter*–relationships of non–centrosymmetric point groups.[14]

A second–order Jahn–Teller distortion occurs in the octahedral d^0 transition metal centres, when non–degenerate d orbitals of the metal centre mix with excited p orbitals of the oxide or fluoride anion ligands. The consequence of this distortion is an asymmetric coordination environment within the octahedron. The distortions can occur in three possible directions (see Figure 1.3);

1. Towards the edge– distortion will be along the 2–fold axis of the octahedron, which results in two short, two long and two normal bond distances around the central metal atom.

2. Towards the face– distortion will be along the 3–fold axis of the octahedron, which results in three short and three long bond distances within the octahedron.

3. Towards the corner– distortion along the 4–fold axis, this results in one short, one long and four normal bond distances within the octahedron.

Metal centre (*eg.* V^{5+}, Nb^{5+}, Mo^{6+})

F^- ligand

O^{2-} ligand
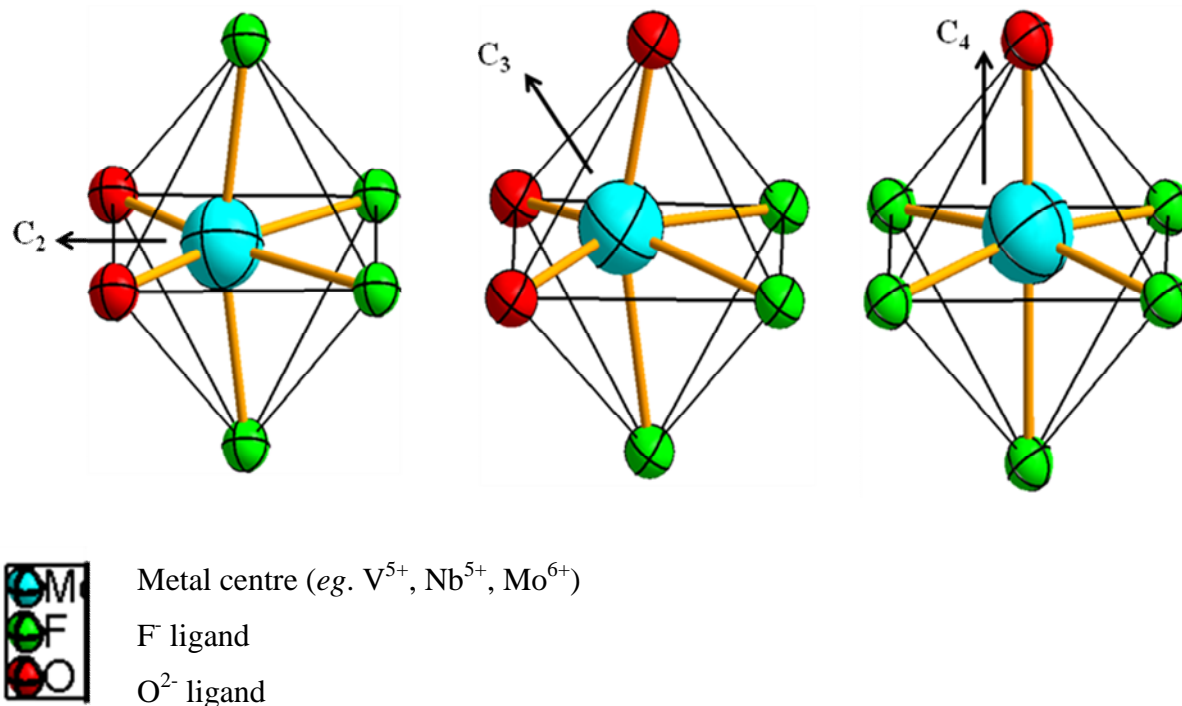
Figure 1.3 Three possible directions of *intra–octahedral distortion*

According to the Cambridge structural database none of the cations V^{5+}, Nb^{5+}, Mo^{6+} show all three types of *intra–octahedron* distortions. The C_4 *intra–octahedron* distortion occurs in vanadium and niobium oxides and oxyfluorides, while molybdenum shows C_2 and C_3 distortions in its highest oxidation states. The following section describes all three distortions using transition metal oxyfluorides.

Despite the availability of these polar building units, the rational design of polar crystalline solids still remains a challenge for solid state chemists. This is because the overall arrangement of these highly anisotropically distorted octahedra should be directed in the same sense, such that all anisotropic effects will be directed in a particular direction with resultant non–centrosymmetric space groups. The crystal structure of $[C_2N_2H_{10}][VOF_4(H_2O)]$ contains octahedral vanadium in the +4 oxidation state and exhibits polar ordering of monomers, as can be seen in Figure 1.4, all the dipoles align along the *b* axis.[18] The coordination environment of these highly distorted octahedra (C_4 *intra–octahedral* distortion) contain four terminal fluoride ligands at the equatorial sites, a short terminal V=O bond and *trans* aqua ligand occupy the axial sites. The 'underbonded'

nucleophilic oxygen or fluorine has to be stabilised either by protonation or by hydrogen bonding interactions or by bridging neighbouring metal centres. Therefore the polar crystal structure is dominated by *inter*–chain and *intra*–chain hydrogen bond interactions in a 'head–to–tail' manner from the water molecules coordinated to vanadium centres and the organic moiety forming infinite chains parallel to the *b* axis.
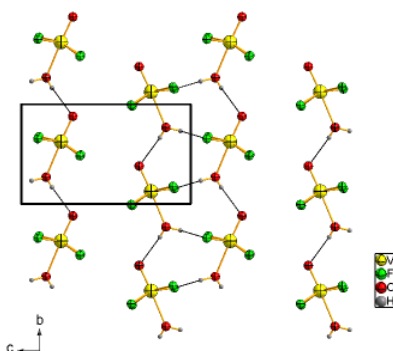
Figure 1.4 View of the crystal structure of $[C_2N_2H_{10}][VOF_4(H_2O)]$ along the *a* axis with *inter*–chain and *intra*–chain hydrogen bonding interactions. Organic moieties have been omitted for clarity.

Vanadium also shows the C_4 distortion in the compound $[pyH]_2[Cu(py)_4(VOF_5)_2]$, which crystallises in the centrosymmetric space group C2/c.[19]
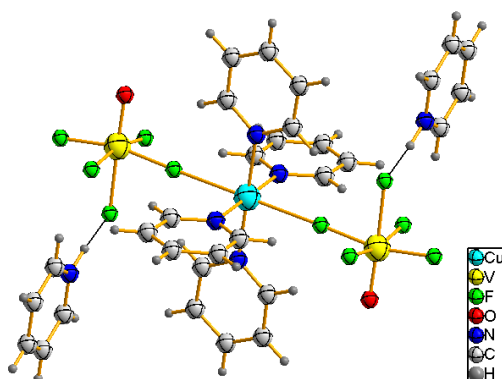
Figure 1.5 The building unit in $[pyH]_2[Cu(py)_4(VOF_5)_2]$.

The anion unit $[VOF_5]^{2-}$ exhibits a C_4 distortion, which results in an elongated V–F bond *trans* to the short V=O bond. The stability of the V–F bond is reinforced by a hydrogen bond interaction from the pyridinium cation. The building unit consists of two anion units

on opposite sides of the $[Cu(py)_4]^{2+}$ cation in a non–centrosymmetric manner forming a neutral cluster (see Figure 1.5). However, the non–centrosymmetric clusters are arranged in a centrosymmetric space group. A similar system is observed for $[pyH]_2[Cu(py)_4(NbOF_5)_2]$, which crystallises in the $I4_122$ space group.[20] Further studies on this system yielded a 1–D chain with composition $[Cu(py)_4(NbOF_5)]$ as shown in Figure 1.6. The bridging atom between the copper and niobium determines the overall crystal symmetry, which has been proved by second harmonic generation (SHG) measurements. An ordered O/F arrangement would be non–centrosymmetric, with Cc space group. However, the negative result from the powder SHG measurements requires the bridging atom to be O/F disordered, which makes the overall packing into a centrosymmetric space group C2/c. Both the $[Cu(py)_4]^{2+}$ cation and $[NbOF_5]^{2-}$ anion build the connectivity in a *trans* manner.
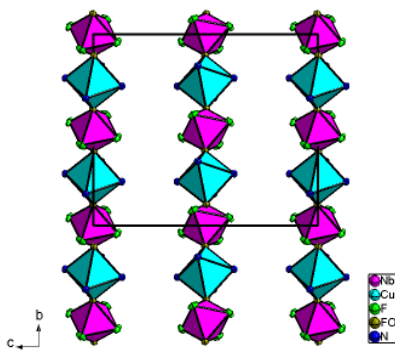
Figure 1.6 Packing in $[Cu(py)_4(NbOF_5)]$; carbon and hydrogen atoms have been omitted for clarity.

The C_2 distortion is observed in the non–centrosymmetric crystal structure of $[Zn(pyz)(H_2O)_2 MoO_2F_4]$, (pyz = pyrazine).[21] The crystals were twinned and exhibit two enantiomorphic forms, with space group $P3_121$ for one and $P3_221$ for the other. The anionic moiety $[MoO_2F_4]^{2-}$ exhibits an *intra*–octahedral distortion in which two longer *cis* Mo–F bonds are *trans* to two short *cis* Mo=O bonds. The more nucleophilic fluorides are stabilised either by forming hydrogen bonds or by linking to the cationic moiety. The *cis* directing anion, $[MoO_2F_4]^{2-}$ and *trans* directing cation, $[Zn(pyz)(H_2O)_2]^{2+}$ are alternately arranged through nucleophilic fluorides and lead to a helical packing

arrangement as shown in Figure 1.7. The connectivity between the helical chains occurs through pyrazine rings.
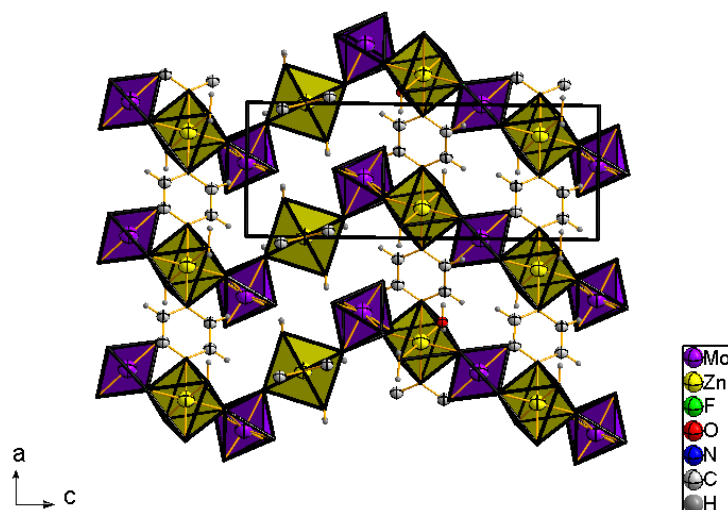
Figure 1.7 Crystal packing in [Zn(pyz)(H$_2$O)$_2$MoO$_2$F$_4$].

A similar system is observed in the non–twinned crystal of [Cd(pyz)(H$_2$O)$_2$MoO$_2$F$_4$]. [22] Both crystals are active for SHG, but the Zn phase shows a weaker response compared to the Cd phase due to the presence of twinning.

The material [(Ag$_3$MoO$_3$F$_3$)(Ag$_3$MoO$_4$)Cl] crystallises in a polar non–centrosymmetric space group P3m1.[23] There are two types of coordination environment of Mo; C$_3$ *intra–* octahedron distorted [MoO$_3$F$_3$]$^{3-}$ and the tetrahedral [MoO$_4$]$^{2-}$ as shown in Figure 1.8. Both the anions are comprised into chains and connected through Ag$^+$ cations. There are compounds reported by other researchers with the anion [MoO$_3$F$_3$]$^{3-}$, but all exhibit O/F disorder.[24] So far this is the only structure without O/F disorder in the [MoO$_3$F$_3$]$^{3-}$ group, the connectivity of Ag$^+$ helps to avoid the disorder of O/F. The chloride anions maintain the charge neutrality of the structure.
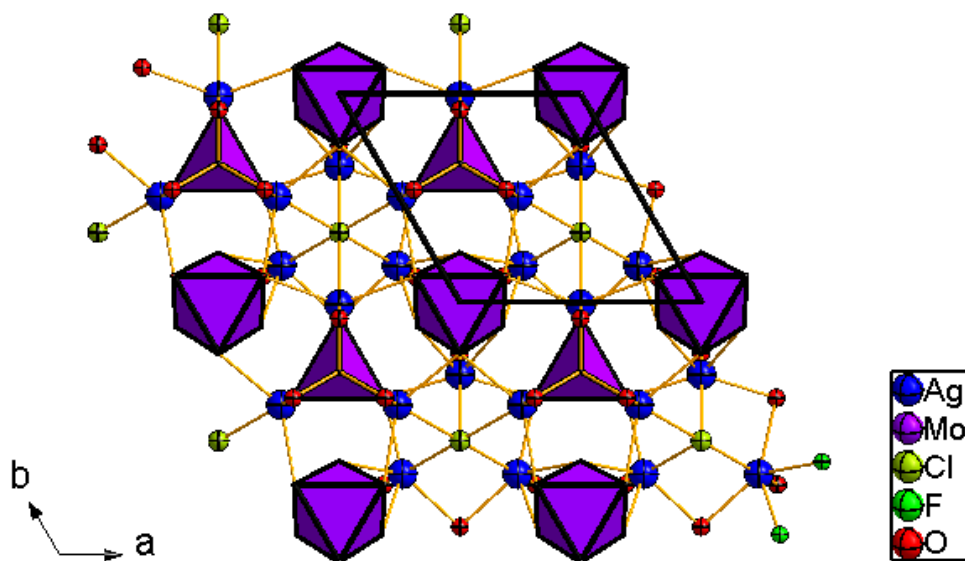
Figure 1.8 Crystal packing in [(Ag$_3$MoO$_3$F$_3$)(Ag$_3$MoO$_4$)Cl].

1.1.2 Crystal Chemical and Topographical Aspects

Under hydrothermal conditions vanadium can adopt a range of oxidation states from +3 to +4 and +5. Consequently the geometry of the vanadium centre may vary from tetrahedral to trigonal bipyramidal to square pyramidal and octahedral. The overall crystal packing is influenced by these different coordination environments, and can exhibit cluster, chain, layer and 3–D networks. Tetrahedrally coordinated vanadium is only possible when vanadium is in the +5 oxidation state. An excellent review article, by Zavalij and Whittingham[25] explains the oxidation state changes with geometry in vanadium oxides and also discusses the structural parameters used to distinguish square pyramidal geometry from trigonal bipyramidal geometry. However, the vanadium oxyfluoride system has not been sufficiently well explored or documented up to now. The following section discusses the available well characterised examples based on the geometry of the oxyfluoride units and oxidation state of vanadium, as well as various combinations of fluoride and oxide ligands and number of vanadyl bonds for each combination under a particular geometry.

Tetrahedral Geometry in Vanadium Oxyfluorides

[VO₃F] composition with two vanadyl bonds in a vanadium dimer

The crystal structure of $[Cu_2(tpyprz)\{HO_3P(CH_2)_3PO_3H\}][V_2O_5F_2]$ (tpyprz = tetra–4–pyridylpyrazine) with space group C2/c exhibits a 1–D chain.[26] The tetrahedron dimerises into the $[V_2O_5F_2]^{2-}$ anion unit and does not take part in the formation of the chain and occurs as an isolated anionic cluster in the crystal structure, as shown in Figure 1.9. The copper complexes link to one another through phosphate linkers and extend into a chain. Two tetrahedral V^{5+} centres share corners through an oxygen ligand, while the other two vanadyl bonds and fluorine ligands occupy the terminal sites. The similar anionic system "pyrovanadate", $[V_2O_7]^{4-}$, is well characterised in vanadium oxides.[1] The presence of the secondary metal and organic template contribute to increase the dimensionality whereas the purely tetrahedral vanadium geometry favours a 1–D chain in the absence of other linkers such as phosphates, organo amines, secondary metals etc. However, the bulky tpyprz ligand coordinates to the copper centre, reflecting the influence of keeping the $[V_2O_5F_2]^{2-}$ anions as isolated clusters without connecting to the copper complex.
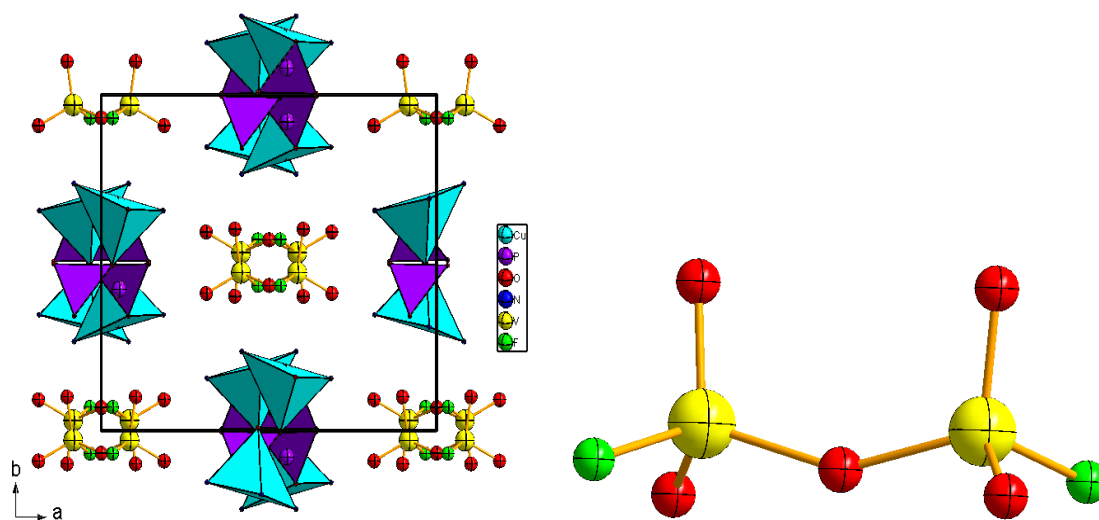
Figure 1.9 Crystal packing in $[Cu_2(tpyprz)\{HO_3P(CH_2)_3PO_3H\}][V_2O_5F_2]$ (left) and the dimer, $[V_2O_5F_2]^{2-}$ (right). Carbon and hydrogen atoms have been omitted for clarity.

[VO₃F] composition with a short vanadyl bond in a vanadium tetramer

Vanadium exists exclusively in a tetrahedral environment in the crystal structure[27] of $[Cu_2(bisterpy)V_4O_{11}F_2]$, (bisterpy= 2,2':4',4":2",2'''–quarter–pyridyl–6',6"–di–2–pyridine). A 1–D neutral chain is built up from the nearly linear tetrameric tetrahedral anion motif $[V_4O_{11}F_2]^{4-}$ and the copper cation complex parallel to the *b* axis, as shown in Figure 1.10. The [VO₃F] units contain a single vanadyl bond, two oxygen ligands connect to [VO₄] and [Cu₂(bisterpy)] and the terminal fluoride ligand. There are two crystallographically different vanadium sites: [VO₄] share the corner of the apical site in square pyramidal copper, while [VO₃F] share the corner of an in–plane site of square pyramidal copper complex. Vanadium and copper are linked through oxide ligands forming a bimetallic ring, $[Cu_2V_4O_6]$ within the chain. Each chain extends into 2–D layers by connecting through bisterpy ligands.
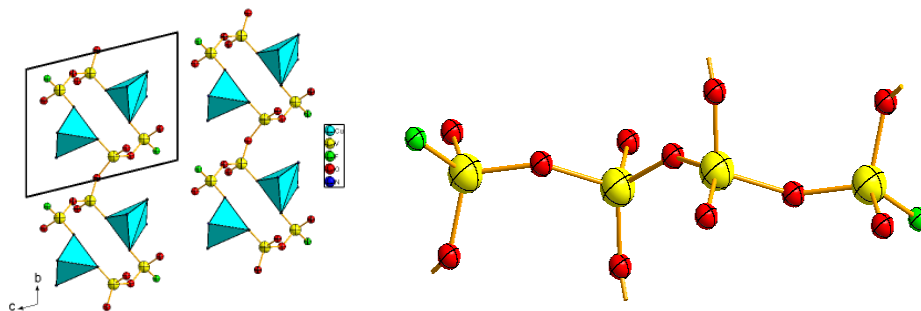
Figure 1.10 Crystal packing in $[Cu_2(bisterpy)V_4O_{11}F_2]$ (left) and the tetramer, $[V_4O_{11}F_2]^{4-}$ (right) with the connections of the bridging ligands. Carbon and hydrogen atoms have been removed for clarity.

Square Pyramidal Geometry in Vanadium Oxyfluorides

[VOF₄] composition

$[Cu(py)_4VOF_4]$ has a non–centrosymmetric structure with space group C222₁, and contains 1–D chains constructed from the square pyramidal anion $[VOF_4]^{2-}$, with V^{4+} oxidation state, and the $[Cu(py)_4]^{2+}$ cation linked through fluoride ligands in an alternate

manner.[6] The coordination environment can be defined as two bridging fluoride ligands, two terminal fluoride ligands and a short terminal V=O vanadyl bond on the apical site. The copper equatorial sites are occupied by pyridine rings, while the axial sites, occupied by fluoride ligands, link to the anion motif in a *trans* manner. Both the cation and anion are connected in a *trans* manner, which favours a linear chain instead of a non–linear arrangement like a helix. The V=O bond alignment in a particular chain remains the same. These similar chains are arranged alternately in (110) and (1−10) planes. Both chains are distinguished by giving different colours for the copper polyhedron in Figure 1.11, but both are crystallographically identical, the only difference between these chains being the V=O bond direction. This makes a significant contribution in the magnitude of SHG response.
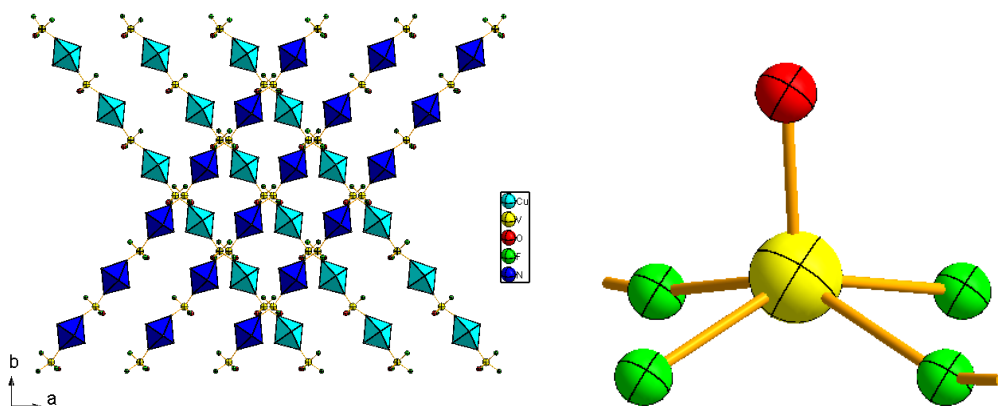
Figure 1.11 The crystal packing in $[Cu(py)_4VOF_4]$ (left) and the square pyramidal anion, $[VOF_4]^{2-}$, with the connections of the bridging ligands (right). Carbon and hydrogen atoms have been omitted for clarity.

$[VO_4F]$ composition

The compound $[Cu_2(bisterpy) V_2O_2F_2(H_2O)_2\{HO_3P(CH_2)_2PO_3\}_2].2H_2O$ exhibits a 2–D layer[28] structure, as shown in Figure 1.12, constructed from a square pyramidal $[VO_4F]$ anion linked through ethylene–diphosphonate ligands to a copper cation complex $[Cu_2(bisterpy)]^{4+}$. The vanadyl bond is at the apical site of the V^{4+} square pyramid, while the other two oxide ligands from diphosphonates, fluoride ligand and an aqua ligand

occupy the planar sites. There is no direct contact between the metal centres, only bridging through the diphosphonate ligand. The diphosphonate ligands are coordinated to vanadium and copper, forming different sizes of rings in the layer.
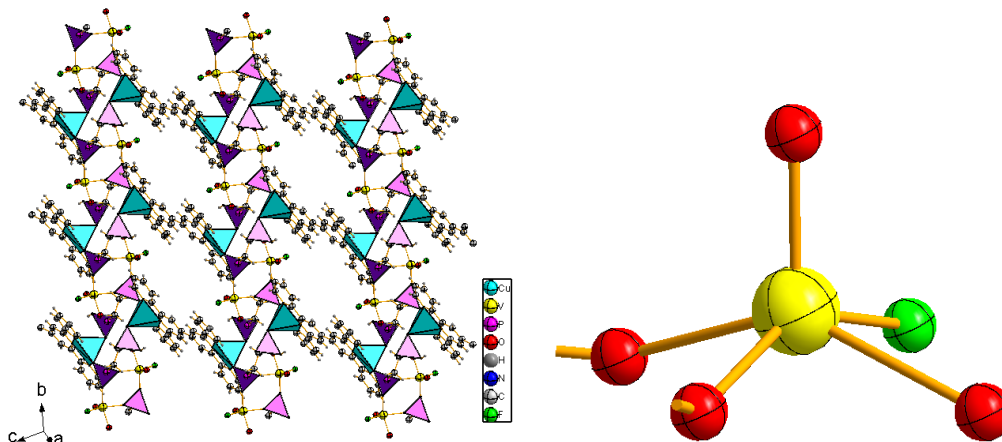
Figure 1.12 The layer arrangement in [Cu$_2$(bisterpy) V$_2$O$_2$F$_2$(H$_2$O)$_2${HO$_3$P(CH$_2$)$_2$PO$_3$}$_2$] .2H$_2$O (left) and the square pyramidal vanadium, [VO$_4$F], with the connections of the bridging ligands (right).

[VO$_3$F$_2$] composition

The 1–D chain compound with formula [{Cu$_2$(bisterpy)}V$_2$O$_4$F$_4${HO$_3$P(CH$_2$)$_2$PO$_3$H}][28] is constructed from another different square pyramidal ligand combination, the [VO$_3$F$_2$] anion, with vanadium in the +5 oxidation state. The apical position of the square pyramid is occupied by the vanadyl bond, the planar sites are occupied by two terminal fluoride ligands and bridging oxide ligand to the copper complex and another oxide from the organophosphonate ligand. Bimetallic rings are formed by the phosphonate ligands connecting the copper cations and vanadium anions. These rings are linked through bisterpy ligands coordinated to copper, into a chain parallel to the *b* axis, as shown in Figure 1.13.
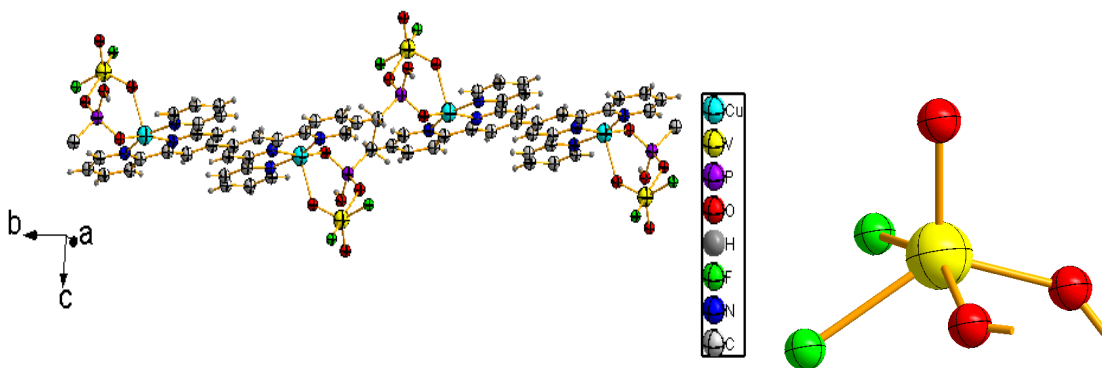
Figure 1.13 Chain fragment in [{Cu$_2$(bisterpy)}V$_2$O$_4$F$_4${HO$_3$P(CH$_2$)$_2$PO$_3$H}] (left) and the square pyramidal vanadium, [VO$_3$F$_2$], with the connections of the bridging ligands (right).

Trigonal Bipyramidal Geometry in Vanadium Oxyfluorides

[VOF$_4$] composition

The trigonal bipyramidal anion [VOF$_4$]$^{2-}$ unit is incorporated into two independent 1–D chains with overall formula of [Cu(py)$_4$VOF$_4$][Cu(py)$_4$(H$_2$O)VOF$_4$].H$_2$O (Figure 1.14).[6] Vanadium is present in the +4 oxidation state in both chains and exhibits distorted geometry. The chain of [Cu(py)$_4$VOF$_4$] is built up from [Cu(py)$_4$]$^{2+}$ cations and [VOF$_4$]$^{2-}$ anions arranged in an alternate manner and connected through fluoride ligands. The clusters of [Cu(py)$_4$(H$_2$O)VOF$_4$] connect one to another through hydrogen bonding interactions and lead to 1–D chains. The distorted trigonal bipyramidal anion unit bridges [Cu(py)$_4$]$^{2+}$ through an oxide ligand on the axial site of copper, while pyridine occupies the four equatorial coordination sites. There is no direct bond between these chains. However, the strong hydrogen bonds donate from the water molecule of the [Cu(py)$_4$(H$_2$O)VOF$_4$] cluster to nucleophilic fluorides of the adjacent [Cu(py)$_4$VOF$_4$] chain. Overall, the 3–D supramolecular network is dominated by hydrogen bonding interactions.
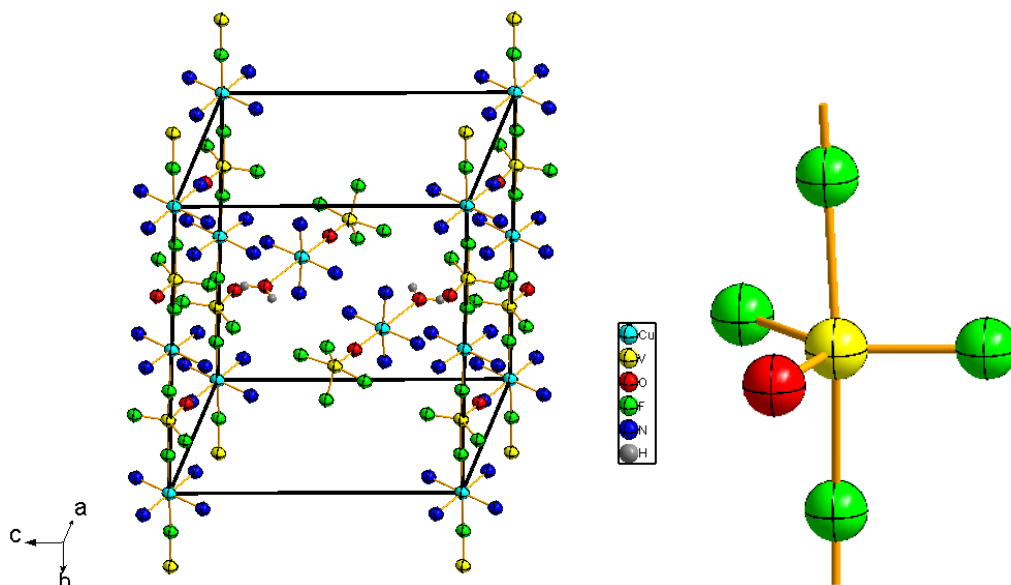
Figure 1.14 The arrangement of two independent chains in $[Cu(py)_4VOF_4]$ $[Cu(py)_4(H_2O)VOF_4].H_2O$ (left) and the trigonal bipyramidal $[VOF_4]^{2-}$, with the connections of the bridging ligands (right). Carbon and hydrogen atoms have been omitted for clarity.

Octahedral Geometry in Vanadium Oxyfluorides

[VOF₅] composition

The compound $[C_{12}H_{12}N_2]_{0.5}[VOF_3]$ exhibits 'ladder–like' chains running parallel to the *c* axis.[11] The asymmetric unit contains one distorted octahedron due to the presence of a short V=O and *trans* elongated V–F, causing an asymmetric environment within the octahedron. The *trans* fluoride ligands are highly nucelophilic and stabilised by sharing edges of neighbouring octahedral vanadium. Vanadium is present in the +4 oxidation state and the coordination environment contains four doubly bridging fluoride ligands, such that the octahedral vanadiums share corners along the *c* axis to form chains, and share edges parallel to the *b* axis, to form the rungs of the ladder as shown in Figure 1.15.
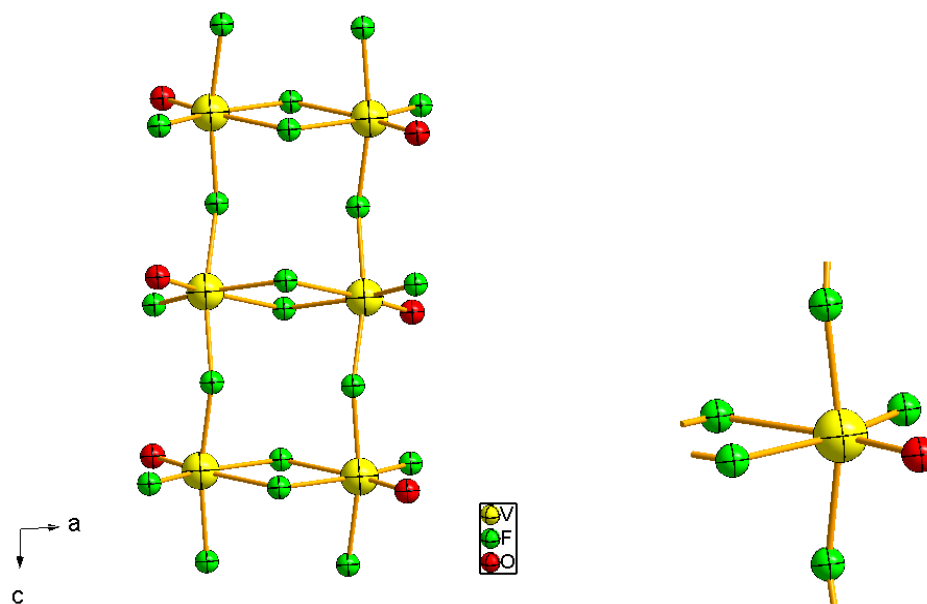
Figure 1.15 The 'ladder–like' chain running parallel to the *c* axis in $[C_{12}H_{12}N_2]_{0.5}[VOF_3]$ (left) and the octahedral vanadium (right), with the connections of the bridging ligands (right). Carbon and hydrogen atoms have been omitted for clarity.

$[VO_2F_4]$ composition

The crystal structure of $[C_4N_2H_{12}][VF_3(SO_4)]$ contains octahedral $[VO_2F_4]$ units, with vanadium in the +3 oxidation state with a centrosymmetric bonding environment within the octahedron and average angle between the *cis* and *trans* ligands being 90° and 180° respectively.[29] Corner–sharing fluoride ligands form linear infinite chains parallel to the *a* axis as shown in Figure 1.16. All the fluoride ligands occupy the equatorial sites, while the axial sites are occupied by oxygens from the sulphate ligands. Tetrahedral sulphate ligands bridging neighbouring octahedral vanadium of *trans* directing chain in *trans* form along the *a* axis.
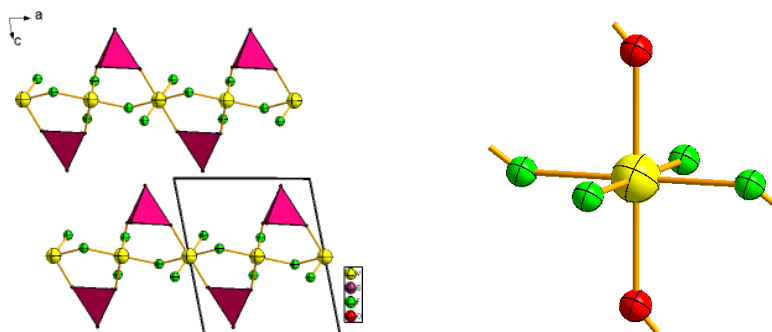
Figure 1.16 1–D chain in $[C_4N_2H_{12}][VF_3(SO_4)]$ (left) and the octahedral vanadium (right), with the connections of the bridging ligands (right). Organic moieties have been omitted for clarity.

$[VO_2F_4]$ composition with two short vanadyl bonds

The building unit of $[N(CH_3)_4]_2[KV_2O_4F_5].H_2O$ contains face-sharing octahedral dimers, with vanadium in the +5 oxidation state[30] (Figure 1.17). Each octahedron contains three bridging fluorides, terminal fluoride and two terminal vanadyl bonds. There are hydrogen bonding interactions from water molecules and organic moieties to the fluoride ligands of the bioctahedron. K^+ ions are located between the dimeric units and bridge the neighbouring dimers through fluoride ligands to form infinite chains parallel to the *a* axis.
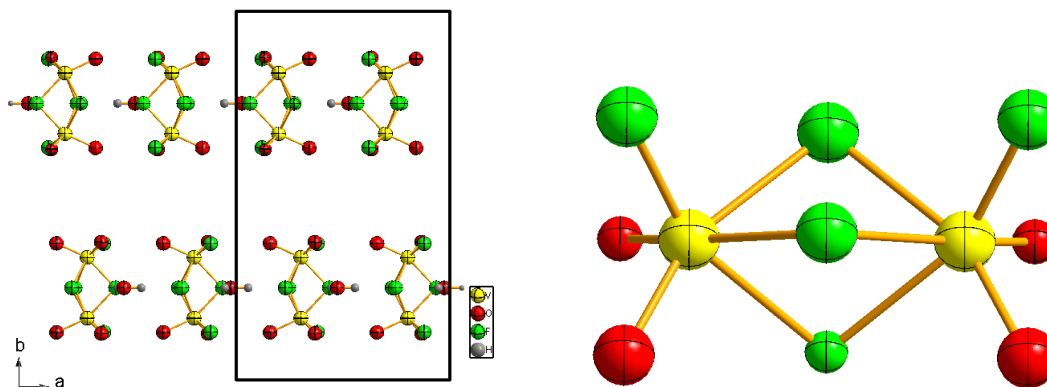
Figure 1.17 The arrangement of bioctahedral vanadium in $[N(CH_3)_4]_2[KV_2O_4F_5].H_2O$ (left) and the face–sharing octahedral dimers (right). Organic moieties and K^+ ions have been omitted for clarity.

[VO₃F₃] composition

The 2–D layer structure of $[H_2en]_2[V_6F_{12}(H_2O)_2\{O_3P(CH_2)_5PO_3\}_2\{HO_3P(CH_2)_5PO_3H\}]$, (en = ethylenediamine)[31] is constructed from corner–sharing octahedral vanadium present in the +3 oxidation state, with organoamine and diphosphonate linkers. There are three crystallographically different vanadium sites with two different coordination environments: the coordination environment can be defined by two bridging fluorides linking to two crystallographically different vanadium sites, three phosphonate oxygen donors and a terminal fluoride ligand, while the other vanadium has two bridging fluorides connecting crystallographically different vanadium sites, two phosphonate oxygen donors, a water molecule and a terminal fluoride ligand. A combination of corner–sharing octahedral vanadium and tetrahedral phosphonate form a 2–D layer, as shown in Figure 1.18. The *inter*–layer region is occupied by organic moieties.
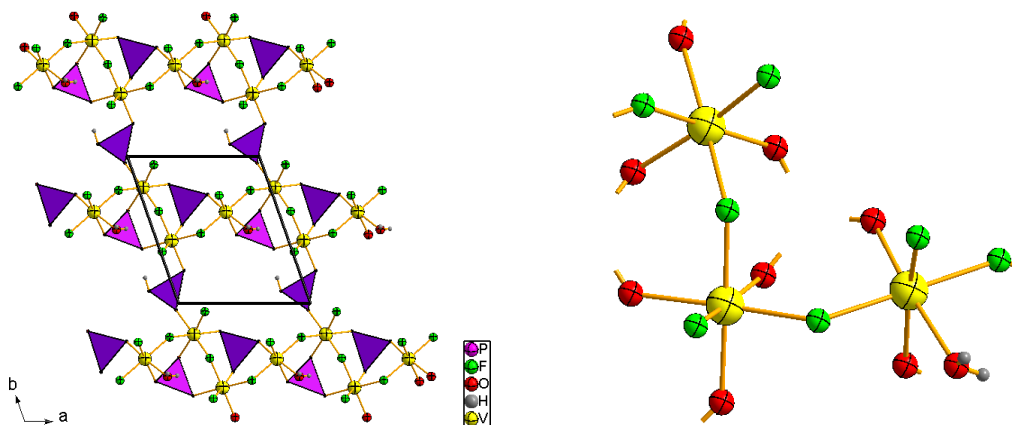
Figure 1.18 2–D layer in $[H_2en]_2[V_6F_{12}(H_2O)_2\{O_3P(CH_2)_5PO_3\}_2\{HO_3P(CH_2)_5PO_3H\}]$ in the *ab* plane (left) and the building unit with the connections of the bridging ligands (right). Carbon and hydrogen atoms have been removed for clarity.

The crystal structure of $[\{Cu(tpyprz)(H_2O)_2\}V_4F_6O_6(O_3PCH_2CH_2PO_3)]$ exhibits a 2–D layer constructed from mixed valence vanadium octahedra, diphosphonate ligands and a copper cationic complex, as shown in Figure 1.19.[26] The building unit contains edge–sharing octahedral vanadium tetramers with two crystallographically different vanadium

atoms present in +4 and +5 oxidation states. The phosphonate ligands bridge both the crystallographically different vanadium sites as well as the square pyramidal copper complex. Two of the vanadium octahedra contain two bridging fluorides, bridging oxide, oxide ligand from phosphonate donors, terminal fluoride and short terminal vanadyl bond in the coordination environment. The other two contain three bridging fluorides, bridging oxide, oxide from phosphonate donor and terminal vanadyl bond. The tetramer in cluster is linked through copper cations $[Cu_2(tpyprz)(H_2O)_2]^{4+}$, forming a layer structure.
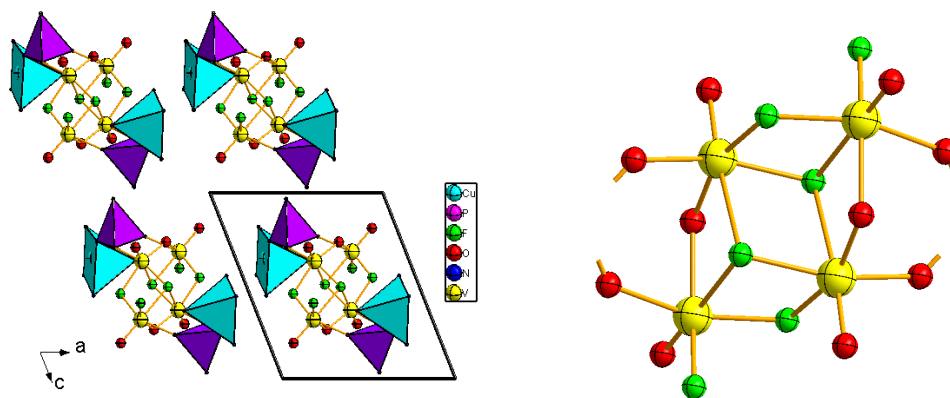
Figure 1.19 The 2–D layer in $[\{Cu(tpyprz)(H_2O)_2\}V_4F_6O_6(O_3PCH_2CH_2PO_3)]$ (left) and the octahedral tetramer with the connections of the bridging ligands (right). Carbon and hydrogen atoms have been removed for clarity.

$[VO_4F_2]$, $[VO_5F]$, $[VO_3F_3]$ composition

Various research groups use different linkers with vanadium metal centres such as phosphates, sulphates and arsenate ligands to extend the structural dimensions. The crystal structure of $[\{V_6O_{12}F_4(Ph_3AsO_2)(Ph_2AsO_2)_2\}.2MeCN]$, (Ph = phenyl) contains vanadium in octahedral environments with different fluoride/oxide anion stoichiometry; $[VO_5F]$, $[VO_3F_3]$, $[VO_4F_2]$.[32] The asymmetric unit contains 3 crystallographically different vanadium sites present in the +5 oxidation state; oxide and fluoride ligands bridging them and forming trimetallic ring. The coordination environment can be defined for $[VO_5F]$ as two bridging oxides, two oxides ligand from arsenic donors, bridging fluoride and the short terminal vanadyl. There are two bridging oxides, three bridging

fluoride and the terminal vanadyl in the coordination environment of [VO$_3$F$_3$] unit. The [VO$_4$F$_2$] unit contains two bridging oxides, two bridging fluorides, oxide ligand from arsenic donor and the terminal vanadyl. The building unit remains as a cationic cluster without further connectivity, as can be seen in Figure 1.20. The bulky phenyl groups around arsenic favour a low dimensional structure.
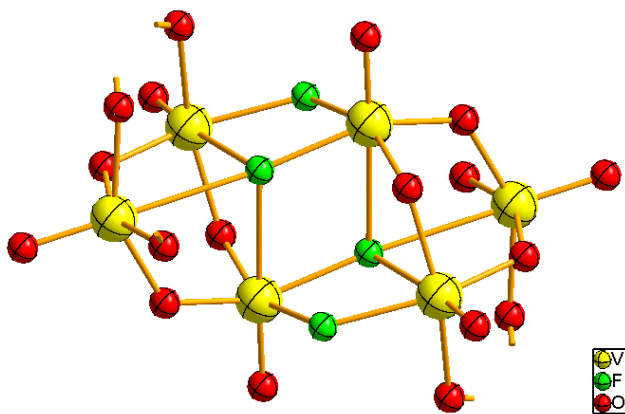
Figure 1.20 The building unit in [{V$_6$O$_{12}$F$_4$(Ph$_3$AsO$_2$)(Ph$_2$AsO$_2$)$_2$}.2MeCN] with the connections of the bridging ligands.

[VO$_5$F] composition

The crystal structure of the anionic cluster with the formula of [Et$_4$P][(V$_2$O$_3$)$_2$(O$_3$PPh)$_4$F], (Et = ethyl) contains four crystallographically different vanadium atoms exclusively present in the +5 oxidation state.[33] The cluster exhibits distorted tetrahedral geometry, with the corners of the tetrahedra occupied by phosphonate ligands and each face occupied by a different octahedral vanadium site. The coordination environment of all vanadium centres are identical; three oxide ligands from phosphonate donors, bridging oxide ligand, bridging fluoride ligand and the terminal vanadyl bond. As expected the short vanadyl bond lies *trans* to fluoride and both occupy the axial sites of C$_4$ *intra–* octahedral distorted vanadium. The unusual tetrahedral fluoride ligand bridges all four crystallographically different vanadiums, occupying the centre of the each cluster, as shown in Figure 1.21. The phenyl rings around the phosphonate ligand again favour a cluster rather than an extended structure.
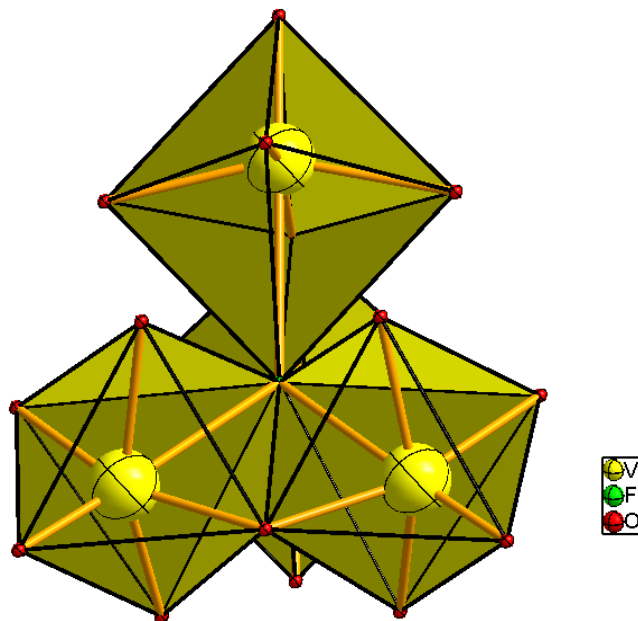
Figure 1.21 The tetrahedral cluster in [Et$_4$P][(V$_2$O$_3$)$_2$(O$_3$PPh)$_4$F].

1.1.3 Mixed Metal Frameworks

It is frequently observed that exclusively vanadium oxyfluoride systems with structure directing organic amines provide oligomeric building units or clusters.[34] In an attempt to further increase the dimensionality towards framework structures, a secondary metal can be included in the same systems. These mixed metal frameworks offer the possibility of combining properties, for example magnetic and optical.[6] The early transition metal, vanadium, is a hard acid and prefers to coordinate with a hard base (Hard Soft Acid Base –HSAB theory), such as fluoride or oxide, which are available in the reaction medium. Therefore the bonding affinity towards the amine compound is relatively less. Most of the vanadium oxyfluorides form hydrogen bonding interactions with these organoamine compounds which act as isolated cations instead of being a ligand. Introducing a late transition metal as a secondary metal in similar reaction media, these soft acids prefer to bind with soft bases such as organoamines. Therefore, bimetallic systems in the presence of organoamines can produce various structures with the following four different possibilities:

(1) Organoamine acting as isolated cation.

(2) Organoamine only bound to vanadium oxide/oxyfluoride system; this is only possible if the secondary metal is absent in the crystal structure.

(3) Organoamine acts as ligand to secondary metal, while the secondary metal is bound to the vanadium oxide/oxyfluoride moiety.

(4) Organoamine completely bound to secondary metal, while the vanadium oxide/oxyfluoride occupies the *inter*–region as an isolated monomer, oligomer, cluster or chain.

Organoamine acting as isolated cation

The crystal structure of $[C_2H_{10}N_2]_2[V_6MnO_{18}]$ exhibits a 2–D layer structure built from metal oxide layers.[35] Tetrahedral vanadium and octahedral manganese exhibit +5 and +2 oxidation states, respectively. Tetrahedral vanadium engages exclusively in corner-sharing interactions, three sites contribute to bridge manganese and another vanadium, while the remaining site is a terminal ligand. Each manganese octahedron shares corners with six vanadium tetrahedra and forms a metal oxide open framework with different sizes of –V–Mn– centred rings such as $[V_2Mn]$, $[V_6Mn_2]$ and $[V_7Mn_2]$. The protonated ethylenediammonium cations occupy cavities (Figure 1.22) and form hydrogen bonds with oxygen coordinated to vanadium. The organoamines maintain the charge neutrality of the overall structure.
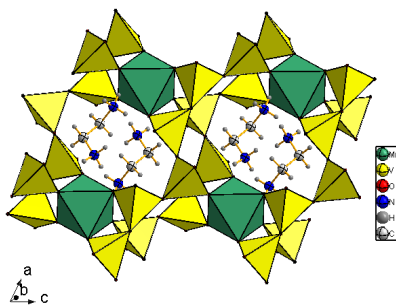
Figure 1.22 Ethylenediammonium cations occupying the cavity of $[C_2H_{10}N_2]_2[V_6MnO_{18}]$.

Organoamine only bound to vanadium

Generally organic N–donor ligands prefer to bind with late transition metals, according to HSAB theory. However, in the absence of those metals, vanadium may bind with organoamine ligands such as 2,2'–bipyridyl, phenanthroline, pyridine, etc. Vanadium exhibits mixed valence, +4 and +5 in the layered structure with composition $[C_{12}H_8N_2][V_3O_7]$.[36] The coordination environment of distorted octahedral vanadium (IV) can be defined by a bidentate phenanthroline ligand, terminal oxygen and three bridging oxygens. The corner-sharing tetrahedral vanadium (V) and $[VO_4(1,10–phenanthroline)]$ octahedra form infinite double chains linked through oxygen ligands and forming a layered structure, as shown in Figure 1.23.
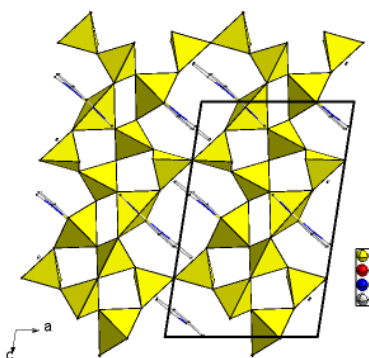
Figure 1.23 The 2–D sheet in $[C_{12}H_8N_2][V_3O_7]$; phenyl rings have been shown using wire model for clarity.

Organoamine acts as ligand to secondary metal, while the secondary metal is bound to vanadium.

Vanadium oxyfluoride units linked to secondary metal complexes with organoamine ligands provide various structures with different dimensionalities. The crystal structure of $[Cu(py)_4VOF_4][Cu(py)_4(H_2O)VOF_4].H_2O$ exhibits an infinite 1–D chain, as explained in the previous section 1.1.2. Cu, Ni, Co, Zn and Mn have been introduced as secondary metals in various systems with different amines, to provide chains, layers and 3–D networks.[1] Organoamines with phenyl rings significantly affect the formulations of extended structures due to their steric constraints and alignments.[26] Consequently, responses may be reduced on measurements of properties such as extended magnetism.[11]

Organoamine completely bound to secondary metal, while the vanadium occupies the *inter*–region without any direct bonding towards secondary metal or organoamine.

The crystal strucutre of $[VO(H_2O)_5][Cu_2(bpym)_2(H_2O)(SO_4)_3].7H_2O$, (bpym = 2,2'–bipyrimidine) exhibits a *zig–zag* chain built up from the copper complex anion, while the vanadium cation occupies the *inter*–chain region.[37] The two crystallographically different Jahn–Teller active copper centres exhibit distorted octahedra due to the steric and geometric constraints of the bidentate ligands. The coordination environment of copper can be defined by two bidentate ligands and oxygen atoms from tetrahedral sulphate and aqua ligands. The octahedral vanadium complex is in the +4 oxidation state and contains five aqua ligands and the terminal vanadyl bond in the coordination sites. The copper anionic chain runs parallel to the *a* axis, while the cationic vanadium complex and water molecules occupy the inter-region as shown in Figure 1.24. There is no direct bonding between the copper complex and vanadium cation, but strong hydrogen bonding interactions between the water molecules coordinated to vanadium and sulphate groups coordinated to copper.
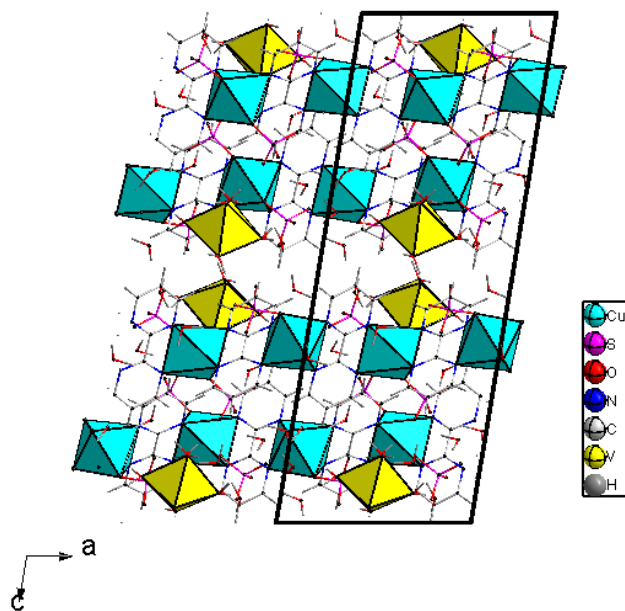
Figure 1.24 $[VO(H_2O)_5][Cu_2(bpym)_2(H_2O)(SO_4)_3].7H_2O$; phenyl rings have been shown using a wire model for clarity.

The addition of organoamine compounds leads to a variety of roles based on the crystal structures:

1. Mostly in vanadium oxyfluoride systems, protonated organic moieties occupy the inter–region and act to maintain the charge neutrality of the overall structure.[35]

2. The interstices of the lattice are occupied by these amine compounds as space filling species and increase the framework stability by minimising void volume.[35]

3. Organoamines act as ligands to metal complexes and lead to inorganic-organic hybrid structures.[36]

4. Mostly organonitrogen compounds are hydrogen bond donors leading to strong hydrogen bonding networks.[18]

5. Ultimately, they may act as structure directing agents.[1]

The incorporation of a secondary metal (transition metal) into the vanadium systems plays different roles in the crystal structures;

1. Improving the structural diversity

    Mostly, hydrothermal synthesis in vanadium oxyfluoride systems produces oligomers rather than extended structures, in the absence of linkers such as phosphates, sulphates or arsenate ligands. The literature survey reveals the addition of a secondary metal into the system widens the structural diversity into chains, layers and 3–D networks.

2. Magnetic properties

    Introducing transition metals such as manganese, copper, nickel or cobalt may provide extended magnetic properties due to the presence of unpaired electrons in the d orbitals. The crystal structure of $[Cu_2(tpyprz)\{HO_3P(CH_2)_3PO_3H\}][V_2O_5F_2]$ was discussed previously in section 1.1.2; the magnetic susceptibility data proved the presence of antiferromagnetic coupling between the copper(II) centres. The crystal structure shows two possible pathways through organoamine and

26

diphosphonate ligands along the chain. However, a Heisenberg spin ½ model fitted well with susceptibility data and shows a dimeric spin interaction due to the long distance between copper centres along the chain.

3. Mostly, organoamines act as ligands with these secondary metal centres to form different metal complexes.

4. First–order Jahn–Teller distortion

The octahedrally coordinated d^9 copper complexes exhibit a first–order Jahn–Teller distortion, with tetragonal elongation via four short equatorial and two long axial bonds. This has been observed in the combination of vanadium oxyfluoride system with copper complexes.[6] The combination of first and second–order Jahn–Teller active metal centres provides a stable bonding network.

1.1.4 Hydrothermal Synthesis in Vanadium Oxyfluoride Systems

Hydrothermal synthesis has been used widely and successfully in the field of vanadium chemistry in the past decade. A review about the hydrothermal approach to layered and 3–D network of vanadium oxides with smaller organic compounds by Whittingham *et al*, discusses the key parameters in this field.[38] Mild hydrothermal reactions are carried out in the temperature range 100–260˚C under autogenous pressure. All the reactants are placed in Teflon lined autoclaves and the molar ratios of soluble starting materials are varied. Teflon pouches have also been used as reaction containers by Poeppelmeier and co–workers; these are sealed into large volume autoclaves with a significant amount of water as backfill, to develop the required pressure under low temperature. This type of synthetic route is possible for products which can lose their crystallinity in water. The simplest technique helps to introduce organic compounds into vanadium oxyfluorides with minimal solubility problems. It is also noteworthy that various oxidation states and coordination environments of vanadium can occur in different materials or in the same material.

1.2 Borates

Borates are considered interesting candidates in the field of synthesis, structural characterisation and property development. The distribution of very small B atoms in an oxide matrix has been found to give valuable physical properties such as luminescence, NLO properties, pyroelectric, piezoelectric, dielectric properties etc.[39] NLO properties are exhibited by a material with non–centrosymmetry, i.e., lacking an inversion centre. The probability of borate materials crystallising in non–centrosymmetric space groups is about 36%, whereas the probability for non borate materials is only 15%.[40] Therefore, borate chemistry is a very attractive field for material scientists interested in symmetry dependent properties.

1.2.1 Fundamental Building Blocks

The boron atom usually coordinates with either three or four oxygen atoms by forming planar $[BO_3]^{3-}$ or tetrahedral $[BO_4]^{5-}$ groups (see Figure 1.25) by hybridising 2s and 2p orbitals of boron and oxygen respectively into a trigonal planar sp^2 or a three–dimensional sp^3 structure. The condensation of $[BO_3]$ and $[BO_4]$ groups, can happen only by sharing corners, these forming a vast array of oligomeric and polymeric B_xO_y structural units which are called fundamental building blocks (FBB). These FBB are found in isolated clusters, chains, layers and 3–D networks. Therefore, borate networks can be well understood by breaking down into their constituent FBBs.
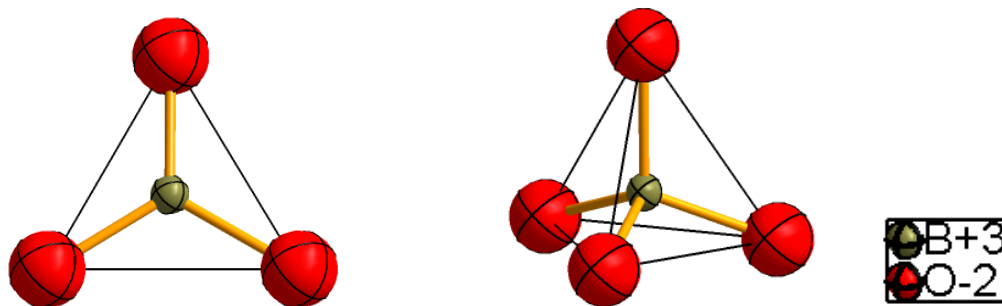
Figure 1.25 Planar $[BO_3]^{3-}$ and tetrahedral $[BO_4]^{5-}$ groups.

[BO$_3$] is the smallest FBB in the borate materials. The linear [BO$_2$]$^-$ is only found in apatite structures where phosphate positions are partially occupied by borates. The first two-fold coordinated [BO$_2$]$^-$ was observed in the apatite crystal structure with the composition Sr$_{9.042}$Na$_{0.209}$(PO$_4$)$_6$B$_{0.996}$O$_2$ by Calvo and co–workers in 1974.[41]

FBB of [BO$_3$]

Li$_3$AlB$_2$O$_6$ has been synthsised by a solid state technique and crystallises into space group P−1.[42] All the polyhedra are exclusively sharing their corners. There are two crystallographically different boron sites. Isolated planar borate [BO$_3$] groups are connected to tetrahedral units of [AlO$_4$] forming infinite chains parallel to the *a* axis. The chain contains six–membered rings with the connectivity of Al–O–B (see Figure 1.26). These chains are connected through tetrahedral [LiO$_4$] vertices forming a 3–D network.
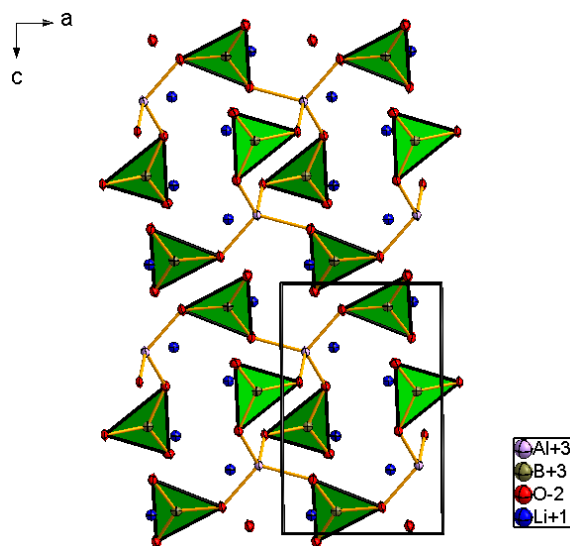
Figure 1.26 [BO$_3$] groups represented in polyhedral form, forming chains through tetrahedral [AlO$_4$] groups parallel to *a* axis; Li atoms occupy the *inter*–chain region.

Similar FBBs are observed in polar SHG active materials such as NdAl$_3$(BO$_3$)$_4$ and BiBO$_3$. It has been reported that rather than having continuous borate rings, isolated [BO$_3$] or [BO$_4$] groups contribute more to the directional dependent properties.[43] Chen

has shown that second-order susceptibility of borates based on NLO crystals will be $[B_3O_6] \approx [B_3O_7] > [BO_3] >> [BO_4]$.[44]

FBB of [BO₄]

The tetrahedral $[BO_4]$ as a FBB exists generally in the hydrated alkali and alkaline earth metal borates. Almost regular $B(OH)_4$ tetrahedra exist in the composition $Li(H_2O)_4B(OH)_4.2H_2O$.[45] Both $Li(H_2O)_4$ and $B(OH)_4$ are isolated. Water molecules are located in the wide tunnels and *inter*–connecting $Li(H_2O)_4$ and $B(OH)_4$ groups by forming hydrogen bonds.

$LiBO_2$ exhibits various phases which are determined by synthetic conditions. Under normal conditions of temperature and pressure α–$LiBO_2$ crystallises with a monoclinic structure and forms infinite trigonal borate chains with Li–O bonds bridging the chains.[46] However, the extreme conditions of 35 kbar pressure and 850˚C provide γ–$LiBO_2$ with space group I−42d. The γ–$LiBO_2$ structure consists of a 3–D infinite borate network formed by sharing all the corners of tetrahedral borate, as shown in Figure 1.27. A similar coordination environment is maintained in all the B atoms: two oxygen sites connect boron and the other two are bonded to tetrahedrally coordinated lithium.
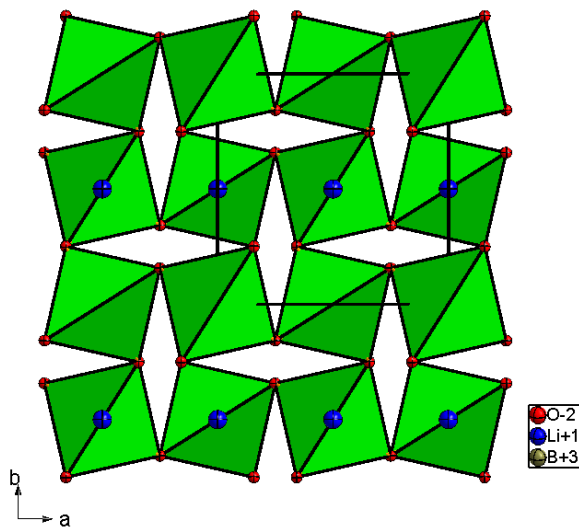
Figure 1.27 View down the *c* axis of the borate network in γ–$LiBO_2$.

FBB of [B$_2$O$_5$]

Single crystals of Li$_6$CuB$_4$O$_{10}$ crystallise in the non–centrosymmetric triclinic space group P1.[47] Each [BO$_3$] group contains three different B–O bond lengths with significant distortion. Two planar trigonal units are corner–shared to form the non–planar FBB, [B$_2$O$_5$]. There is no direct interaction between the FBBs (see Figure 1.28). Square planar copper shares corners with two different FBBs, forming an isolated pseudosymmetric [CuB$_4$O$_{10}$]$^{6-}$, as shown in Figure 1.28. However, the connectivity extends through square planar [CuO$_4$] and tetrahedral [LiO$_4$] cations to form the network. Within the network, the corners of the two trigonal planar borates of each FBB point along the +*a* and −*a* directions. The resulting network could therefore lead to some cancellation of the polarisabilities. However, the SHG activity is similar to a standard NLO material, KH$_2$PO$_4$.
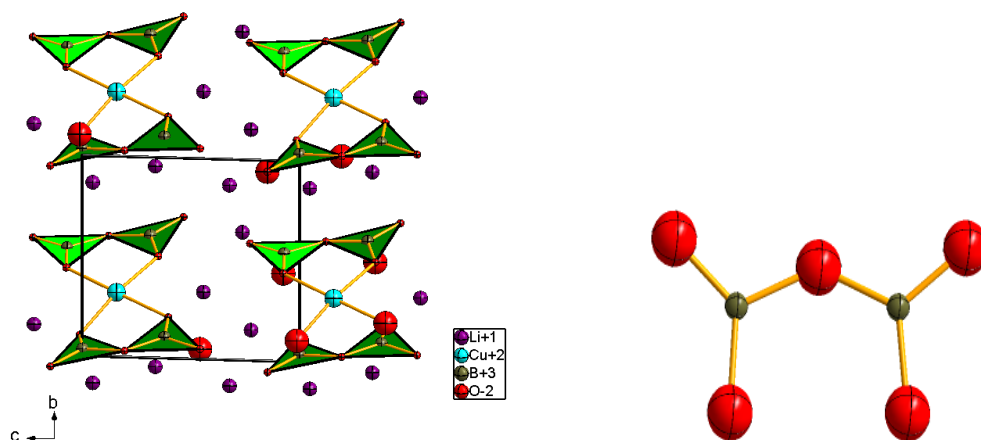
Figure 1.28 Square planar copper sharing corners with the FBB in Li$_6$CuB$_4$O$_{10}$ (left), and the FBB, [B$_2$O$_5$] (right).

FBB with the combination of [BO$_3$] and [BO$_4$]

There are three polymorphs, which exist with the chemical composition BiB$_3$O$_6$. α–BiB$_3$O$_6$ crystallises in the non–centrosymmetric space group C2 and is obtained from high temperature reactions. The β and γ polymorphs exhibit the centrosymmetric space

group P2$_1$/n and are synthesised at low temperature by developing high pressure of boric acid flux in an autoclave.[48] α–BiB$_3$O$_6$ contains 2–D borate layers built up from the combination of trigonal planar and tetrahedral FBBs in an alternate manner. The FBBs are arranged into eight–membered borate rings with the ratio of tetrahedral to trigonal planar 1:2 (see Figure 1.29). This structure shows a remarkable response of SHG activity. It has been shown that a significant contribution arises from the lone pair electron of the square pyramidal [BiO$_4$]$^{5-}$ anionic unit and also a contribution from the [BO$_3$] group, which is relatively smaller in α–BiB$_3$O$_6$.
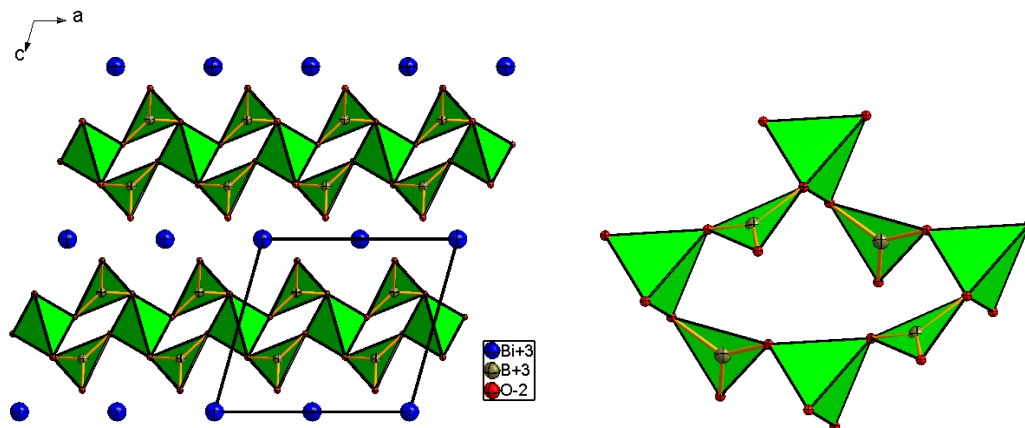
Figure 1.29 Borate layer of α–BiB$_3$O$_6$ on the *ac* plane (left) and eight-membered borate ring (right).

FBB of [B$_3$O$_8$]

The β–BiB$_3$O$_6$ structure possesses a 2–D borate layer built up from a three–membered borate ring as the FBB, as shown in Figure 1.30. The FBB exhibits a non–planar ring [B$_3$O$_8$], which consists of two tetrahedral and a trigonal planar borate group. The three–membered borate rings are further *inter*–connected to each other and form seven–membered borate rings where the ratio of tetragonal: trigonal is 2:1.
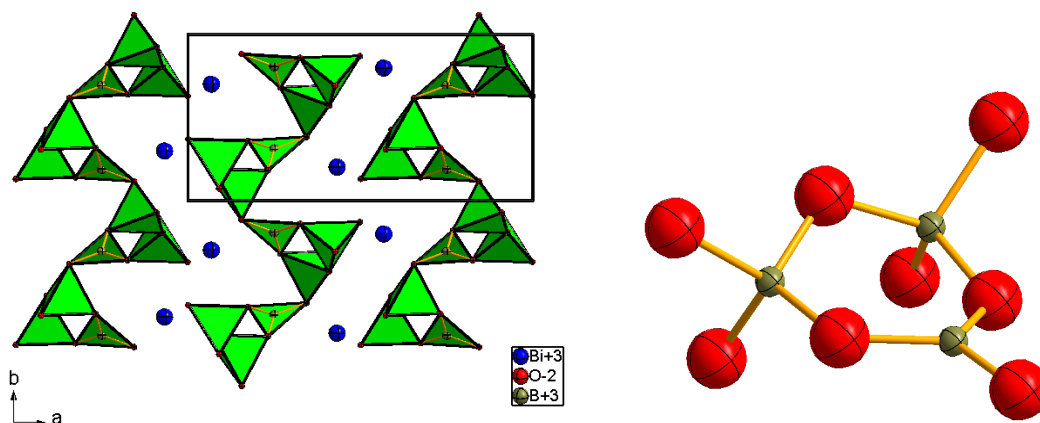
Figure 1.30 The 2–D borate network in β–BiB$_3$O$_6$ on the *ab* plane (left), and the FBB, [B$_3$O$_8$] (right).

FBB of [B$_3$O$_9$]

The γ–BiB$_3$O$_6$ exhibits [B$_3$O$_9$] as FBB, which contains a three–membered borate ring with only tetrahedral [BO$_4$]. The FBBs interact in all directions to form an extended 3–D borate network (see Figure 1.31). The borate framework contains different sizes of rings with four, six and ten–membered rings.
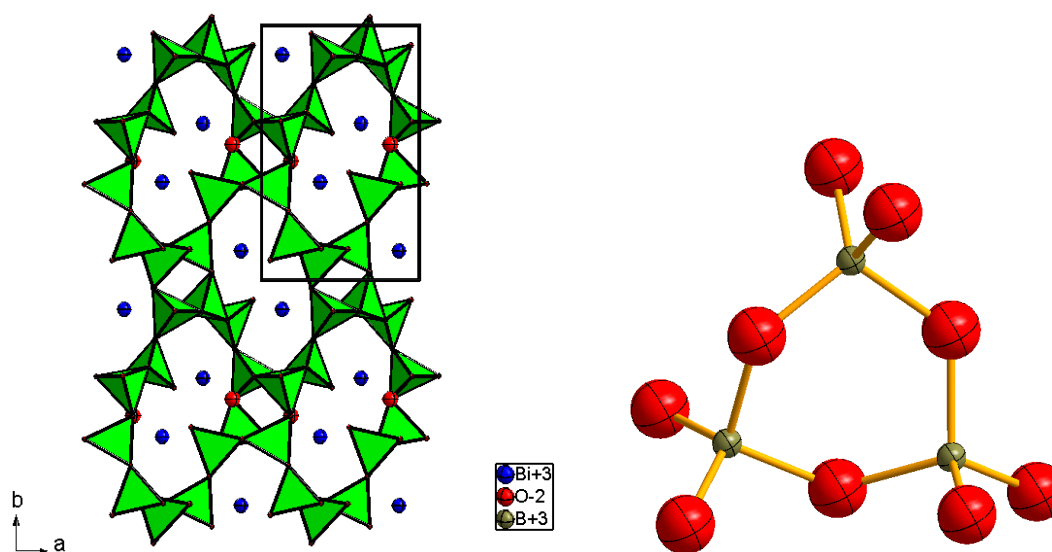
Figure 1.31 The 3–D borate network of γ–BiB$_3$O$_6$ (left) and the FBB, [B$_3$O$_9$] (right).

FBB of [B₃O₆]

β–BaB$_2$O$_4$ is the well known NLO material reported by Chen et al. in 1985.[44] The space group of this material has been examined over a decade and claimed to be R3 rather than R3c based on the NLO behavior.[49] The FBB is a nearly planar [B$_3$O$_6$] group composed of three trigonal planar borate units. The planar rings are arranged in a staggered manner along the c axis, as shown in Figure 1.32. A three–fold axis runs through the centre of the ring. There is no direct interaction between the FBBs, being an isolated cluster in the crystal structure, but Ba^{2+} cations *inter*–connect the FBBs to form a 3–D network.
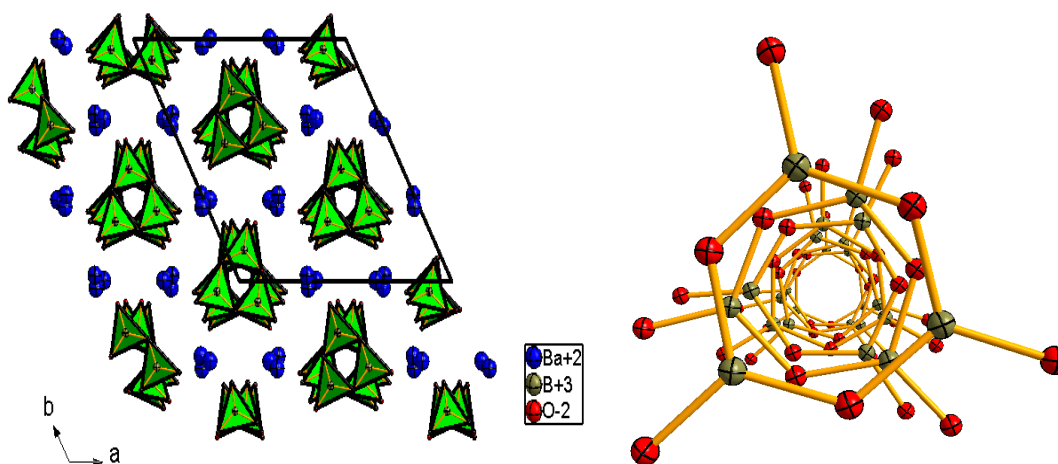
Figure 1.32 The crystal packing in β-BaB$_2$O$_4$ (left) and staggered arrangement of FBBs, viewed down the c axis (right).

FBB of [B₃O₇]

The composition MB$_3$O$_5$ (M is an alkali metal, Tl) metal borates exhibit [B$_3$O$_7$] as a FBB of the borate network.[50] All of these compounds were synthesised by conventional solid state techniques with the metal carbonates and boric acid as the reagents. NaB$_3$O$_5$ is the only structure, which belongs to a centrosymmetric space group P2$_1$/c in the series. RbB$_3$O$_5$ exhibits two temperature dependent phases such as α–RbB$_3$O$_5$, the low temperature phase and β–RbB$_3$O$_5$, the high temperature phase, but both crystallise in the same space group P2$_1$2$_1$2$_1$ and exhibit the same FBB of the borate network.[51] The

condensation of two trigonal borate and a tetrahedral borate forms the six–membered B–O ring of the FBB [B_3O_7], as shown in Figure 1.34. The borate network is built up into a continuous helical chain with the repetition of two FBBs. The helical chains extend into two directions: in α–RbB_3O_5 the chains run parallel to the *a* and *c* axes; in β–RbB_3O_5 the chain run parallel to the *a* and *b* axes. Rb^+ cations are located in the channels of the 3–D network (see Figure 1.33). Similar frameworks are observed in other NLO active materials such as LiB_3O_5, CsB_3O_5, $CsLiB_6O_{10}$ and TlB_3O_5.
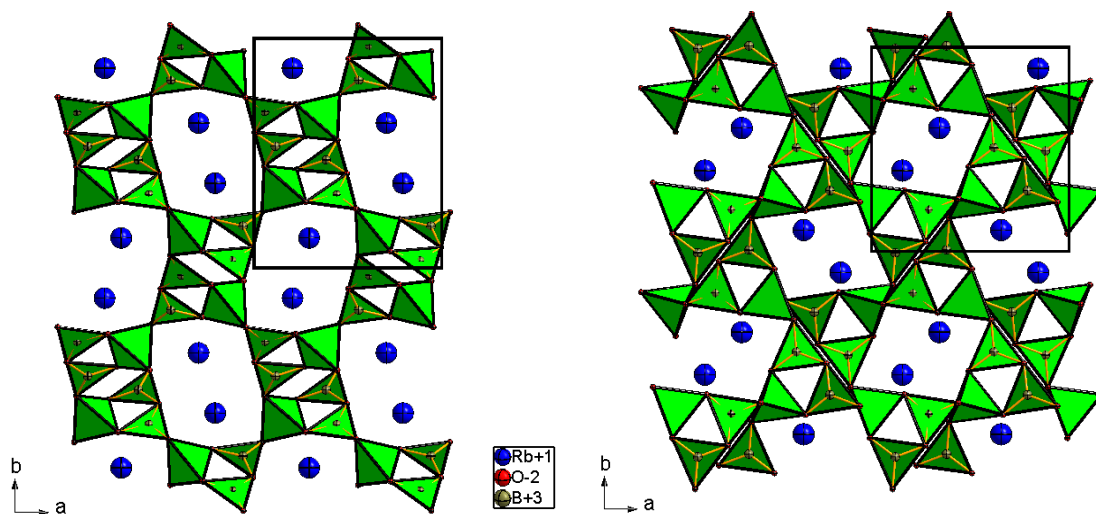
Figure 1.33 Helical borate chains in α–RbB_3O_5 (left) and β–RbB_3O_5 (right).
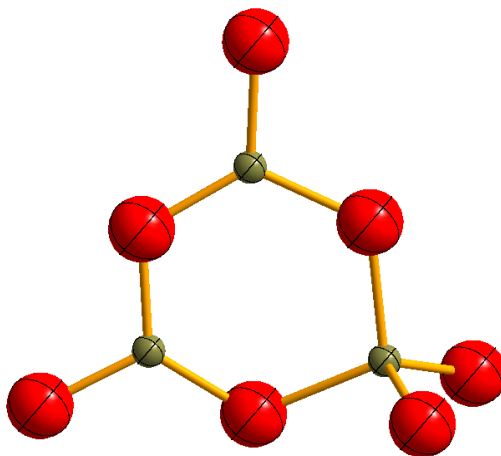
Figure 1.34 The FBB, [B_3O_7]

35

FBB of [B$_4$O$_9$]

The borate framework of Li$_2$B$_4$O$_7$ is comprised of tetraborate [B$_4$O$_9$], FBBs.[52] Similar FBBs exist in hydrated alkali metal borates. Li$_2$B$_4$O$_7$ exhibits various physical properties such as piezoelectricity, thermoluminescence and NLO properties. The FBB is built from units formed by four boron atoms, two trigonal borates and two tetrahedral borates. Both tetrahedral boron atoms share a common oxygen as well as sharing a corner with the trigonal borates forming a six–membered double B–O ring within the FBB. All the trigonal borates share corners with the tetrahedral borates within the FBB, as well as with neighbouring FBBs. However, the tetrahedral borate shares only with tetrahedral borate within the FBB. Similar borate networks interpenetrate each other and form an infinite 3–D network, as shown in Figure 1.35.
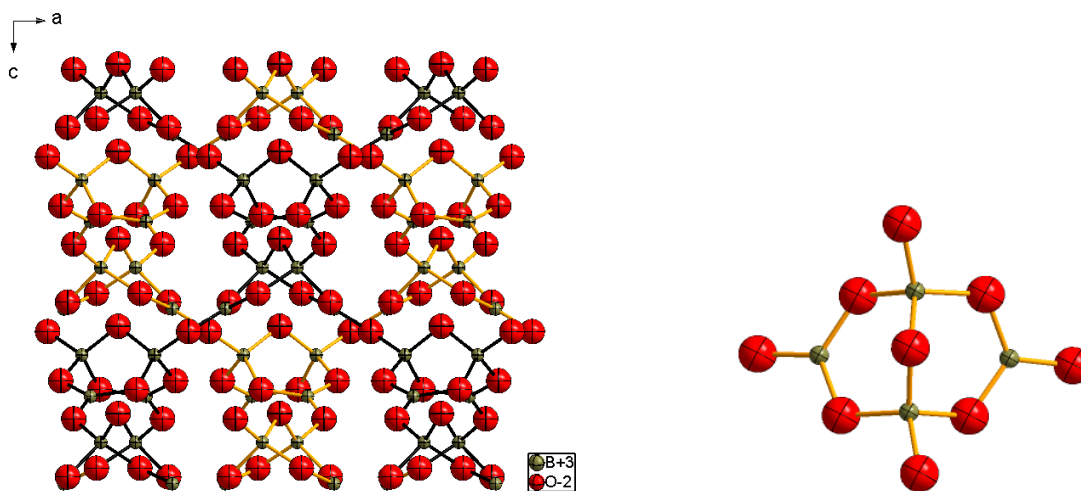
Figure 1.35 Interpenetration of similar borate chains on the *ac* plane of Li$_2$B$_4$O$_7$ (left) and the FBB, [B$_4$O$_9$] (right).

FBB of [B$_4$O$_{11}$]

BaBi$_2$B$_4$O$_{10}$ crystallises in the monoclinic space group P2$_1$/c.[53] The FBB of the crystal structure contains a triborate ring [B$_3$O$_3$] of three tetrahedral borates and a trigonal borate which share corners with tetrahedral borates (see Figure 1.36). The FBBs link through

trigonal planar borates to form spiral chains parallel to the *b* axis. Distorted tetragonal pyramids of [BiO$_4$] share the edges and form chains parallel to the borate chains in an alternate manner, while the Ba^{2+} cations connect the layers and form the 3–D network.
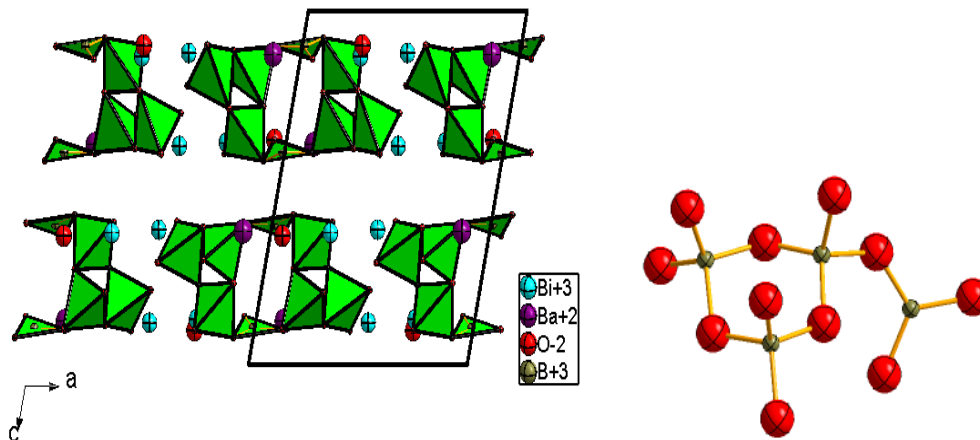
Figure 1.36 Spiral borate chain arrangement on the *ac* plane in BaBi$_2$B$_4$O$_{10}$ (left) and the FBB, [B$_4$O$_{11}$] (right).

FBB of [B$_5$O$_{10}$]

TlB$_5$O$_8$ was synthesised from its hydrated precursor TlB$_5$O$_6$(OH)$_4$.2H$_2$O by the removal of water followed by heating and slow cooling of the melt.[54] TlB$_5$O$_8$ crystallises in the orthorhombic space group Pbca and is iso-structural to β–KB$_5$O$_8$ and β–RbB$_5$O$_8$.[55, 56]. The pentaborate unit, [B$_5$O$_{10}$] is built from the complete condensation of two [B$_3$O$_3$] rings shared by a common boron, which contains four trigonal planar borates sharing the corners with a tetrahedral borate, as shown in Figure 1.37. The connectivity of FBBs extends to the formation of two similar interpenetrating 3–D networks with tunnels. Commonly, cations occupy the tunnels of the borate framework, but nine coordinated Tl$^+$ cations are located around the pentaborate groups with empty tunnels.
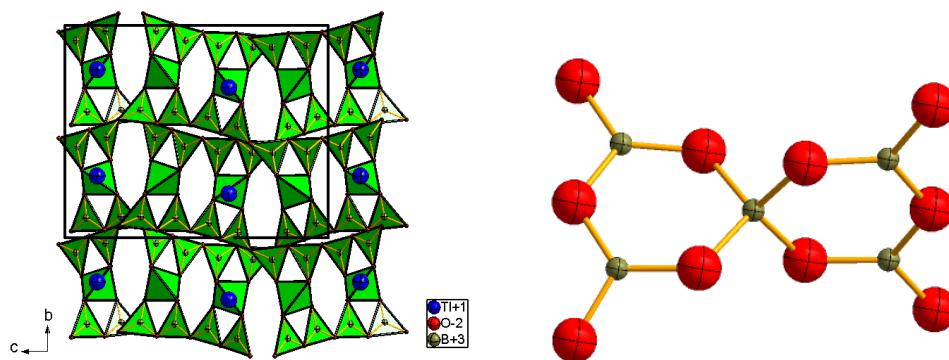
Figure 1.37 3–D borate network in TlB_5O_8 (left) and the FBB, $[B_5O_{10}]$ (right).

FBB of $[B_5O_{11}]$

Conventional solid state techniques yield a polyborate of composition $Cs_2Na_2B_{10}O_{17}$ with the centrosymmetric space group C2/c.[57] The layered borate matrix is built up from $[B_5O_{11}]$ as a FBB. This FBB contains two $[B_3O_3]$ rings which share a common tetrahedral boron with the other trigonal borates and tetrahedral borate (see Figure 1.38). Nine coordinated Cs^+ cations are located in the tunnels of particular a layer, while seven coordinated Na^+ cations bridge the adjacent layers. A similar FBB is observed in $Bi_3B_5O_{12}$, but as an isolated five-membered borate ring arranged in an alternate manner with $[BiO_4]$ units to form *zig–zag* chains.[58]
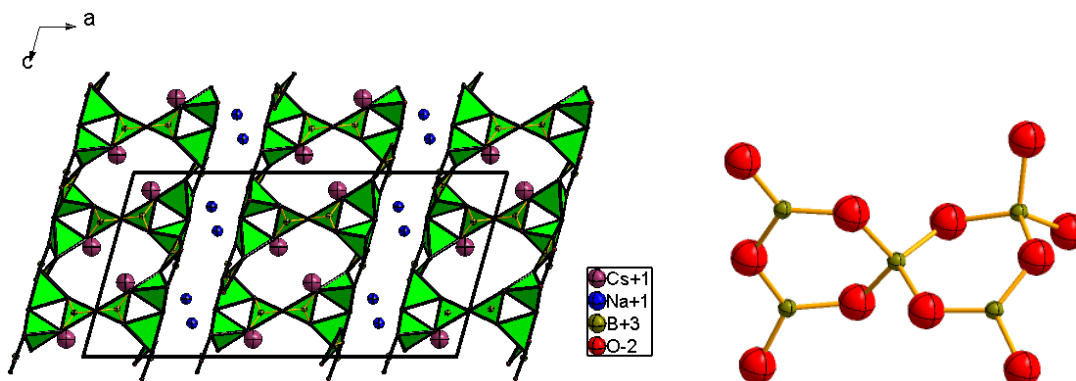
Figure 1.38 Borate layer on the *ac* plane in $Cs_2Na_2B_{10}O_{17}$ (left) and the FBB, $[B_5O_{11}]$ (right).

FBB of [B$_5$O$_{12}$]

Hilgardites are minerals with the composition M$_2$B$_5$O$_9$X, where M is a large divalent cation and X is a halide. Ca$_2$B$_5$O$_9$Cl.H$_2$O was found in the form of an insoluble residue from a brine well in Louisiana.[59] Further crystallographic studies on both natural and synthetic hilgardites attracted various research groups due to their potential application for luminescence and NLO properties. There are hydrated hilgardites; Al, Ga substitution onto the borate sites and divalent cation doping onto the metal sites is also possible. [60] The crystal structure of hilgardite exhibits an open 3–D borate framework, as shown in Figure 1.39.[61] The FBB of the borate network is the pentaborate polyanion [B$_5$O$_{12}$], containing two [B$_3$O$_3$] rings built up from three tetrahedral borates and two trigonal planar borates. The neighbouring FBBs share the tetrahedral boron and form chains parallel to the *c* axis. Tetrahedral borates of one chain connect to trigonal borates of the neighbouring chain and extend into a 3–D network with channels. In Eu$_2$B$_5$O$_9$Br, Eu^{2+} and Br$^-$ are arranged in an alternating manner on the *ab* plane in the tunnels, while Eu^{2+} exhibits a nine coordinated environment.
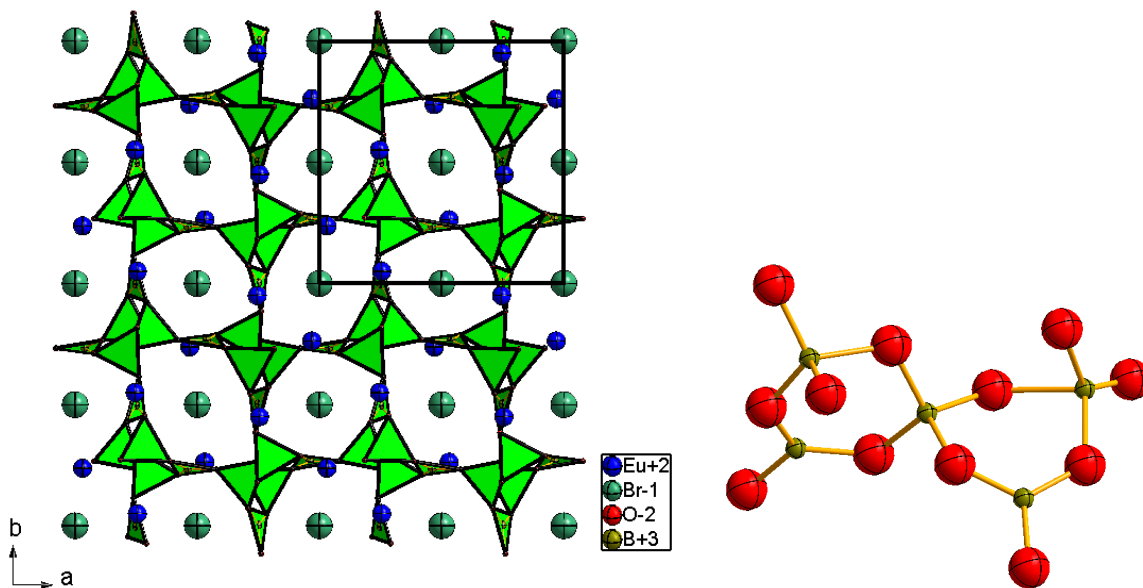
Figure 1.39 3–D borate framework of Eu$_2$B$_5$O$_9$Br (left) and the FBB, [B$_5$O$_{12}$] (right).

FBB of [B$_6$O$_{13}$]

Single crystals of Na$_3$[B$_6$O$_9$(VO$_4$)] exhibit the non–centrosymmetric space group P2$_1$2$_1$2$_1$.[62] The FBB of this crystal structure contains three trigonal planar borates and three tetrahedral borates, as shown in Figure 1.40. All three tetrahedral borates of the six–membered B–O ring, share a common oxygen atom and join the three [B$_3$O$_3$] rings together to form hexaborate [B$_6$O$_{13}$] as a FBB. Connectivity of FBBs extends into 2–D sheets, which are connected by tetrahedral [VO$_4$] and form a 3–D network. Eight coordinated Na$^+$ cations are located within the channels.
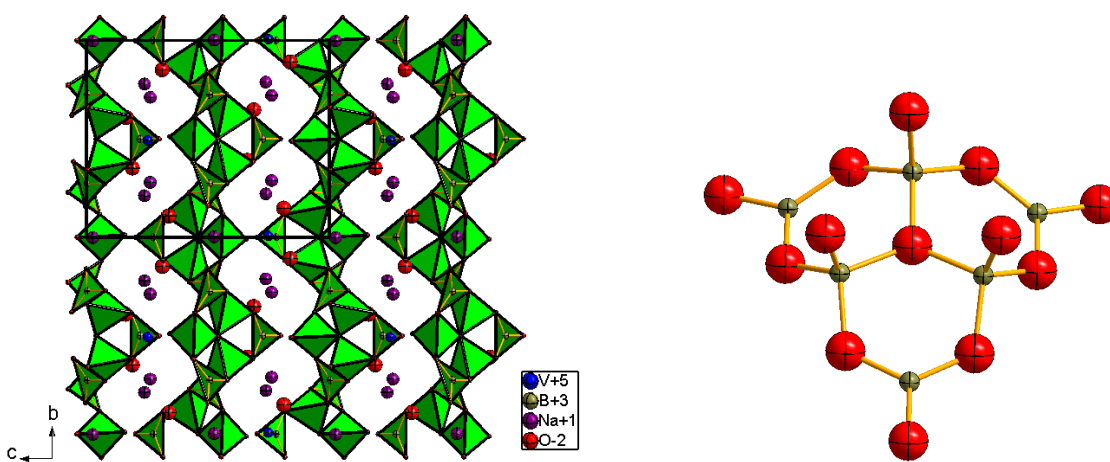
Figure 1.40 2–D borate sheet in Na$_3$[B$_6$O$_9$(VO$_4$)] (left) and the FBB, [B$_6$O$_{13}$] (right).

FBBs exist in various compounds with chains, layers or 3–D networks by sharing the corners of the borate polyhedra. FBBs with seven, eight etc., boron atoms can be catagorised under one of the above FBBs. Nowogrocki and co–workers have reported the crystal structure of Cs$_3$B$_7$O$_{12}$, which contains 63 boron atoms in the asymmetric unit.[63] So far this is biggest building block in the borate framework. However it can be broken down into smaller FBBs. The same research group have synthesised the Na analogue of this compound, which only contains seven crystallographically different heptaborates in the 3–D borate network.[64]

1.2.2 Synthesis of Borates

Mostly, borate crystals have been synthesised by melt or flux methods. The recently discovered piezoelectric material, $Li_2B_4O_7$ was grown[65] from the melt phase in the system Li_2CO_3–H_3BO_3 and the NLO material, LiB_3O_5 was grown on a seed from the solution–melt using the method of temperature lowering over a period of 30–35 days.[66] Solid state techniques are also used to obtain polycrystalline materials to prepare by heating stoichiometric amounts of reactants such as rare earth fluorides, $Ln_3(BO_3)_2F_3$ (Ln= Sm, Eu and Gd).[67]

During the past two decades hydrothermal synthesis has developed as a new technique in the field of borate chemistry. Several borate systems have been studied under hydrothermal conditions. A series of lithium borates, as well as lithium mixed borate systems have been successfully obtained in the range of 250–450˚C. It has been observed that the hydrothermal method helps in growing pure and large single crystals with enhanced properties such as piezoelectricity, ferroelectricity and superionic behaviour. [68]

1.2.3 Properties of Borates

Borates exhibit interesting physical properties with potential applications such as luminescence, ferroelectricity, pyroelectricity, piezoelectricity, superionic conductivity and NLO properties. These depend on their crystal structure and composition.

Luminescent materials

Most of the luminescent borate materials are doped with lanthanides, especially Eu^{2+} oxides. An example is $Eu_2B_5O_9Br$, and other members of the hilgardite family, doped with Ce^{3+}/Na^+ for Eu^{2+}, for example.[69] The host systems $Ba_2LiB_5O_{10}$ and $Ba_2Mg(BO_3)_2$, doped with Eu^{2+}, exhibit long wavelength emission. The simplest alkali borate system, α–

$LiBO_2$, when doped with Mn^{2+} shows weak luminescence. The nature of emission wavelength has been described based on the dopant ion.[39]

Non–linear optical materials

Compared to other materials, borates apparently exhibit non-centrosymmetric crystal structures with much higher frequency. Intense research has been carried out to find new NLO materials which are useful in the field of laser medicine, fibre optical communication, signal processing and storage devices.[44] NLO materials are capable of expanding the frequency range of device operation from UV to IR. Most of the Nd–containing non–centrosymmetric borate materials, such as $NdAl_3(BO_3)_4$ and $NdSc_3(BO_3)_4$, and other Nd–doped materials, have been used as laser materials. However the crystal growth of $NdAl_3(BO_3)_4$ is a very expensive time–consuming process from the melt.[40] Therefore, intense studies have been carried out on β–BaB_2O_4, LiB_3O_5, $Li_2B_4O_7$ and the hilgardite borate family.[61]

Ferroelectric, pyroelectric, piezoelectric and superionic materials

It has been reported that single crystals of β-BaB_2O_4 exhibit dielectric and piezoelectric properties in the range of −180˚C to 50˚C, but their piezoelectric coefficient is low compared to other commercial materials. However the pyroelectric coefficient is constant over the entire temperature range, which could be attractive in various applications. Zhang *et al*[70] characterised single crystals of $YCa_4O(BO_3)_3$ which exhibit piezoelectric properties over a wide temperature range; that material could be an interesting candidate for high temperature applications. The superionic and ferroelectric properties of $K_3Nb_3O_6(BO_3)_2$ have been reported by Kojima and co-workers in the temperature range of 300-870K.[71]

References

1. P. J. Hagrman, R. C. Finn, J. Zubieta, *Solid State Sci*., **2001**, 3, 745.

2. J. Howing, *Acta Cryst*., **2003**, B59, 747.

3. "The United Kingdom Chemical Database Service", D. A Fletcher, R. F. McMeeking, D. Parkin, *J. Chem. Inf. Comput. Sci.* **1996**, 36, 746-749.

4. G. Huan, J. W. Johnson, A. J. Jacobson, J. S. Merola, *J. Solid State Chem*., **1991**, 91, 385.

5. P. J. Hagrman, C. Bridges, J. E. Greedan, J. Zubieta, *J. Chem. Soc*., *Dalton Trans*., **1999**, 2901.

6. M. E. Welk, C. L. Stern, K. R. Poeppelmeier, A. J. Norquist, *Cryst. Growth. Des*., **2007**, 7, 956.

7. "Magnetism and the Chemical Bond", J. B. Goodenough, John Wiley & Sons, London, **1963**.

8. "Magnetochemistry", R. L. Carlin, Springer, Berlin, **1986**.

9. E. E. Kaul, H. Rosner, V. Yushankai, J. Sichelschmidt, R. V. Shpanchenko and C. Geibel, *Phys. Rev. B*, **2003**, 67, 174417.

10. C. P. Landee, M. M. Turbill, C. Galeriu, J. Giantsidis and F. M. Woodward, *Phys. Rev. B*, **2001**, 63, 100402.

11. D. W. Aldous, R. J. Goff, J. P. Attfield, P. Lightfoot, *Inorg. Chem*., **2007**, 46, 1277.

12. D. W. Aldous, A. M. Z. Slawin, P. Lightfoot, *J. Solid State Chem*., **2008**, 181, 3033.

13. A. P. Ramirez, *Annu. Rev. Mater. Sci*., **1994**, 24, 453.

14. P. Halasyamani, K. R. Poeppelmeier, *Chem. Mater*., **1998**, 10, 2753.

15. Y. Nakanishi, H. Mizota, Y. Ito, M. Takano, S. Fukao, S. Yoshikado, K. Ohyama, K. Yamada, S. Fukushima, *Phys. Scr*., **2006**, 73, 471.

16. S. C. Abrahams, J. M. Reddy, J. L. Bernstein, *J. Phys. Chem. Solids*., **1966**, 27, 997.

17. P. S. Halasyamani, *Chem. Mater*., **2004**, 16, 3586.

18. N. F. Stephens, M. Buck, P. Lightfoot, *J. Mater. Chem*., **2005**, 15, 4298.

19. M. E. Welk, A. J. Norquist, C. L. Stern, K. R. Poeppelmeier, *Inorg. Chem.*, **2000**, 39, 3946.

20. P. Halasyamani, M. J. Willis, C. L. Stern, P. M. Lundquist, G. K. Wong, K.R.Poeppelmeier, *Inorg. Chem.*, **1996**, 35, 1367.

21. P. A. Maggard, C. L. Stern, K. R. Poeppelmeier, *J. Am. Chem. Soc.*, **2001**, 123, 7742.

22. P. A. Maggard, A. L. Kopf, C. L. Stern, K. R. Poeppelmeier, *Inorg. Chem.*, **2002**, 41, 4852.

23. P. A. Maggard, T. S. Nault, C. L. Stern, K. R. Poeppelmeier, *J. Solid State Chem.*, **2003**, 175, 27.

24. A. A. Udovenko, N. M. Leptash, *Acta. Cryst.*, **2008**, B64, 305.

25. P. Y. Zavalij, M. S. Whittingham, *Acta. Cryst.*, **1999**, B55, 627.

26. W. Ouellette, V. Golub, C. J. O'Connor, J. Zubieta, *J. Solid State Chem.*, **2007**, 180, 2500.

27. W. Ouellette, J. Zubieta, *Solid State Sci.*, **2007**, 9, 658.

28. W. Ouellette, V. Golub, C. J. O'Connor, J. Zubieta, *J. Chem. Soc.*, *Dalton Trans.*, **2005**, 291.

29. J. N. Behera, C. N. R. Rao, *Chem. Asian J.*, **2006**, 1, 742.

30. N. Buchholz, M. Leimkuhler, L. Kiriazis, R. Mattes, *Inorg. Chem.*, **1988**, 27, 2035.

31. W. Ouellette, M. H. Yu, C. J. O'Connor, J. Zubieta, *Inorg. Chem.*, **2006**, 45, 7628.

32. M. F. Davis, W. Levason, J. Paterson, G. Reid, M. Webster, *Eur. J. Inorg. Chem.*, **2008**, 802.

33. D. L. Thorn, R. L. Harlow, N. Herron, *Inorg. Chem.*, **1995**, 34, 2629.

34. D. W. Aldous, N. F. Stephens, P. Lightfoot, *Dalton Trans.*, **2007**, 2271.

35. T. S. C. Law, I. D. Williams, *Chem. Mater.*, **2000**, 12, 2070.

36. C. Y. Duan, Y. P. Tian, Z. L. Lu, X. Z. You, *Inorg. Chem.*, **1995**, 34, 1.

37. G. D. Munno, C. Bazzicalupi, J. Faus, F. Lloret, M. Julve., *J. Chem. Soc. Dalton Trans.*, **1994**, 1879.

38. T. Chirayil, P. Y. Zavalij, M. S. Whittingham, *Chem. Mater.*, **1998**, 10, 2629.

39. D. A. Keszler, *Current Opinion in Solid State and Mater. Sci.*, **1999**, 4, 155.

40. P. Becker, *Adv. Mater.*, **1998**, 10, 979.

41. C. Calvo, R. Faggiani, N. Krishnamachari, *Acta Crystallogr.*, **1975**, B31, 188.

42. M. He, X. L. Chen, V. Gramlich, C. Baerlocher, T. Zhou, B. Q. Hu, *J. Solid State Chem.*, **2002**, 163, 369.

43. D. Xue, K. Betzler, H. Hesse, *Trends in Optics and Photonics Series.*, **2000**, 34, 542.

44. C. Chen, Z. Lin, Z. Wang, *Appl. Phys.*, **2005**, B 80, 1.

45. M. Touboul, E. Betourne, *J. Solid State Chem.*, **1995**, 115, 549.

46. M. Marezio, J. P. Remeika, *J. Chem. Phys.*, **1966**, 44, 3348.

47. S. Pan, J. P. Smit, B. Watkins, M. R. Marvel, C. L. Stern, K. R. Poeppelmeier, *J. Am. Chem. Soc.*, **2006**, 128, 11631.

48. L. Li, G. Li, Y. Wang, F. Liao, J. Lin, *Inorg. Chem.*, **2005**, 44, 8243.

49. D. F. Xue, S. Y. Zhang, *Acta Cryst.*, **1998**, B54, 652.

50. Y. F. Shepelev, R. S. Bubnova, S. K. Filatov, N. A. Sennova, N. A. Pilneva, *J. Solid State Chem.*, **2005**, 178, 2987.

51. M. G. Krzhizhanovskaya, Y. K. Kabalov, R. S. Bubnova, E. V. Sokolova, S. K. Filatov, *Crystallogr. Rep.*, **2000**, 45, 572.

52. S. Natalia, B. Rimma, S. Jurii, F. Stanislav, Y. Olga, *J. Alloys and Compounds.*, **2007**, 428, 290.

53. R. S. Bubnova, S. V. Krivovichev, S. K. Filatov, A. V. Egorysheva, Y. F. Kargin, *J. Solid State Chem.*, **2007**, 180, 596.

54. M. Touboul, G. Nowogrocki, *J. Solid State Chem.*, **1998**, 136, 216.

55. J. K. Moe, *Acta. Cryst.*, **1972**, B28, 168.

56. N. Pennin, L. Seguin, M. Touboul, G. Nowogrocki, *J. Solid State Chem.*, **2001**, 161, 205.

57. J. M. Tu, D. A. Keszler, *Inorg. Chem.*, **1996**, 35, 463.

58. S. Filatov, Y. Shepelev, R. Bubnova, N. Sennova, A. V. Egorysheva, Y. F. Kargin, *J. Solid State Chem.*, **2004**, 177, 515.

59. S. Ghose, C. Wan, *Amer. Miner.*, **1979**, 64, 187.

60. J. Barbier, *Solid State Sci.*, **2007**, 9, 344.

61. K. Machida, G. Adachi, , N. Yasuoka, N. Kasai, J. Shiokawa, *Inorg. Chem.*, **1980**, 19, 3807.

62. M. Touboul, N. Pennin, G. Nowogrocki, *J. Solid State Chem.*, **2000**, 150, 342.

63. G. Nowogrocki, N. Pennin, M. Touboul, *Solid State Sci.*, **2003**, 5, 795.

64. N. Pennin, M. Touboul, G. Nowogrocki, *J. Alloys and Compounds.*, **2004**, 363, 104.

65. J. K. Moe, *Acta Cryst.*, **1962**, 15, 190.

66. Y. F. Shepelev, R. S. Bubnova, S. K. Filatov, N. A. Sennova, N. A. Pilneva, *J. Solid State Chem.*, **2005**, 178, 2987.

67. G. Corbel, R. Retoux, M. Leblanc, *J. Solid State Chem.*, **1998**, 139, 52.

68. "Handbook of Hydrothermal Technology for Crystal growth and Material processing" K. Byrappa, Academic Press: New York, **2001**.

69. A. V. Sidorenko, A. J. J. Bos, P. Dorenbos, P. A. Rodnyi, C. W. E. van Eijk, I. V. Berezovskaya, V. P. Dotsenko, *J. Phys. Condens. Matter.*, **2003**, 15, 3471.

70. S. Zhang, Y. Fei, B. H. T.Chai, E. Frantz, D. W. Snyder, X. Jiang, T. R. Shrout, *Appl. Phys. Lett.*, **2008**, 92, 202905.

71. M. Maczka, J. Hanuza, S. Kojima, *Phys. Rev.*, **2008**, B77, 104116.

CHAPTER TWO

Crystallography, Properties, Techniques

Materials in this work were synthesised by conventional synthesis techniques under solvothermal and solid state conditions. This chapter contains a discussion about basic crystallography, principles behind synthesis techniques, characterisation techniques used and a qualitative description of magnetic measurements. Fluorine analysis, thermogravimetric analysis and microanalysis have also been employed.

2.1 Crystallography[1,2]

Crystals contain a basic motif, which can be a molecule or a building block of a network structure which is repeated again and again in all three directions. To understand the crystal structure, it is necessary to know this repeating motif, called the unit cell, and the lengths and directions of its three vectors; both together completely describe the periodicity of the crystal structure. There are seven possible crystal systems based on the consideration of symmetries, as shown in the Table 2.1. The crystal packing and the shape are determined by these underlying building units. For example, sometimes the morphology of a perfect cubic crystal appears to be a cubic with perfect edges.

The positions of the atoms in the unit cell are described by the fraction of the unit cell dimensions a, b and c respectively. A crystal can be described by an abstract mathematical concept called a lattice. There are different types of lattices such as primitive (P), face–centred (F), body-centred (I) and side–centred (A or B or C) lattices. The cell which contain lattice points only at the corner of the unit cell is called P; an additional lattice point at the centre of the cell is I; additional lattice points at the centre of the each face is F; an additional lattice point at centre of a particular face is A or B or C. The combination of both crystal system and lattice types gives fourteen different Bravais lattices. Symmetry elements can be defined as physically identifiable by point, line or a plane. The symmetry operations are applied on symmetry elements, such as

inversion through a point, rotation about a line and reflection in a plane, which leads to an arrangement that is indistinguishable from the initial arrangement. Each symmetry element provides a number of possible symmetry operators. The collection of symmetry elements, which are compatible with translational symmetry to describe a 3–dimensional crystal, is called a point group. There are 32 point groups, of which 21 point groups do not possess a centre of symmetry. The combination of point groups and translational symmetries provide 230 space groups, which include all the possible symmetry operations. Space groups determine the type and the positions of the symmetry elements that are possible for a crystal structure.

Crystal system	Unit cell shape	Defining symmetry	Bravais lattices	Symmetry operations applied order of direction
Cubic	$a = b = c$, $\alpha = \beta = \gamma = 90°$	Four three–fold axes	P, F, I	c, [111], [110]
Tetragonal	$a = b \neq c$, $\alpha = \beta = \gamma = 90°$	One four–fold axis	P, I	c, a, [110]
Orthorhombic	$a \neq b \neq c$, $\alpha = \beta = \gamma = 90°$	Three two–fold axes or mirror planes	P, F, I, A (B or C)	a, b, c
Hexagonal	$a = b \neq c$, $\alpha = \beta = 90°$, $\gamma = 120°$	One six–fold axis	P	c, a, [210]
Trigonal (a)	$a = b \neq c$, $\alpha = \beta = 90°$, $\gamma = 120°$	One three–fold axis	R	c, a, [210]
Trigonal (b)	$a = b = c$, $\alpha = \beta = \gamma \neq 90°$	One three–fold axis	P	c, a, [210]
Monoclinic	$a \neq b \neq c$, $\alpha = \gamma = 90°$, $\beta \neq 90°$	One two–fold axis or mirror plane	P, C	b
Triclinic	$a \neq b \neq c$, $\alpha \neq \beta \neq \gamma \neq 90°$	None	P	-

Table 2.1 The seven different crystal systems

Translational symmetry coupled with other symmetry elements provides screw axes and glide reflections. Coupling of a translation and a reflection is a glide reflection; the direction of glide must be parallel to the plane of reflection and this is called a glide plane a, b, c or n, where n is along the face diagonal. Coupling of rotation and translation leads to a screw axis, the translation will be in the direction of the rotational axis. The symmetry elements with translational components lead to the systematic cancelling of certain reflections called systematic absences; this is very useful in determining the space group.

2.2 Properties

2.2.1 Concepts of Non–Linear Optics[3,4]

When light travels through a non–centrosymmetric crystal, a variety of NLO effects may occur. The interaction of light with such a material will cause its properties to change, such that another photon that arrives will see a material with a different polarisability and a different anisotropy than in the absence of radiation. As light goes through the crystal, its electric field interacts with charges in the crystal producing a force. This force displaces the centre of electron density away from the nucleus.

 These interactions can cause significant changes in frequency, phase, polarisation, or path of the original optical beam. The manipulation of light in this manner has many important technological aspects in optical signal processing, generation of variable frequency laser light, tunable filters and optical data storage. In order to control light, materials chemists design and synthesise an optimal medium within which the modulation of both the magnitude and response time of these optical processes can be controlled. These materials are called NLO materials.

The charges are distributed in an acentric manner in a non–centrosymmetric crystal. When the light hits the crystal, the electric field, E of the light interacts with the charges in the material and produces force, as a result the electron density is displaced away from the

nucleus and causes charge separation, which is called polarisation (see Figure 2.1). The induced dipole moment is equal to its charge multiplied by the distance between the opposite charges.
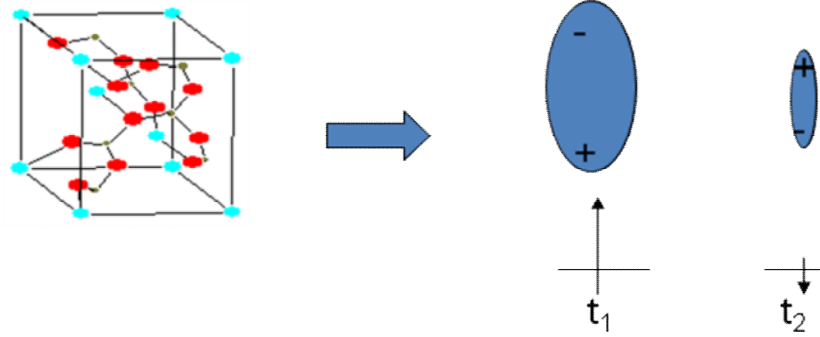
Figure 2.1 Induced polarisation of a non–centrosymmetric material as a function of time.

The electromagnetic radiation induces force to oscillate the charges. These oscillating dipoles re–emit radiation with the frequency of its oscillation.

This happens only in linear polarisation, which can be written as

$$P = P_0 + \chi^{(1)}.E \qquad \qquad \text{Eq (2.1)}$$

Where P is bulk polarization density, $\chi^{(n)}$ are susceptibility coefficients, P_0 is the intrinsic static dipole moment density of the sample and E is the electric field of the incident radiation.

The deviation from the linear dependence results in the generation of non–linear polarisation , the oscillation of induced dipoles consists of a range of oscillations at ω, 2ω, 3ω….which are called fundamental, second–harmonic, third–harmonic etc.

$$P = P_0 + \chi^{(1)} E + \chi^{(2)} E^2 + \chi^{(3)} E^3 + \dots \qquad \qquad \text{Eq (2.2)}$$

The electric field of plane light can also be expressed as

$$E = E_0 \cos(\omega t) \qquad \qquad \text{Eq (2.3)}$$

Therefore Eq (2.2) can be rewritten as

$$P = P_0 + \chi^{(1)} E_0\cos(\omega t) + \chi^{(2)} E_0{}^2\cos^2(\omega t) + \chi^{(3)} E_0{}^3\cos^3(\omega t) + ... \qquad \text{Eq (2.4)}$$

Since $\cos^2(\omega t) = [1/2+1/2\cos(2\omega t)]$

Therefore the Eq (2.4) can be expressed as

$$P = [P_0+(1/2)\,\chi^{(2)}E_0{}^2] + \chi^{(1)}E_0\cos(\omega t) + (1/2)\chi^{(2)} E_0{}^2\cos(2\omega t) +\dots \quad \text{Eq (2.5)}$$

The most important NLO phenomenon is second harmonic generation (SHG), which is widely used for producing visible and near ultraviolet coherent light from infrared radiation. Materials with a lack of centrosymmetry can re–emit the radiation with SHG effects due to polarization. From Eq (2.5) the SHG can be seen as a new frequency doubled component 2ω, i.e., SHG is a form of three wave mixing; two similar frequency photons combined into a single photon with double the frequency of the component photons. When light passes through a second-order NLO material, light with frequencies of both the sum and the difference of the original frequencies is produced, as shown in Figure 2.2. These are called sum frequency generation and difference frequency generation, respectively.
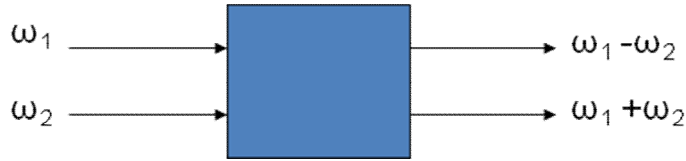
Figure 2.2 Two light waves with different frequencies passing through a NLO material.

Not all materials are suitable for NLO applications. Non–linear second–order susceptibility only occurs in crystals without a centre of symmetry.

2.2.2 Magnetic Properties[1,5,6]

The magnetic moment of a transition metal ion arises from the d electrons due to their spin and orbital motion. It depends on the availability of unpaired electrons; the transition

metal ion can therefore possess a net magnetic moment. The magnetisation, M can be defined as the magnetic moment per unit volume,

$$M = m/V \qquad\qquad Eq\ (2.6)$$

When the sample is placed in a magnetic field, H, a magnetisation is induced, given by;

$$M = \chi H \qquad\qquad Eq\ (2.7)$$

where χ is magnetic susceptibility of the material. The density of the lines of force or magnetic flux or magnetic induction, B, in free space is $\mu_0 H$, while the contribution to the induction from the magnetisation of a material is $\mu_0 B$. Therefore the magnetic flux density of the material is simply the vector sum of these,

$$B = \mu_0\ (H+M) \qquad\qquad Eq\ (2.8)$$

where μ_0 is permeability of free space.

Lenz's law states that the induced voltage is in a direction which opposes the flux change producing it. Magnetic field obeys Lenz's law in that a material with no unpaired electrons placed under magnetic field generates a small moment opposing the applied field, resulting in a small negative susceptibility. This is known as diamagnetism and is observed in any material containing paired electrons. All materials exhibit this diamagnetic effect due to their closed shells, but if unpaired electrons are present they will lead to paramagnetism, where both the electron spin and orbital angular momentum contribute to the observed magnetisation with a positive magnetic susceptibility and a tendency of these materials to attract a magnetic field. The various different types of magnetic materials are traditionally classified according to their bulk susceptibility. For diamagnetic materials, $\chi \approx -10^{-5}\ m^3 mol^{-1}$, for paramagnetic materials, $\chi \approx 10^{-3} - 10^{-5}\ m^3 mol^{-1}$ and for ferromagnetic materials, $\chi \approx 50 - 10,000\ m^3 mol^{-1}$. There are other materials closely related to ferromagnets are ferrimagnets and antiferromagnets.

In a paramagnetic material, spins are randomly oriented due to their thermal energy. When the field is applied to an ideal paramagnetic material, all the spins align parallel to

the applied field, resulting in a net moment in the same direction as the applied field. As can be defined by the Curie law, the susceptibility varies inversely with temperature,

$$\chi = \frac{C}{T}$$

Eq (2.9)

where C is the Curie constant.

However there are some materials which deviate from this law due to their strong magnetic interactions at a critical temperature. Such materials may exhibit order below the critical temperature and can be described by a generalised law known as the Curie–Weiss law,

$$\chi = \frac{C}{T \pm \theta}$$

Eq (2.10)

where C and θ are the Curie and Weiss constants, and T is the temperature. The Curie constant, C was found to be

$$C = \frac{N \mu_{eff}^2 \mu_B^2}{3k}$$

Eq (2.11)

where N is the number of magnetic ions and μ_{eff} is the effective magnetic moment.

$$\mu_{eff}^2 = g^2 J(J+1)$$

Eq (2.12)

where J is the spin orbital angular momentum quantum number for the ions of the individual unpaired electrons. The effective magnetic moment of first row transition metals uses the approximated spin only formula 2.13.

$$\mu_{eff}^2 = g^2 S(S+1)$$

Eq (2.13)

where g is the gyromagnetic ratio, which usually has a value about 2, and S is the sum of the spin quantum numbers of the individual unpaired electrons.

When we carry out magnetic measurements, the magnetic susceptibility of the sample is measured by scanning the temperature at a particular applied field. The type of magnetic

interaction can be deduced from the data after suitable diamagnetic corrections. The plot of magnetic susceptibility versus temperature according to the Curie–Weiss law can fall into the following categories.
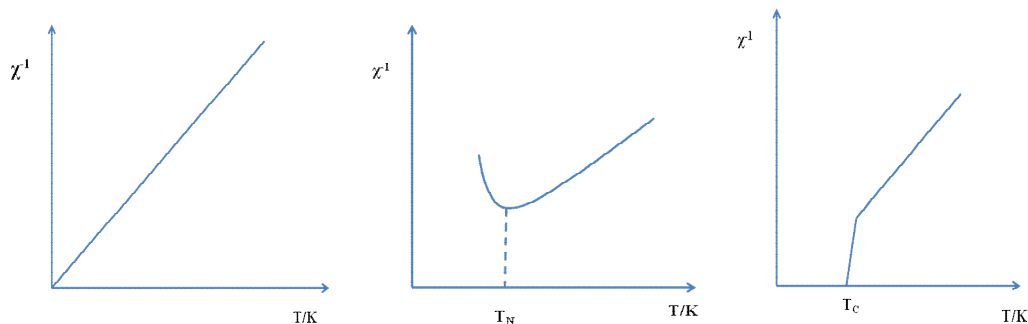
Figure 2.3 χ^{-1} vs. T for paramagnetic (only if θ=0) (left), antiferromagnetic (centre) and ferromagnetic (right) interactions.
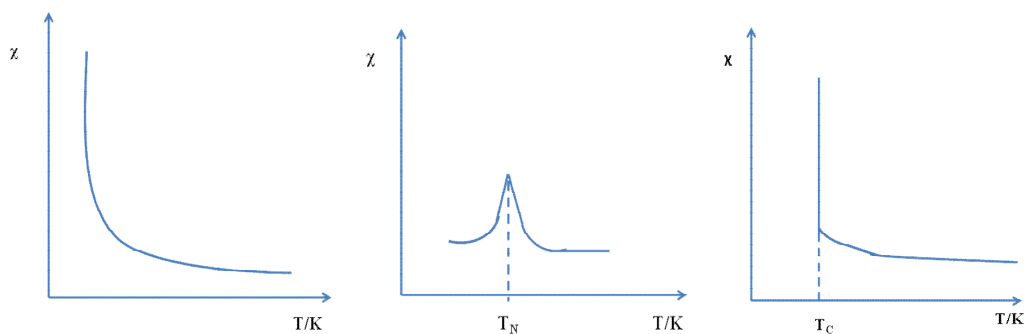
Figure 2.4 χ vs. T for paramagnetic (left), antiferromagnetic (centre) and ferromagnetic (right) interactions.

The above plots demonstrate three different magnetic interactions below the critical temperature. In ferromagnetic ordering, the magnetic moments within domains are aligned parallel below the Curie temperature T_C, which is the transition temperature between the paramagnetic and ferromagnetic phases. If the magnetic spins of neighbouring atoms align in an anti–parallel manner, then an antiferromagnetic interaction occurs below the Nèel temperature–T_N is the transition temperature between paramagnetic and antiferromagnetic phases. Ferrimagnetism usually occurs when unequal moments align antiparallel resulting in a net non–zero moment. It should be

54

remembered that the susceptibility only follows the Curie–Weiss law in the paramagnetic region. Once the material becomes ordered the susceptibility behaves in a very complicated way and no longer has a unique value for a given field strength. Therefore the Curie–Weiss law applies only above their ordering temperature. The Weiss constant, θ is the temperature at the intercept of the straight line plotted as $1/\chi$ against temperature. When the Weiss constant has negative value, it indicates antiferromagnetic interactions whereas a positive Weiss constant implies ferromagnetic interactions.

The most common way to represent the macroscopic magnetic properties of a ferromagnetic material is by a plot of magnetic induction B for various field strengths H, or hysteresis loop. From this, magnetisation can be calculated at every point on the hysteresis curve using the general formula $B=\mu_0(H+M)$. A typical hysteresis loop of a ferromagnetic material is shown in Figure 2.5.
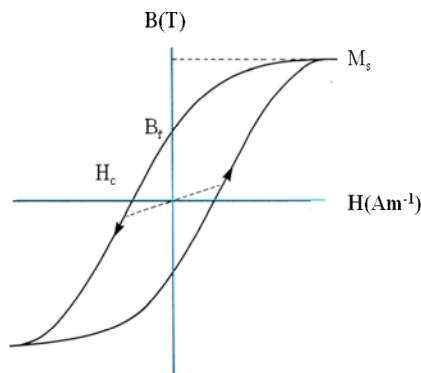
Figure 2.5 A typical hysteresis loop of a ferromagnetic material. H_c is the coercivity and B_r is the remanent magnetic induction.

From the hysteresis plot, it is seen that the ferromagnet in its initial state is not magnetized. Application of field, H causes the magnetic induction to increase in the field direction. If H is increased indefinitely, all the magnetic dipoles within the material are aligned in the direction of the magnetic field, H. This is called saturation magnetisation. The saturation magnetisation depends only on the magnitude of the atomic magnetic moments, m and the number of atoms per unit volume, n; i.e. $M_s=nm$. When the field is reduced to zero after magnetising a magnetic material the remaining magnetic induction

55

is called the remanent induction B_r and the remaining magnetisation is called the remanent magnetisation M_r. The retention of magnetisation distinguishes ferromagnets from paramagnets which, although they acquire a magnetic moment in an applied field, H cannot maintain the magnetisation after the field is removed. The magnetic induction can be reduced to zero by applying a reverse magnetic field of strength H_c. This field strength is known as the coercivity. It is strongly dependent on the condition of the sample, being affected by such factors as heat treatment or deformation. Imperfections, whether in the form of dislocation or impurity elements in the metal, cause an increase in the energy loss during the magnetisation process, in the form of a kind of internal friction, giving rise to the hysteresis. All ferromagnets when heated to sufficiently high temperatures become paramagnetic. At the transition temperature or Curie temperature from ferromagnetic to paramagnetic behaviour, the suceptibility of the material drops suddenly and both coercivity and remanence become zero.

Materials can show different types of exchange interactions. The communication between the electrons of the metal centres occurs through the orbitals overlapping. If both metals are close enough to each other, this is called direct exchange. Superexchange can also occur, when the magnetic d orbitals of the metal centres are mediated through diamagnetic anion ligands. When the angle between cation–anion–cation is 180˚, for example in NiO as shown in Figure 2.6, antiferromagnetic coupling arises. The electrons singly occupying the d_{z^2} and $d_{x^2-y^2}$ orbitals of Ni^{2+} are able to couple with electrons in the p orbitals of the O^{2-} according to the Pauli exclusion principle; when the two electrons occupy one orbital, their spins must be paired.
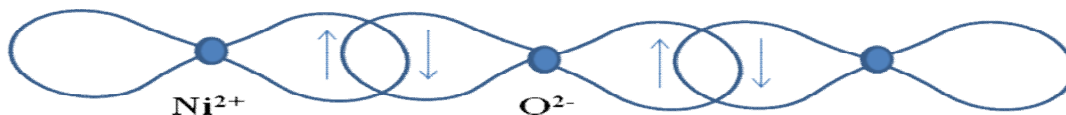
Figure 2.6 180˚ exchange pathway with antiferromagnetic superexchange interactions.

When the angle between cation–anion–cation is 90˚, as shown in Figure 2.7, ferromagnetic ordering may occur. This interaction occurs between the d orbitals of the transition metal and the two different p orbitals, p_x and p_y of the oxygen ligand.

Depending on the two transition metal centres, the remaining p electrons will either have spins which are parallel or antiparallel. Hund's rule suggest that two electrons would have the lowest energy when they are parallel, which facilitates that the two spins on both metal ions must be parallel, i.e. ferromagnetic.
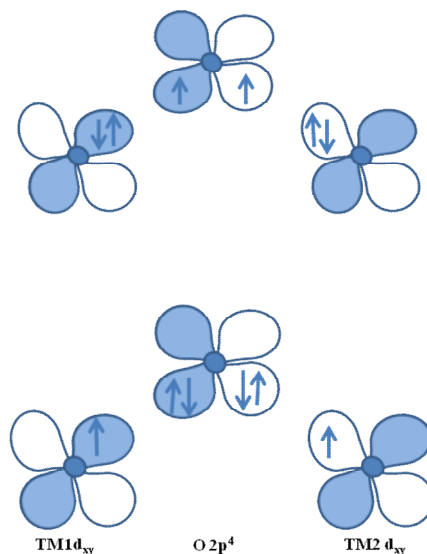
Figure 2.7 90˚ exchange pathway with ferromagnetic interactions; ground state and the low lying excited state is shown.

2.3 Techniques

2.3.1 Synthesis Techniques

Hydrothermal Synthesis[1,7]

Synthesis of a material through solid state methods is dependent on the fusion of the solid starting reagents such as metal oxides, metal carbonates etc. In order to ensure a rapid reaction, reactions are carried out at very high temperature. However, hydrothermal synthesis has proven to be an excellent, relatively low-temperature synthetic approach for many novel solid-state materials. Hydrothermal synthesis shares advantages from both high temperature solid state synthesis and solution phase synthesis. This method is

particularly suited for the synthesis of phases that are unstable at higher temperatures. Mineral formation in nature, under elevated temperature and pressure in the presence of water, led to develop this technique. Mineral extraction is the first successful commercial application of the hydrothermal technique. Today the technique has grown into several branches in science and technology.

Various researchers define the hydrothermal technique in different ways and there is no unanimous definition, however Byrappa defines the technique as any heterogeneous reaction in an aqueous medium carried out above room temperature and at a pressure greater than 1 atm. Using the term "hydrothermal" may also be ambiguous. Chemists prefer to use the term "solvothermal", based on any chemical reaction in the presence of a solvent above its normal boiling points.

Hydrothermal methods use water as a solvent under pressure and at temperatures above 100°C to speed up the reactions between solids. The water has two functions, as a pressure–transmitting medium and as a solvent, in which the solubility of the reactant is pressure and temperature dependent. The reactants and water are placed inside a Teflon–lined cylinder or bomb which is sealed. The bomb is usually heated at a temperature in the range 100–300°C. Pressure can be controlled either externally or by the degree of filling in a sealed bomb. The autogenous pressure is dependent upon how much water is present in the vessel. Filled with 90% water for example, a higher pressure is attained at a lower temperature than for a vessel filled up with only 10% water.

The mechanisms of hydrothermal synthesis are very complex due to the wide range of chemical reactions, equilibria, and solubility variations that occur throughout the heterogeneous synthesis mixture during the crystallisation process. However, a large number of reaction variables such as reaction temperature, reaction time and pH influence the hydrothermal synthesis. The maximum pressure inside the closed vessel is dependent on the strength of the walls, the temperature, the volume of the fluid and the mechanical properties of the vessel. This is partially the reason that hydrothermal reactions are complex. If the pressure exceeds that of the vessel capabilities, it may explode so it must be placed inside an autoclave. Teflon is only usable within a certain

pressure and temperature range because it can be slightly porous. Unlike glasses, Teflon can also be used with alkaline solutions. A hydrothermal autoclave should contain the following characteristics: inertness to acids, bases and other reagents, easy to assemble and disassemble with sufficient length to provide the desired temperature gradient, leakproof and able to withstand high pressure and temperature for a long duration. The selection of the autoclave is usually based on the type of materials under investigation, the reaction medium and experimental pressure–temperature conditions. The typical autoclave used in our lab is shown in Figure 2.8; this can be used under mild hydrothermal conditions up to the temperature limit of 220˚C.

Figure 2.8 Schematic autoclave (left) and Teflon liner (right) used in hydrothermal synthesis.

Another advantage of hydrothermal synthesis is in the preparation of compounds in unusual oxidation states stabilised by the raised temperature and pressure, particularly in transition metal complexes. The super–heated water can also dissolve metal oxides that would not normally dissolve in water at room temperature. If these conditions fail to dissolve the oxides, then a mineraliser can be added with the reactants. For example, quartz is insoluble in water at 400°C and 2 kbar; by adding mineraliser, it crystallises under the same conditions. This technique provides bulk single crystals of quartz and zeolites with bigger size, pure and dislocation–free for further studies. Further, the hydrothermal method is useful to synthesise low temperature phases as well as metastable compounds.

The viscosity of water decreases with temperature. Consequently, this increases the mobility of the molecules and ions in solution, much greater than in water in normal conditions. In the autoclave, the starting materials dissolve in the hottest part of the reaction vessel and then they are transported throughout the vessel via convection currents and are precipitated in the cooler parts of the vessel where their solubility is lower. The dielectric constant of water decreases with rising temperature and increases with rising pressure. The temperature effect is the most important, so at low temperature and high pressure the dielectric constant will be high. Electrolytes therefore tend to associate under these conditions, between 200 and 500°C and the ionic content of water increases so hydrolytic reactions are favoured.

Solid State Synthesis[1]

The solid state method is the most widely used technique in the preparation of polycrystalline materials. This is the oldest and simplest method; mix the powdered reactants together in a stoichiometric ratio and press them into pellets, then heat in a furnace for prolonged periods. Solids usually do not react together at room temperature over normal timescales, because nucleation of the reaction is very difficult and it is necessary to heat them to much higher temperatures to break the bonds, allow migration of the atoms and reform the bonds. Often heating up to 1000–1500ºC is required, in order for reaction to occur at an appreciable rate to overcome the activation energy barrier of the reaction. There are two factors important in solid state reactions; thermodynamic and kinetic factors. Thermodynamic factors consider the changes in free energy of the reaction; kinetic factors determine the rate at which the reaction occurs. The rate of reaction between the solids is determined by the following factors:

1. The area of contact between the reacting solids and hence their surface areas.
2. The rate of nucleation of the product phase.
3. The rates of diffusion of ions through the various phases and especially through the product phase.

It is necessary to maximise all of these factors in order to reduce the time taken for solids to react together. The preparation of pellets can improve the area of contact between the reacting grains in the mixture.

2.3.2 Diffraction Experiments[1, 2, 6]

The determination of a crystal structure from X–ray or neutron diffraction data is dependent not only on the type of instrument or radiation source where the experiment is carried out but also on the characteristics of the sample and its chemical composition. Thus, the experimental conditions, absorption, crystallinity and crystal structure are the main factors to be taken into consideration. Crystalline solids are composed of regular arrays of atoms and ions with an *inter*–atomic spacing of the order of 1 Å. The periodic nature of the internal structure may thus be regarded as a three–dimensional grid with the unit cell as the repeating unit. The grid can be divided up into sets of planes in various orientations with an *inter*–planar spacing, d_{hkl}. In the Bragg approach to diffraction, each of these planes act as a semi-transparent mirror, and some of the incident radiation reflects off a plane with the angle of reflection equal to the angle of incidence, as shown in Figure 2.9.

The rest of the radiation is transmitted and subsequently reflected by succeeding planes. The X–rays are not reflected by planes of atoms, but are diffracted in all directions by the interaction of the X–rays with the electron density of the atoms. However, these two descriptions are equivalent and give the same results.

Only when Bragg's law

$$n\lambda = 2d_{hkl}\sin\Theta_{hkl} \qquad\qquad\qquad \text{Eq (2.14)}$$

satisfies the conditions for constructive interference, Bragg reflection can occur. Then n is an integer and λ is the wavelength for the radiation, with the same order of magnitude as the *inter*–atomic distances.
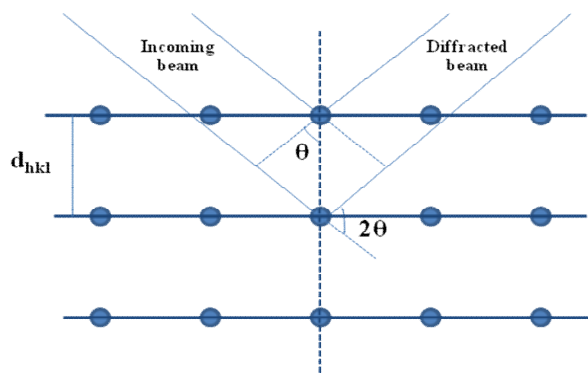
Figure 2.9 X-ray scattering by the planes of atoms

The Bragg angle, Θ_{hkl}, is the angle where reflections from the hkl planes, with *inter–planar* distance d_{hkl}, are observed, and hkl are the Miller indices. Higher–order (n = 2, 3, etc.) scattering from planes d_{hkl} is indistinguishable from the first–order scattering (n=1) from planes $d_{hkl/2}, d_{hkl/3}$, etc. Hence, $\lambda = 2d_{hkl} \sin\Theta_{hkl}$, known as the Bragg equation, represents the condition for diffraction to take place.

The resultant of all the waves scattered by all the atoms in the unit cell, in the direction of the hkl reflection, is called the structure factor, F_{hkl}. It depends on both the position of each atom, j, and its scattering factor, f_j. If the structure factors are known, it is possible to calculate how the scatterers are distributed in the unit cell, i.e. the position of the atoms. In diffraction experiments the intensity, I_{hkl}, of the diffracted beam is measured, and the relation between structure factor and intensity is

$$I_{hkl} \; \alpha \; F_{hkl}{}^2 \hspace{5cm} Eq \; (2.15)$$

This can provide information about the atoms and their positions within the unit cell.

In the process of X–ray diffraction, the X–rays are scattered by the electrons surrounding the nucleus, and the scattering factor, f_j, increases with the number of electrons. The scattering factor also decreases with the angle of diffraction, $\sin\Theta/\lambda$, due to the destructive interference associated with the size of the atom. Hence, in the presence of heavy atoms, accurate determination of light atom positions is quite difficult with the use of X–ray powder diffraction (XPD) data. On the other hand, neutrons are scattered by the nucleus, which behaves as a point scatterer.
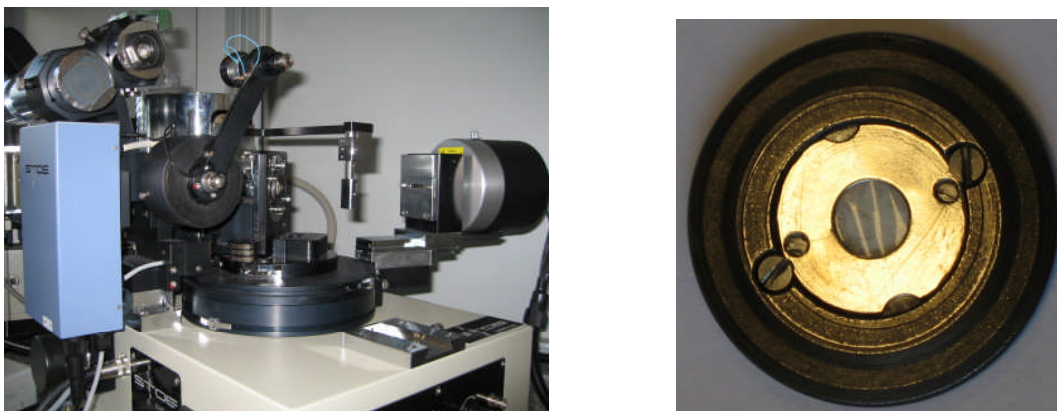
Figure 2.10 X–ray diffractometer (in house) (left) and Mylar disc (right).

Throughout this research, the X–ray powder diffraction information has only been used for identification of phases. All crystalline products were examined by X–ray powder diffraction on a Stoe diffractometer (in house) with Ge monochromated Cu $K_{\alpha 1}$ radiation (λ=1.54056 Å). The samples were ground into fine powder and mounted between two Mylar discs, then examined in transmission geometry (see Figure 2.10). Theoretical powder patterns were simulated using the Stoe WinXPow software.

Generation of X–rays

X–rays are short wavelength (~1 Å), high–energy electromagnetic radiation, which occur in that part of electromagnetic spectrum between γ–rays and the ultraviolet, having the properties of both waves and particles. They can be generated in two different ways: either by electrons changing energy levels within an atom or by interactions encountered by free electrons.

A high energy beam of electrons is generated by passing current through a wire filament in a laboratory X–ray tube, and accelerated through high voltage, allowed to strike a metal target, often copper (λ = 1.54184 Å) or molybdenum (λ = 0.71073 Å), which determines the wavelength of generated X–rays. The incident electrons have sufficient energy to ionize some of the copper 1s (K shell) electrons, therefore an inner orbital electron is displaced. An electron in an outer orbital (2p or 3p) immediately jumps to

replace the displaced higher–energy electron in the 1s level. This results in the generation of a X–ray photon equal to the quantum energy of the transition.

$E=hc/\lambda$ Eq (2.16)

E is the energy of the electron flux

h is Planck's constant (6.626×10^{-34} Js)

c is the speed of light (3.0×10^{18} Å/s)

λ is the wavelength

For copper, the 2p→1s transition is called K_α and the 3p→1s transition is called K_β, as shown in the Figure 2.11.
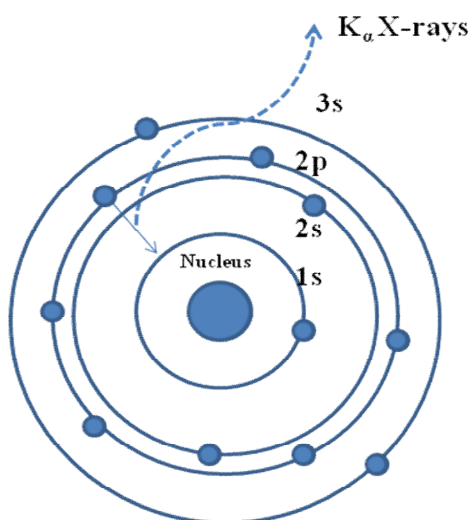
Figure 2.11 Generation of Cu K_α X–rays

X–rays are produced whenever matter is irradiated with a beam of high–energy charged particles or photons. Any interaction which occurs between the particles will result in a loss of energy. Since energy must be conserved, the energy loss results in the release of X–ray photons of energy (wavelength) equal to the energy loss. This process generates a broad band of a continuous radiation (bremsstrahlung or white radiation), as shown in Figure 2.12. This can be overcome by filtering out all other than K_α by using a suitable monochromator.

64
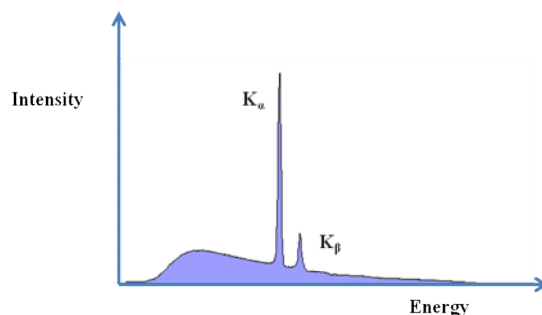
Figure 2.12 X–ray emission spectrum of copper.

2.3.3 Neutron Diffraction[1, 8]

Neutron diffraction is a very expensive technique. However, it can provide an alternative source of radiation to X–rays and provide valuable information, especially on magnetic materials, that is not attainable with any other technique.

Neutron diffraction has several advantages over X–ray diffraction:

- The neutron has zero net electric charge; therefore neutrons can easily and deeply penetrate into most materials without any repulsion, especially in the studies of materials in bulk.
- Neutrons possess spin ½, magnetic moment, therefore they can be scattered by unpaired electrons as well as nuclei. Based on this, magnetic structures of materials are explored.
- The scattering power of atoms in neutron diffraction depends on the atomic nuclei. Therefore location of light atoms can be determined in the presence of heavy atoms and also adjacent elements scatter neutrons very differently. The reason for this is the method of scattering of neutrons compared to that for X– rays. X–rays are scattered by electron density, which means that neighbouring elements scatter similarly because they have very similar electron densities. In comparison, neutrons are scattered by the atomic nuclei, which means that neighbouring elements and even different isotopes scatter differently.

The scattering lengths vary in an irregular fashion for the elements, no simple progression is observed. The fall–off in scattering power versus $\sin\theta/\lambda$ for X–rays is due to the finite size of the electron cloud that scatters the X–rays. Neutrons, however, are scattered by the nucleus, so that the neutrons are effectively scattered from a point, the only fall–off that occurs is due to thermal vibrations within the lattice. Neutrons are also scattered by unpaired spins because they have a magnetic dipole moment. Neutron sources are usually of lower intensity than X–ray sources and the interactions are much weaker. Therefore larger samples are required, and commonly powder diffraction methods used, because it is difficult to grow large single crystals (at least $1mm^3$). Neutron diffraction can be used to solve magnetic structures also.

There are two different types of neutron source, nuclear reactors are used in conventional angle–dispersive experimental methods and pulsed spallation sources generate neutrons by accelerating protons into a heavy metal target.
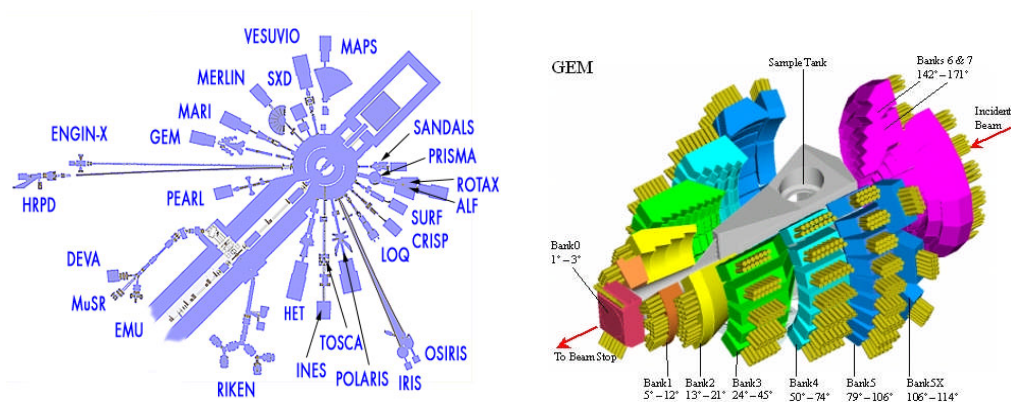
Figure 2.13 The different experimental stations in ISIS (left) and the General Materials Diffractometer (GEM) (right).

Some of our experiments were performed on the D2B high-resolution two-axis diffractometer at the ILL, Grenoble, which uses a nuclear reactor source. A complete diffraction pattern is obtained after about 25 steps of $0.05°$ in 2θ in the presence of 128 detectors spaced at $1.25°$. D2B is well suited for typical small inorganics and large structures, such as zeolites containing absorbed molecules. Patterns were recorded in the

2θ range of 10–160° at a wavelength of 1.594Å. This will be discussed in chapter 6. It is possible to measure small samples about 200 mg with high resolution in D2B.

The ISIS facility at Rutherford Appleton Laboratory, UK provides a pulsed spallation source, well suited to time–of–flight wavelength-dispersive methods. The neutrons are generated by accelerating a proton beam with 800 keV at a certain frequency into a set of thin tantalum sheets surrounded by cooling water. The high energy neutrons are moderated into useful thermal ones by, for example, H_2O, liquid CH_4 or liquid H_2, therefore the neutrons have approximately the same wavelength for diffraction from crystals. The detector is placed at a fixed scattering angle 2θ, and the time taken for neutrons to reach the detector can be measured by the time–of–flight method and the scattered intensity is determined as a function of wavelength or d–spacing.

The wavelength of the neutrons can be determined from the De Broglie equation

$$\lambda = \frac{h}{mv}$$
Eq (2.17)

The kinetic energy can be written as

$$\frac{1}{2}mv^2 = \frac{3}{2}kT$$
Eq (2.18)

where m is the neutron mass. In a time–of–flight experiment, all the wavelengths are used and a complete diffraction pattern is collected from each pulse of neutrons. The neutrons arrive at different times, diffracted from planes with different d–spacing. If the total flight path is L, then time–of–flight, t is related to the d–spacing through De Broglie's equation, substituting the wavelength from Bragg's law.

$$V = L\big/t$$
Eq (2.19)

$$t_{hkl} = \left(\frac{2mL\sin\theta}{h}\right)d_{hkl}$$
Eq (2.20)

The time taken for a neutron to reach the detector, t, is proportional to the d–spacing of the Miller planes, from which the neutrons are diffracted. The larger 2θ and longer pathlength, L, can increase the resolution.

Figure 2.14 A vanadium sample container used in neutron diffraction experiments.

2.3.4 Powder Diffraction[1, 2]

Powder diffraction is often used because large enough good quality single crystals cannot be grown for many materials. A powder sample contains crystallites in many different orientations, but some will be in the correct position to satisfy the Bragg equation for each set of hkl planes present. The same set of planes in different crystallites will lie at different angles around the incident beam, resulting in a cone of diffracted beams, as shown in Figure 2.15. These cones are monitored electronically, and the data are obtained as a plot of intensity versus 2Θ.
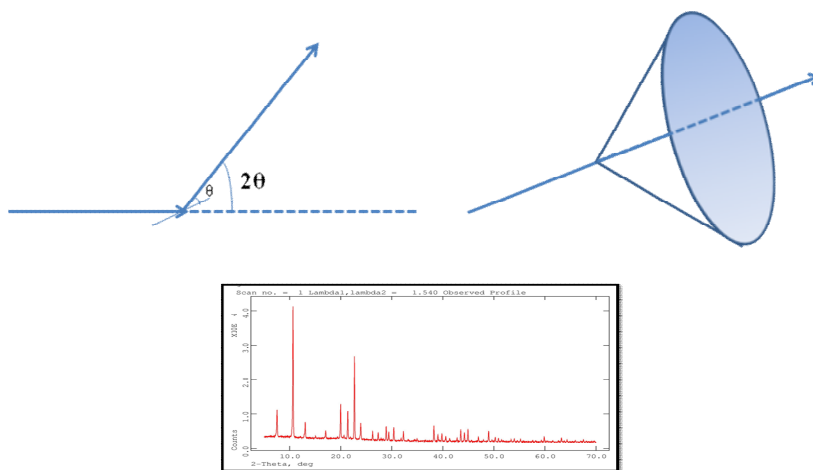
Figure 2.15 Cones of X–rays diffracted from a powder sample and a powder pattern

A powder pattern is characteristic of a particular structure and is used as a fingerprint for a substance. An unknown sample can be identified if its powder pattern can be matched to a known pattern. This is also used as a check on phase purity. If a powder pattern can be indexed, it is possible to calculate the dimensions of the unit cell. Despite the compression of the data from three dimensions into one dimension, powder diffraction can be used to determine simple structures, the main advantage being its speed. Structures can be refined from powder data provided a suitable starting model is available. The Rietveld method is a least–squares refinement which minimises the difference between observed and calculated powder patterns, rather than individual structure factors, to take overlapping peaks into account.

The Rietveld Method[9]

Structure determination using powder diffraction is difficult due to random orientation of crystallites resulting in superposition of the crystallographic axes onto the same axis of the diffraction pattern. Structure refinement is the most common use of powder diffraction using the Rietveld method, introduced by Rietveld in 1969. However, this requires that an approximation to the correct structure should be known in advance. The technique used for powder diffraction assumes that contain all possible Bragg planes would be simultaneously available for diffraction. This does not always occur, therefore preferred orientation statistics sometimes need to be considered.

Especially in the case of low symmetry structures, crystallographic information can be poor, when using powder diffraction rather than a single crystal due to the random orientation of the crystallites and the overlap of diffraction peaks. Compressing the three dimensional data of crystallographic information into the single dimension of a powder diffraction pattern leads to loss of information. Therefore the conventional method of refinement using the total intensities of the peaks (reflections) cannot be used.

The Rietveld method overcomes this difficulty based on linear least–squares minimisation of a function, S_y, composed of the observed and the calculated intensities

for each individual point, i, in the powder profile. The refinement is typically done by using the GSAS program[10], the weighted difference between the data sets can be calculated as follows,

$$S_y = \sum_i w_i \left(y_{i,\,obs} - y_{i,\,calc} \right)^2 \qquad\qquad \text{Eq (2.21)}$$

where $y_{i,obs}$ is the observed intensity for an ith point, $y_{i,calc}$ is the calculated intensity at the ith point and w_i is a suitable weight, based on the uncertainity of each reflection, and is defined by;

$$W_i = \frac{1}{y_{i,\,obs}} \qquad\qquad \text{Eq (2.22)}$$

The parameters that can be refined by this method include the lattice parameters, the atomic coordinates, temperature factors, peak shapes and intensity corrections.

The goodness of the fit between the calculated pattern and the observed data can be judged from the R_p, wR_p, RF^2 and χ^2 values.

$$Rp = \frac{\sum_i | y_{i,obs} - y_{i,calc} |}{\sum_i y_{i,obs}} \qquad\qquad \text{R–pattern} \qquad\qquad \text{Eq (2.23)}$$

$$wRp = \sqrt{\frac{\sum_i w_i (y_{i,obs} - y_{i,calc})^2}{\sum_i w_i \, y^2{}_{i,obs}}} \qquad\qquad \text{R–weighted pattern} \qquad\qquad \text{Eq (2.24)}$$

$$R_F{}^2 = \frac{\sum_K (F_{k,obs})^2 - (F_{k,calc})^2}{\sum_K (F_{k,obs})^2} \qquad\qquad \text{R–structure factor} \qquad\qquad \text{Eq (2.25)}$$

$$\chi^2 = \frac{\sum_i w_i (y_{i,obs} - y_{i,calc})}{N - P + C} \qquad \text{goodness–of–fit} \qquad \text{Eq (2.26)}$$

Where N, P and C are the number of observations, refined parameters and constraints. The R–structure factor is calculated using integrated intensities for the kth reflection and is equivalent to the quantity calculated for single crystal structure solution.

2.3.5 Single Crystal Diffraction[11, 12]

This is the most important technique for structural characterisation. A computer controlled diffractometer can be used to examine single crystals of reasonable size (0.01– 0.5 mm) in order to determine lattice parameters, symmetry information and intensity data. The lower limit of single crystal size is 10 μm for conventional single crystal techniques. Single crystal X–ray diffraction data were collected with a Rigaku Mercury CCD (in house) with silicon monochromated Mo K$_\alpha$ radiations, as shown in Figure 2.16.

The datasets were corrected for absorption via multi-scan methods. The structures were solved by direct methods and refined by full–matrix least–squares techniques, using the SHELXS, SHELXL[13] and WinGX [14] packages.

Initially peaks are indexed by assigning correct hkl values; the crystal system and unit cell parameters are calculated. The orientation of the crystal to the incident beam is then determined. Data are then collected, to give a list of hkl, intensity and error values for all measured reflections corresponding to each spot in the diffraction pattern.
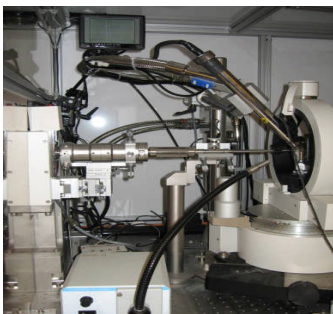
Figure 2.16 Single crystal X–ray diffractometer (in house).

The space group is determined from the systematic absences of these hkl values: reflections which are expected based on the unit cell and crystal system but which have zero intensity due to the effects of symmetry. Corrections to the data can be applied, such as an absorption correction, which accounts for X–rays losing intensity as they pass through the crystal. This is more important for needles or plates, which have a large relative difference between different crystal edges. In order to determine the type and position of atoms within the unit cell, the diffraction data are converted into a 3–dimensional map of electron density by doing complex calculation. This is not straightforward due to the loss of phase information. Based on the calculations, the structure factor, F_{hkl}, is converted into an electron density map, ρ_{xyz}.

$$\rho_{xyz} = \left(\frac{1}{V}\right) \sum_{hkl} F_{hkl} e^{-2\pi i(hx + ky + lz)} \qquad \text{Eq (2.27)}$$

Direct Methods

Direct methods are used to obtain phase information from mathematical relationships between structure factor and amplitudes. Direct methods are implemented based on two conditions: that the electron density must be positive or zero everywhere (i.e. not negative), and only discrete atoms, which are treated as equal, make up the structure. Direct methods uses structure factors E_{hkl}, which are normalised for variation in scattering factor f with angle of incidence and element. E_{hkl} values are given by

$$|E_{hkl}|^2 = \frac{|F_{hkl}|^2}{\varepsilon \sum_n f_n^2} \qquad \text{Eq (2.28)}$$

For all n atoms randomly distributed in the unit cell. ε is normally equal to 1. The normalised structure factors have the same phases as F_{hkl}.

The Sayre probability equation is used to predict phase relationships:

$$S(hkl) \sim S(h'k'l').S(h-h', k-k', l-l') \qquad \text{Eq (2.29)}$$

where S relates the sign of E_{hkl}. Thus the phase of a reflection can be predicted from others which are known. The probability P that this prediction is acceptable, is given by

$$P = \frac{1}{2} + \frac{1}{2}\tanh\left(\frac{1}{N} \mid E_{hkl}.E_{h'k'l'}.E_{h-h',k-k',l-l'}\mid\right) \qquad \text{Eq (2.30)}$$

for N atoms in the unit cell.

A small set of reflections is selected with E_{hkl} values that are most likely to give a correct prediction. The possible phase combinations of these are used to generate phases for other E_{hkl} values of the crystal structure. A map of E_{hkl}s, is Fourier transformed into an electron density map, using the most self–consistent set of phases.

Patterson Methods

This method uses the amplitude of the structure factor squared, taken from the diffraction data.

$$P_{xyz} = \frac{1}{V}\sum_{hkl} \mid F_{hkl}\mid^2 \exp^{-2\pi i(hx+ky+lz)} \qquad \text{Eq (2.31)}$$

All waves are taken as being in phase. This gives a map similar in appearance to an electron density map, but indicates vectors between pairs of atoms in the structure, rather than the atoms themselves. This method is more suitable when a heavy atom is present in the unit cell; whereas direct methods treats all atoms as being equal.

2.3.6 Bond Valence Sums[15]

The bond valence sum rule has developed from Pauling's concept of bond order applied to metals and implies that the sum of the bond valences around an atom equals the formal valence of the atom. Ionic as well as covalent bonds can be evaluated, although the correlation between the bond valences and bond lengths is much better for ionic

compounds. The relationship between the length of a bond (R_{ij}) and its valence (S_{ij}), stated by Brown[16] is

$$S_{ij} = \exp\left(\frac{(R_0 - R_{ij})}{B}\right)$$
Eq (2.32)

Where R_0 is a parameter characteristic of the atom pair i and j, and B is a parameter that can in practice be kept constant for all bonds, at 0.37Å. Both parameters are empirically determined. The bond valence sum, V_i of atom i is then obtained as a sum over all the neighbouring apparent bond valences:

$$V_i = \sum_j S_{ij}$$
Eq (2.33)

There are well established uses of the calculations of the atomic valences. Bond valence sums can be used to describe or evaluate the correctness of a structure when the bond valence sums are not very different from the normal valences and also determine the oxidation states. They can also be used in order to rationalise a distorted environment.

2.3.7 Optical Microscopy[1]

Looking at a sample under magnification under an optical microscope can provide information about its morphology. This technique is useful only if the crystals or powder are larger than the wavelength of visible light (0.4–0.7 µm). This equipment can be used in two ways:

1. Transmission, where light passes through the sample.

2. Reflection where the light is reflected off the sample.

This is also true for electron microscopy where instead of a beam of visible light, a beam of electrons is used. Sample particles are typically within the range of 10–100 µm and must be transparent, but will be opaque when in the bulk form.

The source of light may be white light or monochromatic. This shines on the polariser and only allows light with a direction of vibration parallel to the polariser. The plane polarised light passes through lenses and apertures and onto the sample. Light transmitted by the sample is collected by the objective lens, several interchangeable ones in most cases to select magnification. The analyser may be placed in or out of the path of light. It is similar to the polariser but it is perpendicular to the vibrational direction of the light.

Samples are usually examined initially with the analyser out of the path of light to inspect crystal morphology and size. With the analyser in, it can be made clear whether the sample is isotropic (black) or anisotropic (coloured). Isotropic crystalline substances for example, are usually limited to the cubic crystal system but amorphous solids and glasses appear isotropic as well. They appear dark because plane polarised light passes through them without being modified (since the plane polarised light and analyser are at right angles to each other). Anisotropic substances cause the light to rotate and so they appear light or coloured. These include non–cubic crystal systems. Rotation of the analyser can reveal the extinction directions and whether the crystals are of good quality suitable for X–ray single crystal diffraction. Extinction occurs every 90° and so at every 45°, the sample exhibits maximum brightness. If the sample has parallel extinction where a feature of the crystal (an edge for example) is parallel to the direction of the plane polarised light, it is likely that it possesses some symmetry. Good quality crystals should show sharp extinction. Crystal aggregates may show a more irregular extinction. If the extinction divides into strips, there is a good chance that the crystal is twinned. Light grinding of the sample should give crystals of suitable quality.

The purity of the sample can be checked by optical microscopy. Low impurity levels are easily detected if the optical properties are very much different from the desired product.

Although optical microscopy is not used as much as it was, it is still a valuable tool for the X–ray crystallographer to provide an initial guess of the symmetry of the unit cell to save time in the X–ray single crystal diffraction studies. However, assumptions of crystallinity cannot be made if the crystals are too small to be identifiable.

2.3.8 Scanning Electron Microscopy (SEM)[1]

Figure 2.17 The scanning electron microscope (in house).

The SEM technique provides structural information with a wide range of magnification. It provides detailed information of the material, such as texture, morphology and the features of the surface with reflection technique. For the reflection technique, the thickness of the sample no longer requires a special method of sample preparation. However, if the sample is a poor conductance of electricity, it has to be coated with a thin layer of metal. The SEM, JSM 5600 at University of St Andrews (see Figure 2.17) uses a tungsten filament as the electron source. The probe current can be applied over wide range, from 10^{-12} to 10^{-6} A, with the accelerating voltage being 0.5 to 30 kV. The sample is placed in the microscope, and bombarded with high energy electrons. It generates X–rays, which correspond to the elements present in the sample. Elemental analysis of the sample will be done by scanning the energy of emitted X–rays by using the attached energy dispersive X–ray system (EDX). There is a camera inbuilt in the system, providing images in detail of the structural morphology.

2.3.9 Superconducting Quantum Interference Device (SQUID)[6, 17]

Magnetisation as a function of temperature has been measured in a SQUID at the University of St Andrews (see Figure 2.19). The data were measured between 2 K to 334 K in 4 K steps, following consecutive zero field cooling (ZFC) and field cooling (FC)

cycles with an applied field of 5000 Oe. All data sets were corrected for diamagnetism through the use of Pascal constants.
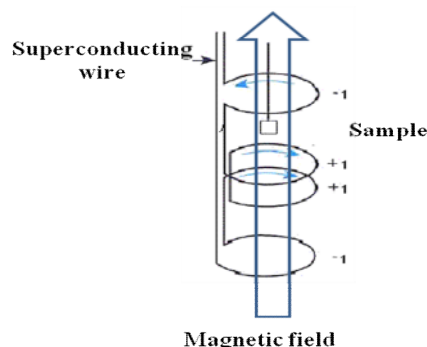
Figure 2.18 Schematic diagram of a SQUID

For measurements in a magnetic field, a helium–cooled superconducting magnet has been used. The sample is placed in the centre of the superconducting wire (see Figure 2.18). This has zero resistance below a characteristic temperature, Tc and is a perfect diamagnet. Therefore current can flow indefinitely at the surface without dissipating energy in the form of heat and internal flux density will be zero with applied field. The two superconducting wires are separated by thin insulating layers, which are small enough to allow the tunnelling of Cooper pairs of electrons, and form two parallel Josephson junctions. Current will flow across this wire with zero voltage; the wire oscillates with the phase differences between either side of the junction, which depends upon the change in magnetic flux.
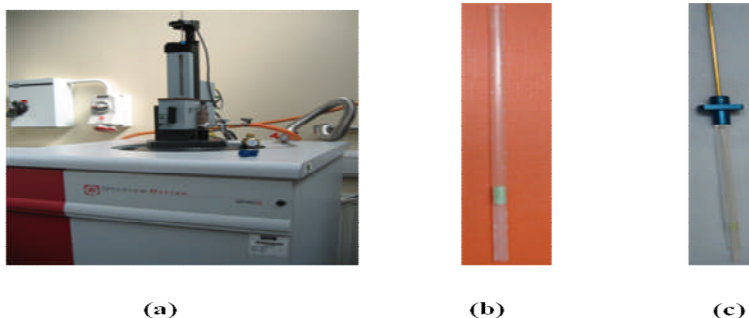
Figure 2.19 Superconducting quantum interferences device (in house) (a), sample packed into a straw (b) and the sample holder and the transport rod (c).

For analysis, the sample was ground into a fine powder, sealed into a gelatine capsule and placed in a straw, which is connected to the sample holder with a sample transport rod. The sample will be placed in the middle of the superconducting detection coil connected to superconducting wire. When current is applied to the system, the superconducting magnet generates a magnetic field from zero to positive and negative values. Until the desired magnetic field is reached, there will be fluctuation in the flux which results in an imbalance between different coils. When the magnet is stabilised at the desired field, the coils will be balanced. The sample moves ups and down, causing changes in flux density within the superconducting detection coils, which changes the current in the superconducting circuit. During the measurements, the sample is stopped at different positions over the scan length, each stop several readings in voltage will be collected and averaged. The measured current is proportional to the magnetic moment of the sample.

2.3.10 TGA Analysis[18]

Thermogravimetric analysis is a simple technique of monitoring the changes in weight of a sample, while changing the temperature. The sample atmosphere can be inert by keeping under Ar or N_2, which could eliminate the oxidation of the sample. Most of the samples undergo characteristic changes, while heating up. These changes could be oxidation or loss of water of crystallisation. The size of the step is analysed quantitatively. When the changes are more complicated in thermograms, derivative curves (differential thermal analysis) can be useful in analysis.

Sensitivity to these changes, under the heating process, is attained by using electronic micro–balances placed inside a furnace. Though the weight undergoes changes, the sample will remain in the same position by the null–point mechanism. The reproducibility of the thermograms is based on the quality of the instrument. Mostly, the instruments use electrical resistance heaters with various different heating techniques such as, infrared, laser irradiation and microwave.

This technique is useful for kinetic studies of weight changes for a particular reaction, chemical reactions, adsorption, desorption and volatilisation. The limitation of this technique occurs when samples undergo melting and crystal phase changes which are difficult to interpret from their thermograms.

2.3.11 Fluorine Analysis[19, 20]

A fluoride ion–selective electrode is useful in the analysis of the amount of F^- ion in the unknown sample. Unlike metal electrodes, ion selective electrodes are not dependent on redox processes. The key feature of an ideal ion–selective electrode is the migration of selected ions across the inorganic crystal/membrane. There are four types of ion–selective electrodes available:

(1) Glass membranes

(2) Solid state electrodes

(3) Liquid–based electrodes

(4) Compound electrodes

(a)   (b)   (c)
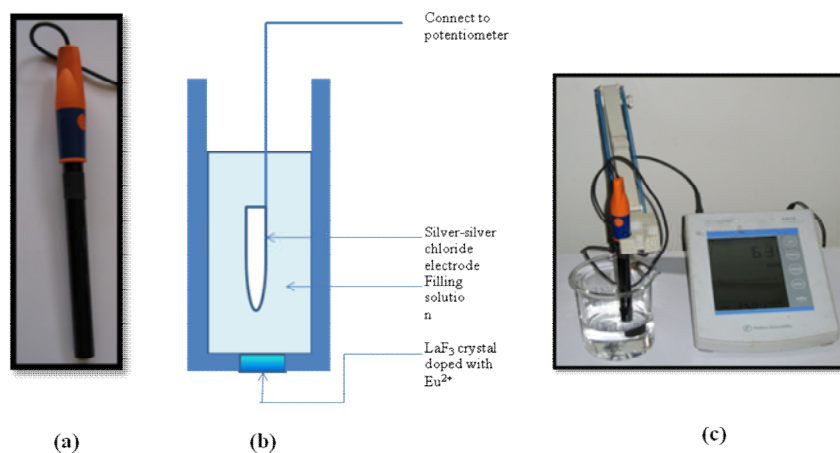
Figure 2.20 Pen type combination fluoride ion–selective electrode (a), the schematic diagram of an ion–selective electrode (b) and the experimental setup (c).
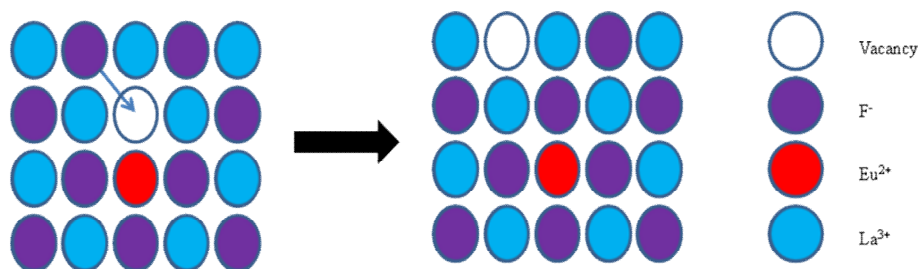
Figure 2.21 Diffusion of F$^-$ ions across the crystal lattice, LaF$_3$ doped with EuF$_2$.

Fluoride ion–selective electrodes fall into the category of solid-state ion–selective electrodes which are based on inorganic crystals of LaF$_3$ doped with Eu^{2+}. Doping divalent cations instead of trivalent cations, makes the crystal structure have vacant sites of fluoride ions. Neighbouring fluoride ions can occupy these vacancies and leave new vacant sites, which makes fluoride ion diffusion through the lattice. This creates a potential difference across the crystal and makes the electrode work, as shown in Figure 2.21. Fluoride activity, AF, and excessive charges of both sides will differ across the crystal which can be related by the free energy change.

$$-RT\ln\left(\frac{AF_1}{AF_2}\right) = -nFE \qquad\qquad \text{Eq (2.34)}$$

where R is the ideal gas constant, n is the charge of the ion, F is the Faraday constant, E is the potential difference across the membrane, AF$_1$ and AF$_2$ activity of fluoride ions outside and inside the membrane and T is the temperature.

$$E = \left(\frac{RT}{nF}\right)\ln\left(\frac{AF_1}{AF_2}\right) = \frac{0.05916}{n}\log\left(\frac{AF_1}{AF_2}\right) \qquad\qquad \text{Eq (2.35)}$$

$$E = const - \beta(0.05916)\log(F_1)\gamma_F \qquad\qquad \text{Eq (2.36)}$$

$$E = const - \beta(0.05916)\log\gamma_F - \beta(0.05916)\log(F_1) \qquad\qquad \text{Eq (2.37)}$$

$const - \beta(0.05916)\log\gamma_F$ is constant, because the fluoride activity coefficient, γ_F is constant at constant ionic strength. A high ionic strength buffer; total ionic strength adjustment buffer (TISAB) is used to keep all the standards and unknown solution of the

same ionic strength and maintain the pH of solution at 5.5, which reduces the interference from hydroxide ions. Therefore the response of the fluoride ion–selective electrode can be written as,

$$E = const - \beta(0.05916)\log(F_1)$$ Eq (2.38)

This pen type ion–selective electrode (see Figure 2.20) contains many advantages such as, an inbuilt reference electrode; there is no need of an additional reference electrode and filling solution.

The fluorine content in the sample was determined by using a fluoride ion-selective electrode calibrated with different concentrations of standard NaF solutions. The sample was ground into a fine powder and dissolved in water with continuous shaking until completely dissolved. TISAB solution with pH 5.5 was used to adjust the ionic strength and keep fluoride activity coefficient constant. The samples were dissolved in an HCl aqueous solution and the pH was then adjusted by adding NH_4OH. For each sample and ten standard solutions with different fluorine concentrations with the same amount of TISAB solution, three measurements were carried out in order to accurately evaluate the average value.

TISAB was prepared by the following experimental procedure; 500 mL of distilled water was placed into 1L beaker. 57 mL of 1 M concentration of glacial acetic acid, 58 g of NaCl and 0.30 g of sodium citrate were added and stirred until completely dissolved. The beaker was placed in a water bath and the pH electrode immersed in the solution and 5 M, NaOH was slowly added into beaker to bring the pH to between 5.0 and 5.5. The content of the beaker was transferred into a 1 L volumetric flask and made up to 1 L solution of TISAB by adding distilled water up to the mark.
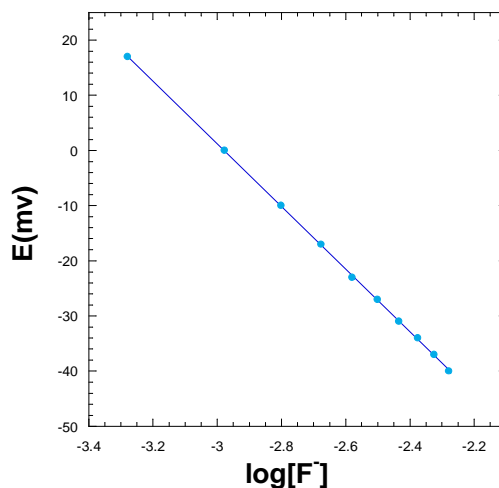
Figure 4.53 Calibration curve for fluoride ion–selective electrode.

2.3.12 CHN Microanalysis

All materials were analysed for carbon, hydrogen and nitrogen content to check whether the stoichiometries are similar to the structural formula refined from single crystal data. Once the phase purity is confirmed, the material will be used for subsequent studies. The analysis was carried out by Carlo Erba Model 1106 Elemental analyser.

References

1. "Solid State Chemistry", A. R. West, John Wiley & Sons, Great Britain, **1984**.

2. "The Basics of Crystallography and Diffraction", C. Hammond, Oxford, **1997**.

3. "Inorganic Materials", D. W. Bruce, D. O'Hare, (Eds), New York, **1992**.

4. "Properties of Materials", R. E. Newnham, Oxford, **2005**.

5. "Magnetism and the Chemical Bond", J. B. Goodenough, John Wiley & Sons, London, **1963**.

6. "Solid State Physics" R. L. Singhal, India, **1989**.

7. "Hand book of Hydrothermal Technology", K. Byrappa, and M. Yoshimura, William Andrew Publishing, U. S. A. **2001**.

8. http://www.isis.rl.ac.uk/Disordered/GEM/GEM_Home.htm

9. "The Rietveld Method", R. A. Young, Oxford University Press, U. K. **1995**.

10. A. C. Larson and R. B. Von Dreele, *General Structure Analysis System (GSAS)*, Los Alamos National Laboratory Report LAUR, **2004**, 86–748.

11. "Fundamentals of Crystallography", C. Giacovazzo, Oxford University Press, U. K. **2002**.

12. "X-ray Structure Analysis" The 11th BCA/CCG Intensive Teaching School, University of Durham, **2007**.

13. G. M. Sheldrick, *Acta Crystallogr., Sect. A: Found. Crystallogr.*, 2008, **64**, 112. 20

14. L. J. Farrugia, WinGX, *J. Appl. Crystallogr.*, 1999, **32**, 837.

15. VALENCE © I. D. Brown, Brockhouse Institute for Materials Research, McMaster University, Hamilton, Ontario. Canada, Used with permission.

16. I. D. Brown, *J. Solid State Chem*., **1989**, 82, 122.

17. http://www.qdusa.com/resources/techdocs.html

18. "Principles and Practice of Analytical Chemistry", F. W. Fifield, D. Kealey, London, **1995**.

19. "Analytical Chemistry", D. A. Skoog, D. M. West, F. J. Holler, S. R. Crouch, London, **1999**.

20. "Quantitative Chemical Analysis", D. C. Harris, New York, **1999**.

CHAPTER THREE

Overview of Experiments

3.1 Synthetic Strategy

During this work, 1525 experiments were carried out using solvothermal techniques and 138 experiments were carried out under solid state conditions. All the solvothermal reactions were performed in a Teflon–lined stainless steel autoclave or polypropylene bottle, depending on the reaction temperature, and heated in an oven. Once the period of reaction was completed, the autoclave was left to cool at room temperature. The contents of the autoclave were filtered and washed, then dried in air at 60˚C. Mostly, the products containing pyridine are soluble in water and lose their crystallinity in other solvents such as ethylene glycol, therefore they were filtered under vacuum and the product was sealed in a vial with a thin film and stored in a refrigerator. The pyridine–containing products decompose in air at room temperature. A general scheme of synthesis is as follows: A transition metal oxide (V_2O_5/MoO_3/Nb_2O_5) was dissolved in hydrofluoric acid, then a structure directing amine was added, followed by powdered CuO and finally the solvent (pyridine/water/ethylene glycol) was added and mixed until homogeneous. The reaction vessel was tightly sealed and heated to the required temperature for an appropriate reaction period.

HF is used as a mineraliser to dissolve metal oxides and also as a source of F⁻ (a hard base) to react with hard acids to provide oxyfluorides/fluorides. The reactions in previous exploratory work were controlled by using so–called 'composition–space' diagrams, whereby hydrofluoric acid/organo amine/metal oxides reactant composition is used as a synthetic variable, varied in a systematic way to produce phase stability fields which map out the chosen reaction products versus composition space. In this work, we seek to expand on these studies, by employing a wider variety of copper species by including different organo amine compounds, which in turn may lead to novel structures containing vanadium, niobium or molybdenum. 'Composition–space' diagrams help to improve the

phase purity as well as crystallinity, which is essential for subsequent studies, and also aids the control of synthetic variables under systematised reaction conditions.

The choice of transition metal oxides used in these reactions was based on the following factors:

Vanadium – various oxidation states can be achieved with polar building units as well as lower oxidation states useful in magnetism studies.

Niobium and molybdenum – To check the effect of periodicity as well as to provide off–centre distorted building units.

Copper – Provides cation complexes which may act as linkers for the polar anionic building units to provide extended structures. Cu^{2+} (d^9) also exhibits magnetism. Moreover it coordinates very well with soft bases, such as nitrogenous compounds.

The reactions were carried out with a wide selection of organic species (see Figure 3.1) to investigate the effect of different structural features and the packing arrangements of similar polymorphs. Based on 'composition–space' diagrams, reactions were performed at 60˚C, 100˚C and 240˚C with different durations of reaction.

Solid state reactions were carried out in alumina boats or crucibles and heated in a box furnace. The reagents used through this work were not air sensitive and preparations were by conventional solid state techniques. All reagents were of 99.9% of higher purity. Prior to use, metal oxides, carbonates, boric oxide and boric acid were heated overnight at 100˚C. Compounds were synthesised by grinding appropriate stoichiometric mixtures of metal oxides, carbonates, boric oxide and boric acid in an acetone slurry using an agate motor and pestle. Approximately 2 g samples were made for each compound initially, but for neutron diffraction larger samples ~10 g were made with ^{11}B isotope as a boron source to reduce neutron absorption. After being allowed to dry, samples were then pressed into a pellet 13 mm in diameter under a pressure of 8 to 10 tonnes. Reaction was carried out using a box furnace. The pellets were contained inside an alumina boat during the heating process. After each heating period samples were reground and repelleted to ensure sample homogeneity. Laboratory X–ray diffraction was used throughout this

process to check the progress of heating and ultimately to determine the best procedure for obtaining highly crystalline, pure, powder samples.

<table>
<tr><td>4,4'–bipyridyl</td><td>2,2'–bipyridyl</td><td>Pyridine(py)</td></tr>
</table>
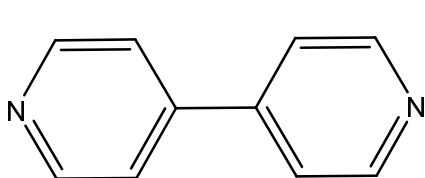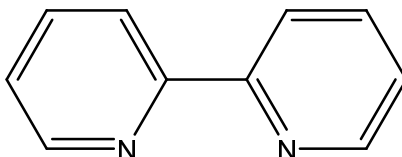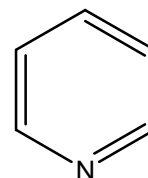
4,4'–bipyridyl   2,2'–bipyridyl   Pyridine(py)
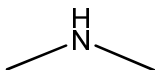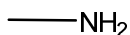
Dimethylamine   Methylamine   Pyrazine (pyz)   Isopropylamine
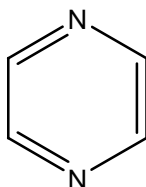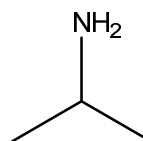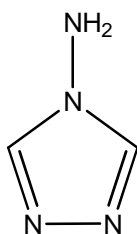
1–amino–1,3,4–triazole(trz)   2,2'–dipyridylamine   Trimethylamine *N*–oxide
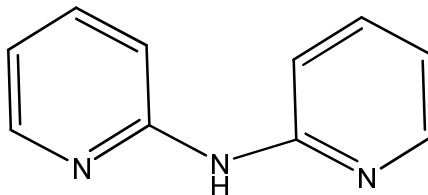
2,6–lutidine   3–picoline   2–picoline   4–picoline

Pyrazole   Imidazole   1,10–phenanthroline
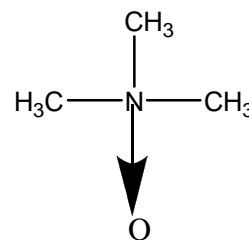
Malonamide   1,2,4–triazole   2,4,6–triaminopyrimidine
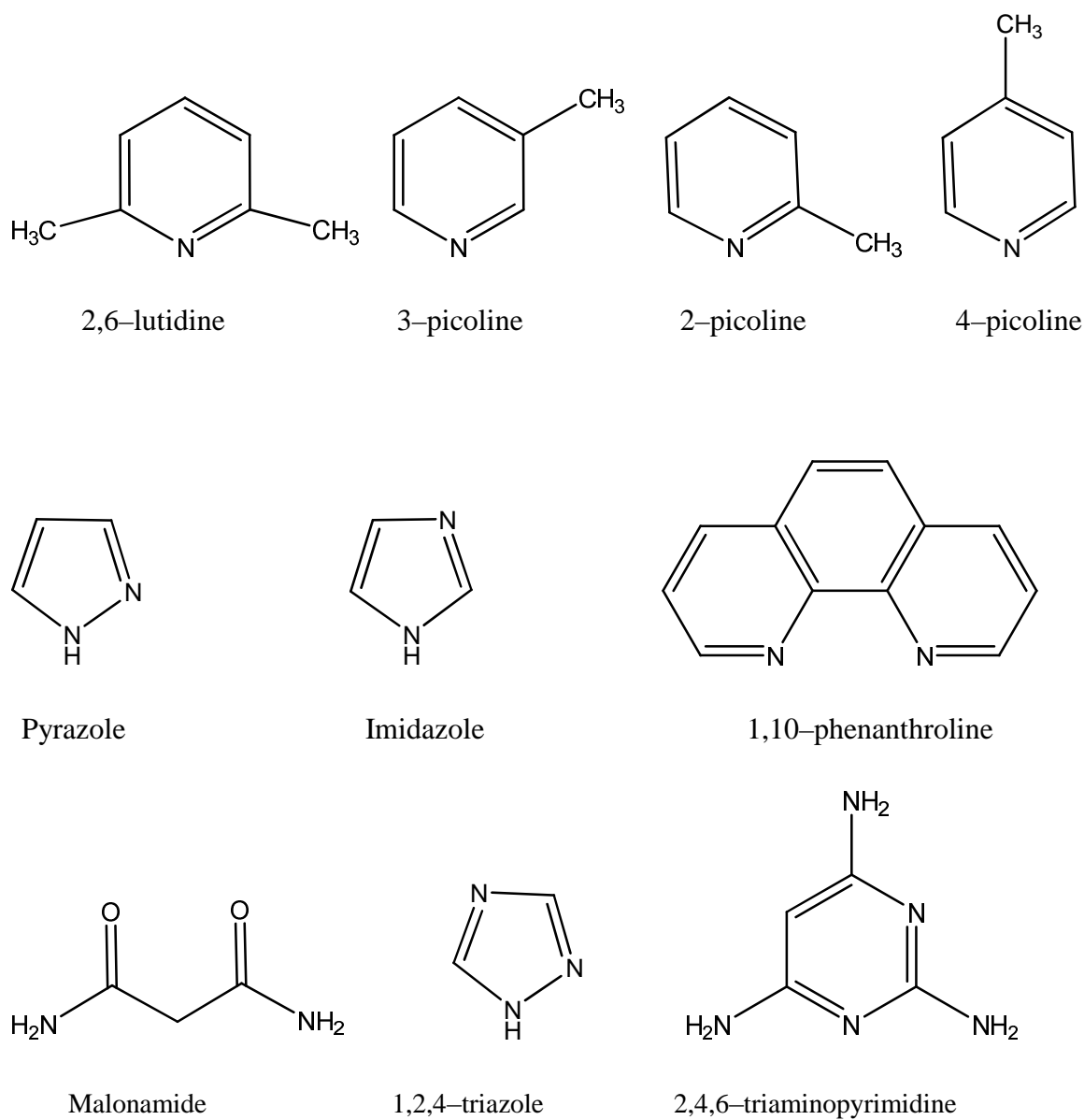
Figure 3.1 Organoamines used as structure directing agents, solvents and templates.

CHAPTER FOUR

Vanadium Oxyfluoride Materials

4.1 Introduction

The structures described in this chapter are categorised into clusters with vanadium monomers, clusters with vanadium dimers, chains, layer and 3–D networks, which are all synthesised solvothermally from vanadium and copper containing reaction media with different amines. These materials have been denoted from **V–1** to **V–8** and **CuV–1** to **CuV–13** and numbered in the chronological order in which they are discussed in this section. Crystallographic information for these structures is presented in Tables 4.1 to 4.5. The synthetic conditions are given in Appendix–III, along with the elemental analysis including fluorine analysis, using a fluoride ion–selective electrode.

In addition, TGA, magnetic measurements and Rietveld refinements have been carried out on those materials which are obtained as a single phase; these will be discussed in this section. Bond valence sum calculations are also carried out to confirm the oxidation states of copper and vanadium metal centres. Atomic co–ordinates are located in Appendix–II. Bond angles and hydrogen bonds are all contained in the appropriate CIF file (see enclosed CD).

Samples were characterised by XRD on a Stoe STADI/P transmission diffractometer using Cu $K_{\alpha 1}$ radiation at 1.5406Å, with a 2Θ range from 5 to 70°. These data were collected 15 hours to assure the best quality pattern to confirm phase purity for subsequent studies. A Rietveld refinement was performed with the GSAS program suite[1] using the atomic co–ordinates determined by single crystal solution as a starting point. Instrumental parameters (background, zero–point, peak profile coefficients) and unit cell parameters were refined. A close final fit to the observed data was achieved with the structure determined from the single crystal experiment. Single crystal X–ray diffraction data were collected with a Rigaku Mercury CCD with silicon monochromated Mo K_{α} radiation. The datasets were corrected for absorption via multi-scan methods. The structures were solved by direct methods and refined by full–matrix least–squares

88

techniques, using the SHELXS, SHELXL[2] and WinGX[3] packages. All non–hydrogen atoms were refined with anisotropic thermal parameters (except where stated). Hydrogen atoms attached to carbon and nitrogen atoms were located at geometrically calculated positions and refined with isotropic thermal parameters, while those attached to oxygen atoms were found, where possible, by Fourier techniques and refined isotropically.

Thermogravimetric analysis (TGA) was carried out on a Standard TG 209 instrument from room temperature to 500˚C at a heating rate of 10˚K/min under argon atmosphere. The fluorine content in the sample was determined by using a fluoride ion–selective electrode[4] as discussed in section 2.3.11 and the analysis included in Appendix–III. Magnetic data of magnetically active materials were measured on a Quantum Design MPMS SQUID. Data were recorded in 5000 Oe field while warming the sample from 2 to 300 K in 4 K steps, following consecutive zero field cooling and field cooling cycles.

The compounds, **V–1** to **V–8** and **CuV–1** to **CuV–13** were synthesised in a systematic manner with linear and cyclic amines as additional nitrogen compounds in the reaction media. All reactions were carried out at 100˚C and 160˚C. CuO and ZnO were initially used as additional metals to carry out similar reactions to those done on previously using only the V_2O_5 as metal source. However, this strategy was not successful and only yields **V–8**. Further experiments using cyclic N–donor compounds with mixed solvents of water and ethylene glycol produced **V–3** and **V–4**. However, this did not produce extended structures under these reaction conditions.

By trying to reproduce the compound[5], $[pyH]_2[Cu(py)_4(VOF_5)_2]$ with derivatives of pyridine as solvent, novel vanadium containing monomers, **V–1**, **V–2**, **V–5**, **V–6** and **V–7** were synthesised. Later on using similar reaction conditions with different heterocyclic N–donors based on 'composition–space' diagrams with water as the only solvent provided three novel extended structures of **CuV–9**, **CuV–10** and **CuV–11**. Further, using linear amines and heterocyclic N–donor compounds in the reaction media with pyridine or derivatives of pyridine as solvent, provided novel compounds with 3–D networks **CuV–13**, layers **CuV–12,** polymorphic chains, **CuV–3** and **CuV–4** and chains containing novel building units (**CuV–5, CuV–6**, **CuV–7** and **CuV–8**).

Table 4.1 Clusters containing vanadium monomers

Compound	**CuV–1**	**V–1**	**V–2**	**CuV–2**
Formula	$[Cu(C_3H_4N_2)_4]$ $[VO_2F_2(C_5H_5N)]_2$	$[VOF_2(H_2O)(C_6H_7N)_2]$	$[VOF_2(H_2O)(C_5H_5N)_2]$	$[C_4H_8N_5]_2[Cu(NH_3)_4(H_2O)_2]$ $[VOF_4(H_2O)]_2$
Formula weight	735.96	309.21	281.16	741.94
Crystal system	Monoclinic	Monoclinic	Monoclinic	Triclinic
Space group	P 2_1/n	C2/c	C2/c	P−1
• a(Å)	12.218(2)	15.720(4)	13.097(8)	7.204(1)
• b(Å)	9.025(1)	10.584(3)	10.554(6)	8.264(1)
• c(Å)	12.705(2)	8.015(2)	8.205(6)	11.903(2)
• α				73.726(10)
• β	94.266(4)	92.894(6)	94.077(18)	86.056(12)
• γ				62.323(8)
volume(Å^3)	1397.1(4)	1331.8(6)	1131.2(12)	600.86(11)
Z	2	4	4	1
total/unique reflns	11486/2552	4620/1441	4314/1029	4296/2321
ind.reflns>2σ(*I*)	1571	1267	962	1508
T(˚C)	−180	−180	−180	−180
λ(Å)	0.7107	0.7107	0.7107	0.7107
ρ_{calcd} (g/cm^3)	1.749	1.542	1.651	2.050
R1[*I*>2σ(*I*)]	0.096	0.045	0.058	0.126
wR2[*I*>2σ(*I*)]	0.213	0.132	0.142	0.396

Table 4.2 Clusters containing vanadium dimers

Compound	**V–3**	**V–4**	**V–5**	**V–6**	**V–7**
Formula	$[V_2O_4F_2(C_{10}H_8N_2)_2]$	$[V_2O_4F_2(C_{12}H_8N_2)_2]$	$[V_2O_2F_4 (C_6H_7N)_4]$	$[C_7H_{10}N]_2[V_2O_2$ $F_6(H_2O)_2]$	$[C_8H_{12}N]_2[V_2O_2$ $F_6(H_2O)_2]$
Formula weight	516.25	570.29	582.38	250.12	264.14
Crystal system	Monoclinic	Triclinic	Monoclinic	Triclinic	Triclinic
Space group	C2/c	P−1	P 2_1/c	P-1	P−1
• a(Å)	9.754(2)	7.840(3)	6.827(1)	7.157(3)	7.118(3)
• b(Å)	12.639(3)	8.535(4)	10.819(2)	8.194(3)	8.742(4)
• c(Å)	16.027(4)	9.183(4)	17.073(3)	9.172(2)	8.917(4)
• α		113.573(14)		73.586(26)	100.224(7)
• β	92.650(6)	102.646(13)	91.661(5)	78.578(29)	102.718(10)
• γ		97.696(12)		77.549(27)	94.703(6)
volume(Å^3)	1973.7(8)	532.4(4)	1260.5(4)	498.4(3)	528.4(4)
Z	4	1	4	2	2
total/unique	6216/1793	3683/1980	8034/2302	3474/1896	3531/1998
ind.reflns>2σ(I)	1608	1392	1869	1482	1777
T(˚C)	−180	−180	−180	−180	−180
λ(Å)	0.7107	0.7107	0.7107	0.7107	0.7107
ρ_{calcd} (g/cm^3)	1.737	1.760	1.534	1.667	1.660
R1[I>2σ(I)]	0.031	0.076	0.057	0.065	0.088
wR2[I>2σ(I)]	0.078	0.252	0.189	0.188	0.307

Table 4.3 1-D chains

Compound	CuV–3	CuV–4	CuV–5	CuV–6
Formula	α-[C$_2$H$_8$N][Cu(C$_5$H$_5$N)$_4$] [V$_2$O$_2$F$_7$]	β-[C$_2$H$_8$N][Cu(C$_5$H$_5$N)$_4$] [V$_2$O$_2$F$_7$]	[Cu(C$_6$H$_7$N)$_4$][VF$_6$]	[Cu(C$_6$H$_7$N)$_4$][VF$_6$].9H$_2$O
Formula weight	692.91	692.91	593.16	706.99
Crystal system	Orthorhombic	Triclinic	Tetragonal	Tetragonal
Space group	Pbcn	P−1	P4/mcc	P4/mcc
• a(Å)	15.291(4)	8.981(3)	8.988(2)	10.402(2)
• b(Å)	9.806(3)	13.533(6)		
• c(Å)	18.028(5)	13.545(6)	17.355(4)	17.238(3)
• α		89.981(3)		
• β		70.65(2)		
• γ		74.19(3)		
volume(Å^3)	2703.0(1)	1489.2(2)	1402.01(5)	1865.2(6)
Z	4	2	8	8
total/unique	16186/2467	10224/5927	7904/671	11853/1173
ind.reflns>2σ(*I*)	1975	4651	617	917
T(˚C)	−180	−180	−180	−180
λ(Å)	0.7107	0.7107	0.7107	0.7107
ρ$_{calcd}$ (g/cm^3)	1.70	1.55	1.42	1.259
R1[*I*>2σ(*I*)]	0.074	0.124	0.079	0.107
wR2[*I*>2σ(*I*)]	0.161	0.339	0.243	0.334

Table 4.4 1-D chains

Compound	**CuV–7**	**CuV–8**	**CuV–9**	**CuV–10**
Formula	$[C_3H_5N_2]_2 [Cu(C_3H_4N_2)_4]$	$[Cu(C_5H_5N)_2 (C_2H_8N_2)]$	$[Cu_2F_2(C_{10}H_{10}N_3)_2]$	$[Cu(C_{10}H_9 N_3)]_2$
	$[V_2O_2F_8]$	$[(VO_3)_2]$	$[V_2O_7]$	$[VOF_4]_2$
Formula weight	759.94	477.72	723.40	755.38
Crystal system	Monoclinic	Orthorhombic	Triclinic	Triclinic
Space group	$P2_1/n$	$P2_12_12_1$	$P-1$	$P-1$
• a(Å)	11.024(2)	10.972(3)	8.047(2)	7.366(3)
• b(Å)	10.095(2)	11.466(3)	8.836(2)	9.445(3)
• c(Å)	12.635(3)	13.842(4)	9.399(1)	16.515(4)
• α			65.531(2)	91.937(7)
• β	103.16(1)		73.97(3)	90.571(6)
• γ			78.14(3)	92.767(7)
volume(Å^3)	1369.1(2)	1741.5(7)	581.5(8)	1146.9(6)
Z	4	4	2	2
total/unique	9229/2809	11816/3614	4029/2209	6076/3626
ind.reflns>2σ(I)	2547	2835	1671	2950
T(˚C)	−180	−180	−180	−180
λ(Å)	0.7107	0.7107	0.7107	0.7107
ρ_{calcd} (g/cm^3)	1.84	1.82	2.07	2.19
R1[I>2σ(I)]	0.046	0.066	0.073	0.112
wR2[I>2σ(I)]	0.135	0.142	0.210	0.300

Table 4.5 2-D layers and 3-D networks

Compound	**CuV–11**	**CuV–12**	**CuV–13**	**V–8**
Formula	$[Cu(C_{10}H_9N_3)]_2[V_6O_{17}]$	$[Cu_3(C_5H_5N)_{12}][V_6O_{18}]$	$[CH_3NH_3]_8[Cu(py)_4]_3$ $[V_7F_6O_{30}]$	$VZnF_5(H_2O)_2$
Formula weight	1047.14	1733.49	2418.97	247.36
Crystal system	Triclinic	Monoclinic	Cubic	Orthorhombic
Space group	P−1	P2$_1$/c	Pn−3n	Icmm
• a(Å)	7.331(1)	23.757(6)	16.494(1)	6.516(2)
• b(Å)	10.123(1)	16.688(4)		7.506(3)
• c(Å)	10.578(1)	17.021(4)		10.752(4)
• α	95.986(4)			
• β	110.160(4)	80.727(6)		
• γ	92.605(3)			
volume(Å^3)	730.11(16)	6660(3)	4487.5(7)	525.9(3)
Z	1	4	2	4
total/unique	5153/2758	42024/12032	25150/694	1577/276
ind.reflns>2σ(*I*)	2423	5623	644	271
T(˚C)	−180	−180	−180	−180
λ(Å)	0.7107	0.7107	0.7107	0.7107
ρ$_{calcd}$ (g/cm^3)	2.382	1.729	1.790	3.125
R1[*I*>2σ(*I*)]	0.038	0.130	0.034	0.019
wR2[*I*>2σ(*I*)]	0.122	0.374	0.101	0.051

4.2 Clusters Containing Vanadium Monomers

The crystal structures of $[Cu(C_3H_4N_2)_4][VO_2F_2(C_5H_5N)]_2$ (**CuV–1**), $[VOF_2(H_2O)(C_6H_7N)_2]$ (**V–1**), $[VOF_2(H_2O)(C_5H_5N)_2]$(**V–2**) and $[C_4H_8N_5]_2[Cu(NH_3)_4(H_2O)_2][VOF_4(H_2O)]_2$ (**CuV–2**) exhibit neutral clusters containing vanadium monomers and are discussed in this section.

4.2.1 Discussion

Structure

The crystal structure of **CuV–1** exhibits a novel, finite cluster. The asymmetric unit contains one unique anion, $[VO_2F_2(C_5H_5N)]^-$ unit and a cationic complex $[Cu(C_3H_4N_2)_2]^{2+}$ situated on a mirror plane. The neutral cluster is constructed by the coordination of two anions to a central cation, as shown in Figure 4.1. Vanadium is present in the +5 oxidation state, and exhibits a distorted trigonal bipyramidal environment, and copper is present in the +2 oxidation state as expected from the colour of the crystal, further confirmed by BVS analysis (see Table 4.6).

The vanadium coordination environment can be defined by a short terminal vanadyl bond, bridging oxide ligand, two terminal fluoride ligands and nitrogen ligand from pyridine. There are two different nitrogen coordinating–donor ligands, pyridine is coordinated to vanadium whereas imidazole occupies the equatorial sites of copper, which is quite unusual. The Jahn–Teller active Cu^{2+} binds to the four imidazole molecules in a square planar arrangement with Cu–N bond length between 2.004(7) Å–2.015(7) Å, while the Cu–O bonds are 2.510(5) Å. The neutral clusters are arranged in parallel in the *ab* plane (see Figure 4.2).

There are strong *inter*–molecular hydrogen bonding interactions (see Figure 4.3) between the terminal fluoride ligand of the anion motifs and imidazole coordinated to neighbouring copper cations, thus forming a 2–D layer structure. (N5–H5A…F1 1.84 Å; N5…F1 2.69 Å).

Bond	Bond Length(Å)	S_{ij}	Bond	Bond Length(Å)	S_{ij}
V1–O1	1.621(5)	1.638	Cu1–O2 x 2	2.510(1)	0.106
V1–O2	1.638(5)	1.560	Cu1–N2 x 2	2.004(7)	0.522
V1–F1	1.897(5)	0.587	Cu1–N4 x 2	2.015(7)	0.507
V1–F2	1.856(5)	0.656			
V1–N1	2.172(7)	0.449			
		ΣV1=4.89			ΣCu1=2.27

Table 4.6 Selected bond lengths and BVS for **CuV–1**
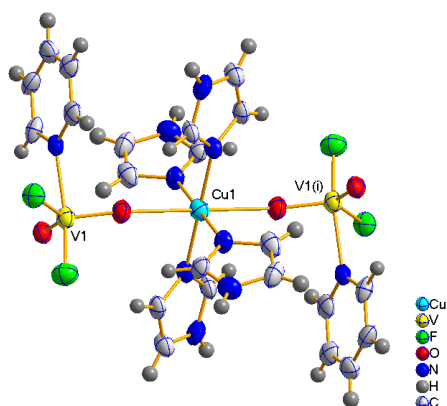
Figure 4.1 The building unit in **CuV–1** with ellipsoids at 50% probability. Symmetry operators (i) 2–x,−y,2−z.
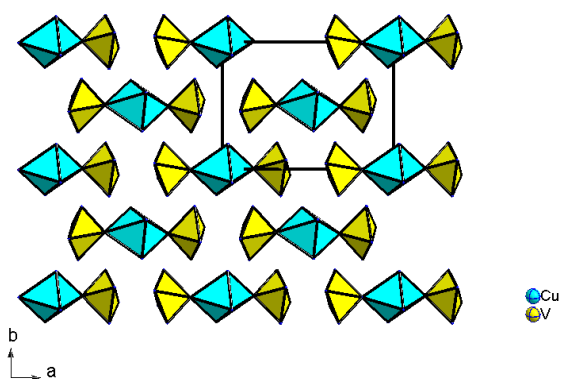
Figure 4.2 Neutral cluster, **CuV–1** packed on the *ab* plane. Carbon and hydrogen atoms have been omitted for clarity.
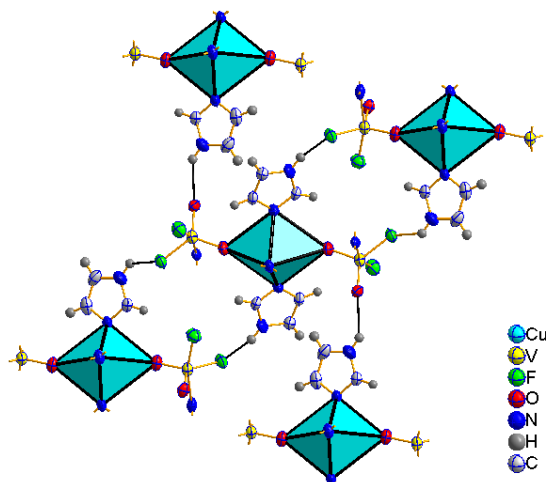
Figure 4.3 *Inter*–molecular hydrogen bonding interactions in **CuV–1**; for clarity coordinated atoms around some of the vanadium and oxygen have been shown with the connections of the bridging ligands.

The Magnetic susceptibility data for **CuV–1** fit very well to a Curie–Weiss law in the range of 2–100 K (see Figure 4.4). The linear plot of low temperature $1/\chi_p$ versus T suggests paramagnetism with a small positive Weiss constant (θ_{esd}=+0.7(1) K). The experimental value 1.739 μB, is consistent with one spin ½ Cu^{2+} per formula unit (ideal value of 1.73 μB).
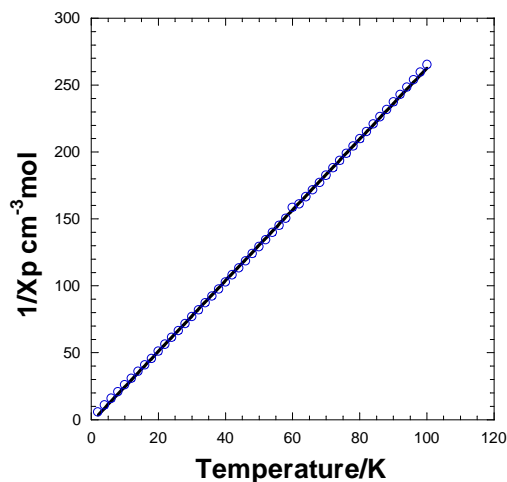
Figure 4.4 χ_p^{-1} vs. T for **CuV–1**.

The crystal structures of **V–1** and **V–2** are iso–structural except for the organic ligand. The building unit of both structures contains moderately distorted $[VOF_2(H_2O)N_2]$ octahedral vanadium present in the +4 oxidation state (see Table 4.7 and 4.8) . The octahedral vanadium displays a *cis* and *trans* effect[6] within the crystal structure; the short terminal vanadyl bond significantly contributes in the lengthening of the *trans* V=O bond, whereas the *cis* F atom is also under the influence of the short vanadyl bond. Therefore both *cis* and *trans* to the short V=O bond are fluoride and aqua ligand respectively, these 'underbonded' atoms are reinforced by strong hydrogen bonds. Neighbouring octahedra are linked 'head–to–tail' through strong *inter*–molecular hydrogen bonding interactions with contacts O1–H1A…F1 1.77 Å; O1…F1 2.60 Å for **V–1** and O1–H1A…F1 1.88 Å; O1…F1 2.64 Å for **V–2**. However, the asymmetric octahedra are packed into H–bonded 'dimeric' chains with centrosymmetric space group C2/c (see Figure 4.5). Polar octahedra are arranged 'head–to–tail' on the *bc* plane, as shown in Figure 4.6, which means that the crystal structure is packed into higher symmetry with an inversion centre.
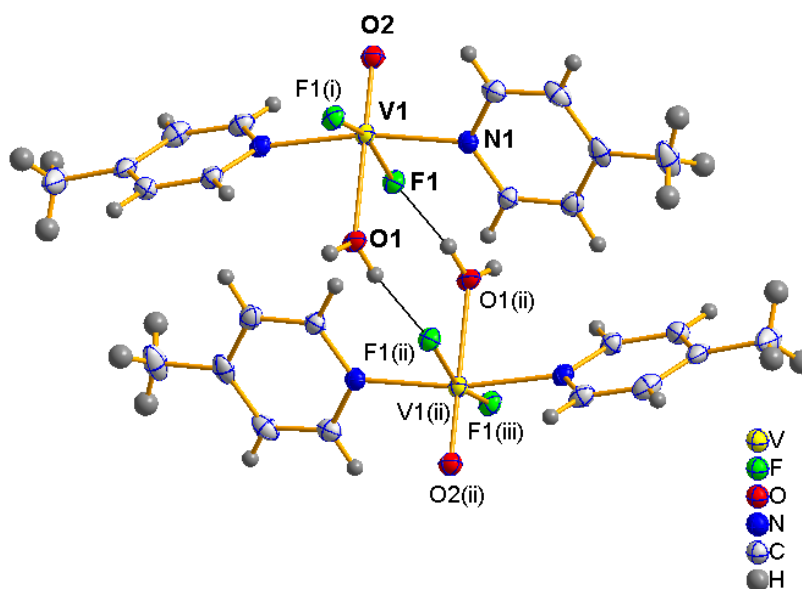
Figure 4.5 *Inter*–molecular hydrogen bonding interaction between the neutral clusters, **V–1** with ellipsoids at 50% probability and symmetry operators (i) 1−x,y,3/2−z, (ii) 1−x,−y,1−z (iii) x,−y,−½+z.

Bond	Bond Length(Å)	S_{ij}
V1–O1	2.215(3)	0.309
V1–O2	1.598(2)	1.640
V1–F1 x 2	1.915(1)	0.574
V1–N1 x 2	2.147(2)	0.480
		$\Sigma V1=4.06$

Table 4.7 Selected bond lengths and BVS for **V–1**

Bond	Bond Length(Å)	S_{ij}
V1–O1	2.187(4)	0.301
V1–O2	1.605(4)	1.477
V1–F1 x 2	1.917(2)	0.559
V1–N1 x 2	2.140(4)	0.413
		$\Sigma V1=3.72$

Table 4.8 Selected bond lengths and BVS for **V–2**.
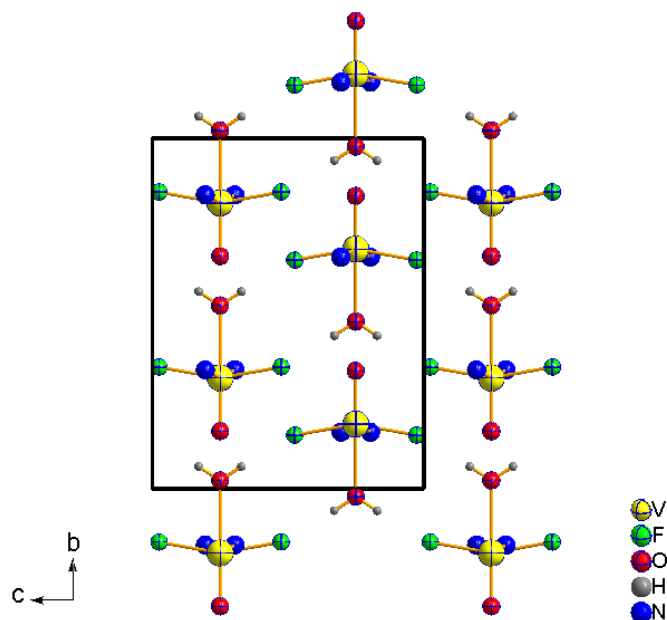
Figure 4.6 V–2 units arranged 'head–to–tail' on the *bc* plane; carbon and hydrogen atoms have been omitted for clarity.

A similar unit has been observed in the neutral monomer compound, $[VOF_2(C_4H_{13}N_3)]$ where vanadium exhibits the +4 oxidation state. The organoamine acts as a tridentate ligand to vanadium and forms hydrogen bonds to other neutral clusters leading to a 3–D network.[7]

The asymmetric unit of the crystal structure of **CuV–2** contains a $[VOF_4(H_2O)]_2^{2-}$ unit and organic cation moiety, $[C_4H_8N_5]_2^{+}$ which are on general positions and copper lying on an inversion centre (see Figure 4.7). The vanadium is present in the +4 oxidation state (see Table 4.9) and adopts a moderately distorted octahedral environment, consistent with the presence of a very short V=O bond, an aqua ligand *trans* to this vanadyl bond and also *cis* fluoride ligands which are supported by hydrogen bond interactions from neighbouring organic cations and copper cation complexes.

A similar polar vanadium monomer, $[VOF_4(H_2O)]_2^{2-}$ has been previously reported (see Section 1.1.1).[8] The copper cation complex and vanadium anion are stacked in alternating sheets along the *c* axis, and between the sheets organic cation moieties occupy the interstices. The asymmetric octahedra are arranged in a 'head–to–tail' manner within the sheet parallel to the *c* axis (see Figure 4.8). Crystal packing is dominated by hydrogen bonding interactions from the protonated pyrimidine, ammonia and aqua ligands coordinated to the copper cation to the anion of neighbouring anion motifs. Strong hydrogen bonding interactions in the range of D–H…A 1.81–1.99 Å; D…A 2.64–2.66 Å and the weaker interactions are in the range of D–H…A 2.06–2.53 Å; D…A 2.69–3.33 Å).
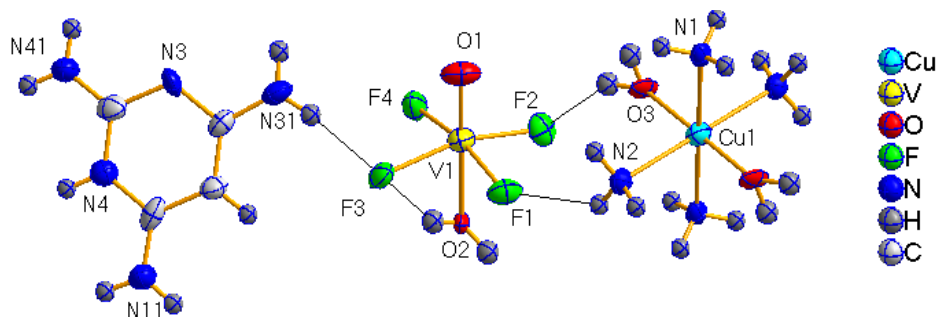
Figure 4.7 The building unit in **CuV–2**; with hydrogen bonding interactions and ellipsoids at 50% probability.

Bond	Bond Length(Å)	S_{ij}	Bond	Bond Length(Å)	S_{ij}
V1–O1	1.605(6)	1.426	Cu1–O3 x 2	1.913(5)	0.524
V1–O2	2.109(6)	0.406	Cu1–N1 x 2	2.213(6)	0.296
V1–F1	1.924(5)	0.550	Cu1–N2 x 2	2.135(6)	0.360
V1–F2	1.930(5)	0.540			
V1–F3	1.937(4)	0.521			
V1–F4	1.955(5)	0.502			
		ΣV1=3.95			ΣCu1=2.36

Table 4.9 Selected bond lengths and BVS for **CuV–2**.
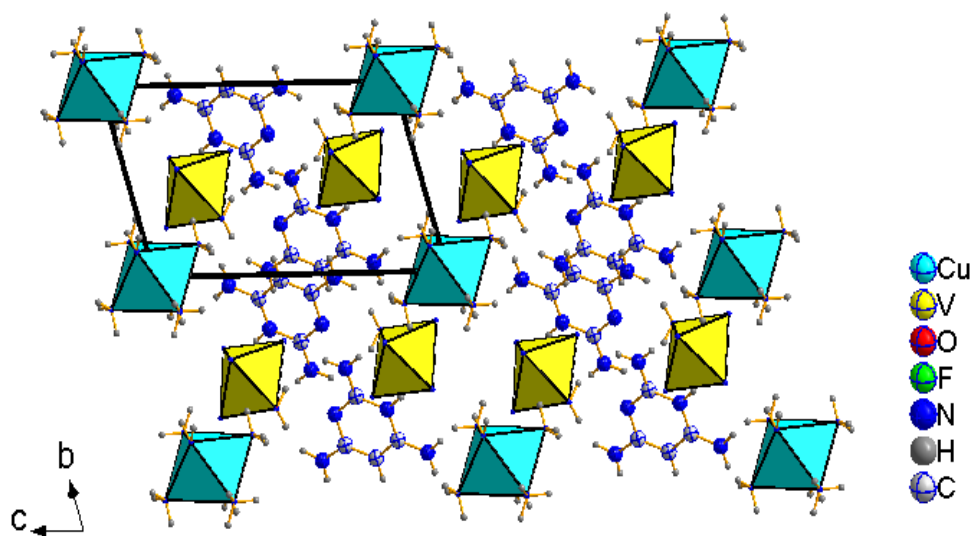
Figure 4.8 The crystal packing in **CuV–2**; showing alternating copper complex and vanadium anion layers.

4.3 Clusters Containing Vanadium Dimers

$[V_2O_4F_2(C_{10}H_8N_2)_2]$ (**V–3**), $[V_2O_4F_2(C_{12}H_8N_2)_2]$ (**V–4**), $[V_2O_2F_4(C_6H_7N)_4]$ (**V–5**), $[C_7H_{10}N]_2[V_2O_2F_6(H_2O)_2]$ (**V–6**) and $[C_8H_{12}N]_2[V_2O_2F_6(H_2O)_2]$ (**V–7**) contain edge–sharing vanadium dimers in the building unit.

4.3.1 Discussion

Structure

The crystal structures of **V–3** and **V–4** are closely related. Vanadium is present in the +5 oxidation state and, although the core of the dimer is the same, the complexes crystallise into different space groups (see Figure 4.9 and Figure 4.10). $[V_2O_4F_2(C_{10}H_8N_2)_2]$ has previously been reported[9], but that polymorph crystallised into space group $P2_1/c$ with cell dimensions: a=6.43(1) Å, b=15.80(2) Å, c=13.94(2) Å and β=134.8(3)° with cell volume 1004 Å^3. Details of the synthetic route were not included. In any case, a different synthesis technique or the same technique with different reaction conditions has produced a different polymorph (see section 1.2.1). The crystal structures contain distorted octahedral units due to the short V=O bond, fused together *via* a common edge, such that the vanadyl bonds remain *exo* to the dimer and in an equatorial configuration. The oxide ligand *trans* to this short V=O bond shares the edge of the symmetry equivalent vanadium, with the complex situated on an inversion centre.
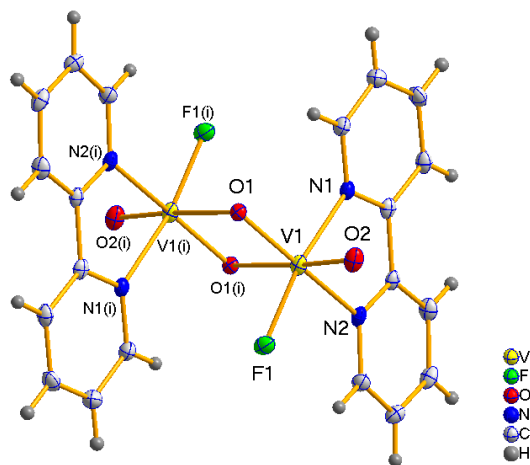
Figure 4.9 The building unit in **V–3**; with ellipsoids at 50% probability and symmetry operator (i) 1–x,−y,1−z.

The bulky bidentate ligands bond to vanadium with two different V–N bond distances, due to the presence of oxygen and fluorine atoms in the *trans* positions. The phenyl rings of the bidentate ligands are almost co-planar. As anticipated from the BVS analysis (see

Tables 4.10 and 4.11), the nucleophilic oxide ligand *trans* to the V=O bond is supported by bridging the vanadium octahedra. The dimeric clusters are well separated and the bulky ligands occupy the region between the clusters in the overall crystal packing, as shown in Figure 4.11 and Figure 4.12. The distance between vanadium centres is comparable to that in the vanadium dimer, $[V_2O_4F_2(C_{10}H_8N_2)_2]$. The separation V…V is 3.175(4) Å in $[V_2O_4F_2(C_{10}H_8N_2)_2]$; 3.118(1) Å in **V–3** and 3.213(2) Å in **V–4**. Neither structure contains any H–bond donors to mediate hydrogen bond interactions.

Bond	Bond Length(Å)	S_{ij}
V1–O1	1.706(1)	1.297
V1–O2	1.614(2)	1.665
V1–O1'	2.288(1)	0.270
V1–F1	1.804(1)	0.755
V1–N1	2.163(2)	0.458
V1–N2	2.199(2)	0.418
		$\Sigma V1=4.86$

Table 4.10 Selected bond lengths and BVS for **V–3**

| Bond	Bond Length(Å)	S_{ij}
V1–O1	1.612(4)	1.659
V1–O2	1.726(4)	1.219
V1–O2'	2.330(4)	0.238
V1–F1	1.783(3)	0.799
V1–N1	2.185(5)	0.432
V1–N2	2.207(4)	0.408
		$\Sigma V1=4.76$

Table 4.11 Selected bond lengths and BVS for **V–4**.
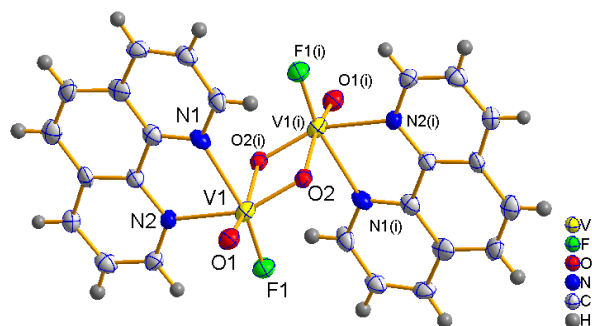
**Figure 4.10** The building unit in **V–4**; ellipsoids at 50% probability and symmetry operator (i) 1–x,1−y,1−z.
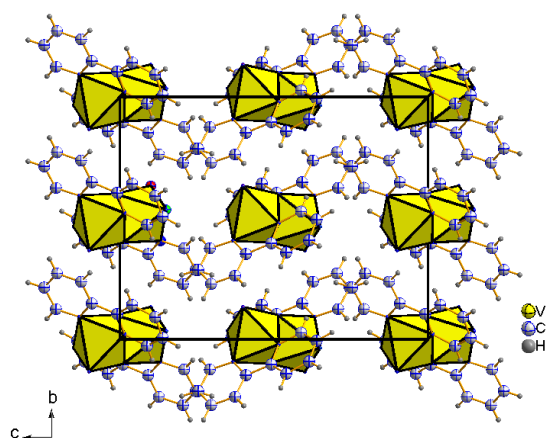
Figure 4.11 Packing in **V–3**
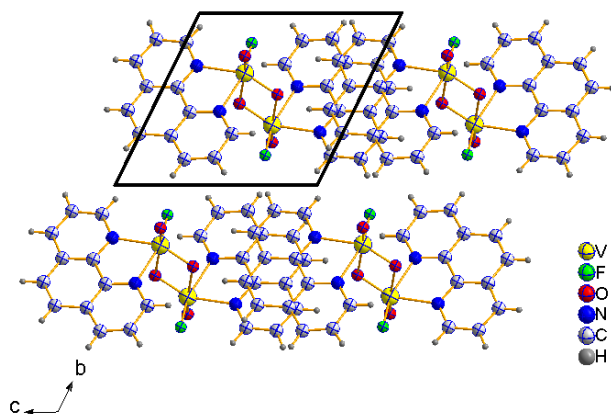
Figure 4.12 *Inter*–dimer region occupied by aromatic rings in **V–4**.

Heated under Ar, **V–3** undergoes a weight loss between 170˚C and 450˚C with series of steps, as shown in Figure 4.13. This is thought to be due to the loss of organic template from the material; 60.5% loss corresponding to the removal of 2,2'–bipyridyl (calculated composition is 60.44%). The final product at 500˚C is largely amorphous.
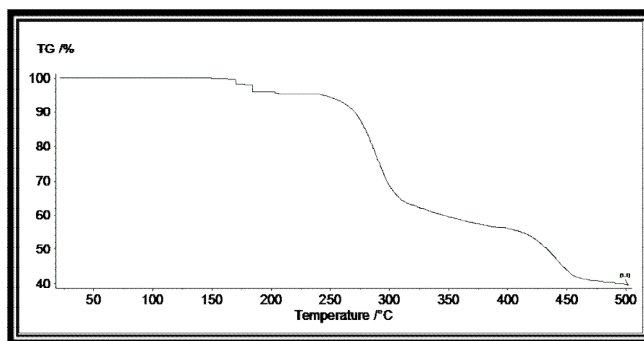
Figure 4.13 TGA of **V–3**

The crystal structure of **V–5** contains a dimeric building unit situated on an inversion centre with vanadium present in the +4 oxidation state, as confirmed by BVS analysis (see Table 4.12). In contrast to the above structures, this distorted octahedral unit is fused together *via* a common fluoride edge in the equatorial position. The short V=O bond and the terminal fluoride ligands are *exo* to the dimeric unit. The two axial sites of the octahedron are occupied by 3–picoline, as shown in Figure 4.14. When such nitrogen compounds are directly coordinated to vanadium centres as a ligand, then there is no possibility of finding hydrogen bonding interactions in the absence of other H–bond donors. The nucleophilic fluoride ligand *trans* to the short V=O bond, links to a symmetry equivalent vanadium octahedron.

The bonding geometry within the dimer is comparable to a previously reported dimer unit.[9] The building units are arranged in a *zig–zag* manner on the *bc* plane, as shown in Figure 4.15.

Bond	Bond Length(Å)	S_{ij}
V1–O1	1.685(2)	1.307
V1–F1	2.090(2)	0.411
V1–F1'	2.028(2)	0.349
V1–F2	1.776(2)	0.813
V1–N1	2.151(3)	0.477
V1–N2	2.124(3)	0.510
		$\Sigma V1=3.87$

Table 4.12 Selected bond lengths and BVS for **V–5**.
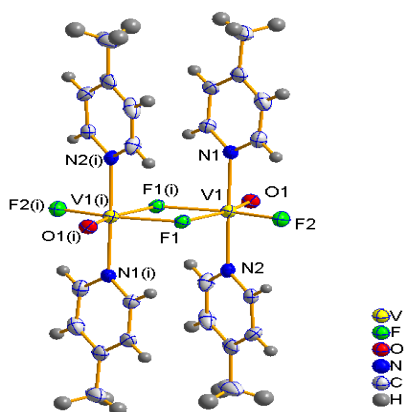
Figure 4.14 The building unit in **V–5** with ellipsoids at 50% probability and symmetry operator (i) 2–x,−y,1−z.
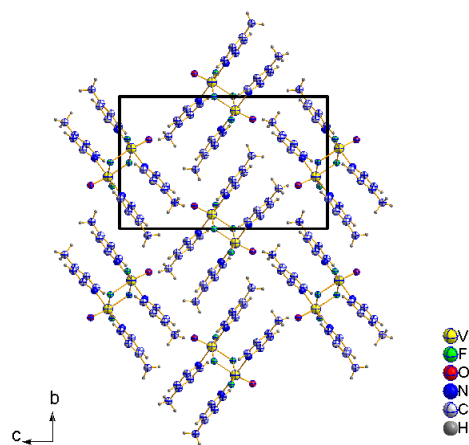
Figure 4.15 Crystal packing in **V–5**.

The crystal structures of **V–6** and **V–7** exhibit a similar arrangement of common edge–sharing dimeric units with different organic templates. In both structures, the asymmetric unit consists of a $[V_2O_2(H_2O)_2F_6]^{2-}$ dimeric unit on an inversion centre, thus containing only one distinct vanadium site, together with an organic cation (see Figure 4.16 and Figure 4.17). Vanadium adopts the +4 oxidation state (see Table 4.13 and 4.14) in a distorted octahedral environment consistent with the presence of the short terminal vanadyl bond. The anions and cations are arranged alternately parallel to the *b* axis. The bond distances and bond angles of the anionic dimer are comparable to similar vanadium dimers in previously reported structures.[10]

The crystal packing is dominated by strong hydrogen bonding interactions from the organic cation moieties to fluoride ligands of the anion moieties. The network of hydrogen bonds holds the structures together; the strong hydrogen bonding interactions in **V–6** are in the range of D–H…A 1.99-2.00 Å; D…A 2.60-2.78 Å and the weaker interactions are in the range of N1–H1A…F3 2.32 Å; N1…F3 2.87 Å; in **V–7,** O1–H1B…F3 2.26 Å; O1…F3 2.75 Å, N1–H1…F3 1.81 Å; N1…F3 2.65 Å. The organic moieties fill the *inter*–dimer regions, as shown in Figure 4.18.
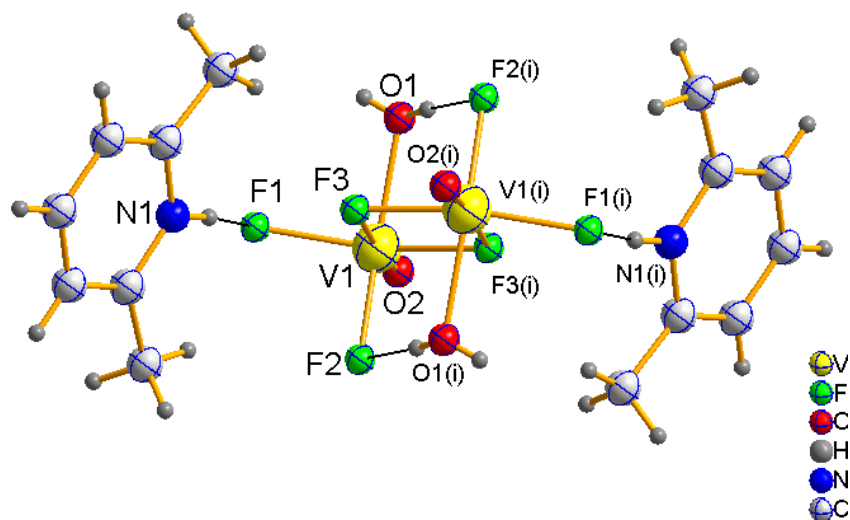
Figure 4.16 The building unit in **V–6** with hydrogen bonding interactions. Ellipsoids at 50% probability and symmetry operator (i) 2−x,−y,−z.

Bond	Bond Length(Å)	S_{ij}
V1–O1	2.066(4)	0.414
V1–O2	1.601(5)	1.472
V1–F1	1.933(7)	0.531
V1–F2	1.909(4)	0.570
V1–F3	1.932(6)	0.533
V1–F3'	2.182(6)	0.273
		$\Sigma V1=3.79$

Table 4.13 Selected bond lengths and BVS for **V–6**.

Bond	Bond Length(Å)	S_{ij}
V1–O1	2.051(3)	0.485
V1–O2	1.600(4)	1.631
V1–F1	1.959(3)	0.497
V1–F1'	2.154(3)	0.294
V1–F2	1.907(3)	0.573
V1–F3	1.954(3)	0.505
		$\Sigma V1=3.99$

Table 4.14 Selected bond lengths and BVS for **V–7**.
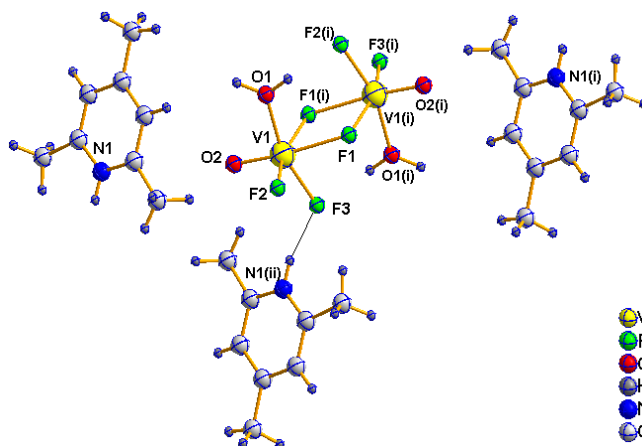
Figure 4.17 The building unit in **V–7** with hydrogen bonding interactions. Ellipsoids at 50% probability and symmetry operators (i) 1−x,−y,−z; (ii) –x,−y,1−z.
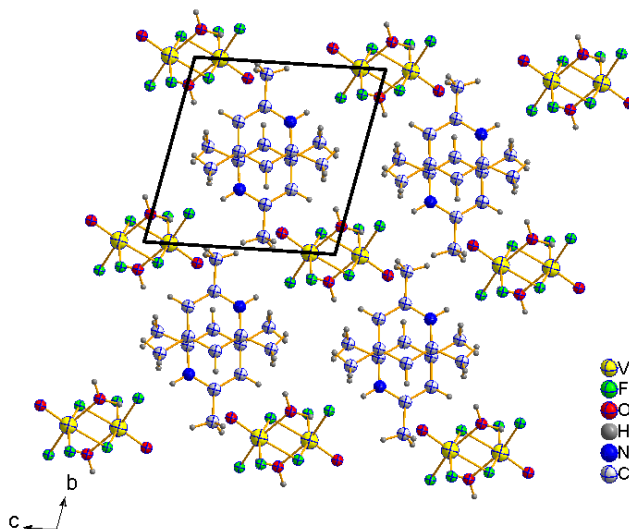
Figure 4.18 Crystal packing in **V–7**.

4.4 Chains

Hydrothermal synthesis of vanadium oxyfluorides with copper coordination complexes produces the novel structures of **α–[C$_2$H$_8$N][Cu(C$_5$H$_5$N)$_4$][V$_2$O$_2$F$_7$]** (**CuV–3**), β–[C$_2$H$_8$N][Cu(C$_5$H$_5$N)$_4$][V$_2$O$_2$F$_7$] (**CuV–4**), [Cu(C$_6$H$_7$N)$_4$][VF$_6$] (**CuV–5**), [Cu(C$_6$H$_7$N)$_4$][VF$_6$].9H$_2$O (**CuV–6**), [C$_3$H$_5$N$_2$]$_2$[Cu(C$_3$H$_4$N$_2$)$_4$][V$_2$O$_2$F$_8$] (**CuV–7**), [Cu(C$_5$H$_5$N)$_2$(C$_2$H$_8$N$_2$)][(VO$_3$)$_2$] (**CuV–8**), [Cu$_2$F$_2$(C$_{10}$H$_{10}$N$_3$)$_2$][V$_2$O$_7$] (**CuV–9)** and [Cu(C$_{10}$H$_9$N$_3$)]$_2$[VOF$_4$]$_2$ (**CuV–10**); these are discussed in the following section.

Rietveld refinements of X–ray powder data were performed (see Section 2.1) using the unit cell dimensions and atomic co–ordinates determined by the single crystal solution as a starting point. A close final fit to the observed data was achieved, with Rwp=8.54% for **CuV–3**; 4.52% for **CuV–5**; 3.48% for **CuV–9**; 5.29% for **CuV–10** with the structure determined from the single crystal experiment (see Figures 4.19, 4.20, 4.21 and 4.22).
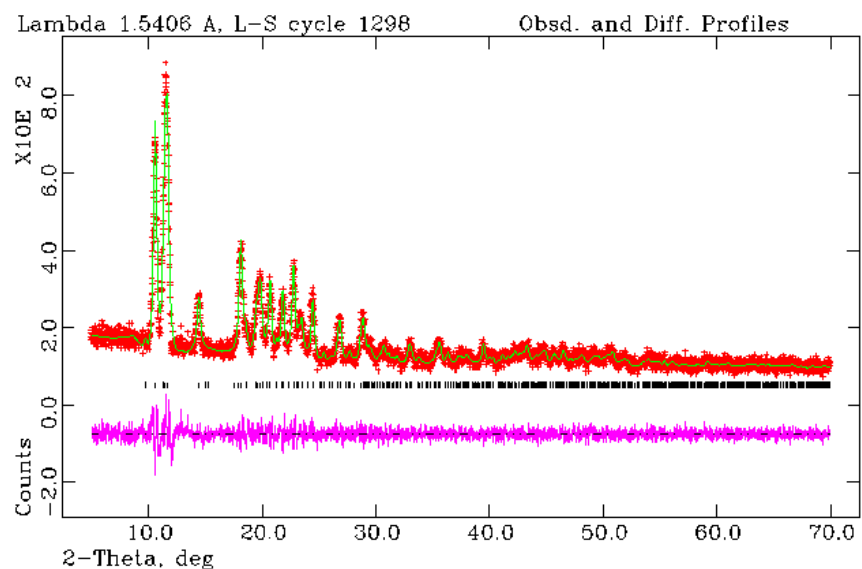
Figure 4.19 The Rietveld refinement of **CuV–3**. Observed data red, calculated profile green, difference profile purple.
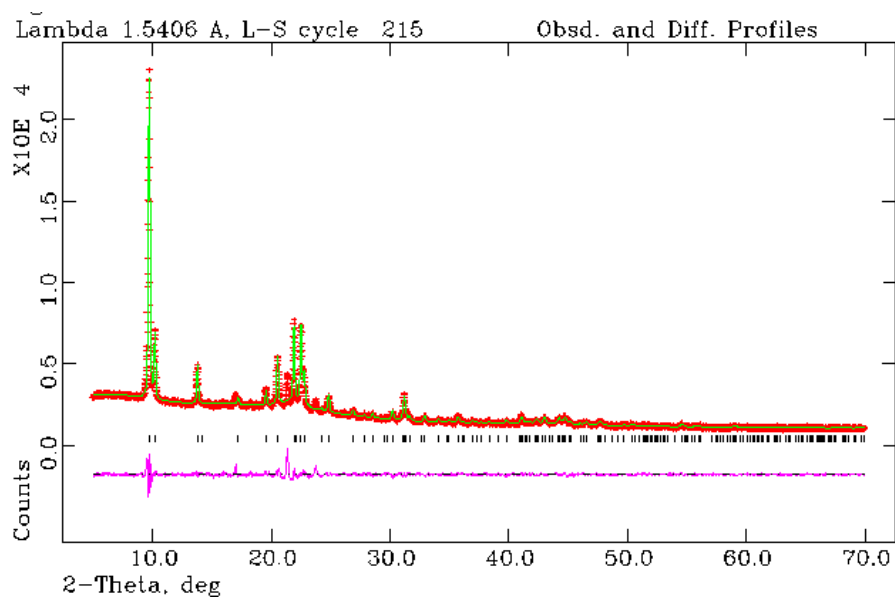
Figure 4.20 The Rietveld refinement of **CuV–5**. Observed data red, calculated profile green, difference profile purple.
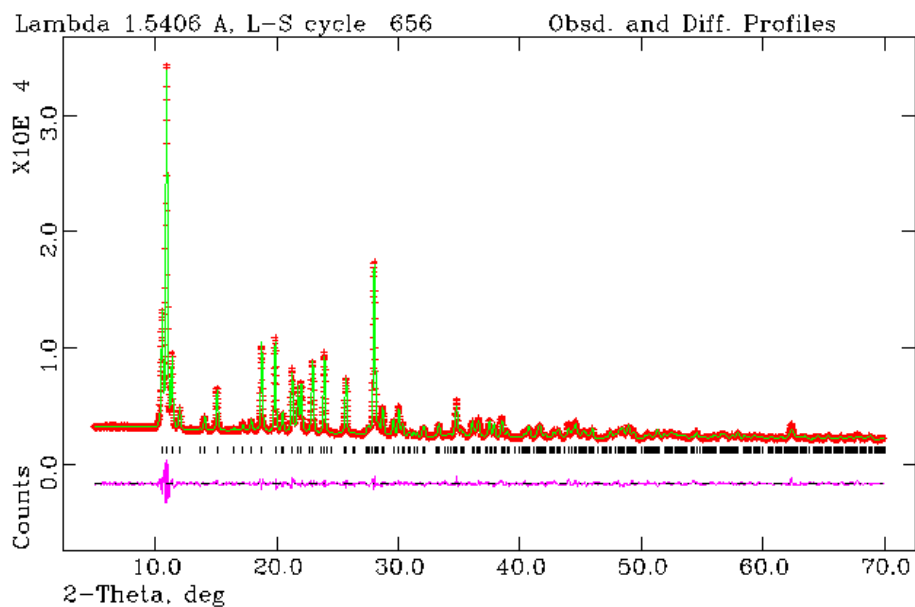
Figure 4.21 The Rietveld refinement of **CuV–9**. Observed data red, calculated profile green, difference profile purple.
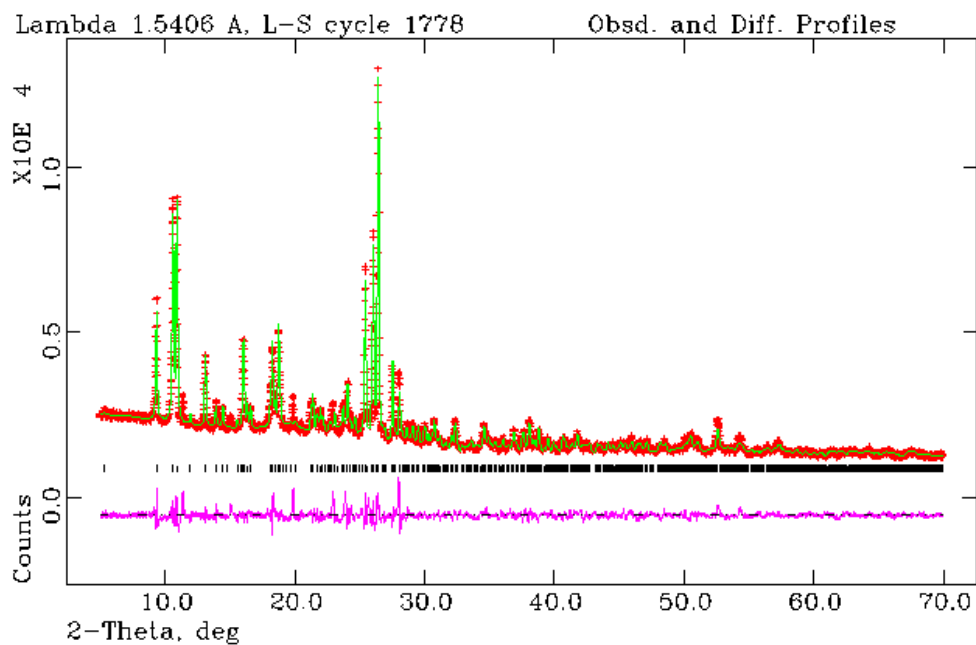
Figure 4.22 The Rietveld refinement of **CuV–10**. Observed data red, calculated profile green, difference profile purple.

4.4.1 Discussion

Structure

The crystal structure of **CuV–3** exhibits an infinite 1–D chain parallel to the *c* axis. The asymmetric unit of the structure consists of a face–sharing octahedral dimer, $[V_2O_2F_7]^{3-}$ on an inversion centre together with the copper complex and protonated dimethylamine cation, as shown in Figure 4.23. The $[V_2O_2F_7]^{3-}$ anion motif has already been reported in $Cs_3V_2O_2F_7$ by Pausewang[11] and structurally characterised by Waltersson.[12] The anion in that case exhibits crystallographic disorder of the terminal O/F positions. Vanadium is present in +4 oxidation state and exhibits a characteristically short V=O and lengthened *trans* V–F bond without any O/F disorder (see Table 4.15).

The Cu^{2+} centre exhibits a characteristic Jahn–Teller environment with "4+2" coordination environment (see Table 4.15). The four pyridine rings occupy the equatorial sites of a Cu^{2+} square planar arrangement, while the axial sites are occupied by fluoride ligands coordinated to vanadium. A 1–D chain is constructed from the *trans* directing copper complex $[Cu(C_5H_5N)_4]^{2+}$ and face–sharing dimeric anion unit in an alternating manner.
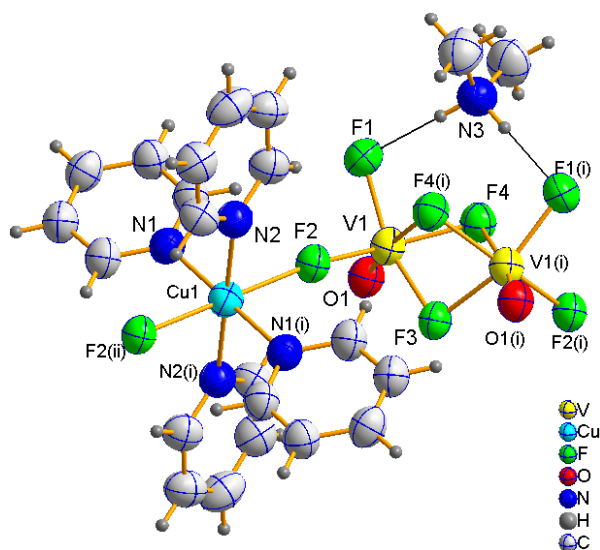
Figure 4.23 The building unit in **CuV–3** with ellipsoids at 50% probability and symmetry operators (i) 2−x,y,−3/2−z; (ii) 2−x,−y,−1−z.

The protonated dimethylamine cations are accommodated in the *inter*–chain region, forming hydrogen bonds with the nearest terminal fluoride ligands which are either *cis* or *trans* to the short V=O bond of the anion motif. In this case *trans* nucleophilic fluoride ligands are exclusively engaged in face–sharing within the octahedral dimers. Strong *intra*–chain hydrogen bonding interactions occur between *cis* fluorine atoms and dimethylamine cations with the contacts of N3–H3A/B…F1 1.90 Å; N3…F1 2.79 Å.

The compound **CuV–4** is a polymorph of **CuV–3** and is produced under similar reaction conditions with a different amine source. This may lead to a different pH of the reaction medium and yields a different crystal packing. The crystal structure of **CuV–4** may contain some disordered solvent or guest moieties according to the X–ray refinement, which is supported by the observation that **CuV–4** is less stable in air than **CuV–3**. Both structures contain similar building units, though the calculated density is lower for **CuV–4** than **CuV–3**; the unit cell packing further emphasises that the **CuV–4** exhibits a more 'open' structure. The asymmetric unit of **CuV–4** contains two crystallographically different vanadium and copper, present in +4 and +2 oxidation states, as shown in Table 4.16.
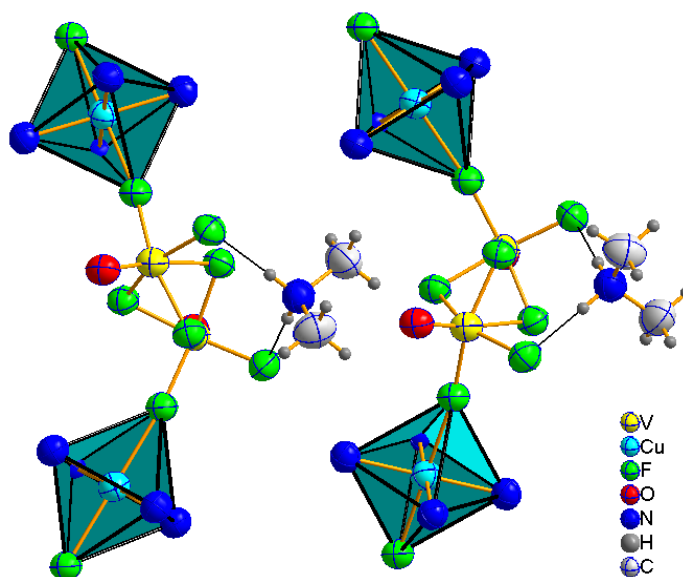
Figure 4.24 Hydrogen bonding interactions in **CuV–3** with ellipsoids at 50% probability.
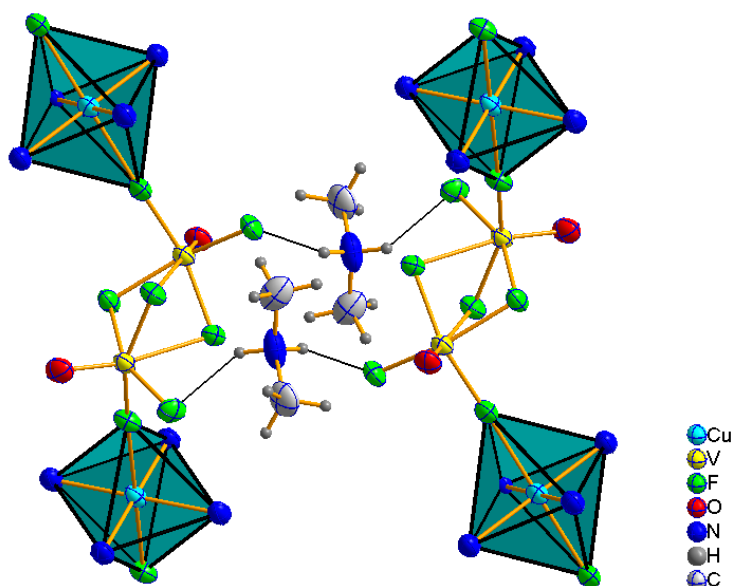
Figure 4.25 Hydrogen bonding interactions in **CuV–4** with ellipsoids at 50% probability.

Dimethylamine is the structure directing agent of both structures and plays the major role to determine the overall crystal packing through hydrogen bonding interactions. In **CuV–3**, the dimethylammonium cation is positioned on a 2–fold axis and forms two symmetrically equivalent H-bonds to one particular $[V_2O_2F_7]^{3-}$ anion of a single chain; there are no H–bonded *inter*–chain interactions, as shown in Figure 4.24. In **CuV–4**, on the other hand, the dimethylammonium cation forms hydrogen bonds (N5–H5B…F1 2.07 Å; N5…F1 2.84 Å, N5–H5A…F6 1.91 Å; N5…F6 2.74 Å) with two separate $[V_2O_2F_7]^{3-}$ anions of different chains (see Figure 4.25).

This difference makes a significant contribution both to the individual chain configurations and to the orientation of chains relative to each other. The relative chain configurations may be understood by comparing the Cu–V–V–Cu torsion angles, *viz.* 128.2˚ for **CuV–3** and 143.6˚ for **CuV–4**. The orientation of the chains may be understood by comparing key *inter*–chain distances; in the **CuV–3** the closest *inter*–chain V---V distances are about 7.2 Å, whereas in the **CuV–4** these alternate between 7.4 and 12.0 Å (see Figures 4.26 and Figure 4.27).

Bond	Bond Length(Å)	S_{ij}	Bond	Bond Length(Å)	S_{ij}
V1–O1	1.602(4)	1.635	Cu1–F2 x 2	2.257(3)	0.167
V1–F1	1.893(3)	0.594	Cu1–N1 x 2	2.063(5)	0.429
V1–F2	1.904(3)	0.576	Cu1–N2 x 2	2.045(5)	0.451
V1–F3	1.997(3)	0.448			
V1–F4	1.945(3)	0.516			
V1–F4(i)	2.277(3)	0.210			
		ΣV1=3.98			ΣCu1=2.09

Table 4.15 Selected bond lengths and BVS for **CuV–3.**

Bond	Bond Length(Å)	S_{ij}	Bond	Bond Length(Å)	S_{ij}
Cu1–F2 x 2	2.297(5)	0.150	Cu2–F7 x 2	2.325(5)	0.139
Cu1–N1 x 2	2.054(7)	0.441	Cu2–N3 x 2	2.033(9)	0.467
Cu1–N2 x 2	2.054(7)	0.441	Cu2–N4 x 2	2.047(8)	0.449
		ΣCu1=1.86			ΣCu2=2.11

Bond	Bond Length(Å)	S_{ij}	Bond	Bond Length(Å)	S_{ij}
V1–O1	1.598(7)	1.653	V2–O2	1.599(7)	1.649
V1–F1	1.895(5)	0.590	V2–F3	2.026(5)	0.414
V1–F2	1.915(5)	0.559	V2–F4	2.288(6)	0.204
V1–F3	2.008(5)	0.435	V2–F5	1.947(5)	0.513
V1–F4	1.952(5)	0.506	V2–F6	1.909(5)	0.568
V1–F5	2.317(5)	0.189	V2–F7	1.923(6)	0.547
		ΣV1= 3.93			ΣV2=3.90

Table 4.16 Selected bond lengths and BVS for **CuV–4**.

Above 50 K, the magnetic susceptibility for **CuV–3** obeys a Curie–Weiss law, with no evidence of long range magnetic ordering. A fit to the $1/\chi_p$ versus T plot reveals a negative Weiss constant ($\theta_{esd}=-5.0$ K) and the fall–off χ_pT versus T reveals short–range antiferromagnetic correlations between the metal centres. The experimental value of $\mu_{eff}=2.72$ μB, obtained from the Curie–Weiss plot is consistent with the ideal system of three non-interacting isolated spin ½ centres per formula unit (2 V^{4+}, Cu^{2+} per formula

unit), also confirming the BVS analysis of V^{4+} and Cu^{2+}. Within the temperature range 50–300 K, the saturation value of $\chi_P T$ is 0.92 $cm^3 mol^{-1}K$ which is close to the ideal value of 1.12 $cm^3 mol^{-1}K$ and this is consistent with the study of Darriet et al. on $Cs_3V_2O_2F_7$; above 25 K, the agreement between theoretical and experimental data appeared to be poor due to the effect of lattice specific heat.[13] Below 50 K deviations from the Curie-Weiss behavior may be expected due to the alternating V–V and V–Cu interactions along the chain (V---V separation within the face–sharing dimer, is 2.97 Å, whereas the V---Cu distance is 4.15 Å.
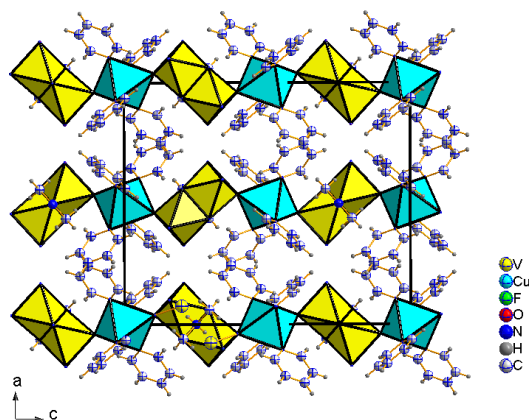
Figure 4.26 Crystal packing in **CuV–3**
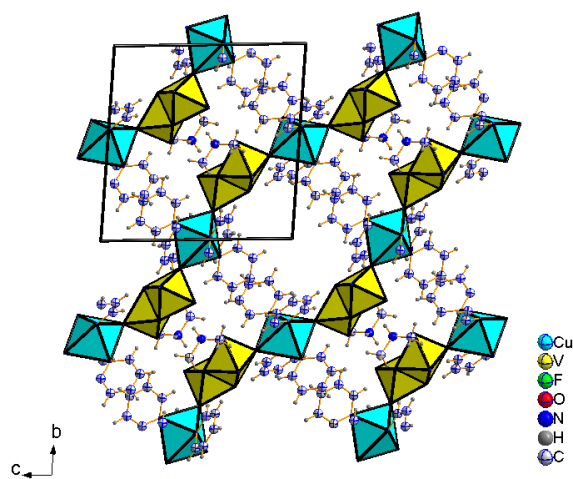
Figure 4.27 Crystal packing in **CuV–4**
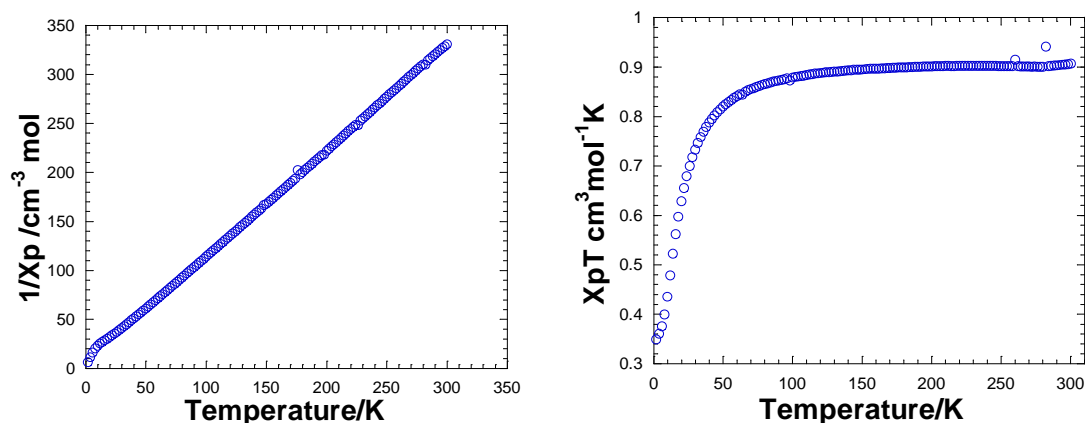
Figure 4.28 χ_p^{-1} vs. T (left) and χ_pT vs. T (right) for **CuV–3.**

The crystal structures of **CuV–5** and **CuV–6** are iso-structural and crystallise in the tetragonal space group P4/mcc. The building unit contains one unique monomeric $[VF_6]^{2-}$ anion and one $[Cu(C_6H_7N)_4]^{2+}$ cationic unit on a four–fold axis, as shown in Figure 4.29. Both cation and anion are bound in an alternating manner by Cu–F–V linkages to form 1–D linear chains running parallel to the *c* axis (see Figure 4.31). In both crystal structures, vanadium and copper are present in the +4, +2 oxidation states respectively, as confirmed by BVS analysis (see Tables 4.14 and Table 4.15). Although it is uncommon in comparison to the $[VOF_5]^{3-}$ and $[VF_6]^{3-}$ units, $[VF_6]^{2-}$ has been observed previously[14]. The high symmetry of the crystal structure necessitates some disorder in the model, firstly due to the mirror plane running through the 3–methylpyridine/4–methlypyridine ligand, which occupies the equatorial coordination sites on copper and, secondly, due to the degree of freedom allowed at the equatorial F sites of the $[VF_6]$ octahedral unit, whereby the F atoms have been positioned as four–fold disordered: there is no additional coordination to impose a preferred in–plane orientation. There is no hydrogen bonding or other *inter*–chain interaction in this structure. However, it seems that there are some water molecules in the *inter*–chain region of **CuV–6**, evidenced by X–ray diffraction and it is difficult to find suitable hydrogen atoms around the oxygen atoms due to the high thermal vibration. The low temperature single crystal X–ray data also did not solve the problem.
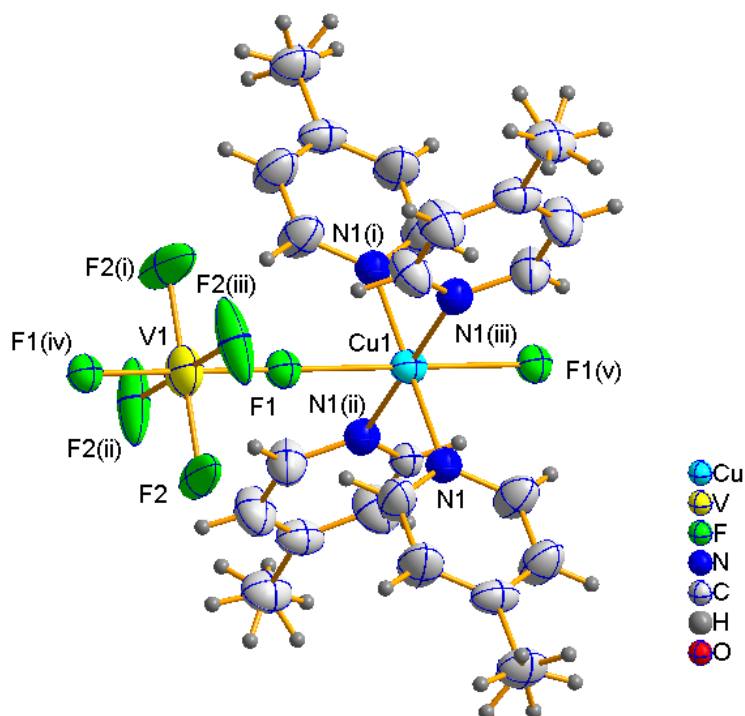
Figure 4.29 The building unit in **CuV–6**   with ellipsoids at 50% probability and symmetry operators (i) −x,−y,z; (ii) x,−y,z; (iii) −x,y,z; (iv) x,−y,½−z; (v) −x,−y,1−z.

Bond	Bond Length(Å)	S_{ij}	Bond	Bond Length(Å)	S_{ij}
V1–F1 x 2	1.907(6)	0.564	Cu1–F1 x 2	2.432(1)	0.104
V1–F2 x 4	1.826(22)	0.704	Cu1–N1 x 4	2.033(5)	0.421
		ΣV1=3.94			**ΣCu1=1.99**

Table 4.17 Selected bond lengths and BVS for **CuV–5**

Bond	Bond Length(Å)	S_{ij}	Bond	Bond Length(Å)	S_{ij}
V1–F1 x 2	1.900(6)	0.582	Cu1–F1 x 2	2.409(6)	0.111
V1–F2 x 4	1.843(10)	0.679	Cu1–N1 x 4	2.033(4)	0.421
		ΣV1=3.88			**ΣCu1=2.08**

Table 4.18 Selected bond lengths and BVS for **CuV–6**

When checking the crystallinity of the material under an optical microscope, it appeared to be cubic and further SEM images also confirmed pseudo–cubic crystals (see Figure 4.30). The single crystal X–ray diffraction shows the cell dimension is tetragonal with c approximately close to 2a, which gives the morphology of the compound as cubic.
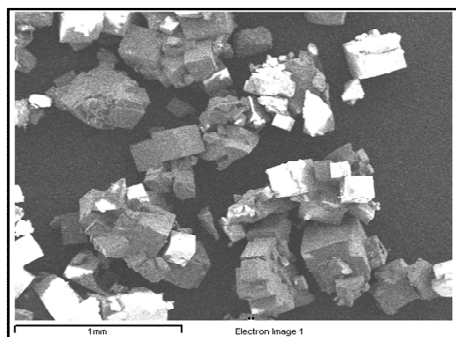
Figure 4.30 SEM image of **CuV–5**
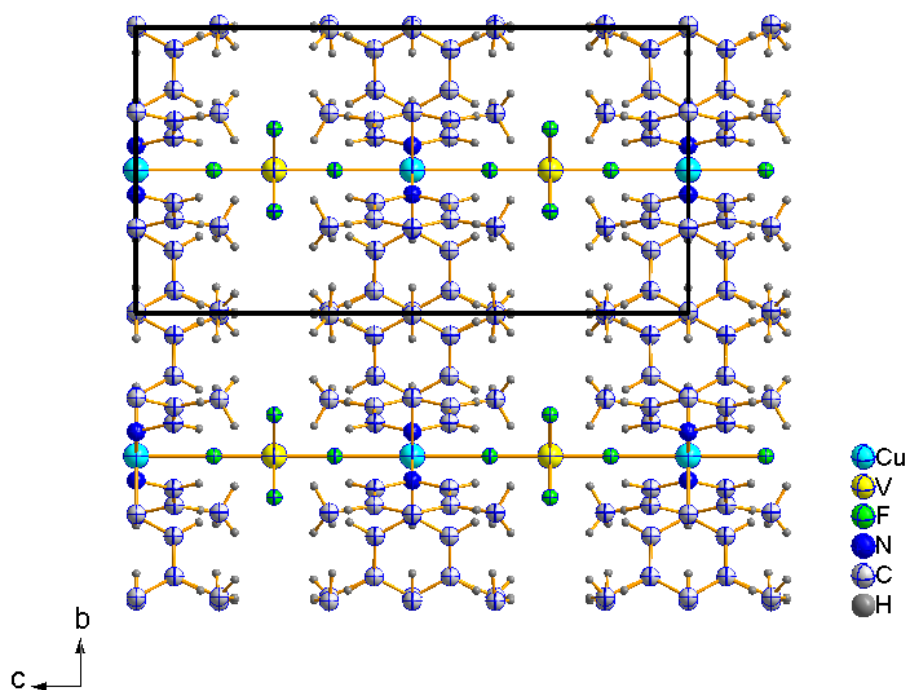
Figure 4.31 1–D linear chains running parallel to the *c* axis in **CuV–5**

Heated under Ar, **CuV–5** undergoes a weight loss continuously between 120˚C and 450˚C. The calculated weight loss of 63% from Figure 4.32, corresponds to the removal of 3–methylpyridine (calculated composition is 62.71%). The final product at 500˚C is largely amorphous.
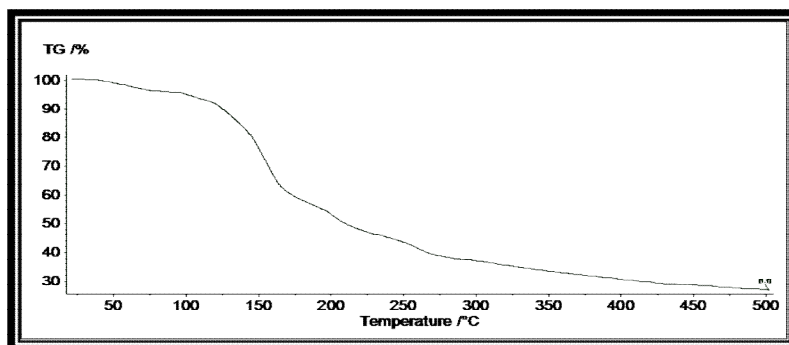
Figure 4.32 TGA of **CuV–5**.

The magnetic susceptibility data for **CuV–5** fit very well to the Curie–Weiss law in the range of 50–300 K (see Figure 4.33). The linear plot of $1/\chi_p$ versus T reveals paramagnetism, with the small positive Weiss constant (θ_{esd}=+1.66 K) suggesting a tendency towards weak ferromagnetic interactions. The μ_{eff} experimental value 2.16 µB represents two non–interacting isolated spin ½ centres of Cu^{2+} and V^{4+}, which is slightly lower than the theoretical value, μ_{eff}=2.44 µB.
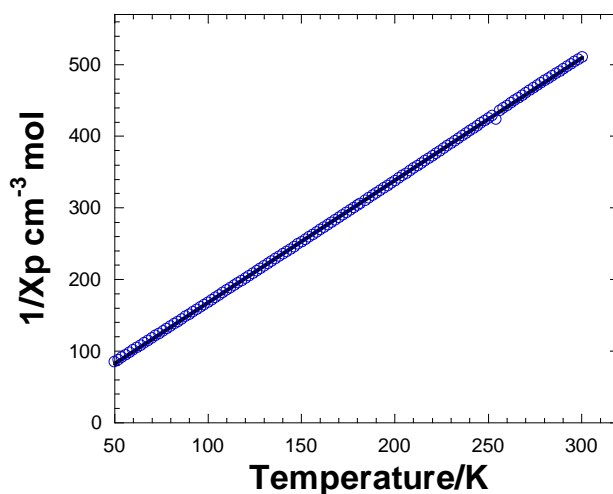
Figure 4.33 χ_p^{-1} vs. T above 50 K for **CuV–5**.

The crystal structure of **CuV–7** exhibits an infinite 1–D chain propagating along the *a* axis, as shown in Figure 4.36. The building unit consists of a dimeric unit $[V_2O_2F_8]^{4-}$ situated on an inversion centre, together with a copper cation lying on a two–fold axis. The imidazole acts as both a protonated template and a neutral ligand to Cu^{2+} in this case. The Jahn–Teller Cu^{2+} binds to four imidazole molecules in the equatorial sites in a square planar arrangement with the long axial sites bound to oxide ligands coordinated to octahedral vanadium (see Figure 4.34). Vanadium adopts the +4 oxidation state (see Table 4.19), and occurs in an edge–sharing dimeric unit $[V_2O_2F_8]^{4-}$, which has previously been seen in both organically templated VOFs[5] and in the inorganic compound[15] $Na_4V_2O_2F_8$. The crystal packing is stabilized by hydrogen bond interactions (see Figure 4.35) between the imidazolium cations and the F atoms of the chain, and also *via* direct H–bonds from the $[Cu(C_3H_4N_2)_4]^{2+}$ moiety to neighbouring chains leading to a 3–D supramolecular network. The protonated imidazole moieties form relatively strong hydrogen bonds with contacts in the range N–H… F: 1.73–1.85 Å and N…F 2.57–2.69 Å. The direct *inter*–chain interactions from the $[Cu(C_3H_4N_2)_4]^{2+}$ cation are somewhat weaker: N–H…F and N...F distances in the range of 2.05–2.19 Å and 2.76–2.82 Å. The overall result is that all the F atoms are involved as H–bond acceptors.
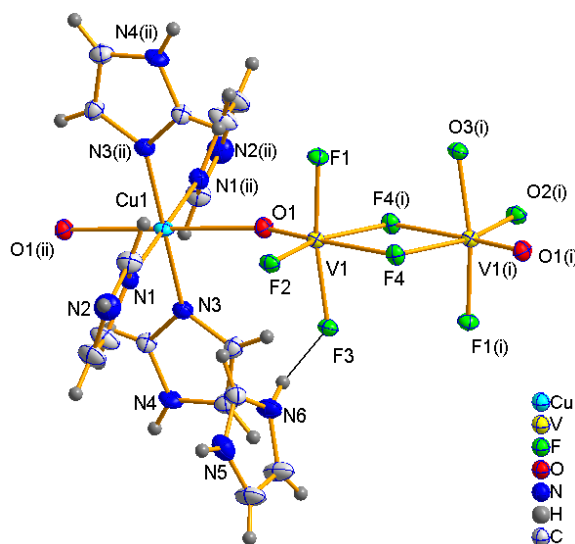
Figure 4.34 The building unit in **CuV–7** with ellipsoids at 50% probability and symmetry operators (i) 1−x,−y,−z; (ii) 2−x,−y,−z.
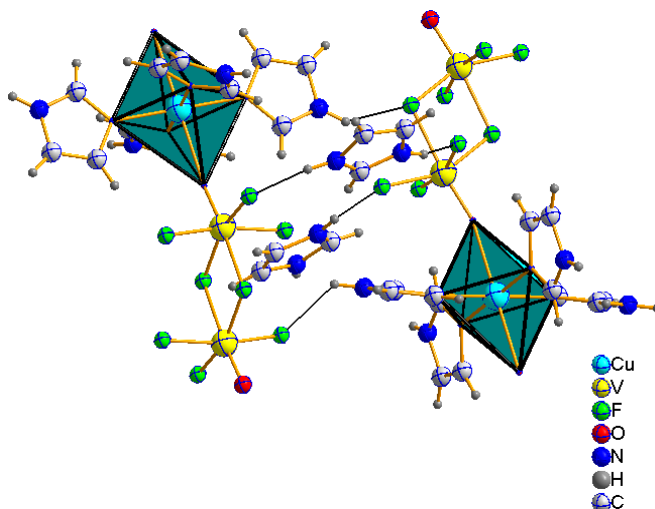
Figure 4.35 Hydrogen bonding interactions in **CuV–7**.

Bond	Bond Length(Å)	S_{ij}	Bond	Bond Length(Å)	S_{ij}
V1–O1	1.605(2)	1.622	Cu1–O1 x 2	2.450(1)	0.115
V1–F1	1.918 (2)	0.555	Cu1–N1 x 2	2.031(3)	0.468
V1–F2	1.937(2)	0.527	Cu1–N2 x 2	2.017(3)	0.486
V1–F3	1.940(2)	0.523			
V1–F4	2.202(2)	0.257			
V1–F4'	1.964(2)	0. 490			
		$\Sigma V1= 3.97$			$\Sigma Cu1=2.13$

Table 4.19 Selected bond lengths and BVS for **CuV–7**.
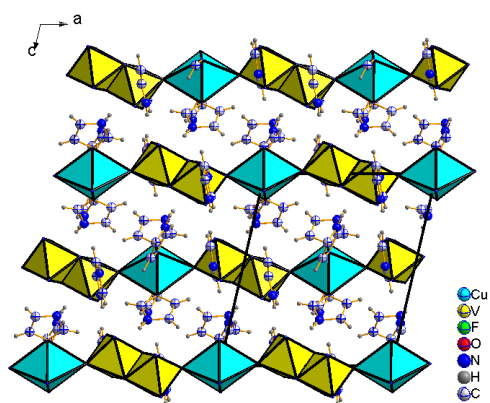
Figure 4.36 Packing in **CuV–7**.

The crystal structure of **CuV–8** is the only case in which fluoride is not incorporated into the product. The asymmetric unit contains two distinct corner–sharing tetrahedral vanadium $[(VO_3)_2]^{2-}$ units present in +5 oxidation state and the square pyramidal copper cation in +2 oxidation state (see Table 4.20), each situated on general positions. Infinite corner–sharing chains of vanadate tetrahedra occur, $[VO_2O_{2/2}]^-$, which is a common structural motif in hybrid copper-vanadium oxide chemistry, for example in $Cu(bipy)_2[V_2O_6]^{16}$. The $[VO_2O_{2/2}]^-$ motif consists of four tetrahedra per chain repeat unit propagating along the *a* axis, as shown in Figure 4.39. Two crystallographically independent vanadates are arranged alternately along the chain, only one of which coordinates to the Cu–containing moiety. The Cu centre itself is unusual in containing two different N–donor ligands, pyridine and ethylenediamine coordinated in a square planar arrangement, while the oxide ligand occupies the apical site leading to overall square pyramidal coordination around Cu (see Figure 4.37). The copper complex acts as 'decoration' to the vanadium oxide chain, rather than being directly involved in chain formation itself. There are weak *intra*–chain and *inter*–chain hydrogen bonding interactions (*Intra*–chain H–bond interactions:N1–H1B…O1 2.16 Å; N1…O1 2.98 Å; N2-H2A…O2 2.21 Å; N2…O2 3.08 Å, *inter*–chain H–bond weaker interactions: N2–H1A…O2 2.21 Å; N2…O2 3.08 Å; N2–H2B…O6 2.03 Å; N2…O2 2.86 Å) between the ethylenediammonium moiety of copper cation unit (see Figure 4.38) and the $[VO_2O_{2/2}]^-$ unit which is not bonded to the cation directly, in the case of *intra*–chain H–bond interactions.
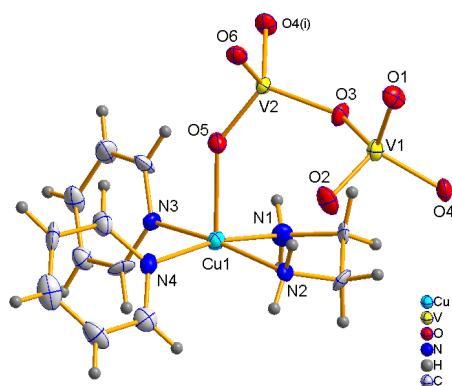
Figure 4.37 The building unit in **CuV–8** with ellipsoids at 50% probability and symmetry operator (i) −½+x,½−y,−z.

Bond	Bond Length(Å)	S_{ij}	Bond	Bond Length(Å)	S_{ij}
V1–O1	1.638(5)	1.545	V2–O3	1.801(5)	1.011
V1–O2	1.655(5)	1.496	V2–O4	1.813(5)	0.965
V1–O3	1.813(5)	0.971	V2–O5	1.668(5)	1.452
V1–O4	1.805(5)	1.000	V2–O6	1.644(5)	1.537
		ΣV1= 5.01			ΣV2=4.97

Bond	Bond Length(Å)	S_{ij}
Cu1–O5	2.249(5)	0.213
Cu1–N1	2.005(5)	0.501
Cu1–N2	2.029(5)	0.468
Cu1–N3	2.055(6)	0.440
Cu1–N4	2.036(6)	0.458
		ΣCu1=2.08

Table 4.20 Selected bond lengths and BVS for **CuV–8**.
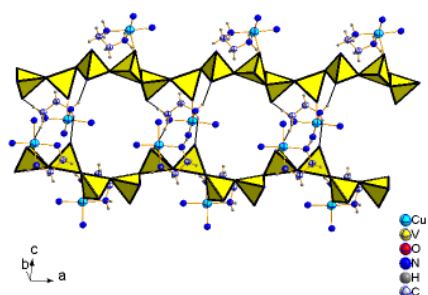
Figure 4.38 *Inter*–chain hydrogen bonding interactions in **CuV–8**.
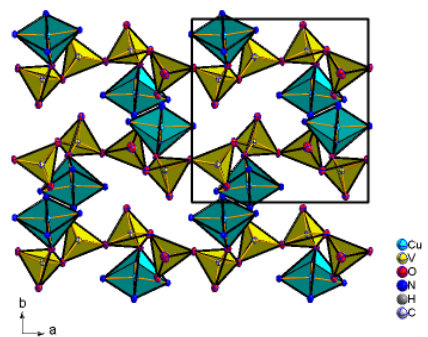
Figure 4.39 Crystal packing in **CuV–8**.

CuV–9 crystallises as a hybrid inorganic/organic 1–D infinite chain extending along the *a* axis. The building unit consists of a dimeric $[Cu_2F_2(C_{10}H_{10}N_3)_2]^{4+}$ complex situated on an inversion centre and linked via $[V_2O_7]^{4-}$ anionic units through oxygen ligands. The fluoride is contained exclusively within the coordination sphere of copper rather than vanadium, acting as bridge between the two edge–sharing Cu–centred octahedra (see Figure 4.40). The axial sites of the cation motif connect to the $[V_2O_7]^{4-}$ anions, which unusually have a 180° V–O–V bond angle, and the outer equatorial sites are occupied by a bidentate dipyridylamine ligand. The vanadium oxidation state is confirmed as +5 by BVS analysis (see Table 4.21). A similar cationic moiety, bridged by $[SiF_6]^{2-}$ rather than $[V_2O_7]^{4-}$, has been reported previously[17], but in the present case the dipyridylamine is protonated due to the strongly acidic conditions in the HF reaction medium. Crystal packing is dominated by hydrogen bonds from the protonated dipyridylamine to the anion of a neighbouring chain, leading to supramolecular 3–D network interactions (N3–H3B…O3 2.24 Å; N3…O3 2.86 Å) (see Figure 4.41).
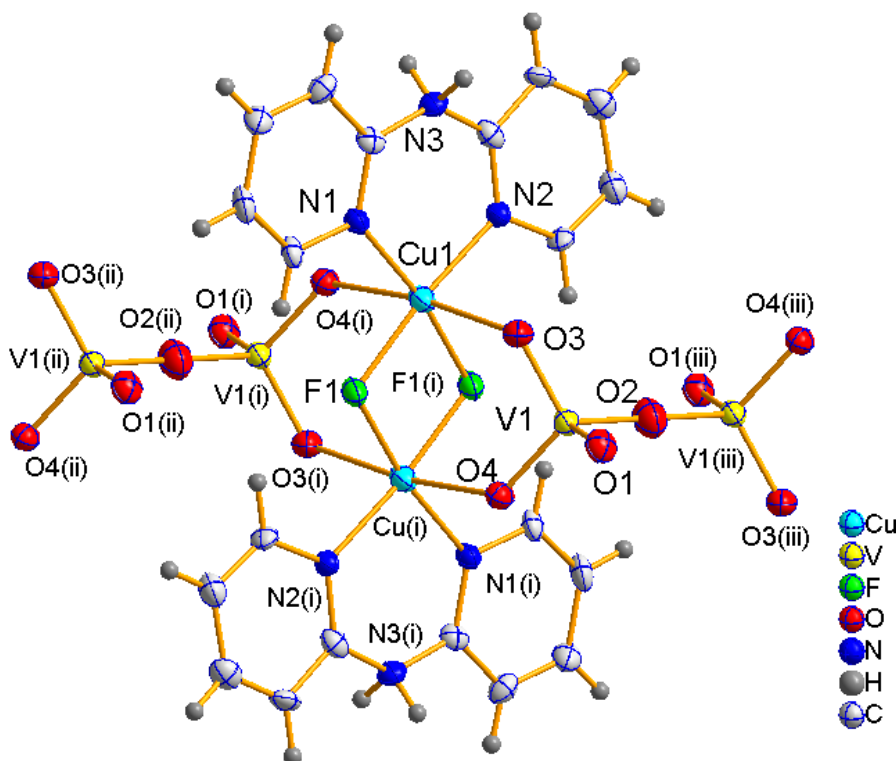
Figure 4.40 The building unit in **CuV–9** with ellipsoids at 50% probability and symmetry operators (i) 1−x,−y,1−z; (ii) −1+x,y,z; (iii) 2−x,−y,1−z.

Bond	Bond Length(Å)	S_{ij}	Bond	Bond Length(Å)	S_{ij}
V1–O1	1.738(5)	1.192	Cu–F1	1.937(4)	0.396
V1–O2	1.770(1)	1.093	Cu–F1'	1.942(4)	0.390
V1–O3	1.653(5)	1.500	Cu–N1	1.974 (5)	0.546
V1–O4	1.693(5)	1.346	Cu–N2	1.977 (5)	0.540
			Cu–O3	2.485(1)	0.110
			Cu–O4	2.466(1)	0.104
		ΣV1= 5.13			**ΣCu1=1.87**

Table 4.21 Selected bond lengths and BVS for **CuV–9**.
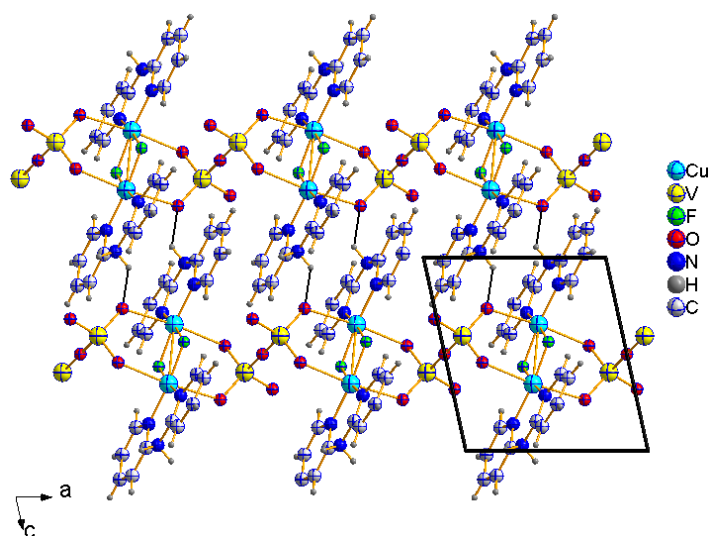
Figure 4.41 Crystal packing with *inter*–chain hydrogen bonding interactions in **CuV–9**.

Heated under Ar, **CuV–9** undergoes a weight loss occurring continuously between 220˚C and 450˚C, as shown in Figure 4.42. This is thought to be owing to the loss of organic template from the material. The total weight loss of 47%, corresponds to the removal of 2,2'–dipyridylamine (calculated composition is 47.55%). The final product at 500˚C is largely amorphous.
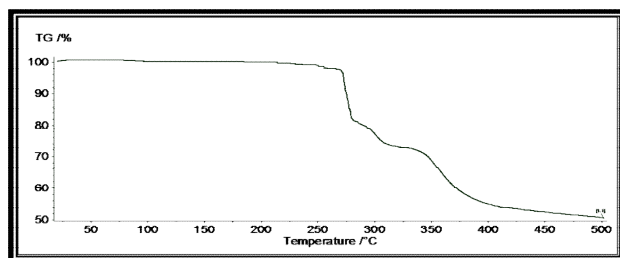
Figure 4.42 TGA of **CuV–9**.

The magnetic data of **CuV–9** are quite complicated, showing three different regions in the plot of $1/\chi_p$ versus T and χ_p versus T, as shown in Figure 4.43.
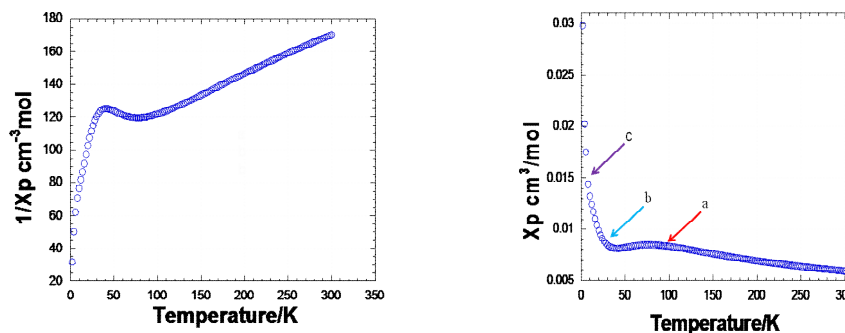
Figure 4.43 χ_p^{-1} vs. T (left), χ_p vs. T (right) for **CuV–9**.

The three regions are (a) low–dimensional antiferromagnetic interactions, (b) ferromagnetic or ferrimagnetic interactions and (c) paramagnetic impurities from straw and gelatin capsules used to mount sample. There are three ways ferro or ferrimagnetism can occur

1. Due to an impurity.

2. A phase transition occurs from antiferromagnetism to ferro or ferrimagnetism on cooling.

3. Two phases existing independently within the crystal structure which exhibit antiferromagnetism and ferromagnetism/ferrimagnetism.

Further to confirm the presence of ferromagnetic interactions, the temperature was kept constant at 5 K and magnetic field was scanned from +5000 Oe to −5000 Oe. The plot of magnetic moment versus applied field shows non–linear behaviour, as shown in Figure

127

4.44. However, much higher fields are required to confirm the presence of ferromagnetism.
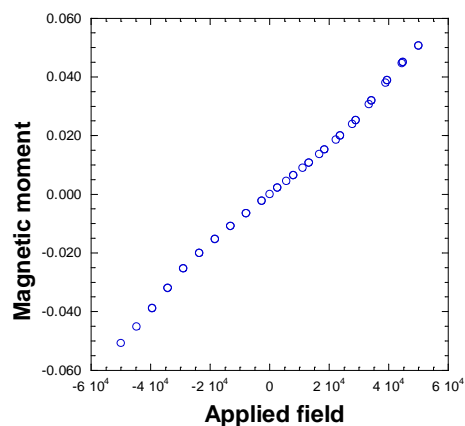
Figure 4.44 Non-linear plot of magnetic moment vs. field for **CuV–9**.

The crystal structure of **CuV–10** reveals an infinite 1–D chain running along the *a* axis, as shown in Figure 4.48. The morphology of the crystals was investigated in an optical microscope as well as SEM; very long needle or wire type of green crystals are observed, as shown in Figure 4.46. The building unit contains two crystallographically different square pyramidal copper centres present in the +2 oxidation state together with two distinct octahedral vanadium centres in +4 oxidation state, confirmed by BVS analysis (see Table 4.22). Each copper centre forms a three–membered bimetallic ring with two distinct vanadium centres linking through fluoride ligands. Each vanadium octahedron shares its edge with copper as well as sharing a corner with crystallographically different vanadium and copper (see Figure 4.45). The anion $[VOF_5]_2^{3-}$ unit adopts a distorted octahedral environment, consistent with the presence of a short V=O bond, *cis* and *trans* positions are occupied by fluoride ligands coordinating to the copper complex. Further, these nucleophilic fluoride ligands accept hydrogen bonds from dipyridylamines of neighbouring chains thus forming a supramolecular 3–D network (N–H…F 1.92–2.11 Å; N…F 2.74–2.96 Å) (see Figure 4.47). The oxide ligands of the anion motifs neither coordinate to the copper centre nor accept a hydrogen bond. When compared to the previous structures, here vanadium oxyfluoride forms a continuous chain and the copper

complex acts as 'decoration' to the chain, rather than being directly involved in chain formation itself.
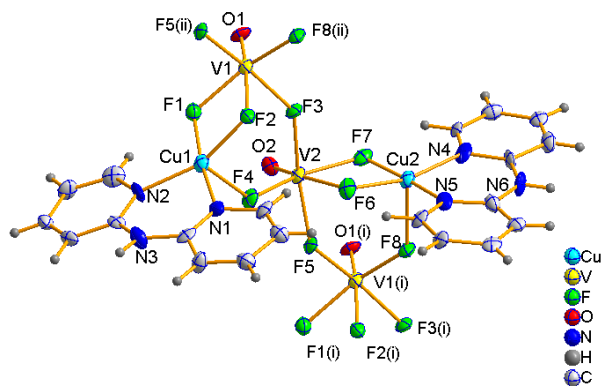
Figure 4.45 The building unit in **CuV–10** with ellipsoids at 50% probability and symmetry operators (i) 1+x,y,z; (ii) −1+x,−y,z.

Bond	Bond Length(Å)	S_{ij}	Bond	Bond Length(Å)	S_{ij}
V1–O1	1.600(10)	1.472	V2–O2	1.592(10)	1.504
V1–F1	1.975(8)	0.476	V2–F3	1.962(8)	0.493
V1–F2	2.079(9)	0.359	V2–F4	1.895(7)	0.590
V1–F3	1.981(8)	0.468	V2–F5	2.009(8)	0.434
V1–F5	1.969(8)	0.483	V2–F6	2.097(9)	0.342
V1–F8	1.926(8)	0.543	V2–F7	1.994(8)	0.452
		ΣV1=3.80			**ΣV2=3.82**

Bond	Bond Length(Å)	S_{ij}	Bond	Bond Length(Å)	S_{ij}
Cu1–F1	1.947(9)	0.385	Cu2–F6	1.908(7)	0.428
Cu1–F2	1.945(7)	0.387	Cu2–F7	1.940(8)	0.393
Cu1–F4	2.139(8)	0.229	Cu2–F8	2.286(8)	0.154
Cu1–N1	1.945(13)	0.590	Cu2–N4	1.971(11)	0.550
Cu1–N2	1.967(10)	0.556	Cu2–N5	1.967(13)	0.556
		ΣCu1=2.15			**ΣCu2=2.08**

Table 4.22 Selected bond lengths and BVS for **CuV–10**.
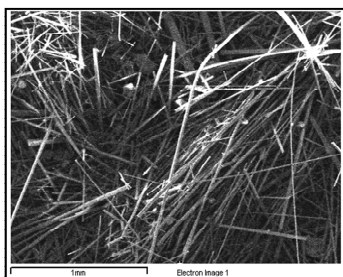
Figure 4.46 SEM image of **CuV–10** shows long needle type crystals.
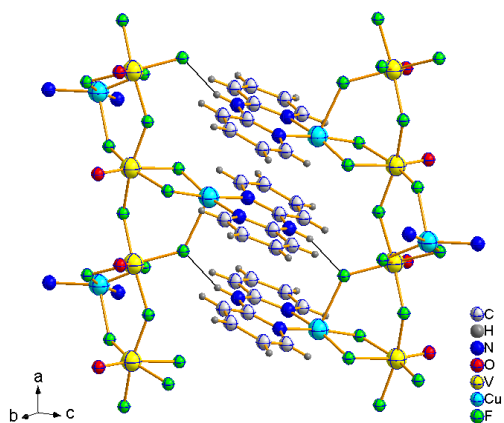
Figure 4.47 *Inter*–chain hydrogen bonding interactions in **CuV–10**.
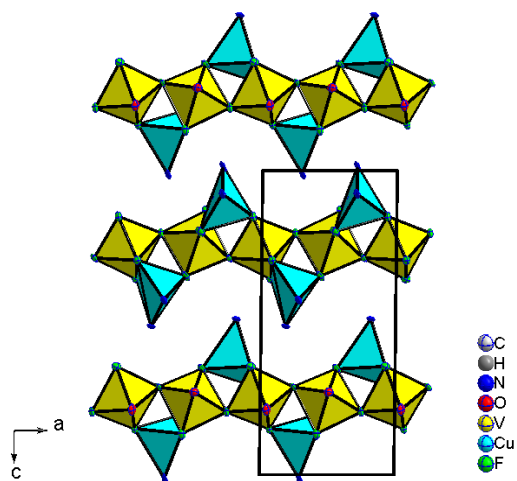
Figure 4.48 Crystal packing in **CuV–10**.

Above 50 K, the magnetic susceptibility for **CuV–10** obeys a Curie–Weiss law. A fit to the inverse susceptibility versus T plot reveals a negative Weiss constant (θ_{esd}=−4.34 K), which corresponds to antiferromagnetic ordering. However the χ_pT versus T plot reveals a special case of antiferromagnetism; ferromagnetic interactions occur in the spin ½ triangular bimetallic ring arrangements. Therefore the combination of both interactions would clearly show ferrimagnetism and magnetic frustration in the structure. The ratio of the ordering temperature (T_N=30 K) and the estimated value of θ indicate the presence of ferrimagnetic interactions according to Ramirez (a value of above 10 indicates geometric frustration).[18] The experimental value of μ_{eff}=3.43 µB, obtained from the Curie-Weiss plot is consistent with the ideal system of four non–interacting isolated spin ½ centres per formula unit (μ_{eff}=3.46 µB), also confirming the BVS analysis of V^{4+} and Cu^{2+}. The saturation value C in the χ_pT versus T plot is 1.49 cm^3mol^{-1}K which is exactly the ideal value 1.49 cm^3mol^{-1}K for the proposed model.
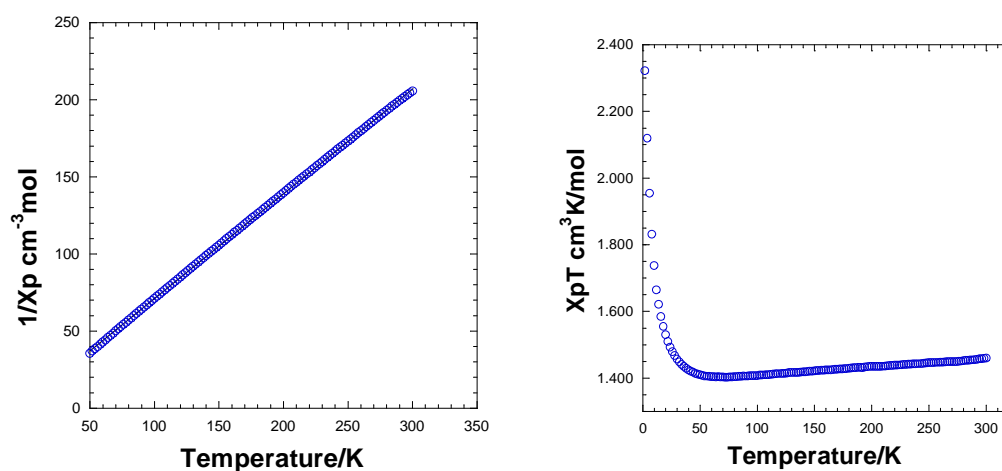
Figure 4.49 χ_p^{-1} vs. T above 50K (left) and χ_pT vs. T (right) for **CuV–10**.

There are four possibilities which might explain this magnetic behaviour, based on the crystallographic evidence:

Case 1: Consider that the longer contact between Cu^{2+} and V^{4+}, will have weaker interactions, as shown in Figure 4.50. These will make little contribution to the magnetic interactions and lead to a magnetic spin ½ 1–D chain with copper pendants. All the spin ½ vanadium sites align anti- parallel to each other, while spin ½ Cu^{2+} of the triangular rings align up and down alternately along the chain. This will result in ideal antiferromagnetic interactions.

Case 2: Assume the weaker interactions occur between vanadium centres. This will result in a 1–D *zig–zag* magnetically active chain. The spin ½ V^{4+} and spin ½ Cu^{2+} align anti-parallel to each other along the *a* axis. However, the magnetic moment of spin ½ V^{4+} and spin ½ Cu^{2+} are unequal and the net moment leads to ferrimagnetic interactions.

Case 3: Based on the crystal structure, there are two crystallographically different rings with different cation–cation contacts. If we assume that longer contacts (Cu2…V1 3.821 Å and V1…V2 3.708 Å) have weaker interactions, this will result in zero magnetic moment from anti-parallel alignment of spin ½ centres of both the vanadium and copper, leading to antiferromagnetic interactions.

Case 4: All the spin ½ aligned 60˚ to each other (crystallographic data suggests that angles between the metal centres of the triangle are in the range of 49.22˚-68.08˚) and spin ½ interactions will give a net magnetic moment and lead to ferrimagnetism.

In the case of 1 and 3 spin canting is necessary to produce ferrimagnetism, while for 2 and 4 this is not needed due to the spin arrangements of different metal centres always resulting in a net magnetic moment.

Case 1:
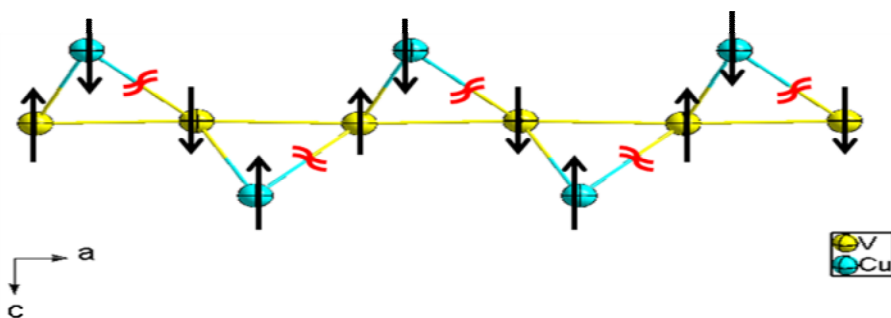
Case 2:
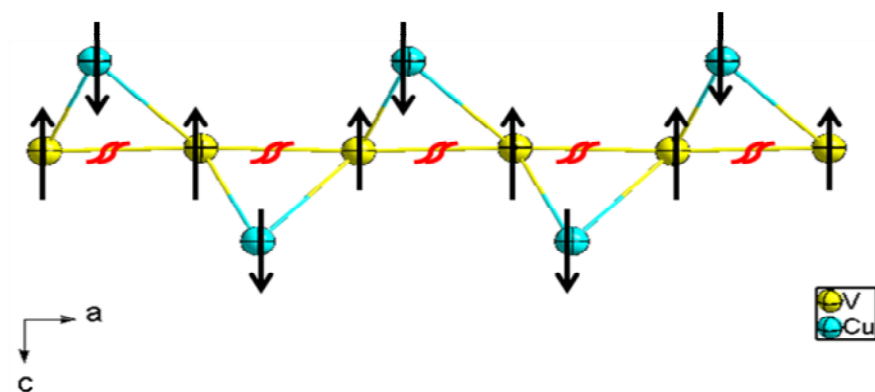
Case 3:
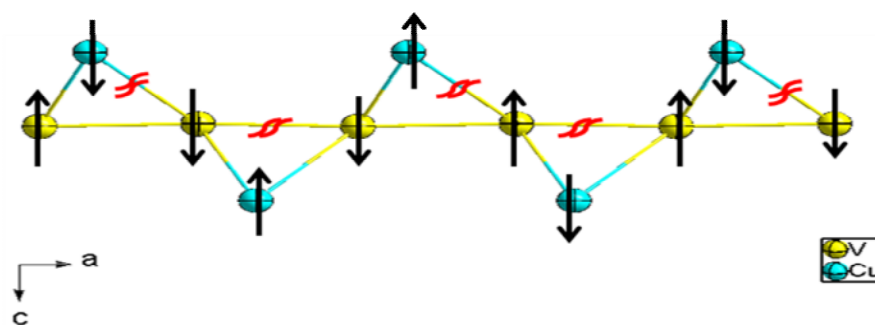
Case 4:
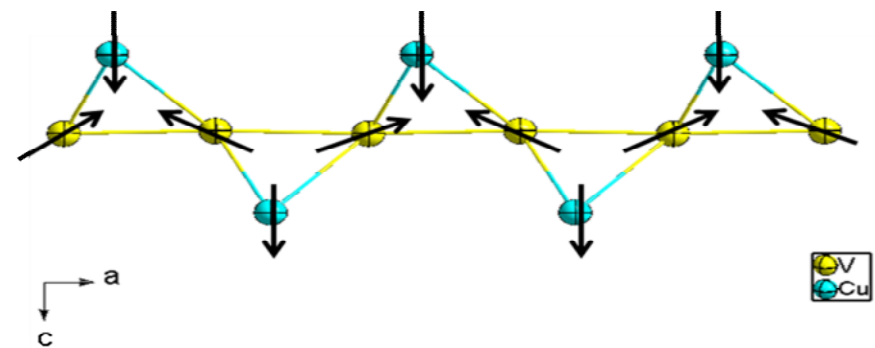
Figure 4.50 The four possibilities of spin ½ arrangement in triangular lattice of **CuV–10**.

4.5 Layers

$Cu(C_{10}H_9N_3)]_2[V_6O_{17}]$ (**CuV–11**) and $[Cu_3(C_5H_5N)_{12}][V_6O_{18}]$ (**CuV–12**) exhibit novel 2-D structures. Fluoride is not incorporated into the product even though HF is present in the reaction medium.

A Rietveld refinement of X–ray powder data of **CuV–11** was performed (see Section 2.1) using the unit cell dimensions and atomic co–ordinates determined by the single crystal solution as a starting point. Instrumental parameters (background, zero-point, peak profile coefficients and unit cell parameters), were refined. A close final fit to the observed data was achieved, with Rwp=3.63% with the structure determined from the single crystal experiment (see Figure 4.51).
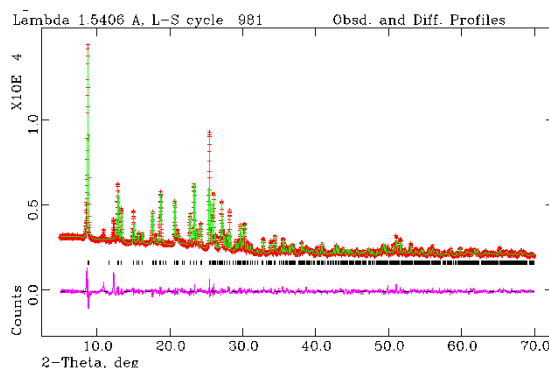
Figure 4.51 The Rietveld refinement of **CuV–11**. Observed data red, calculated profile green, difference profile purple.

4.5.1 Discussion

Structure

The structure of **CuV–11** illustrates some interesting features of hybrid inorganic/organic materials. The asymmetric unit (see Figure 4.52) contains a square of four–membered metal ring [CuV$_3$] linked through oxide ligands, which contains two trigonal bipyramids (2+3 geometry) and a tetrahedral vanadium, all in +5 oxidation state and Cu(II) in a square pyramidal, '4+1' geometry (see Table 4.23).

134

The trigonal bipyramids share their edges, forming an infinite double chain like a 'ladder' with formula of V_2O_5; parallel to the *a* axis (see Figure 4.53). A similar type of double chain of edge–sharing trigonal bipyramids has been observed[19] in β–NaVO$_3$, also the V–O distances within these V_2O_5 double chains are comparable in both structures; for β–NaVO$_3$; 1.979(16) Å and for **CuV–11**; 1.969(3) Å and 1.976(3) Å.

Tetrahedral vanadium forms a V_2O_7 dimer which engages exclusively in corner-sharing interactions. Two oxygen sites of each tetrahedron contribute to bridge copper, the other site connecting the every third particular trigonal bipyramidal of the ladder. The V_2O_7 groups interconnect neighbouring double chains into layers parallel to the *ac* plane. The coordination environment of copper contains three bridging oxide ligands of tetrahedral vanadiums and a bidentate 2,2'–dipyridylamine ligand. Both the copper complex and tetrahedral vanadium form a bimetallic ring, [Cu$_2$V$_2$]; which is alternately linked to either side of the V_2O_5 double chain, forming a 2–D layer (see Figure 4.53).

This framework contains different sizes of bimetallic Cu–V rings such as [CuV$_3$], [Cu$_2$V$_2$], [CuV$_4$] and [CuV$_6$]. The copper coordinated 2,2'–dipyridylamine ligand moieties are situated in between the layers, forming hydrogen bonds with oxygens coordinated to trigonal bipyramidal vanadium. Overall the 3–D supramolecular network is dominated by *inter*–layer hydrogen bonding interactions with distances of N3–H3A…O1 2.04 Å; N3…O1 2.89 Å (see Figure 4.54).
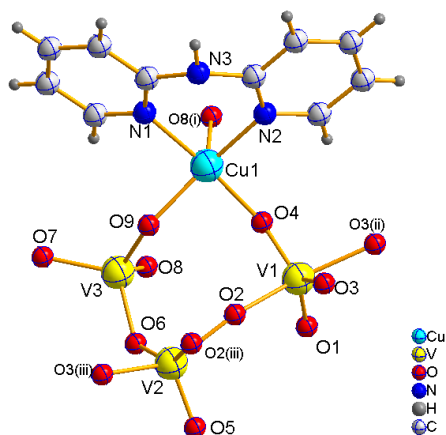
Figure 4.52 The building unit in **CuV–11**. Symmetry operators (i) 1−x,−y,−z ;(ii) 2−x,−y,1−z, (iii) 1−x,−y,1−z.

Bond	Bond Length(Å)	S_{ij}	Bond	Bond Length(Å)	S_{ij}
V1–O1	1.623(3)	1.622	V2–O2	1.874(3)	0.828
V1–O2	1.963(3)	0.649	V2–O2'	1.976(3)	0.627
V1–O3	1.969(3)	0.640	V2–O3	1.895(3)	0.780
V1–O3'	1.947(3)	0.678	V2–O5	1.604(3)	1.712
V1–O4	1.662(3)	1.468	V2–O6	1.779(3)	1.067
		ΣV1=5.06			ΣV2=5.01

Bond	Bond Length(Å)	S_{ij}	Bond	Bond Length(Å)	S_{ij}
V3–O6	1.822(3)	0.950	Cu1–O4	1.968(3)	0.457
V3–O7	1.788(1)	1.041	Cu1–O8	2.259(4)	0.209
V3–O8	1.621(3)	1.635	Cu1–O9	1.931(3)	0.505
V3–O9	1.666(3)	1.452	Cu1–N1	1.975(4)	0.544
			Cu1–N2	1.982(4)	0.534
		ΣV3=5.08			ΣCu1=2.25

Table 4.23 Selected bond lengths and BVS for **CuV–11**.
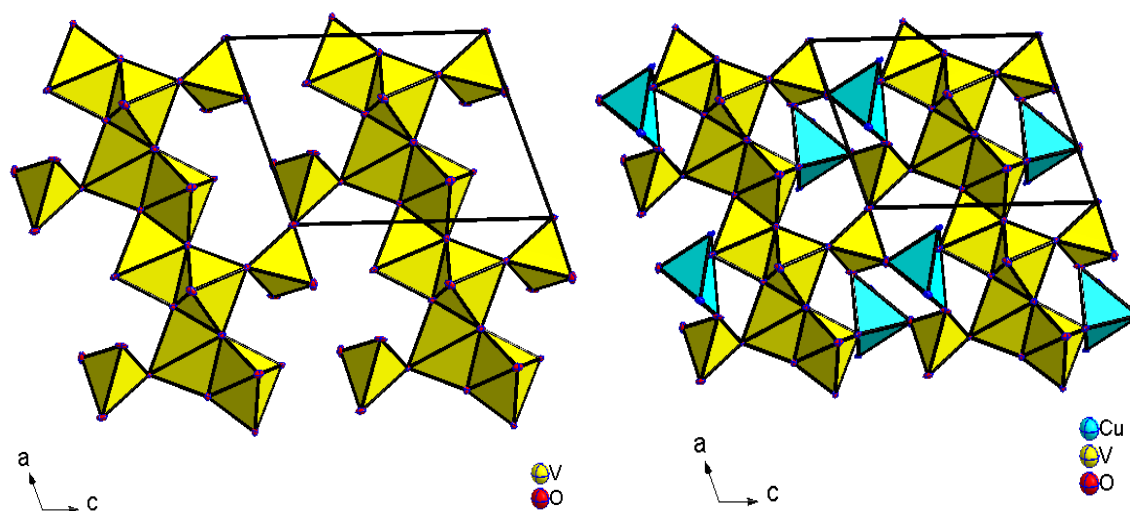
Figure 4.53 Double chain like a 'ladder' of V_2O_5 linked by $[Cu_2V_2]$ rings, forming a 2–D layer in **CuV–11**. Carbon and hydrogen atoms have been omitted for clarity.
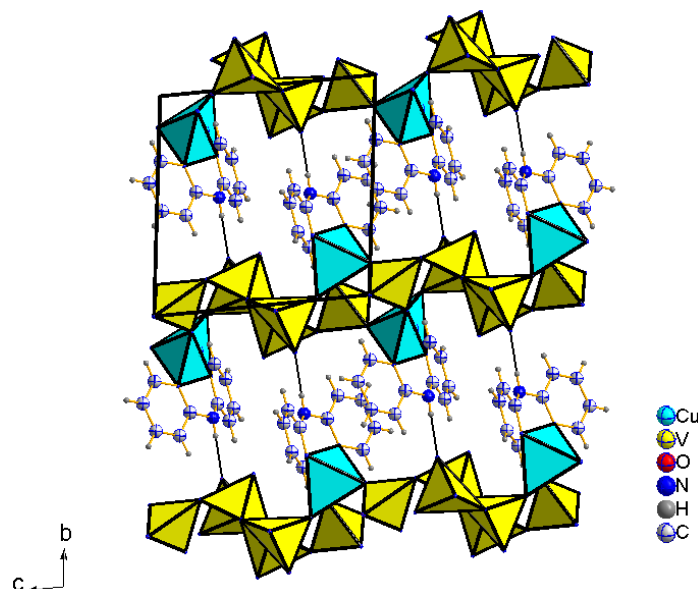
Figure 4.54 Packing of **CuV–11** showing *inter*–layer hydrogen bonding interactions of the supramolecular network.

CuV–12 is a 2–D structure featuring exclusively tetrahedral vanadium as a building block exhibiting ring motifs, linked through octahedral copper complexes forming a bimetallic framework, rather than being simple chain substructures. The asymmetric unit (see Figure 4.55) contains six crystallographically different vanadium sites in +5 oxidation states as confirmed by BVS analysis, adopting tetrahedral geometry, with the coordination environment of three bridging oxide ligands and a terminal vanadyl bond and copper present in the +2 oxidation state in '4+2' octahedral environment (see Table 4.24).

The layered assembly is constructed from four corner-sharing tetrahedra forming a four–membered vanadate ring, $[V_4]$ linked through octahedra, $[CuO_2N_4]$, on the *bc* plane. There are two crystallographically different layers with the same composition, alternately stacked together parallel to the *a* axis (see Figure 4.58). When comparing both layers, there are significant differences in the vanadate ring, $[V_4]$; formed by four corner–sharing tetrahedral vanadiums and the orientation of the pyridyl rings coordinated to the copper complex. The alignment of apical V=O bonds of each tetrahedron and the bond angles,

V–O–V of the vanadate ring, [V$_4$] in both layers differ significantly (see Figure 4.56). The layer which contains two crystallographically different vanadiums is more 'open' compared to the layer which contains four crystallographically different vanadiums. The relative ring configurations may be understood by comparing the V–O–V bond angles, *viz.* V6–O13–V5, 157.5°; V5–O18–V6, 144.2° for the higher symmetry layer, and V1–O4–V2, 145.3°; V2–O9–V3, 140.0°; V3–O10–V4, 132.5°; V4–O3–V1, 156.8° for the lower symmetry layer.

Each layer contains two different sizes of open rings; a vanadate ring, [V$_4$], and a copper/vanadium bimetallic ring, [Cu$_4$V$_8$]. The pyridyl ligands coordinated to copper project into the twelve–membered bimetallic ring as well as in between the layer cavity, as shown in Figure 4.57.
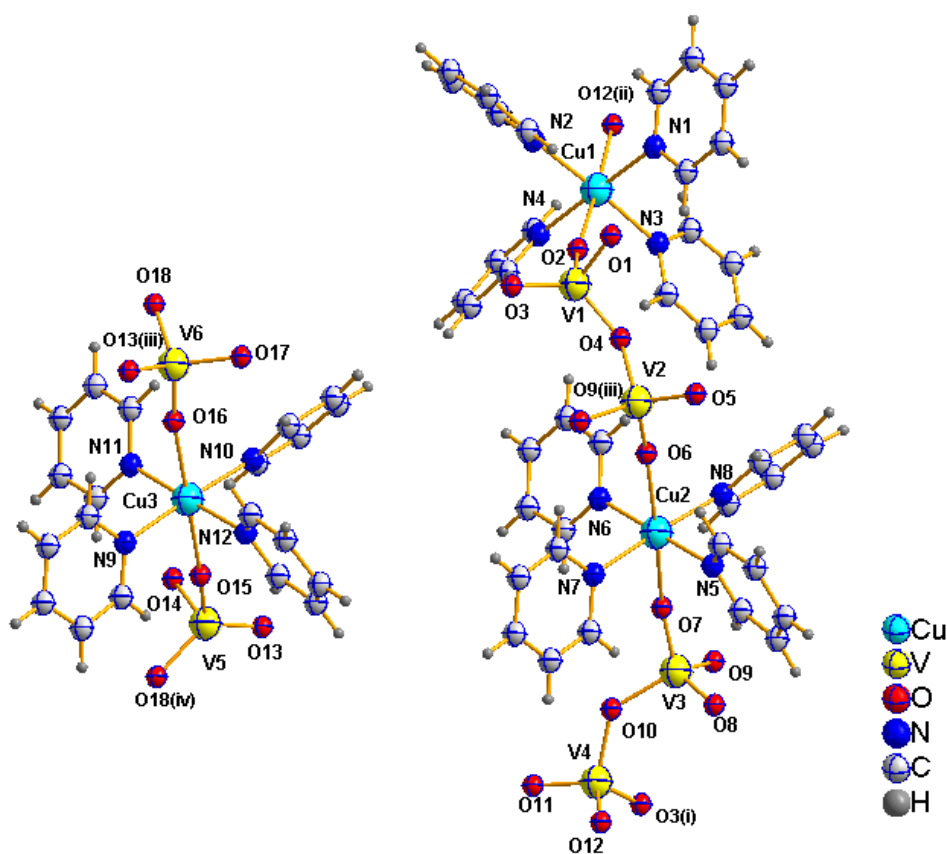
Figure 4.55 The asymmetric unit in **CuV–12**. Symmetry operators (i) x,3/2−y,−½+z; (ii) x,1+y,z (iii) x,3/2−y,½+z; (iv) −1−x,−½+y,3/2−z.

Bond	Bond Length(Å)	S_{ij}	Bond	Bond Length(Å)	S_{ij}
V1–O1	1.699(12)	1.312	V2–O4	1.806(10)	0.982
V1–O2	1.614(10)	1.649	V2–O5	1.636(8)	1.553
V1–O3	1.725(9)	1.123	V2–O6	1.658(9)	1.466
V1–O4	1.682(9)	1.373	V2–O9	1.804(8)	0.987
		ΣV1=5.46			**ΣV2=4.99**

Bond	Bond Length(Å)	S_{ij}	Bond	Bond Length(Å)	S_{ij}
V3–O7	1.686(7)	1.356	V4–O3	1.769(11)	1.086
V3–O8	1.608(7)	1.675	V4–O10	1.815(8)	0.957
V3–O9	1.797(7)	1.007	V4–O11	1.609(7)	1.670
V3–O10	1.795(7)	1.010	V4–O12	1.610(9)	1.668
		ΣV3=5.05			**ΣV4=5.38**

Bond	Bond Length(Å)	S_{ij}	Bond	Bond Length(Å)	S_{ij}
V5–O13	1.638(10)	1.544	V6–O13	1.810(10)	0.828
V5–O14	1.800(14)	0.998	V6–O16	1.647(8)	0.627
V5–O15	1.607(9)	1.680	V6–O17	1.691(13)	0.780
V5–O18	1.720(10)	1.238	V6–O18	1.845(11)	1.712
		ΣV5=5.46			**ΣV6=5.01**

Bond	Bond Length(Å)	S_{ij}	Bond	Bond Length(Å)	S_{ij}
Cu1–O2	2.399(9)	0.134	Cu2–O6	2.247(9)	0.202
Cu1–O12	2.325(9)	0.164	Cu2–O7	2.397(7)	0.135
Cu1–N1	2.034(12)	0.481	Cu2–N5	2.023(9)	0.495
Cu1–N2	2.027(14)	0.490	Cu2–N6	2.043(8)	0.469
Cu1–N3	2.040(12)	0.473	Cu2–N7	2.036(9)	0.478
Cu1–N4	2.054(14)	0.456	Cu2–N8	2.047(9)	0.464
		ΣCu1=2.20			**ΣCu2=2.24**

Bond	Bond Length(Å)	S_{ij}
Cu3–O15	2.347(8)	0.154
Cu3–O16	2.260(8)	0.195
Cu3–N9	2.049(8)	0.462
Cu3–N10	2.041(10)	0.472
Cu3–N11	2.038(9)	0.478
Cu3–N12	2.058(9)	0.451
		ΣCu3=2.21

Table 4.24 Selected bond lengths and BVS for **CuV–12**.
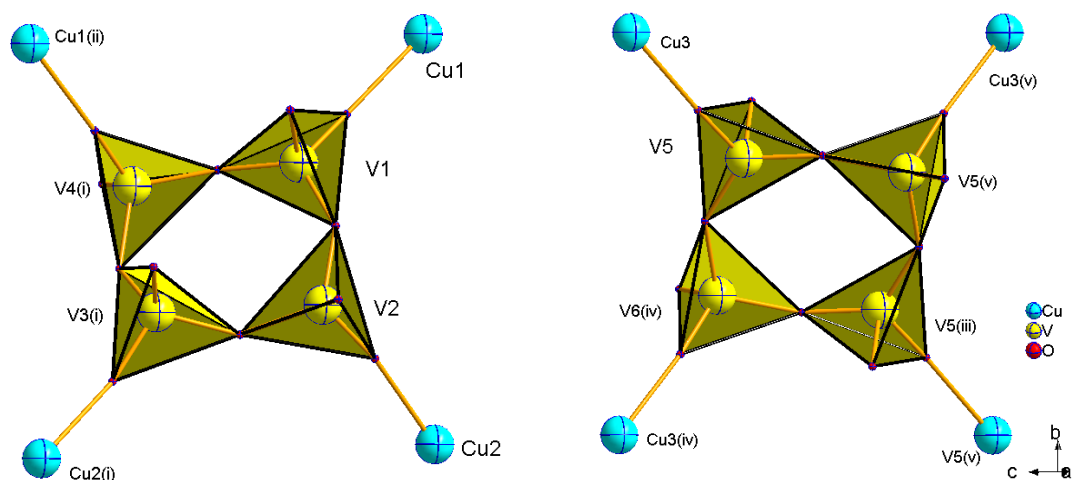
Figure 4.56 Four crystallographically different vanadium sites (left) and two crystallographically different vanadium sites (right) of [V$_4$] rings of two different layers in **CuV–12**. Symmetry operators (i) x,3/2−y,½+z; (ii) x,5/2−y,1/2+z (iii) −1−x,1−y,1−z; (iv) −1−x,−½+y,3/2−z; (v) x,3/2−y,−½+z.
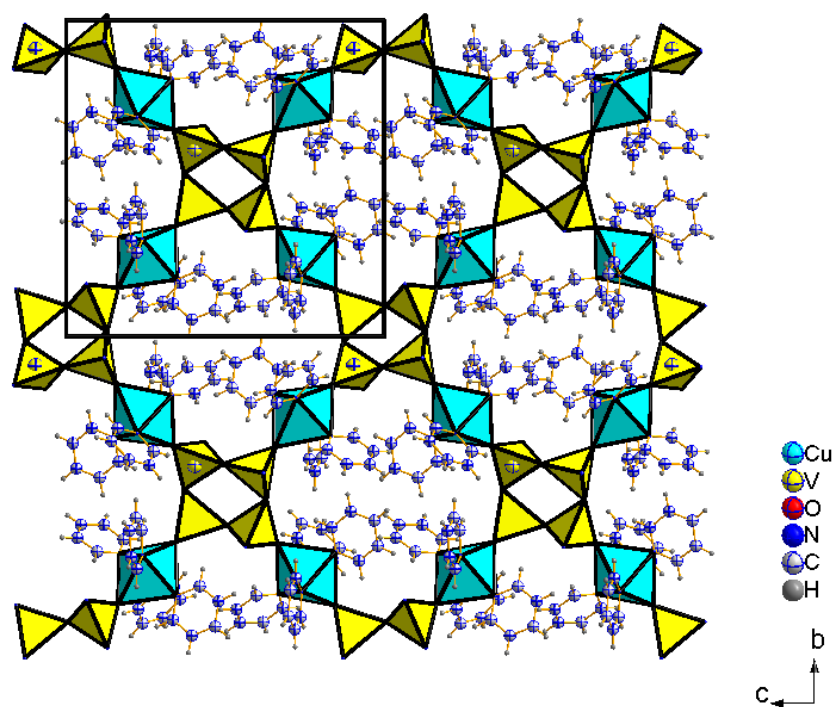
Figure 4.57 Single layer, with pyridyl ligands coordinated to copper projecting into the twelve–membered bimetallic ring in **CuV–12**.
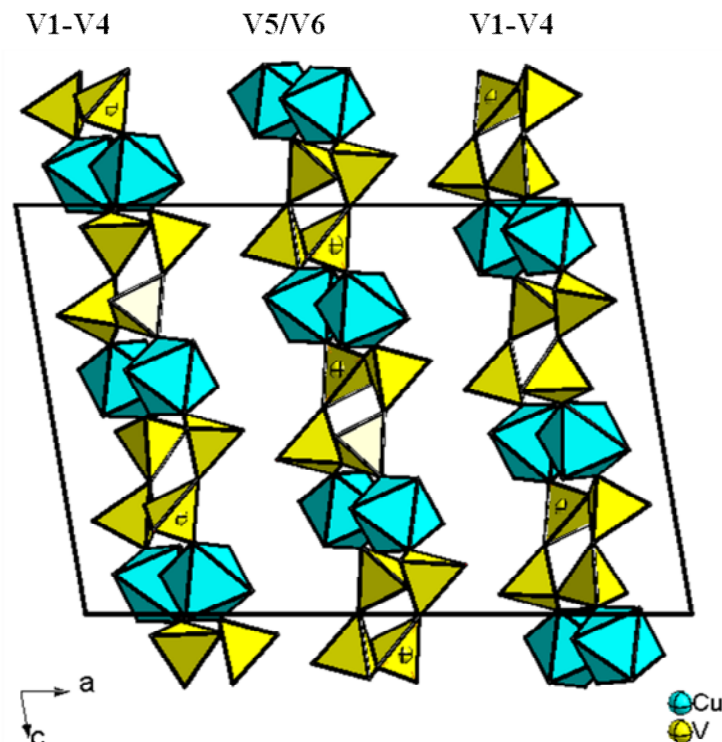
Figure 4.58 Different layers alternately stacked together parallel to the *a* axis in **CuV–12**, carbon and hydrogen atoms have been omitted for clarity.

4.5.2 2,2'–dipyridylamine System

It was decided that a more in-depth examination of the 2,2'–dipyridylamine system was appropriate, as initial experiments suggested that several phases could form. The reaction stoichiometries used to investigate the 2,2'–dipyridylamine system are discussed below as a 'composition-space' diagram. Pure phases were synthesised based on the experimental procedure, as discussed in Appendix–III. The 'composition–space' diagram shows these major phases mixed with other phases in small amounts. Crystallisation fields indicate the major phase as well as mixed phases, as shown in Figure 4.59.

In the low constant concentration of hydrofluoric acid (0.53 M), the crystallisations in the 2,2'–dipyridylamine system occur at relatively low mole percentage of V_2O_5 in comparison to CuO and 2,2'–dipyridylamine. At higher concentration of hydrofluoric

acid (1.05 M) all products were green coloured solutions with no solid product. At very low concentration of hydrofluoric acid (0.26 M), the metal oxides did not dissolve completely and formed poorly crystalline and uncharacterised powder. Changing the ratio of CuO to V_2O_5, resulted in three different phases. However, the reactant ratios do not directly relate to the crystal structure composition. Changing the ratio of hydrofluoric acid and water content, while keeping other reactants and conditions as constant, was also carried out, but only at particularly low concentration, yield **CuV–10**.
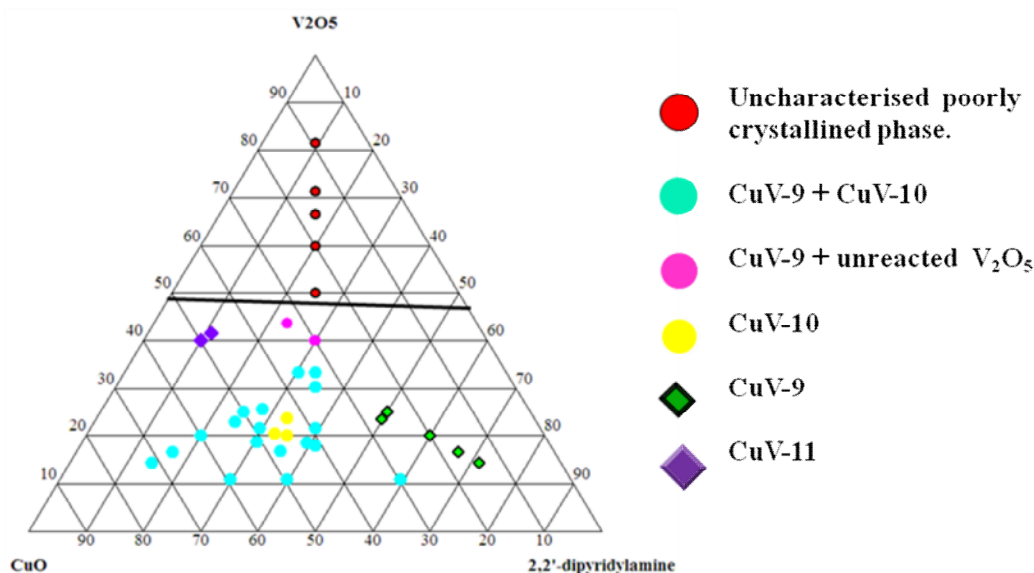
Figure 4.59 'Composition–space' diagram of 2,2'–dipyridylamine system.

4.6 3–D Networks

The crystal structures of two novel 3–D frameworks $[CH_3NH_3]_8[Cu(py)_4]_3[V_7F_6O_{30}]$ (**CuV–13**) and $VZnF_5(H_2O)_2$ (**V–8**) are discussed in this section.

A Rietveld refinement of X–ray powder data of **CuV–13** was performed (see Section 2.1) using the unit cell dimensions and atomic co–ordinates determined by the single crystal solution as a starting point. Instrumental parameters (background, zero–point, peak profile coefficients and unit cell parameters were refined. A close final fit to the observed

data was achieved, with Rwp=4.35% with the structure determined from the single crystal experiment, as shown in Figure 4.60.
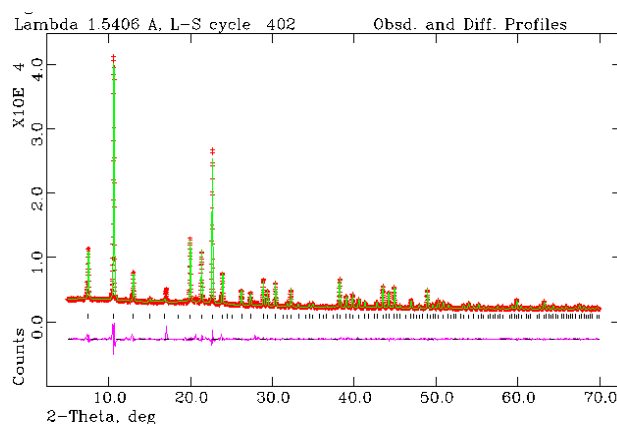
Figure 4.60 The Rietveld refinement of **CuV–13**. Observed data red, calculated profile green, difference profile purple.

4.6.1 Discussion

Structure

The crystal structure of **CuV–13** exhibits a 3–D framework with several novel structural features. The cyan blue crystals were obtained in the presence of a structure directing agent–methylamine and crystallised into remarkably high symmetry, which is further confirmed by its morphology, shiny perfect cubic crystals observed under the optical microscope and scanning electron microscope (see Figure 4.61).
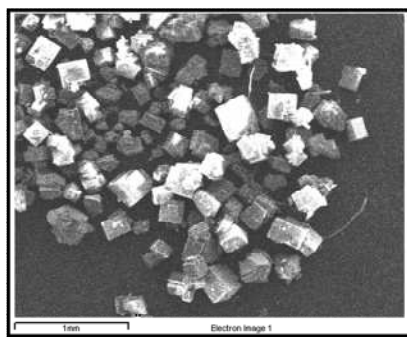
Figure 4.61 SEM image of structure **CuV–13**, showing cubic crystals.

The building unit contains a heptameric $[V_7F_6O_{30}]^{14-}$ anion unit and a copper cation complex. The asymmetric unit contains two crystallographically different vanadium atoms and a copper on special positions. The core of the structure is a 'superoctahedral' $[V_7F_6O_{30}]^{14-}$ anion unit containing seven vanadium–centred octahedra. The central octahedron is $[VF_6]^{2-}$, which shares corners through fluoride ligands with the outer six symmetry equivalent $[VOF_5]^{3-}$ octahedra. However, these six equivalent octahedra are not directly bonded to each other. They exhibit an out–of–centre *intra*–octahedral distortion due to the short vanadyl bond and the elongated V–F bond in the *trans* position.

 The 'superoctahedral' units link through the $[Cu(py)_4]^{2+}$ cation into a 3–D covalent network, as shown in Figure 4.62. The resulting stoichiometry reveals both vanadium and copper has to be +4 and +2 oxidation state respectively. BVS analysis agree to assign outer octahedron in +4 and copper in +2 , although it shows a discrepancy in the bond valence sum of the central octahedron, which may be due to the possible local displacement of vanadium from its ideal site resulting in a higher atomic displacement parameter at this site (see Table 4.24). However, the magnetic data show very good agreement with assignment of all vanadium in the +4 oxidation state.

The solid crystallises as a continuous inorganic network decorated by pyridyl rings, and should be regarded as an 'extended inorganic network hybrid'[20] rather than a metal–organic framework. When we consider only the metal atoms of the network for clarity, it clearly shows the two similar networks of interpenetrated primitive cubic units, which results in a pseudo body–centred cubic overall structure, as shown in Figure 4.63. This can be regarded as an 'augmented' and 'expanded' *pcu* lattice according to O'Keeffe's notation.[21]

The body–centring is broken into primitive only due to the contribution from F1 of the $[VOF_5]^{3-}$ octahedron and C1, C2 of the pyridyl rings. It is also noticed in the crystal structure that the pyridyl rings exhibit 'propeller–like' rotations around the Cu^{2+} at the equatorial position of square planar arrangement (see Figure 4.64). The copper complex exhibits a '4+2' octahedral coordination with elongated axial bonds to oxide ligands.

Both $[VOF_5]^{3-}$ and $[Cu(py)_4]^{2+}$ are *trans* directing which might favour a linear chain structure rather than 2–D/ 3–D network. However, the $[VF_6]^{2-}$ octahedron unambiguously contributes in the connectivity of a 3–D network by sharing six corners exclusively with $[VOF_5]^{3-}$.

Methylammonium, as the structure directing agent, plays a major role in the construction of the superoctahedra. The C–N bond of the amine lies directly along the three–fold axis of each octahedral face of the super octahedron, forming hydrogen bonding interactions with the neighbouring three $[VOF_5]^{3-}$ units of the superoctahedra (N2–H2A…F1 2.04 Å; N2…F1 2.79 Å.) (see Figure 4.65). In addition methylammonium cations maintain the charge neutrality and also fill the voids of the crystal structure.
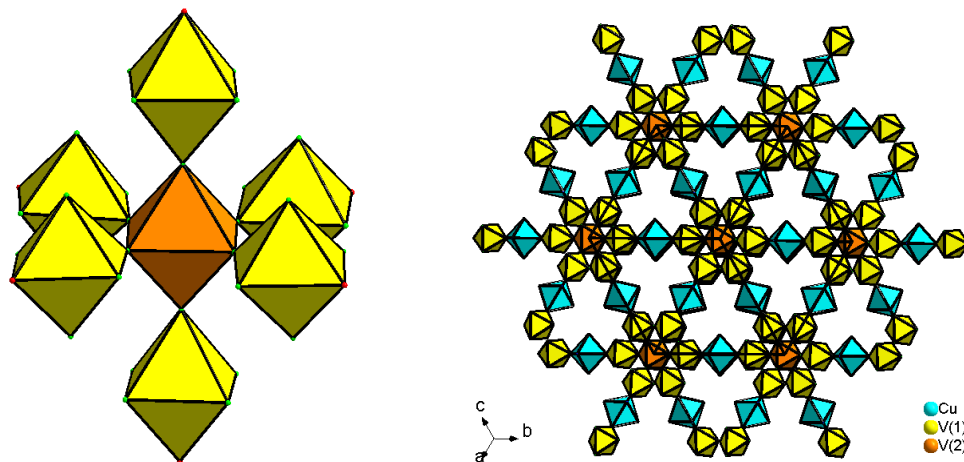
Figure 4.62 The $[V_7F_6O_{30}]^{14-}$, superoctahedron (left) and inorganic framework of **CuV–13** viewed down [111] (right). Organic moieties are omitted for clarity.
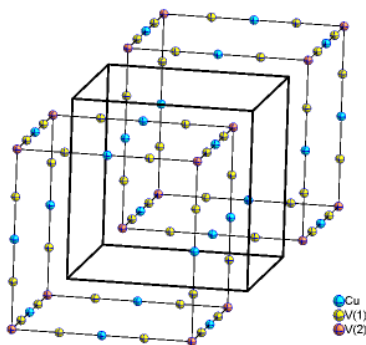
Figure 4.63 Two interpenetrated *pcu* lattices, only the metal atoms have been shown.
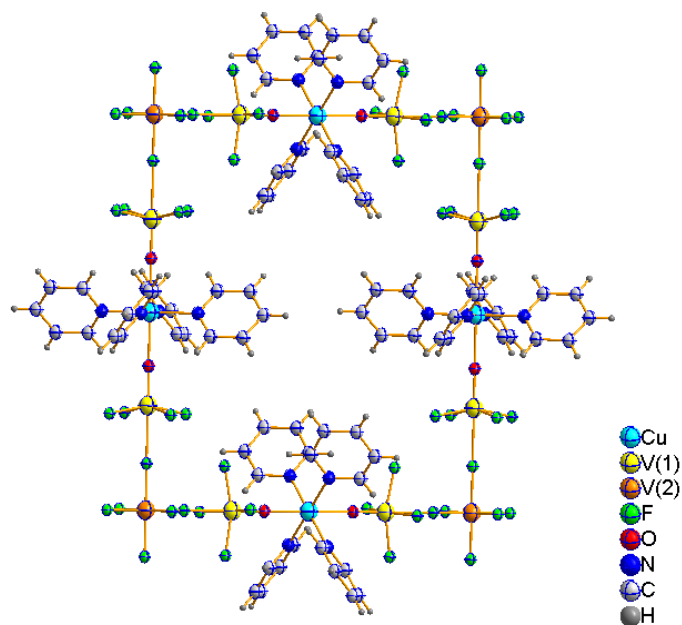
Figure 4.64 'Propeller–like' rotations of the pyridyl groups in $[Cu(py)_4]^{2+}$.
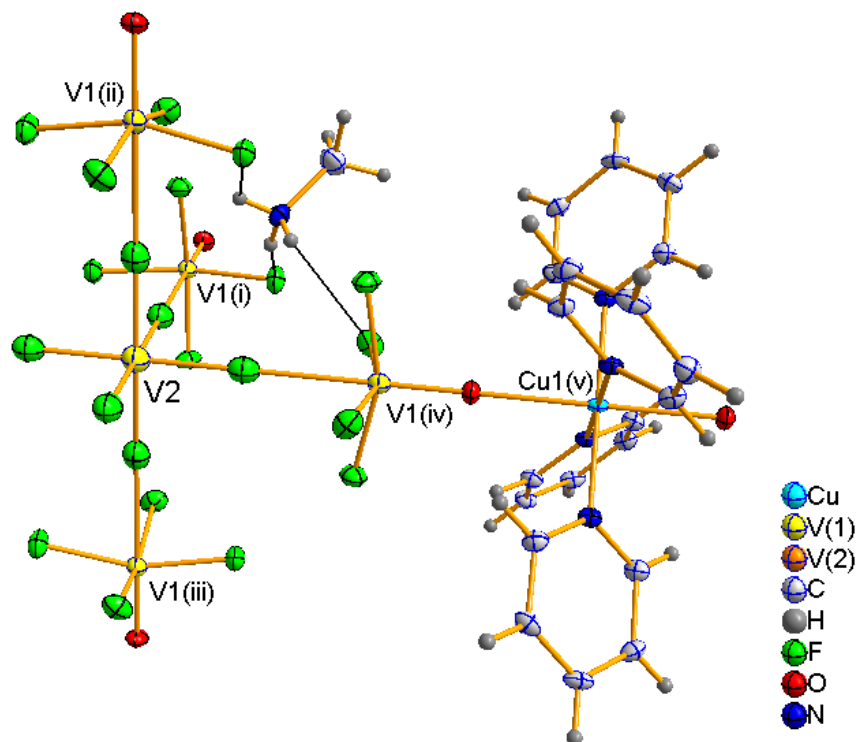
Figure 4.65 Hydrogen bond interactions in **CuV–13** with ellipsoids at 50% probability and symmetry operators (i) ½−x,½−y,z; (ii) ½−x,y,z; (iii) x,½−y,z; (iv) x,y,½−z; (v) 3/2−x,y,z.

Bond	Bond Length(Å)	S_{ij}	Bond	Bond Length(Å)	S_{ij}
Cu1–O1 x 2	2.242(3)	0.205	V–O1	1.644(3)	1.281
Cu1–N1 x 4	2.036(3)	0.334	V1–F1 x 4	1.897(1)	0.588
			V1–F2	2.418(3)	0.144
		ΣCu1=1.75			ΣV1=3.78

Bond	Bond Length(Å)	S_{ij}
V2–F2 x 6	1.943(3)	0.518
		ΣV2=3.11

Table 4.25 Selected bond lengths and BVS for **CuV–13**.

4.6.2 HF/Pyridine/ Dimethylamine System

It was decided to investigate the influence of dimethylamine, pyridine and hydrofluoric acid in the formation of **CuV–13** based on a 'composition–space' diagram of the HF/pyridine/ dimethylamine system, while keeping the V:Cu mole ratio as 7:4. A three component 'composition–space' diagram was constructed to relate the mole fractions of the reactants to the composition of the final crystallined products. The phase stability and the crystallisation field can be understood on the basis of initial reactant concentrations. The pure phase was synthesised based on the experimental procedure, as discussed in Appendix–III. The crystallisation field indicates the occurrence of the major phase as well as [Cu(py)$_4$VOF$_4$], as shown in Figure 4.66. The synthesis of **CuV–13** occurs strictly in particular reaction conditions. Changing the reaction temperature and the stoichiometry of the reactants produces [Cu(py)$_4$VOF$_4$]. However, both phases are decomposable in air within a few weeks. Three regions exist in the 'composition-space' diagram. At higher concentration of hydrofluoric acid the products remain in a blue colour solution. At lower concentration of hydrofluoric acid, the mineraliser is not enough to dissolve the metal oxides. In between, the dimethylamine is protonated in the presence of hydrofluoric acid, and supplying the methylammonium cations needed to crystallise **CuV–13**. The reaction is reproducible by using methylamine, instead of

dimethylamine. Further investigation was carried out in this system, based on changing the stoichiometric ratio of V_2O_5, CuO and water while maintaining other reactants and reaction conditions constant. However, only [Cu(py)$_4$VOF$_4$] was identified, with unreacted metal oxides and poorly crystalline uncharacterised phases.
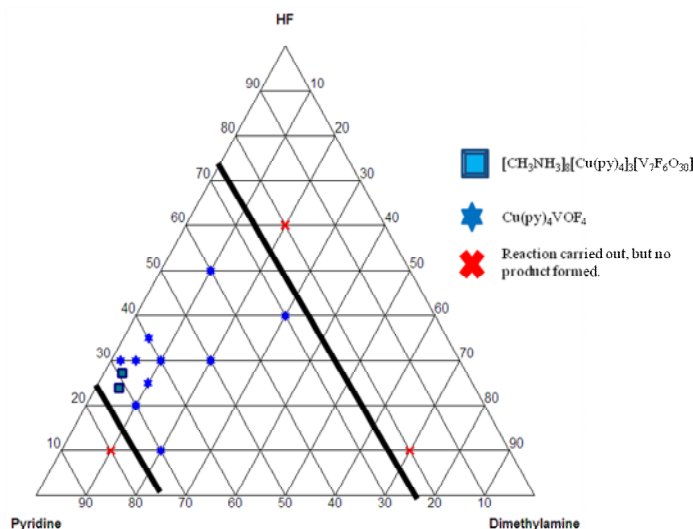
Figure 4.66 'Composition–space' diagram of HF/pyridine/dimethylamine system.

Heated under Ar, **CuV–13** undergoes a weight loss occurring continuously between 200˚C and 240˚C, as shown in Figure 4.67. This is thought to be owing to the loss of organic template from the material. The total weight loss of 45%, corresponds to the removal of pyridine (calculated composition is 38.4%) and methylammonium (calculated composition is 6.5%). The final product at 500˚C is largely amorphous.
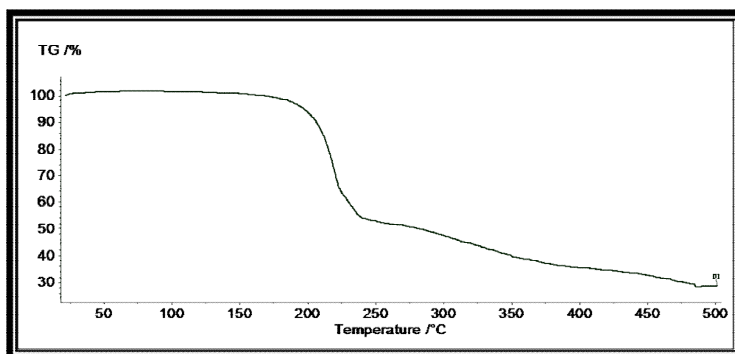
Figure 4.67 TGA of **CuV–13**.

Above 30 K, the magnetic susceptibility for **CuV–13** obeys a Curie–Weiss law, with no evidence of long–range magnetic ordering. A fit to the $1/\chi_p$ versus T plot reveals a negative Weiss constant ($\theta_{esd}=-11.8$ K) and the trend of $\chi_p T$ versus T reveals the short–range antiferromagnetic correlations between the metal centres (see Figure 4.68). The experimental value of $\mu_{eff}=5.46$ µB, obtained from the Curie–Weiss plot is consistent with the ideal system of ten non–interacting isolated spin ½ centres per formula unit ($7V^{4+}$ and $3Cu^{2+}$; $\mu_{ideal}=5.48$ µB), which also confirms the model proposed, and the assignment of V^{4+} and Cu^{2+}. For a system having nine S=1/2 and one S=1 centres the μ_{ideal} would reach 5.91 µB. It can be seen that $\chi_p T$ tends towards saturation at 300 K, the value of $\chi_p T$ is 3.72 cm^{3}mol^{-1}K which is close to the ideal value 3.74 cm^{3}mol^{-1}K for the proposed model. For the alternative V^{3+} containing model this would saturate at 4.37 cm^{3}mol^{-1}K, which further confirms the assignment of all vanadium in the +4 oxidation state.
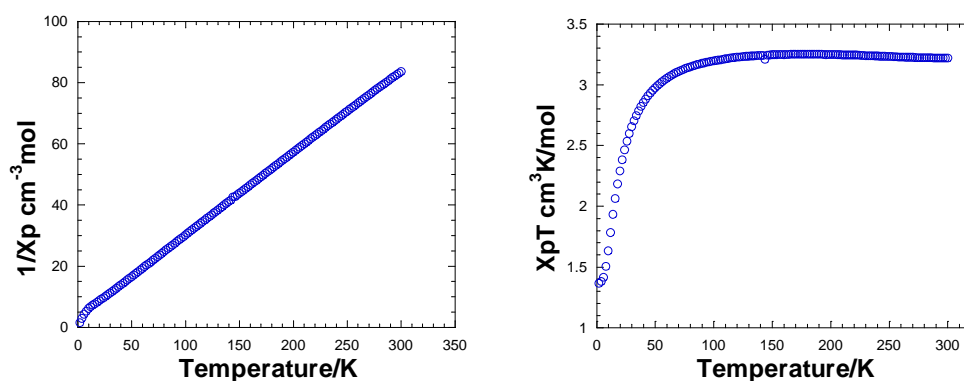
Figure 4.68 χ_p^{-1} vs. T (left) and $\chi_p T$ vs. T (right) for **CuV–13**.

The crystal structure of **V–8** exhibits a 3–D network and is iso–structural with inverse weberite (or anti–weberite) type structures such as $MgAlF_5(H_2O)_2$, $ZnFeF_5(H_2O)_2$ and $MnVF_5(H_2O)_2$.[22,23,24,25] The divalent and trivalent cation sites are inverted compared to weberite, Na_2MgAlF_7. Compared to weberite, in **V–8** two fluoride ligands are replaced by water molecules at the axial sites of octahedral $[ZnF_4(H_2O)_2]^{2-}$ (see Figure 4.69). Vanadium is present in the +3 oxidation state as confirmed by BVS analysis (see Table 4.26). In the octahedral anion $[VF_6]^{3-}$, the axial fluoride ligands share corners to a

neighbouring octahedron $[VF_6]^{3-}$ and the equatorial fluoride ligands share corners with neighbouring $[ZnF_4(H_2O)_2]^{2-}$ units. The alkaline positions of the weberite structure are vacant in **V–8**. In direct weberite, the $[AlF_6]^{3-}$ octahedra share corners at all four equatorial sites to neighbouring $[MgF_6]^{4-}$ *via* bridging fluoride ligands, while in the $[MgF_6]^{4-}$ octahedron, the axial sites are coordinated to neighbouring $[MgF_6]^{4-}$ units and equatorial sites link to $[AlF_6]^{3-}$ units *via* fluoride ligands (see Figure 4.70). Infinite chains of *trans* bridged $[VF_6]^{3-}$ octahedra are connected through common fluoride ligands by isolated $[ZnF_4(H_2O)_2]^{2-}$ octahedra of all the equatorial sites, forming a 3–D network, as shown in Figure 4.71. Significant H–bonding occurs between the water molecules coordinated to Zn^{2+} and the nearest fluorine atoms coordinated to V^{3+} (O1–H1…F2 1.99 Å; O1…F21 2.86 Å.).
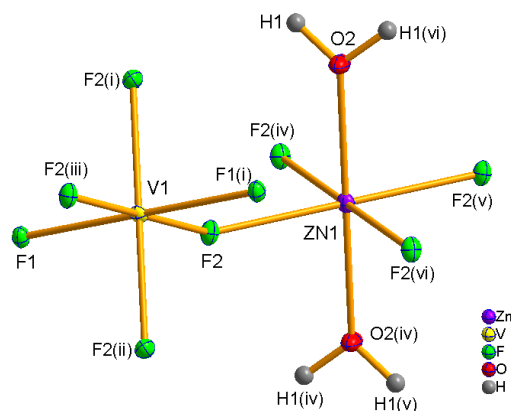
Figure 4.69 Building unit in **V–8** with ellipsoids at 50% probability and symmetry operators (i) −x,1−y,z; (ii) x,y,−z; (iii) −x,1−y,−z; (iv) ½−x,y,½−z; (v) ½−x,½−y,½−z; (vi) x,½−y,z.

Bond	Bond Length(Å)	S_{ij}	Bond	Bond Length(Å)	S_{ij}
V1–F1 x 2	1.963 (1)	0.493	Zn1–O1 x 2	2.039(3)	0.403
V1–F2 x 4	1.916 (1)	0.561	Zn1–F2 x 4	2.048(2)	0.316
		ΣV1=3.23			**ΣZn1=2.07**

Table 4.26 Selected bond lengths and BVS for **V–8**.
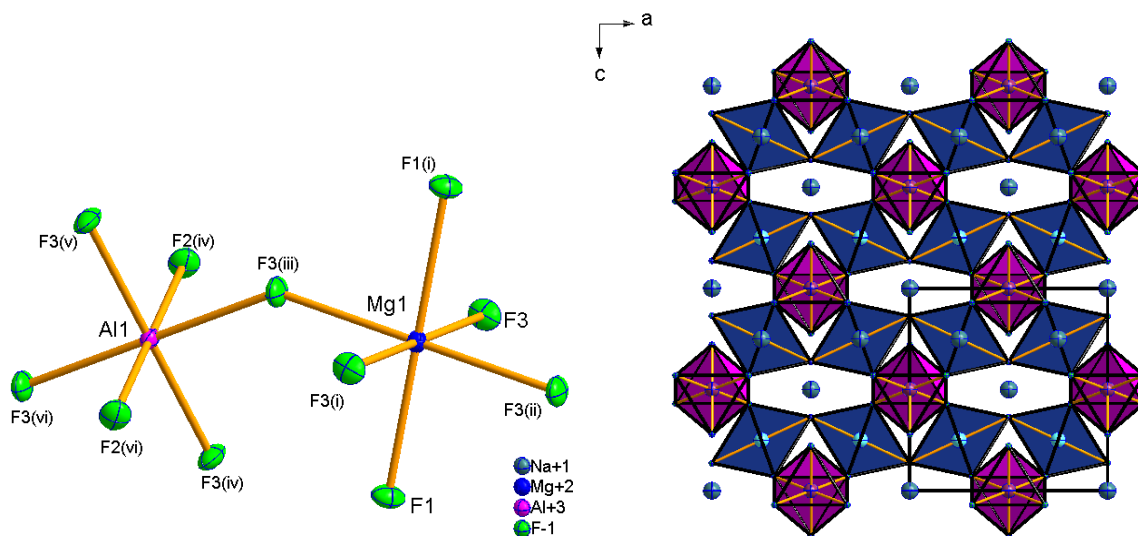
Figure 4.70 Building unit in weberite, Na_2MgAlF_7 with ellipsoids at 50% probability (left), and the crystal packing (right). Symmetry operators (i) ½+x,½−y,½−z; (ii) ½−x,y,½−z; (iii) x,½−y,z; (iv) −x,½−y,z; (v)x,−½+y,1−z; (vi) −x,−½+y,1−z.
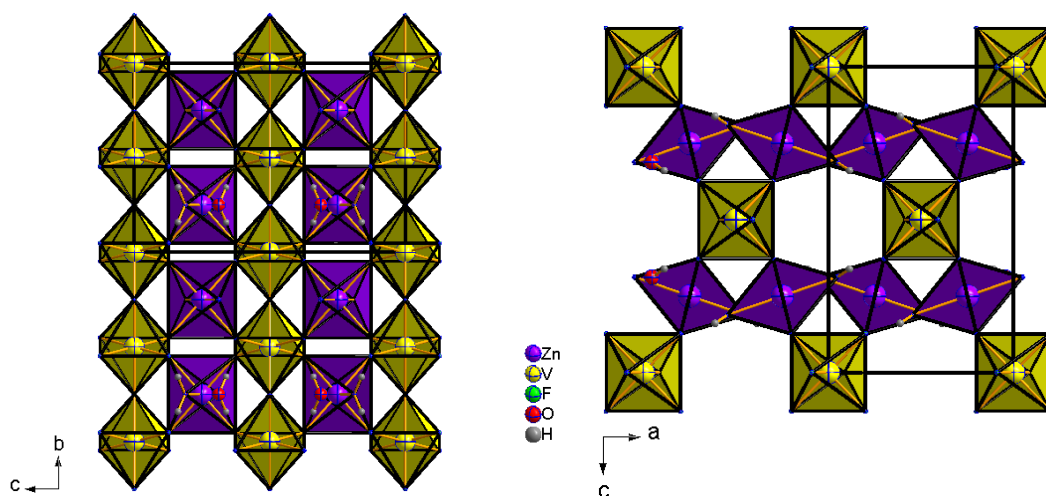
Figure 4.71 Packing in **V–8**.

Above 170 K, the magnetic susceptibility for **V–8** obeys a Curie–Weiss law. A fit to the inverse susceptibility versus T plot reveals a negative Weiss constant (θ_{esd}=−60.60 K), which corresponds to antiferromagnetic ordering and the $\chi_p T$ versus T reveals short–range antiferromagnetic correlations between the metal centres (see Figure 4.72). The

experimental value of μ_{eff}=2.44 μB, obtained from the Curie–Weiss plot is consistent with an ideal system of non–interacting isolated spin 1 centres per formula unit (μ_{eff}=2.83 μB), also confirming the BVS analysis of V^{3+}. The value of $\chi_p T$ is 0.75 $cm^3 mol^{-1}K$ and the ideal value is 1.00 $cm^3 mol^{-1}K$.
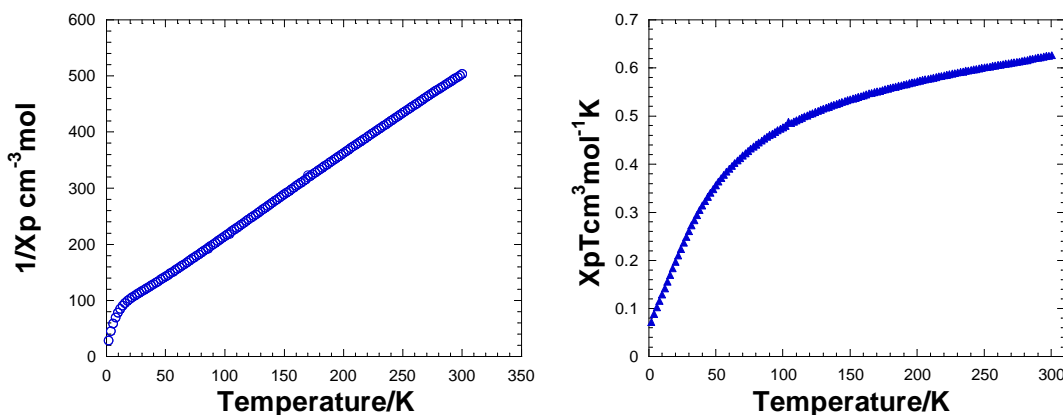
Figure 4.72 χ_p^{-1} vs. T (left) and $\chi_p T$ vs. T (right) for **V–8**.

4.7 Summary

Various organic templates have been successfully incorporated into novel materials with different framework topologies. The exploration toward the hydrothermal chemistry of vanadium oxyfluorides has yielded four clusters including monomeric vanadium units, five clusters including vanadium dimers, eight 1–D chains, two 2–D layers and two 3–D networks, where distinct organic components are encapsulated and form inorganic /organic hybrid frameworks. It is interesting to introduce both Cu and V as these metals show different coordination preferences with nitrogen donating ligands and therefore adopt different environments which increases the diversity of crystal packing in these systems.

Vanadium is directly bonded to nitrogen ligands in three cluster structures. In **CuV–1**, different N–donor ligands are bound to vanadium and copper selectively and the structure shows paramagnetic interactions between the temperatures of 2–100 K. **V–3** contains a

vanadium dimer directly bonded to the 2,2'–dipyridyl ligand, which is iso-structural to **V–4**. Variation of the structure directing amines have resulted these small structural differences in clusters. TGA analysis, fluorine analysis and BVS analysis shows good agreement with crystallographic evidence.

A comparison of **CuV–3** and **CuV–4** shows the subtle effect of reaction conditions, and also the major contribution of hydrogen bonding interactions in the crystal packing of 1–D chains. **CuV–3** exhibits short range antiferrmomagnetic interactions between the metal centres, while for **CuV–4** it is impossible to carry out magnetic measurements accurately owing to rapid sample decomposition during data collection. The crystal structures of **CuV–5** and **CuV–6** are related and exhibit linear infinite 1–D chains. The organic compound acts as both protonated template and neutral ligand coordinated to copper in **CuV–7**. **CuV–9** shows a hybrid inorganic–organic infinite chain containing a dimeric unit of $[Cu_2F_2(C_{10}H_{10}N_3)_2]$. Magnetic data possibly reveals three different magnetic interactions. Copper is coordinated by two different, N–donor ligands in **CuV–8**, which is unusual compared to the other copper containing structures. **CuV–10** exhibits a 1–D chain containing three membered bimetallic rings. Spin ½ arrangements of this triangular lattice also discussed based on four possibilities of interactions according to the crystallographic evidence. Due to the problems with sample stability, purity and also the availability of unpaired electrons on vanadium centres for magnetic measurements, Rietveld refinements, fluorine analysis and TGA analysis were carried out on the 1–D structures, which were consistent with crystallographic evidence.

The layer structure of **CuV–11** contains a continuous sheet of linked VO_x polyhedra. The asymmetric unit of **CuV–12** contains six crystallographically different vanadium sites exclusively in tetrahedral geometry. Fluoride ion is not incorporated into both layered structures, even though hydrofluoric acid was used as a mineraliser in the reaction medium.

The 'composition–space' diagram of 2,2'–dipyridylamine system has also been discussed based on the stoichiometry of the initial reactants of two 1–D chain and a layer structures.

The crystal structure of **CuV–13** contains the new 'superoctahedral' $[V_7F_6O_{30}]^{14-}$ anion linked through $[Cu(py)_4]^{2+}$ cations into a 3–D covalent network. Above 30K, it shows short-range antiferromagnetic correlations between the metal centres. The fluorine analysis, elemental analysis, Rietveld refinement, magnetic data, BVS analysis are consistent with the crystallographic data. Crystallisation fields for **CuV–13** and $[Cu(py)_4VOF_4]$ have been determined *via* a 'composition-space' diagram. The crystal structure of **V–8** exhibits a 3–D network and iso–structural to the inverse–weberite structure and exhibits antiferromagnetic ordering.

4.8 Publications

The work in this chapter has resulted in the following publications:

1. **A new hybrid framework material based on a 'superoctahedral' $[V_7O_6F_{30}]^{14-}$ polyanion**, T. Mahenthirarajah and P. Lightfoot, *Chem. Commun.,* **2008***, 1401-1403.

2. **Hydrothermal synthesis of vanadium oxyfluride chains incorporating covalently bound copper coordination complexes**, T. Mahenthirarajah, Y. Li, and P. Lightfoot, *Inorg. Chem.*, **2008**, *47*, 9097.

Table 4.27 A summary of the vanadium oxyfluoride structures in this chapter

Structures	Compound	Overall dimensionality	Space group	Geometry of copper	Geometry of vanadium	Oxidation state of V/Cu	Connecti-vity
1.$[Cu(C_3H_4N_2)_4][VO_2F_2(C_5H_5N)]_2$	**CuV–1**	0D	P2$_1$/n	(4+2) Octahedron	Trigonal bipyramidal	+5/+2	Cu–O–V
2.$[VOF_2(H_2O)(C_6H_7N)_2]$	**V–1**	0D	C2/c	-	Octahedron	+4	-
3.$[VOF_2(H_2O)(C_5H_5N)_2]$	**V–2**	0D	C2/c	-	Octahedron	+4	-
4.$[C_4H_8N_5]_2[Cu(NH_3)_4(H_2O)_2][VOF_4(H_2O)]$	**CuV–2**	0D	P−1	-	Octahedron	+5	-
5.$[V_2O_4F_2(C_{10}H_8N_2)_2]$	**V–3**	0D	C2/c	-	Octahedron	+5	V–O–V
6.$[V_2O_4F_2(C_{12}H_8N_2)_2]$	**V–4**	0D	P−1	-	Octahedron	+5	V–O–V
7.$[V_2O_2F_4(C_6H_7N)_4]$	**V–5**	0D	P2$_1$/c	-	Octahedron	+4	V–F–V
8.$[C_7H_{10}N]_2[V_2O_2F_6(H_2O)_2]$	**V–6**	0D	P−1	-	Octahedron	+4	V–F–V
9.$[C_8H_{12}N]_2[V_2O_2F_6(H_2O)_2]$	**V–7**	0D	P−1	-	Octahedron	+4	V–F–V
10.α-$[C_2H_8N][Cu(C_5H_5N)_4][V_2O_2F_7]$	**CuV–3**	1D	Pbcn	(4+2) Octahedron	Octahedron	+4/+2	Cu–F–V V–F–V
11.β-$[C_2H_8N][Cu(C_5H_5N)_4][V_2O_2F_7]$	**CuV–4**	1D	P−1	(4+2) Octahedron	Octahedron	+4/+2	Cu–F–V V–F–V
12.$[Cu(C_6H_7N)_4][VF_6]$	**CuV–5**	1D	P4/mcc	(4+2) Octahedron	Octahedron	+4/+2	Cu–F–V
13.$[Cu(C_6H_7N)_4][VF_6].9H_2O$	**CuV–6**	1D	P4/mcc	(4+2) Octahedron	Octahedron	+4/+2	Cu–F–V

14.$[C_3H_5N_2]_2[Cu(C_3H_4N_2)_4][V_2O_2F_8]$	**CuV–7**	1D	$P2_1/n$	(4+2) Octahedron	Octahedron	+4/+2	Cu–O–V V–F–V
15.$[Cu(C_5H_5N)_2(C_2H_8N_2)][(VO_3)_2]$	**CuV–8**	1D	$P2_12_12_1$	Square pyramidal	Tetrahedron	+5/+2	Cu–O–V V–O–V
16.$[Cu_2F_2(C_{10}H_{10}N_3)_2][V_2O_7]$	**CuV–9**	1D	P-1	Octahedron	Tetrahedron	+5/+2	Cu–F–Cu Cu–O–V V–O–V
17.$[Cu(C_{10}H_9N_3)]_2[VOF_4]_2$	**CuV–10**	1D	P−1	Square pyramidal	Octahedron	+4/+2	Cu–F–V V–F–V
18.$[Cu(C_{10}H_9N_3)]_2[V_6O_{17}]$	**CuV–11**	2D	P−1	Square pyramidal	Square pyramidal Tetrahedron	+5/+2	Cu–O–V V–O–V
19.$[Cu_3(C_5H_5N)_{12}][V_6O_{18}]$	**CuV–12**	2D	$P2_1/c$	(4+2) Octahedron	Tetrahedron	+5/+2	Cu–O–V V–O–V
20.$[CH_3NH_3]_8[Cu(py)_4]_3[V_7F_6O_{30}]$	**CuV–13**	3D	Pn−3n	(4+2) Octahedron	Octahedron	+4/+2	V–F–V Cu–O–V
21.$VZnF_5(H_2O)_2$	**V–8**	3D	Icmm	Octahedron	Octahedron	+3/+2	V–F–V Zn–F–V

References

1. A. C. Larson and R. B. Von Dreele, *General Structure Analysis System (GSAS)*, Los Alamos National Laboratory Report LAUR, **2004**, 86–748.

2. G. M. Sheldrick, *Acta Crystallogr., Sect. A: Found. Crystallogr.*, 2008, **64**, 112. 20

3. L. J. Farrugia, WinGX, *J. Appl. Crystallogr.*, 1999, **32**, 837.

4. H. Serier, M. Gaudon, A. Demourgues, A. Tressaud, *J. Solid State Chem.*, **2007**, 180, 3485.

5. M. E. Welk, A. J. Norquist, C. L. Stern, K. R. Poeppelmeier, *Inorg. Chem.*, **2000**, 39, 3946.

6. D. W. Aldous, R. J. Goff, J. P. Attfield, P. Lightfoot, *Inorg. Chem.*, **2007**, 46, 1277.

7. D. W. Aldous, *Thesis*, University of St Andrews, 2008.

8. N. F. Stephens, M. Buck, P. Lightfoot, *J. Mater. Chem.*, **2005**, 15, 4298.

9. A. J. Edwards, D. R. Slim, J. E. Guerchais, J. Sala-pala, *J. C. S. Dalton.*, **1977**, 984.

10. D. W. Aldous, N. F. Stephens, P. Lightfoot, *Dalton Trans.*, **2007**, 2271.

11. G. Z. Pausewang, *Anorg. Allg. Chem.*, **1971**, 38, 189.

12. K. Walterson, *Cryst. Struct. Commun.*, **1978**, 7, 507.

13. J. Darriet, E. Bonjour, D. Beltran-Porter, D. Drillon, *J. Magn. Magn. Mater.*, **1984**, 44, 287.

14. S. Becker, B. G. Muller, *Angew. Chem. Int. Ed. Engl.*, **1990**, 29, 406.

15. D. W. Aldous, P. Lightfoot, *Solid State Sci.*, **2009**, 11, 315.

16. P. J. Hagrman, R. C. Finn, J. Zubieta, *J. Solid State Sci.*, **2001**, 3, 745.

17. H. Casellas, A. Pevec, B. Kozlevcar, P. Gamez, J. Reedijk, *Polyhedron*, **2005**, 24, 1549.

18. A. P. Ramirez, *Annu. Rev. Mater. Sci.*, **1994**, 24, 453.

19. K. Kato, E. Takayama, *Acta Crystallogr.*, **1984**, B40, 102.

20. A. K. Cheetham, C. N. R. Rao, R. K. Feller, *Chem. Commun.*, **2006**, 4780.

21. M. ÒKeefe, M. Eddaoudi, H. Li, T. Reineke, O. M. Yaghi, *J. Solid State Chem.*, **2000**, 152, 3.

22. Y. Laligant, J. Pannetier, P. Labbe, G. Ferey, J. Solid State Chem., **1986**, 62, 274.

23. M. Weil, F. Werner, *Monatshefte fur Chemie.*, **2001**, 132, 769.

24. O. Knop, T. S. Cameron, K. Jochem, *J. Solid State Chem.*, **1982**, 43, 213.

25. Y. Laligant, Y. Calage, E. Torres-Tapia, J. M. Greneche, F. Varret, G. Ferey, *J. Magn. Magn. Mater.*, **1986**, 61, 283.

CHAPTER FIVE

Niobium/Molybdenum Oxyfluoride Materials

5.1 Introduction

The structures described in this chapter are categorised into clusters with molybdenum/copper monomers, chains and layers, which are all synthesised solvothermally from niobium or molybdenum and copper containing reaction media with different amines. These materials have been denoted from **CuMo–1** to **CuMo–5** and **CuNb–1** to **CuNb–4** and numbered in the chronological order in which they are discussed in this section. Crystallographic information for these structures is presented in Tables 5.1 and 5.2. The synthetic conditions are given in Appendix–III, along with the elemental analysis including fluorine analysis, using fluoride ion-selective electrode.

The TGA, magnetic measurements and Rietveld refinements which have been carried out on those materials which are obtained as a single phase will be discussed in this section. Bond valence sum calculations are also carried out to confirm the oxidation states of copper, molybdenum and niobium metal centres. Atomic co–ordinates are located in the Appendix–II. Bond angles and hydrogen bonds are all contained in the appropriate CIF file (see enclosed CD).

Samples were characterised by XRD on a Stoe STADI/P diffractometer using transmitting Cu $K_{\alpha 1}$ radiation at 1.5406 Å, with a 2Θ range from 5 to 70°. These data were collected 15 hours to assure the best quality pattern to confirm phase purity for subsequent studies. A Rietveld refinement was performed with the GSAS program suite[1] using the atomic co–ordinates determined by single crystal solution as a starting point. Instrumental parameters (background, zero–point, peak profile coefficients) and unit cell parameters were refined. A close final fit to the observed data was achieved with the structure determined from the single crystal experiment.

Single crystal X–ray diffraction data were collected with a Rigaku Mercury CCD with silicon monochromated Mo $K_{\alpha.}$ The datasets were corrected for absorption via multi-scan

methods. The structure was solved by direct methods and refined by full–matrix least–squares techniques, using the SHELXS, SHELXL[2] and WinGX[3] packages. All non–hydrogen atoms were refined with anisotropic thermal parameters (except where stated). Hydrogen atoms attached to carbon and nitrogen atoms were located at geometrically calculated positions and refined with isotropic thermal parameters, while those attached to oxygen atoms were found, where possible, by Fourier techniques and refined isotropically.

Thermogravimetric analysis (TGA) was carried out on Standard TG 209 instrument from room temperature to 500˚C at a heating rate of 10˚K/min under argon atmosphere.

The fluorine content in the sample was determined by using a fluoride ion–selective electrode[4] as discussed in section 2.3.11 and the analysis included in Appendix III.

Magnetic data of magnetically active materials were measured on a Quantum Design MPMS SQUID. Data were recorded in 5000 Oe field while warming the sample from 2 to 300 K in 4 K steps, following consecutive zero field cooling and field cooling cycles.

The compounds, **CuMo–1** to **CuMo–5** and **CuNb–1** to **CuNb–4** were synthesised in a systematic manner with cyclic amines in the reaction media. All reactions were carried out at 100˚C and 160˚C. CuO and MoO_3 or Nb_2O_5 were initially used to carry out similar reactions to those done previously (see Chapter 4). Once a novel compound was synthesised, then the key factors in the formation of those crystals were investigated by varying the stoichiometry of the reactants based on the 'composition–space' diagram.

Table 5.1 Clusters and 2-D layer

Compound	**CuMo–1**	**CuMo–5**	**CuNb–4**
Molecular formula	$[Cu(C_{12}H_8N_2)(H_2O)_3]$	$[Cu(C_{10}H_8N_2)_2(H_2O)_2]$	$[Cu(C_{10}H_8N_2)_2(H_2O)_2]$
	$[MoO_2F_4].H_2O$	$[MoO_2F_4]$	$[NbOF_5]$
Crystal system	Triclinic	Tetragonal	Tetragonal
Space group	P–1	P 4/ncc	P 4/ncc
a(Å)	7.525(2)	11.243(3)	11.340(4)
b(Å)	9.805(3)	11.243(3)	11.340(4)
c(Å)	12.449(3)	15.773(4)	15.657(5)
α(deg)	101.849(9)		
β(deg)	91.236(7)	1993.9(9)	
γ(deg)	109.858(5)		
V(Å^3)	841.3(4)		2013.3(11)
Z	2	4	4
total/unique reflns	5177/3017	11179/926	12515/1178
ind.reflns>2σ(I)	2207	904	925
Fw	519.76	615.89	615.86
T(˚C)	−180	−180	−180
λ(Å)	0.7107	0.7107	0.7107
ρ_{calcd} (g/cm^3)	2.052	2.05	2.03
R1[I>2σ(I)]	0.082	0.074	0.052
wR2[I>2σ(I)]	0.250	0.266	0.170

Table 5.2 1-D chains

Compound	**CuMo–2**	**CuNb–1**	**CuMo–3**	**CuNb–2**	**CuMo–4**	**CuNb–3**
Molecular formula	$[Cu(C_2H_4N_4)_2]$ $[MoO_2F_4].H_2O$	$[Cu(C_2H_4N_4)_2]$ $[NbOF_5].H_2O$	$[Cu(C_3H_4N_2)_4]$ $[MoO_2F_4]$	$[Cu(C_3H_4N_2)_4]$ $[NbOF_5]$	$[Cu_2F_2(C_{10}H_9N_3)_2]$ $[MoO_2F_4]$	$[Cu_2F_2(C_{10}H_9N_3)_2]$ $[NbOF_5]$
Crystal system	Monoclinic	Monoclinic	Monoclinic	Monoclinic	Monoclinic	Monoclinic
Space group	P2$_1$/n	P2$_1$/n	C2/c	C2/c	C2/m	C2/m
a(Å)	7.163(2)	7.151(2)	31.427(7)	10.310(2)	9.399(4)	9.469(6)
b(Å)	11.810(3)	11.869(3)	12.608(2)	12.941(3)	17.160(6)	17.173(10)
c(Å)	14.438(4)	14.671(4)	16.951(4)	15.038(3)	7.441(3)	7.419(5)
β(deg)	91.99(1)	91.05(1)	120.48(1)	97.79(1)	113.71(1)	112.57(2)
V(Å^3)	1220.6(5)	1245.0(5)	5788.5(2)	1987.9(7)	1098.8(8)	1114.0(12)
Z	4	4	4	4	2	2
total/unique	8275/2495	8504/2593	18046/5203	6756/1967	3487/1044	3853/1184
ind.reflns>2σ(I	2151	1838	4593	1551	930	974
Fw	453.69	453.66	1619.45	539.79	711.44	711.41
T(˚C)	−180	−180	−180	−180	−180	−180
λ(Å)	0.7107	0.7107	0.7107	0.7107	0.7107	0.7107
ρ_{calcd} (g/cm^3)	2.47	2.42	1.86	1.80	2.15	2.12
R1[I>2σ(I)]	0.037	0.044	0.044	0.046	0.045	0.054
wR2[I>2σ(I)]	0.104	0.130	0.163	0.112	0.128	0.186

5.2 Monomers

The crystal structure of $[Cu(C_{12}H_8N_2)(H_2O)_3][MoO_2F_4].H_2O$ (**CuMo–1**) incorporates isolated monomeric units and is discussed in this section.

5.2.1 Discussion

Structure

The crystal structure of **CuMo–1** exhibits two monomeric units. The asymmetric unit contains the well known acentric anion, $[MoO_2F_4]^{2-}$, the novel copper cation, $[Cu(C_{12}H_8N_2)(H_2O)_3]^{2+}$ and a water molecule as shown in Figure 5.1. Molybdenum is present in the +6 oxidation state, and exhibits *intra*–octahedral distortions, and copper is present in the +2 oxidation state with square pyramidal geometry as expected from the colour of the crystal, and further confirmed by BVS analysis (see Table 5.3). A similar polar molybdenum monomer, $[MoO_2F_4]^{2-}$ with characteristic C_2 distortion has been previously reported (see Section 1.1.1).[5]
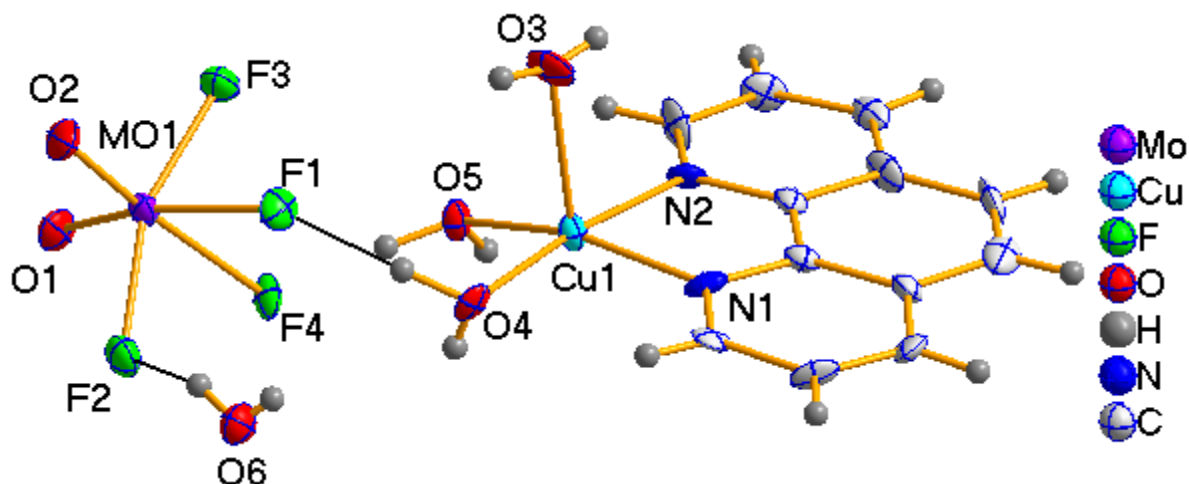
Figure 5.1 The asymmetric unit in **CuMo–1** with hydrogen bonding interactions and ellipsoids at 50% probability.

The copper cation complexes and molybdenum complex anions are arranged alternately on the *bc* plane, and between the monomeric units, phenyl rings coordinated to copper

complexes and water molecules occupy the interstices, as shown in Figure 5.2. Crystal packing is dominated by hydrogen bonding interactions from the coordinated and uncoordinated water molecules to the neighbouring anion motifs. Strong hydrogen bonding interactions exist in the range of D–H…A 1.75–1.96 Å; D…A 2.64–2.74 Å and the weaker interactions are in the range of D–H…A 2.06–2.53 Å; D…A 2.69–3.33 Å).

Bond	Bond Length(Å)	S_{ij}	Bond	Bond Length(Å)	S_{ij}
Mo1–O1	1.709(7)	1.675	Cu1–O3	2.214(8)	0.221
Mo1–O2	1.687(7)	1.780	Cu1–O4	1.972(8)	0.425
Mo1–F1	2.092(6)	0.467	Cu1–O5	1.988(7)	0.406
Mo1–F2	1.955(6)	0.675	Cu1–N1	2.013(8)	0.439
Mo1–F3	1.925(6)	0.732	Cu1–N2	2.010(8)	0.443
Mo1–F4	2.121(5)	0.431			
		ΣMo1=5.76			ΣCu1=1.93

Table 5.3 Selected bond lengths and BVS for **CuMo–1**.
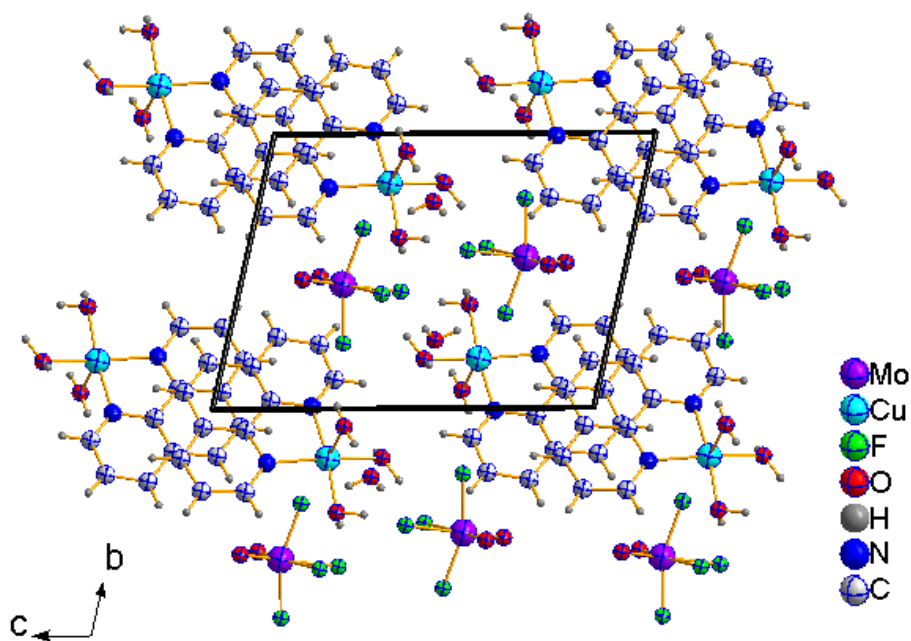
Figure 5.2 Crystal packing in **CuMo–1**

5.3 1-D structures

Hydrothermal synthesis of niobium/molybdenum oxyfluorides with copper coordination complexes produces the novel 1–D chain structures of $[Cu(C_2H_4N_4)_2][MoO_2F_4].H_2O$ (**CuMo–2**), $[Cu(C_2H_4N_4)_2][NbOF_5].H_2O$ (**CuNb–1**), $[Cu(C_3H_4N_2)_4][MoO_2F_4]$ (**CuMo–3**), $[Cu(C_3H_4N_2)_4][NbOF_5]$ (**CuNb–2**), $[Cu_2F_2(C_{10}H_9N_3)_2][MoO_2F_4]$ (**CuMo–4**), and $[Cu_2F_2(C_{10}H_9N_3)_2][NbOF_5]$ (**CuNb–3**); these are discussed in this section.

Rietveld refinements of X–ray powder data were performed in each case using the unit cell dimensions and atomic co–ordinates determined by the single crystal solution as a starting point. Instrumental parameters (background, zero–point, peak profile coefficients) and unit cell parameters were refined. A close final fit to the observed data was achieved, with Rwp=6.26% for **CuMo–2**; Rwp=10.92% for **CuNb–1**; Rwp=4.72% for **CuMo–3**; Rwp=7.81% for **CuNb–2**; Rwp=9.67% for **CuMo–4**; Rwp=10.62% for **CuNb–3** with the structure determined from the single crystal experiment (see Figures 5.3, 5.4, 5.5, 5.6, 5.7 and 5.8).
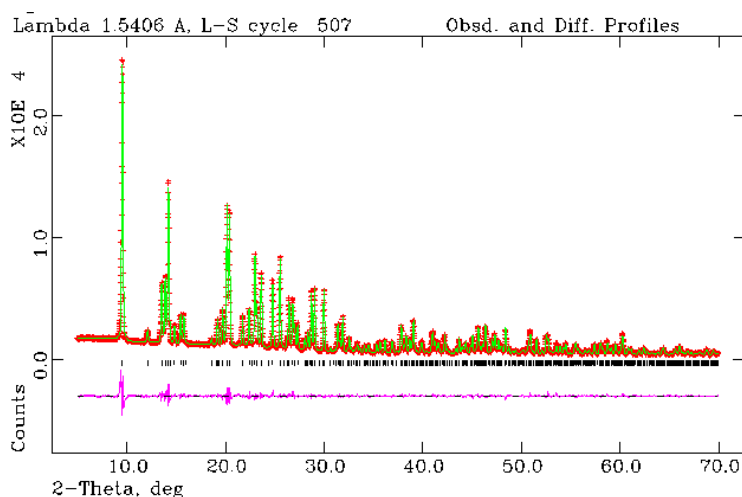
Figure 5.3 The Rietveld refinement of **CuMo–2**. Observed data red, calculated profile green, difference profile purple.
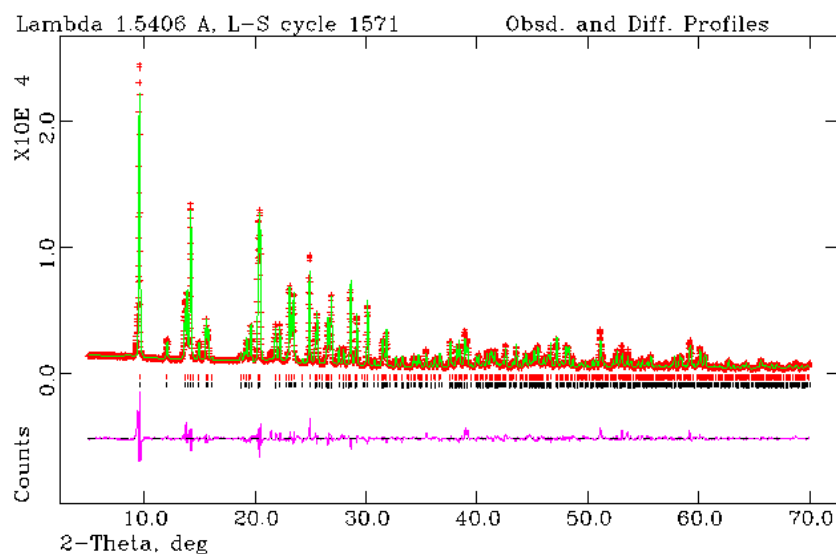
Figure 5.4 The Rietveld refinement of **CuNb–1**. Observed data red, calculated profile green, difference profile purple.
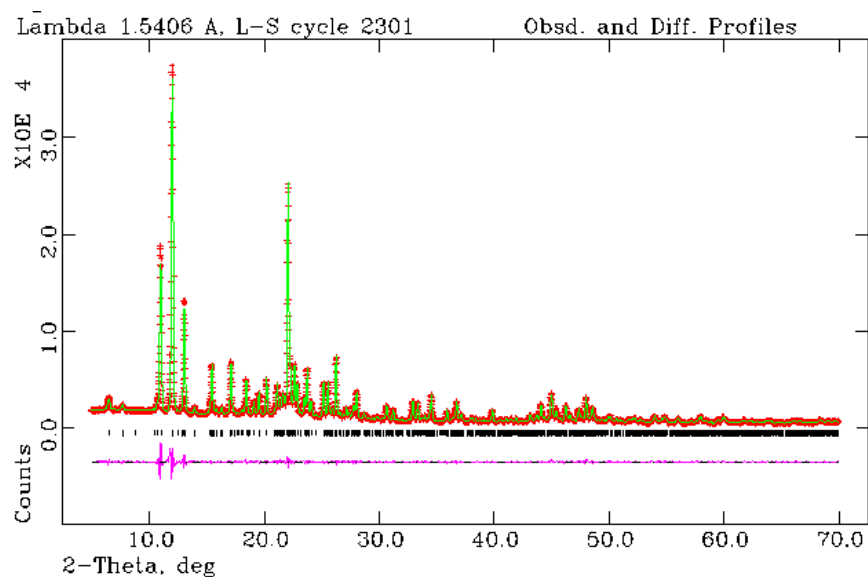
Figure 5.5 The Rietveld refinement of **CuMo–3**. Observed data red, calculated profile green, difference profile purple.
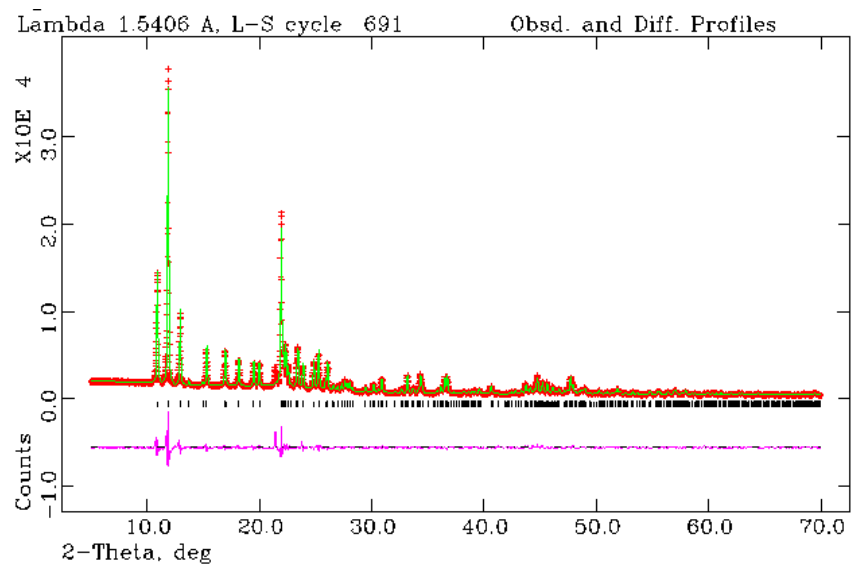
Figure 5.6 The Rietveld refinement of **CuNb–2**. Observed data red, calculated profile green, difference profile purple.
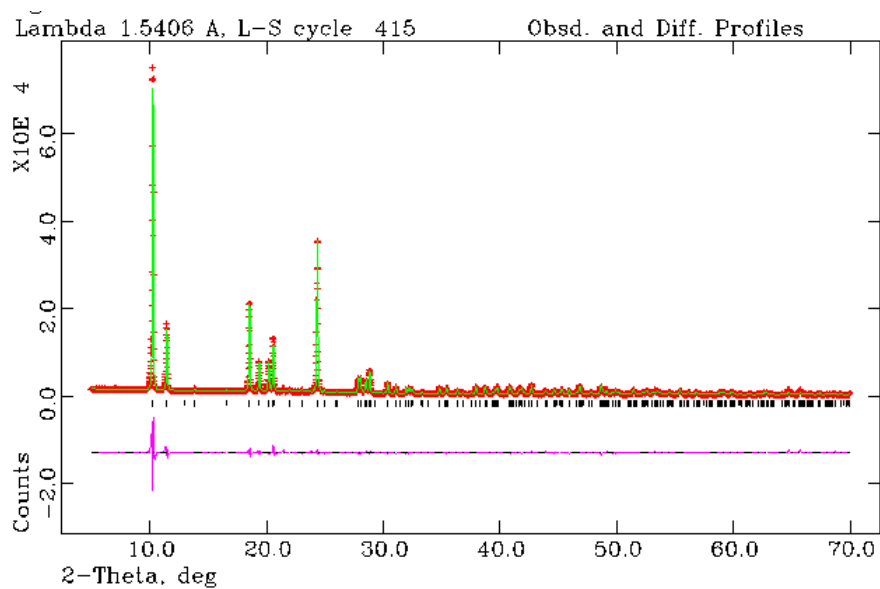
Figure 5.7 The Rietveld refinement of **CuMo–4**. Observed data red, calculated profile green, difference profile purple.
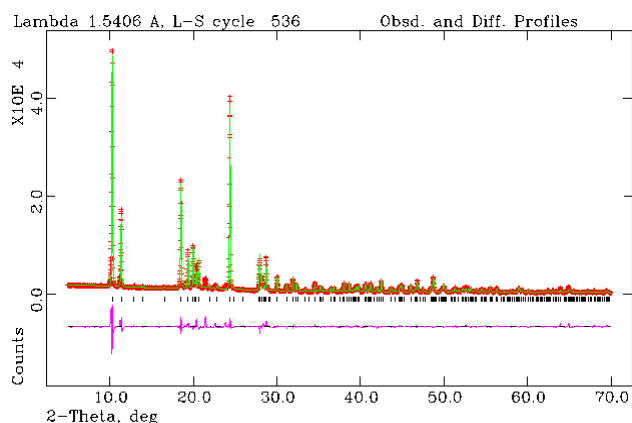
Figure 5.8 The Rietveld refinement of **CuNb–3**. Observed data red, calculated profile green, difference profile purple.

5.3.1 Discussion

Structure

CuMo–2 and **CuNb–1** are isomorphous. When checking the crystallinity of the material under an optical microscope and SEM, they appeared to have different morphology. However, it is not necessary for this to be similar for isomorphous compounds. The SEM image of the **CuNb–1** shows well separated fine needle–type crystals (see Figure 5.10). EDX analysis for structure **CuMo–2**, confirms the presence of all the elements within the block like crystals (see Figure 5.9).

The crystal structures of **CuMo–2** and **CuNb–1** contain an infinite 1–D chain (see Figure 5.13) motif running parallel to the *a* axis, which is constructed by corner-sharing octahedral copper complexes covalently bound through fluoride ligands to each other. The asymmetric unit contains two crystallographically independent copper sites, both lying on an inversion centre (see Figure 5.11). Further acentric anions $[MoO_2F_4]^{2-}$ and $[NbOF_5]^{2-}$ in **CuMo–2** and **CuNb–1** respectively connect to this copper chain through F and O/F ligands. **CuMo–2** is the first hybrid crystal structure containing exclusively – Cu–F–Cu– connectivity throughout the chain. The divalent copper atoms are Jahn–Teller

168

active, so it is not surprising to find that the coordination environment around the copper consists of four equatorial 1–amino–1,3,4–triazole ligands and longer axial bonds to fluoride ligands which connect *trans* directing to another neighbouring copper complex and the acentric anion unit. The μ–coordination of the amino ligand, bridging neighbouring copper cations acts to ʻzip–upʼ the copper fluoride chain tightly, leading to a bridging Cu–F(O)–Cu angle of near 90° and a Cu–Cu distance of 3.58 Å. The anion unit of crystal structure **CuMo–2** exhibits *intra*–octahedral distortions of C_2 type. However, $[NbOF_5]^{2-}$ adopts regular octahedral geometry with disorder of the O/F atoms at the bridging site and the site *trans* to this. The acentric anion motifs act as "decoration" to both the sides of copper fluoride chain, rather than being directly involved in chain formation itself. The oxidation states of the metal centres are confirmed by BVS analysis (see Table 5.4 and 5.5).

There are water molecules in between the chains forming hydrogen bonding interactions. *Intra*–chain hydrogen bonds occur from a water molecule to two neighbouring anion motifs *via* nucleophilic fluoride and oxide ligands in a chain (for **CuMo–2**: O3–H3A…F3 2.18 Å; O3…F3 2.83 Å, O3–H3B…O2 2.32 Å; O3…O2 2.88 Å and for **CuNb–1**: O1–H10A…F2 2.25 Å; O1…F2 3.00 Å, O1–H10B…F4 1.92 Å; O1…F4 2.81 Å). The *inter*–chain hydrogen bonding occurs from the amino ligand of a copper complex of a chain to the nearest anion unit of the neighbouring chain (for **CuMo–2**: N8–H8B…F1 2.49 Å; N8…F1 2.93 Å and for **CuNb–1**: N8–H8A…F1 2.43 Å; N8…F1 2.91 Å) (see Figure 5.12).
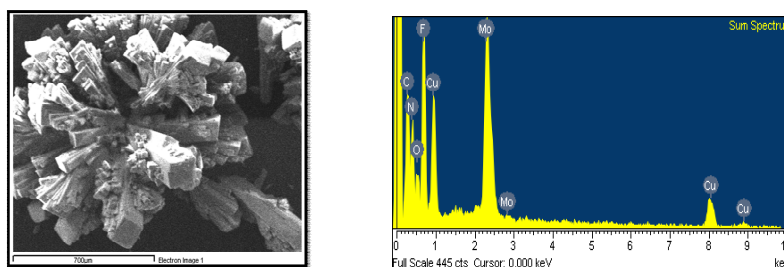
Figure 5.9 SEM image and EDX chart for **CuMo–2**, showing the definite peak presence of expected elements according to single crystal X–ray data.
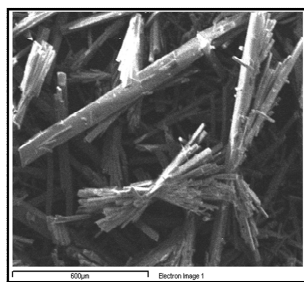
Figure 5.10 SEM image of **CuNb–1**.
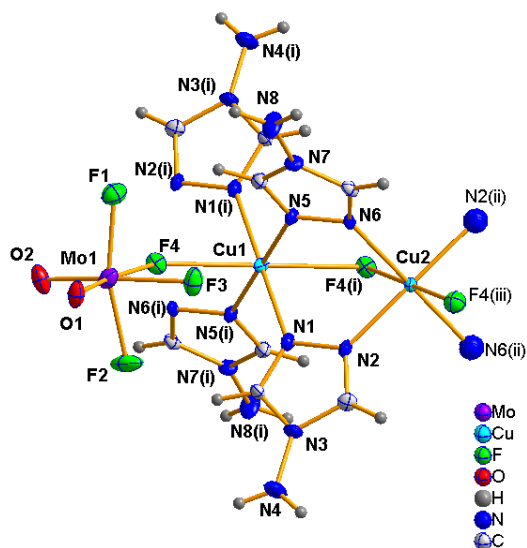
Figure 5.11. The building unit in **CuMo–2** with ellipsoids at 50% probability. Symmetry operators (i) –x,–y,–z; (ii) 1–x,–y,–z; (iii) 1+x,y,z.
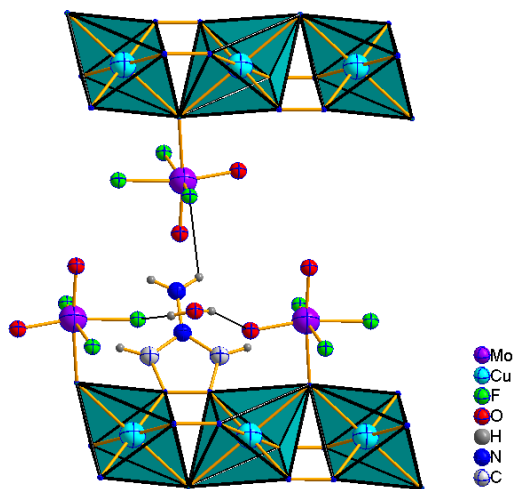
Figure 5.12 *Inter*–chain and *intra*–chain hydrogen bonding interactions in **CuMo–2**

Bond	Bond Length(Å)	S_{ij}
Mo1–O1	1.728(3)	1.624
Mo1–O2	1.755(3)	1.507
Mo1–F1	1.864(3)	0.864
Mo1–F2	1.951(3)	0.683
Mo1–F3	2.013(3)	0.578
Mo1–F4	2.078(2)	0.485
		ΣMo1=5.74

Bond	Bond Length(Å)	S_{ij}	Bond	Bond Length(Å)	S_{ij}
Cu1–F4 x 2	2.412(2)	0.110	Cu2–F4 x 2	2.432(2)	0.104
Cu1–N1 x 2	2.001(3)	0.525	Cu2–N2 x 2	1.991(3)	0.540
Cu1–N5 x 2	1.974(3)	0.566	Cu2–N6 x 2	2.016(3)	0.504
		ΣCu1=2.40			ΣCu2=2.30

Table 5.4 Selected bond lengths and BVS for **CuMo–2**

Bond	Bond Length(Å)	S_{ij}
Nb1–F1	1.934(4)	0.841
Nb1–F2	1.937(4)	0.834
Nb1–F3	1.921(4)	0.871
Nb1–F4	1.906(4)	0.908
Nb1–(F/O)5	1.923(3)	0.923
Nb1–(F/O)6	1.928(3)	0.910
		ΣNb1=5.29

Bond	Bond Length(Å)	S_{ij}	Bond	Bond Length(Å)	S_{ij}
Cu1–(F/O)6 x2	2.483(4)	0.102	Cu2–(F/O)6 x2	2.471(4)	0.105
Cu1–N1 x 2	2.005(4)	0.520	Cu2–N2 x 2	2.002(4)	0.525
Cu1–N5 x 2	1.975(4)	0.563	Cu2–N6 x 2	2.022(4)	0.497
		ΣCu1=2.27			ΣCu2=2.25

Table 5.5 Selected bond lengths and BVS for **CuNb–1**.
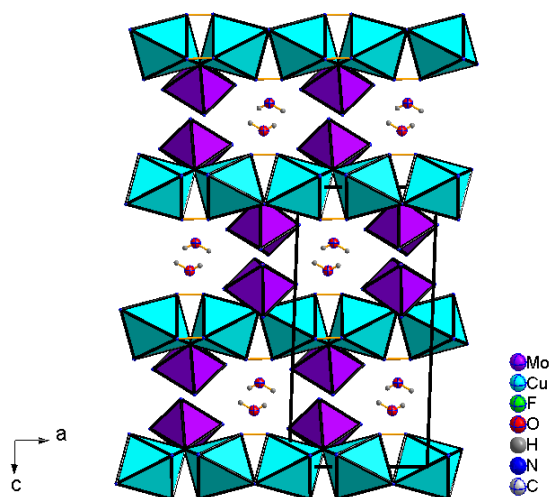
Figure 5.13. Unit cell packing in **CuMo–2**. Hydrogen, carbon atoms are not included for clarity.

Zubieta and co–workers synthesised $[\{Cu_2(triazolate)_2(H_2O)_2\}Mo_4O_{13}]$ using a hydrothermal technique.[6] The structure contains a 1–D anionic chain linked to the 3–D copper cation framework. The copper framework contains a similar 'zip–up' connectivity with a N–donor ligand, forming a honeycomb network on the *ab* plane. However, the copper network is extended through triazolate ligands instead of anionic ligands.

5.3.2 (Nb$_2$O$_5$/MoO$_3$, CuO)/HF/1–amino–1,3,4–triazole System

The 'composition–space' diagram for the (Nb$_2$O$_5$/MoO$_3$, CuO)/HF/1–amino–1,3,4–triazole reactant system shows two distinct regions (see Figure 5.14). Crystals of **CuMo–2** and **CuNb–1** were grown in the concentrated HF region. At lower concentration of hydrofluoric acid, the mineraliser is not enough to dissolve the metal oxides, forming poorly crystalline and uncharacterised powder. Changing the ratio of hydrofluoric acid and water content, while keeping other reactants and conditions constant, was also carried out, but only **CuMo–2** and **CuNb–1** were formed. A pure phase is synthesised based on this experimental procedure, as discussed in Appendix–III. The crystallisation field indicates the major phase, which contains a small amount of unreacted metal oxides.

172
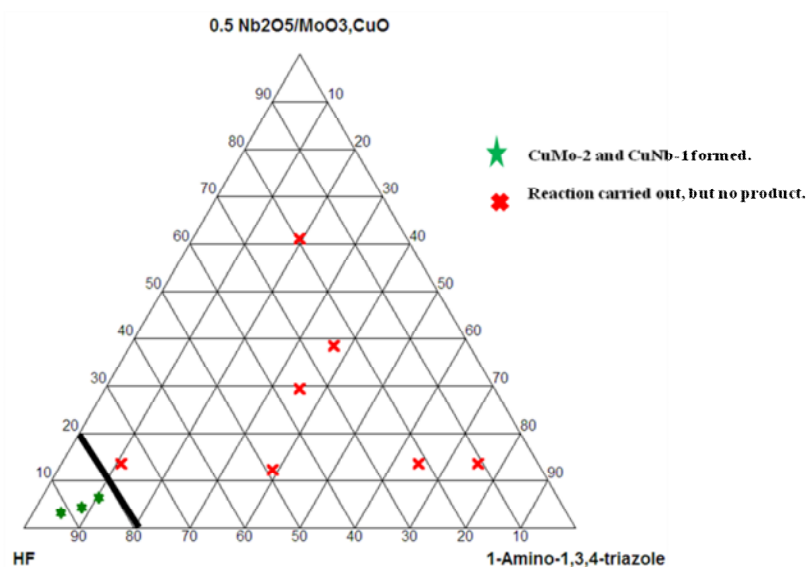
Figure 5.14 'Composition–space' diagram of $(Nb_2O_5/MoO_3,CuO)/HF/1$–amino–1,3,4–triazole.

Heated under Ar, **CuMo–2** undergoes a weight loss occurring continuously between 100˚C and 375˚C (see Figure 5.15). This is thought to be owing to the loss of organic template as well as water from the material. The pure phase shows a weight loss of 41%, which corresponds to the removal of 1–amino–1,3,4–triazole (calculated composition is 37.5%) and water (calculated composition is 3.5%). The final product at 500˚C is largely amorphous.
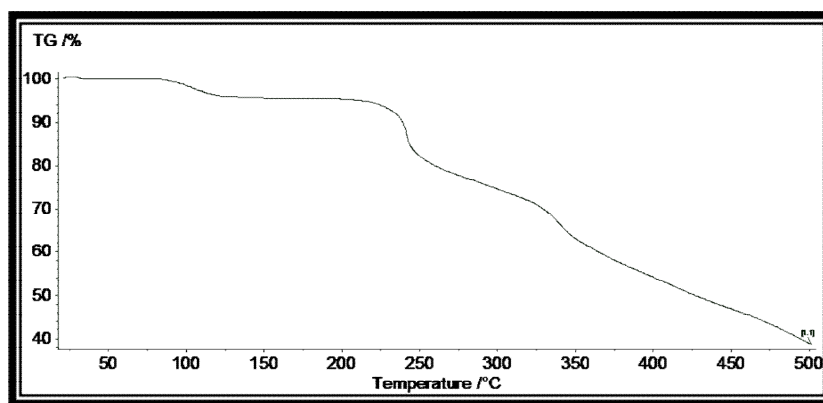
Figure 5.15 TGA of **CuMo–2**

Heated under Ar, **CuNb–1** undergoes a weight loss occurring continuously between 100˚C and 375˚C (see Figure 5.16). This is thought to be owing to the loss of organic template as well as water from the material. The pure phase shows a weight loss of 41%, which corresponds to the removal of 1–amino–1,3,4–triazole (calculated composition is 37%) and water (calculated composition is 4%). The final product at 500˚C is largely amorphous.
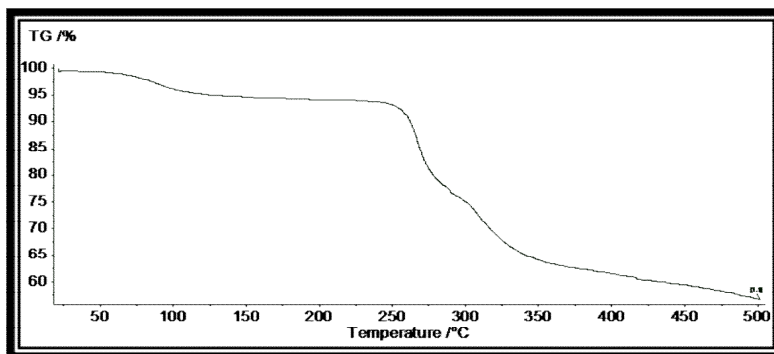
Figure 5.16 TGA of **CuNb–1**
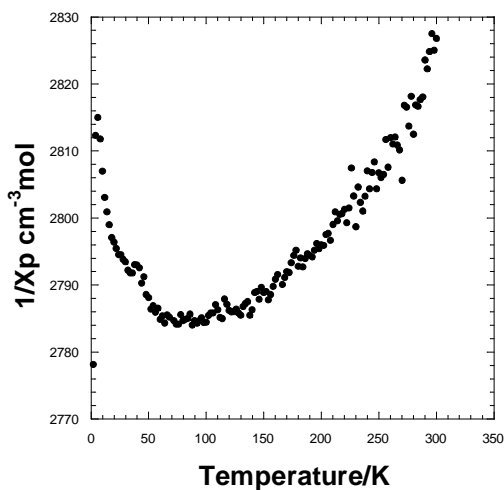
Figure 5.17 χ_p^{-1} vs. T

The magnetic data of **CuMo–2** and **CuNb–1** are quite unusual compared to the crystallographic evidence. The only explanation is that the sample had degraded during the measurement. The crystal structure of $CuF_2(H_2O)_2(pyz)$ exhibits a 1–D chain linked

through Cu–(pyz)–Cu, with the F⁻ ligands being 'equatorial' and perpendicular to the chain direction.[7] These ligands are involved in propagating a very weak 2–D super-exchange interaction *via* hydrogen bonding. Therefore the Cu–F/O–Cu connectivity of **CuMo–2** and **CuNb–1** might suggest interesting magnetic interactions. The Cu^{2+} geometry, however, is such that the half-occupied $d_{x^2-y^2}$ orbital will be perpendicular to the chain direction, and interactions are therefore expected to be weak. Though we repeated the experiment twice, a very weak magnetic signal, with significant background noise was observed, and it was difficult to extract magnetic information for **CuMo–2** or **CuNb–1** (see Figure 5.17). It has been previously reported[8], these the compound of $[Cu(py)_4VOF_4][Cu(py)_4(H_2O)VOF_4].H_2O$ also proved impossible to collect accurate susceptibility values owing to loss of bound water during the data collection.

The compounds **CuMo–3** and **CuNb–2** are iso–structural to $[Cu(C_5H_5N)_4][NbOF_5]$,[9] the only difference being the organic ligand. However, there is no evidence of prior existence of a similar analogous Mo system. The 1–D linear chain is constructed from a *trans* directing copper complex and the acentric anion unit in an alternate manner. The long axial sites of the "(4+2)" octahedral copper cation are occupied by disordered O/F ligands and the four equatorial sites belong to pyrazole ligands. The asymmetric unit of the crystal structure **CuMo–3** contains two crystallographically different copper and molybdenum sites, whereas the crystal structure of **CuNb–2** contains only one niobium and copper site (see Figure 5.18). The alignment of the short Mo–O bond in $[Mo(1)O_2F_4]$ and disordered O/F around the two independent Mo sites causes the cell dimensions of crystal structure **CuMo–3** to be three times bigger along the *a* axis compared to crystal structure, **CuNb–2**. The $[Mo(1)O_2F_4]$ unit exhibits a short Mo1–O bond, while the long *trans* Mo1–F bond is supported by hydrogen bond donors from the pyrazole ligand of the neighbouring copper complex within the chain. However, O/F disorder is observed in the $[Mo(2)O_2F_4]$ anion, the oxide and fluoride ligands are disordered ½ each over the bridging O/F site and the remaining population of terminal O/F site was 0.5 with two symmetrically generated orientations, disordered with ¼ O and ¾ F. The niobium system

also exhibits O/F disorder; the bridging O/F site is disordered ½ each and the terminal ligands remain as fluorides. As has been observed in $[Cu(C_5H_5N)_4][NbOF_5]$ the nucleophilic oxide and fluoride ligands bridge to copper cations forming an alternating cation and anion chain.[9] The oxidation states of the metal centres confirmed by BVS analysis (see Table 5.6 and Table 5.7).

The pyrazole moieties form *intra*-chain hydrogen bonds with contacts in the range N–H… F: 1.88–2.64 Å and N…F 2.74–3.11 Å for crystal structure **CuMo–3** and N–H… F: 2.08–2.55 Å and N…F 2.92–3.12 Å for crystal structure **CuNb–2** (see Figure 5.18). The linear chains align in the *ab* plane and are separated by *c*/2, with neighbouring chains along *c* running in the [110] and [−110] directions, respectively (see Figure 5.19). The *inter*–chain region are filled by pyrazole rings coordinated to the Jahn–Teller distorted copper (II) complex.
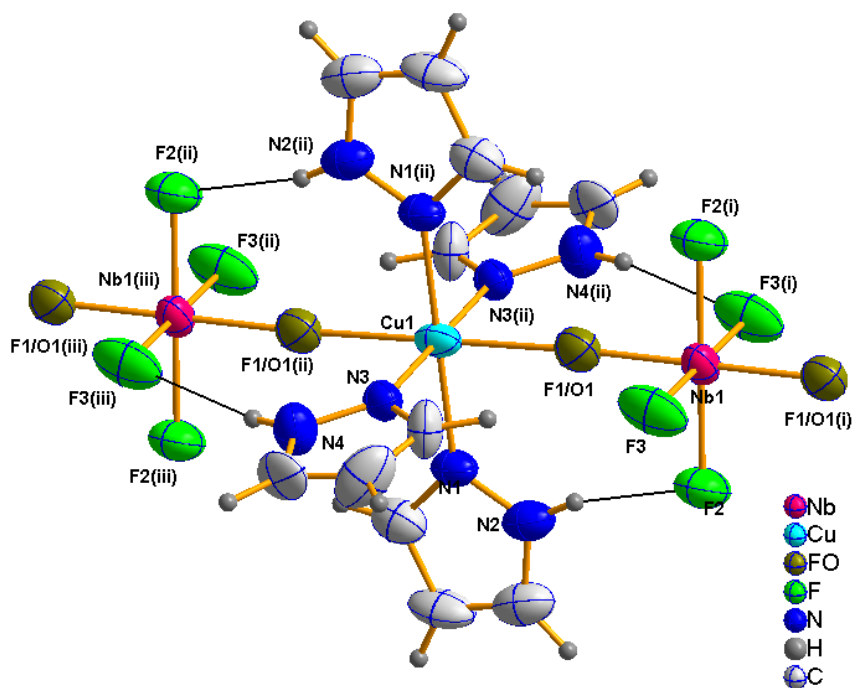
Figure 5.18. The building unit in **CuNb–2** with ellipsoids at 50% probability. Symmetry operators (i) –x,1−y,−z; (ii) −½−x,3/2−y,−z; (iii) −½+x,½+y,z and *intra*–chain hydrogen bonding interactions.

Bond	Bond Length(Å)	S_{ij}	Bond	Bond Length(Å)	S_{ij}
Mo1–O1	1.679(3)	1.854	Cu1–(F/O)4	2.216(3)	0.186
Mo1–F1	1.911(3)	0.761	Cu1–(F/O)8	2.289(3)	0.153
Mo1–F2	2.122(3)	0.431	Cu1–N1	2.007(3)	0.518
Mo1–F3	1.910(3)	0.764	Cu1–N2	2.017(3)	0.503
Mo1–(F/O)4	1.891(3)	1.044	Cu1–N3	2.020(4)	0.499
Mo1–(F/O)5	1.892(3)	1.041	Cu1–N4	2.020(4)	0.499
		ΣMo1=5.90			ΣCu1=2.36

Bond	Bond Length(Å)	S_{ij}	Bond	Bond Length(Å)	S_{ij}
Mo2–(F/O)6x2	1.880(3)	1.075	Cu2–(F/O)5x2	2.244(3)	0.173
Mo2–(F/O)7x2	1.891(3)	1.043	Cu2–N5x2	2.023(4)	0.495
Mo2–(F/O)8x2	1.899(3)	0.787	Cu2–N6x2	2.008(4)	0.516
		ΣMo2=5.71			ΣCu2=2.37

Table 5.6 Selected bond lengths and BVS for **CuMo–3**.

Bond	Bond Length(Å)	S_{ij}	Bond	Bond Length(Å)	S_{ij}
Nb1–(F/O)1x2	1.923(3)	0.924	Cu1–(F/O)1x2	2.216(3)	0.212
Nb1–F2x2	1.928(3)	0.854	Cu1–N1x2	2.027(4)	0.490
Nb1–F3x2	1.921(4)	0.858	Cu1–N3x2	2.038(3)	0.476
		ΣNb1=5.27			ΣCu1=2.36

Table 5.7 Selected bond lengths and BVS for **CuNb–2**.
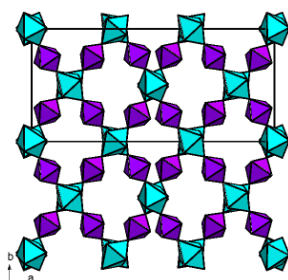
Figure 5.19. Crystal packing in **CuMo–3**. Hydrogen, carbon atoms have not been shown for clarity.

5.3.3 (Nb_2O_5/MoO_3, CuO)/HF/ Pyrazole System

Three distinct regions are observed in the 'composition–space' diagram of the (Nb_2O_5/MoO_3, CuO)/ HF/ pyrazole reactant system (see Figure 5.20). In the high HF concentration region, all the components remain in a blue colour clear solution. In the high metal oxide mole fractional region occur only unreacted metal oxides unsuitable for single crystal diffraction. The crystallization field contains well crystalline deep blue crystals of **CuMo–3** and **CuNb–2** with small amounts of unreacted metal oxides. Changing the ratio of hydrofluoric acid and water content, while keeping the other reactants and conditions as constant, was also carried out, but only **CuMo–3** and **CuNb–2** were formed. The pure phase was synthesised based on the experimental procedure, as discussed in Appendix–III.
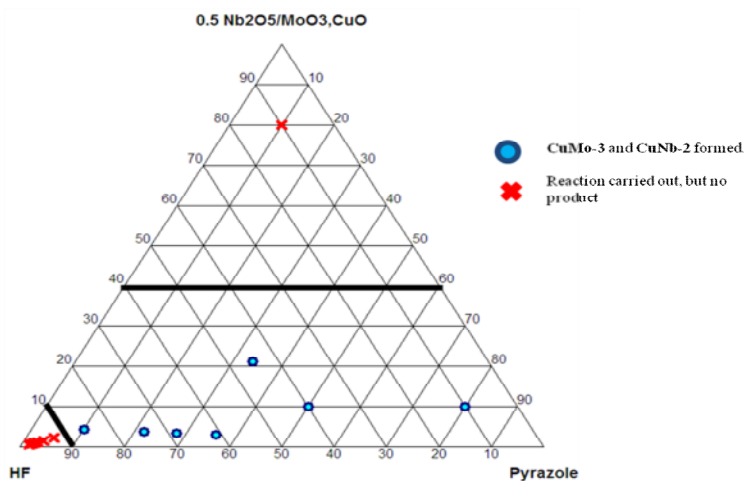
Figure 5.20 'Composition–space' diagram of (Nb_2O_5/MoO_3,CuO)/HF/pyrazole.

Heated under Ar, **CuMo–3** undergoes a weight loss occurring continuously between 200˚C and 400˚C (see Figure 5.21). This is thought to be owing to the loss of organic template from the material. The pure phase shows a weight loss of 50%, which corresponds to the removal of pyrazole (calculated composition is 50.4%). The final product at 500˚C is largely amorphous.
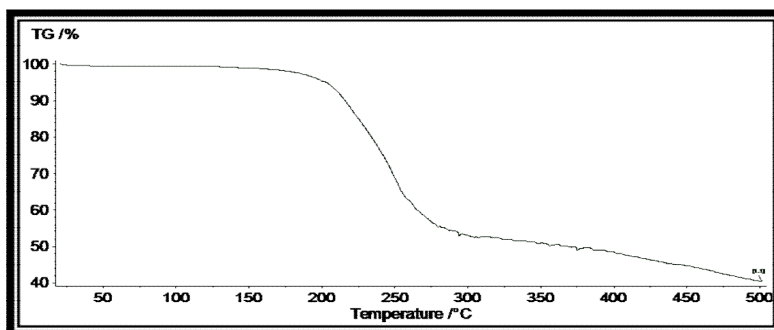
Figure 5.21 TGA of **CuMo–3**

Heated under Ar, **CuNb–2** undergoes a weight loss occurring continuously between 200˚C and 400˚C (see Figure 5.22). This is thought to be owing to the loss of organic template from the material. The pure phase shows a weight loss of 50%, which corresponds to the removal of pyrazole (calculated composition is 50.6%). The final product at 500˚C is largely amorphous.
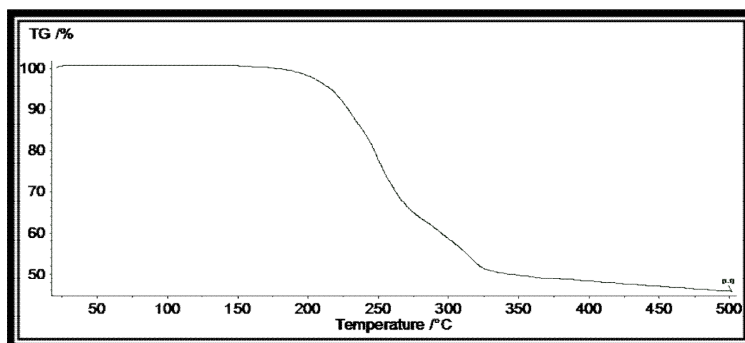
Figure 5.22 TGA of **CuNb–2**

The Magnetic susceptibility data for **CuMo–3** fits very well to a Curie–Weiss law in the range of 2-150 K. The linear plot of $1/\chi_p$ versus T suggests paramagnetic interactions with a small positive Weiss constant (θ_{esd}=+0.77 K) (see Figure 5.23). The spin only experimental value of μ_{eff} =1.78 µB is close to the ideal value of 1.73 µB for spin ½ Cu^{2+}. In the linear chain, the copper cations are well separated by diamagnetic Mo^{6+}.
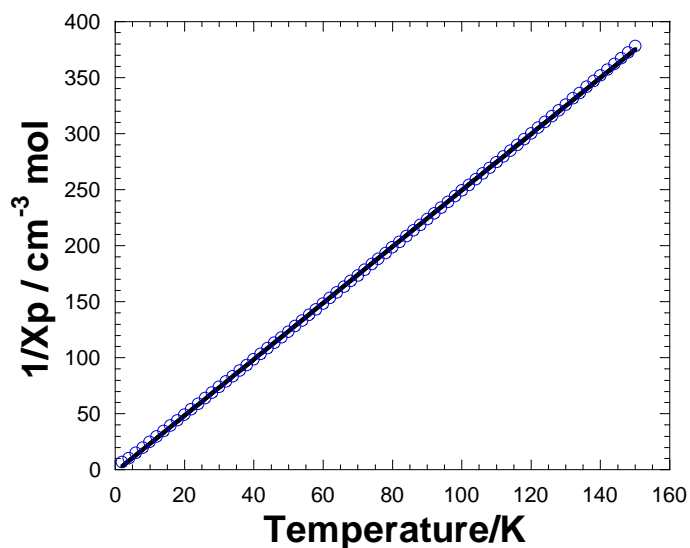
Figure 5.23 $1/\chi_p$ versus T for **CuMo–3**

Between 2-300 K, the magnetic susceptibility for **CuNb–2** obeys a Curie–Weiss law, with no evidence of long–range magnetic ordering. A fit to the $1/\chi_p$ versus T plot reveals paramagnetic interactions with a small negative Weiss constant ($\theta_{esd}=-0.58$ K) (see Figure 5.24). The experimental value of $\mu_{eff}=1.84$ µB, obtained from the Curie-Weiss plot agrees with the ideal value 1.73 µB of non–interacting isolated spin ½ centres, Cu^{2+} per formula unit.
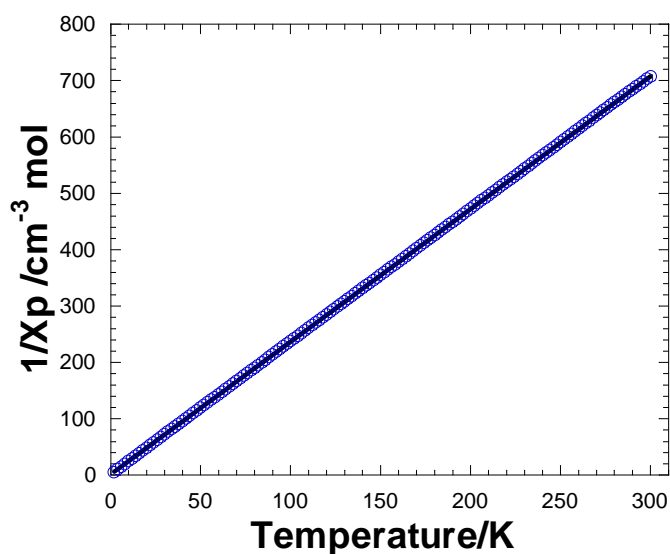
Figure 5.24 $1/\chi_p$ versus T for **CuNb–2**

The crystal structures of **CuMo–4** and **CuNb–3** contain 1–D infinite chains extending along the *c* axis with alternate dimeric copper cations and acentric anions (see Figure 5.27). A similar cation unit has been observed in $[Cu_2F_2(C_{10}H_{10}N_3)_2][V_2O_7]$ (see section 4.4). Other research groups have previously reported similar cations.[10,11,12] However, 2,2'–dipyridylamine did not protonate in **CuMo–4** and **CuNb–3** due to the low concentration of HF acid used in the reaction medium which is only enough to dissolve metal oxides. Each dimeric cation complex $[Cu_2F_2(C_{10}H_2N_3)_2]^{2+}$ contains edge–sharing octahedral copper centres bridged through fluoride ligands at equatorial sites, while the outer sites are occupied by the bidentate dipyridylamine ligand, as shown in Figure 5.25. The long axial sites exhibit O/F disorder. The $[MoO_2F_4]^{2-}$ anion exhibits disorder in the equatorial bridging site to copper as ½ O and ½ F while the terminal ligands remain as fluorides according to the stoichiometry and *trans* configuration. However, the $[NbOF_5]^{2-}$ anion exhibits similar orientational disorder with ¼ O and ¾ F in the bridging sites to reflect its stoichiometry and *trans* configuration. Bond angles and bond distances in the dinuclear copper complex are comparable to $(CH_3OH)_2[Cu_2F_2(C_{10}H_9N_3)_2][SiF_6]$. The bridging Cu1–F4–Cu1 angle is 100.96(2)°, F4–Cu1–F4 angle is 79.04(1)° and the Cu–Cu distance is 2.983(2) Å in **CuMo–4**; for **CuNb–3**: the bridging Cu1–F4–Cu1 angle is 101.30(3)°, F4–Cu1–F4 angle is 78.70(2)° and the Cu–Cu distance is 3.012(2) Å; for $(CH_3OH)_2[Cu_2F_2(C_{10}H_9N_3)_2][SiF_6]$: the bridging Cu1–F3–Cu1 angle is 99.85(8)°, F3–Cu1–F3 angle is 80.15(8)° and the Cu–Cu distance is 2.950 Å The oxidation states of the metal centres are confirmed by BVS analysis (see Table 5.8 and Table 5.9).

Crystal packing is dominated by hydrogen bonds from the 2,2'–dipyridylamine to the anion of a neighbouring chain, leading to supramolecular 3–D network interactions (see Figure 5.26). (For crystal structure in **CuMo–4** N2–H2A…(F/O)1 2.33 Å; N2…(F/O)1 2.86 Å, N2–H2A…(F/O)2 2.22 Å; N2…(F/O)2 2.91 Å and For crystal structure **CuNb–3** N2–H2A…(F/O)2 2.24 Å; N2…(F/O)2 2.79 Å, N2–H2A…(F/O)3 2.26 Å; N2…(F/O)3 3.10 Å).
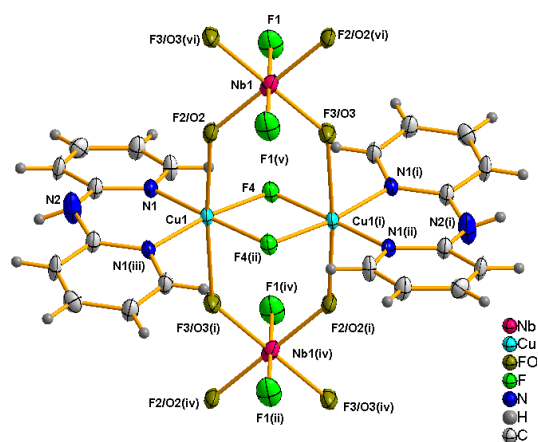
Figure 5.25 The building unit in **CuNb–3** with ellipsoids at 50% probability. Symmetry operators (i) –x,y,–z; (ii) –x,–y,–z; (iii) x,–y,z; (iv) x,y,–1+z; (v) –x,–y,1–z; (vi) –x,y,1–z.
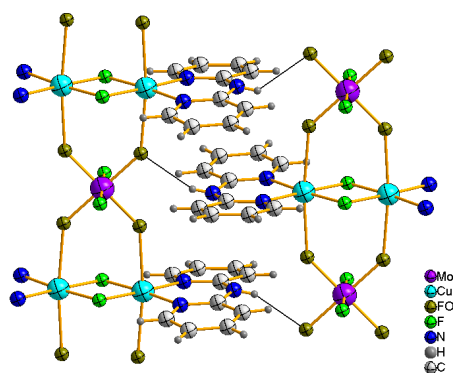
Figure 5.26 *Inter*–chain hydrogen bonding interactions in **CuMo–4**

Bond	Bond Length(Å)	S_{ij}	Bond	Bond Length(Å)	S_{ij}
Mo1–(F/O)1x2	1.897(4)	1.029	Cu1–(F/O)1	2.386(5)	0.148
Mo1–(F/O)2x2	1.877(4)	1.084	Cu1–(F/O)2	2.410(4)	0.110
Mo1–F3x2	1.896(4)	0.793	Cu1–F4x2	1.934(3)	0.399
			Cu1–N1x2	1.989(4)	0.469
		ΣMo1=5.81			ΣCu1=1.99

Table 5.8 Selected bond lengths and BVS for **CuMo–4**.

Bond	Bond Length(Å)	S_{ij}	Bond	Bond Length(Å)	S_{ij}
Nb1–F1x2	1.921(5)	0.870	Cu1–F4x2	1.948(3)	0.385
Nb1–(F/O)2x2	1.940(4)	0.854	Cu1–(F/O)2	2.333(5)	0.219
Nb1–(F/O)3x2	1.926(4)	0.887	Cu1–(F/O)3	2.426(5)	0.112
			Cu1–N1x2	1.992(5)	0.465
		ΣNb1=5.22			ΣCu1=2.03

Table 5.9 Selected bond lengths and BVS for **CuNb–3**.
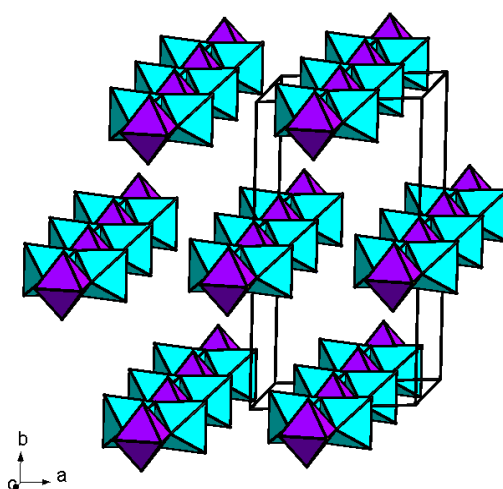
Figure 5.27. Unit cell packing in **CuMo–4**. Hydrogen, carbon atoms not shown for clarity.

5.3.4 (Nb₂O₅/MoO₃,CuO)/HF/2,2'–dipyridylamine System

The crystal structures of **CuMo–4** and **CuNb–3** are formed only when just enough HF acid is present in the reaction medium. Therefore, the low HF concentration was maintained as constant with the (Nb₂O₅/MoO₃,CuO)/HF/2,2'–dipyridylamine reactant system based on a 'composition–space' diagram (see Figure 5.28). There are two distinguishable regions in the diagram; the higher (Nb₂O₅/MoO₃) mole fractional region produces poorly crystalline solids with unreacted oxides and the higher mole fractional region of CuO and 2,2'–dipyridylamine produces the single crystals of **CuMo–4** and

CuNb–3. The pure phase was synthesised based on the experimental procedure, as discussed in Appendix–III.
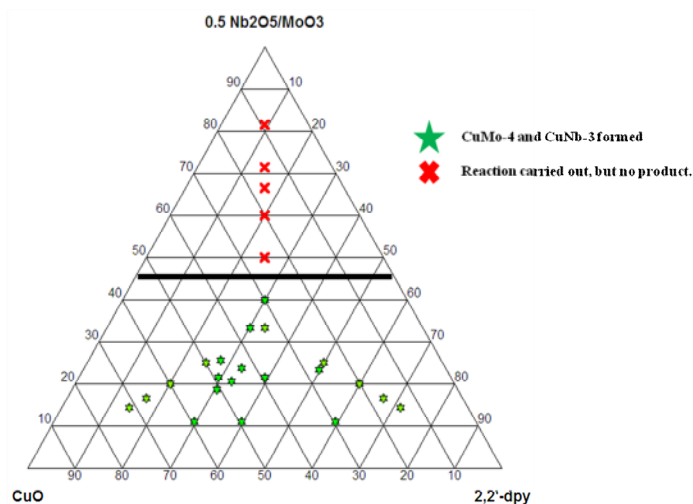
Figure 5.28 'Composition–space' diagram of $(Nb_2O_5/MoO_3)/CuO/2,2'$–dipyridylamine.

Heated under Ar, **CuMo–4** undergoes a weight loss occurring continuously from 250˚C onwards (see Figure 5.29). This is thought to be owing to the loss of organic template from the material. The pure phase shows a weight loss of 48%, which corresponds to the removal of 2,2'–dipyridylamine (calculated composition is 48.1%). The final product at 500˚C is largely amorphous.
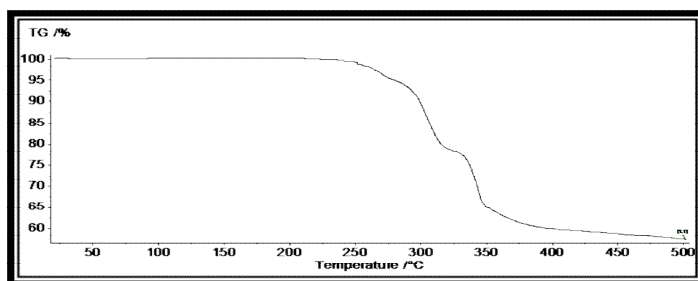
Figure 5.29 TGA of **CuMo–4**

Heated under Ar **CuNb–3** undergoes a weight loss occurring continuously from 250˚C onwards (see Figure 5.30). This is thought to be owing to the loss of organic template

from the material. The pure phase shows a weight loss of 48%, which corresponds to the removal of 2,2'–dipyridylamine (calculated composition is 48.2%). The final product at 500°C is largely amorphous.
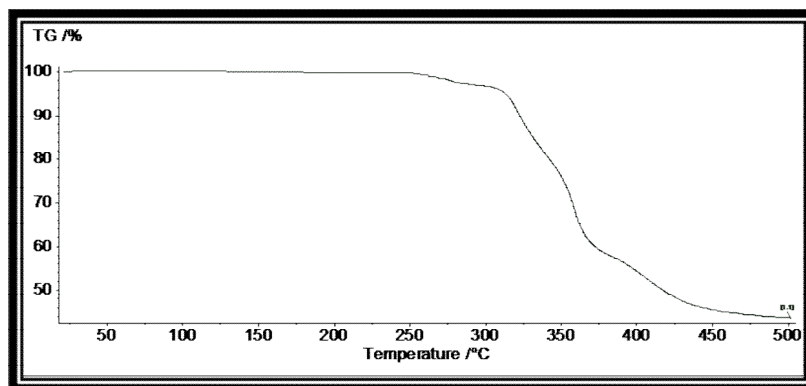
Figure 5.30 TGA of **CuNb–3**

5.4 Layers

The crystal structures of $[Cu(C_{10}H_8N_2)_2(H_2O)_2][MoO_2F_4]$ (**CuMo–5**) and $[Cu(C_{10}H_8N_2)_2(H_2O)_2][NbOF_5]$ (**CuNb–4**) exhibit 2–D layer structures and are discussed in this section.

Rietveld refinements of X–ray powder data were performed (see Figures 5.31 and 5.32) using the unit cell dimension and the atomic co–ordinates determined by the single crystal solution as a starting point. Instrumental parameters (background, zero–point, peak profile coefficients) and unit cell parameters were refined. A close final fit to the observed data was achieved, with Rwp=11.76% for **CuMo–5**; Rwp=7.77% for **CuNb–4**.
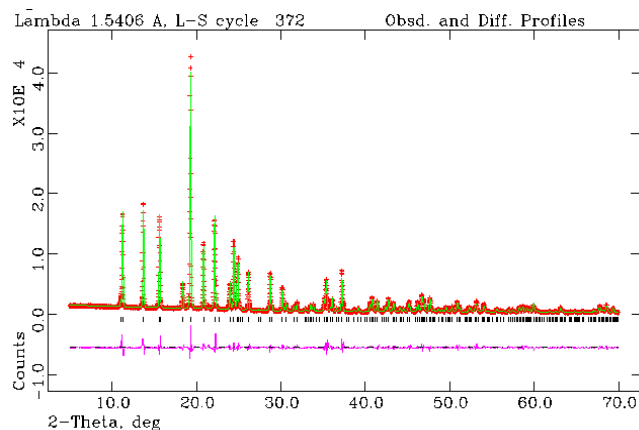
Figure 5.31 The Rietveld refinement of **CuMo–5.** Observed data red, calculated profile green, difference profile purple.
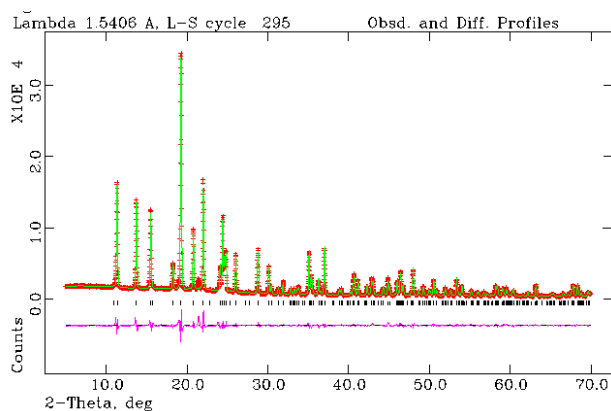
Figure 5.32 The Rietveld refinement of **CuNb–4**. Observed data red, calculated profile green, difference profile purple.

5.4.1 Discussion

Structure

The crystal structures of **CuMo–5** and **CuNb–4** exhibits a 2–D interpenetrated network, which is iso–structural to $[Cu(C_{10}H_8N_2)_2(H_2O)_2SiF_6]$ and $[Cu(C_{10}H_8N_2)_2(H_2O)_2GeF_6]$.[13]

The article by Noro discussed the influence of counter–anion using different sizes and charges in the Cu/4,4'–bpy framework.

The equatorial sites of the "(4+2)" octahedral copper cation (see Figure 5.34) are occupied by the 4,4'–bipyridyl ligand, bridging to four neighbouring copper centres, forming two identical but independent square grids within layers perpendicular to the [110] and [−110] directions. These form an interpenetrated network with channels (see Figure 5.35). The octahedral coordination around copper is completed by two water molecules. The channels are occupied by anions (see Figure 5.36). Both anions of **CuMo–5** and **CuNb–4** exhibit completely disordered O/F occupancies around their metal centres. Molybdenum and niobium are present in +6 and +5 oxidation states respectively, further confirmed by BVS analysis (see Table 5.10 and 5.11).

The 'equatorial' ligands of the anions form strong hydrogen bonds with the water molecules coordinated to the copper centre. (For **CuMo–5** O4–H4A…F1 1.87 Å; O4…F1 2.69 Å and for [**CuNb–4** O4–H4A…F1 1.82 Å; O4…F1 2.66 Å).

The SEM image shows bipyramidal morphology of single crystals of **CuNb–4** (see Figure 5.33), which is consistent with assignment of tetragonal space group P4/ncc.
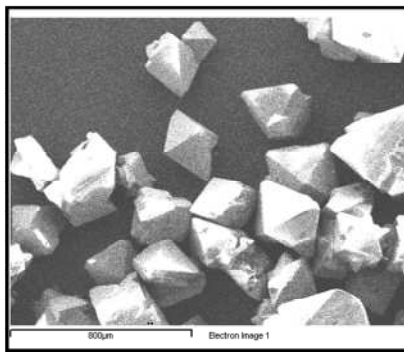
Figure 5.33 SEM image of **CuNb–4**
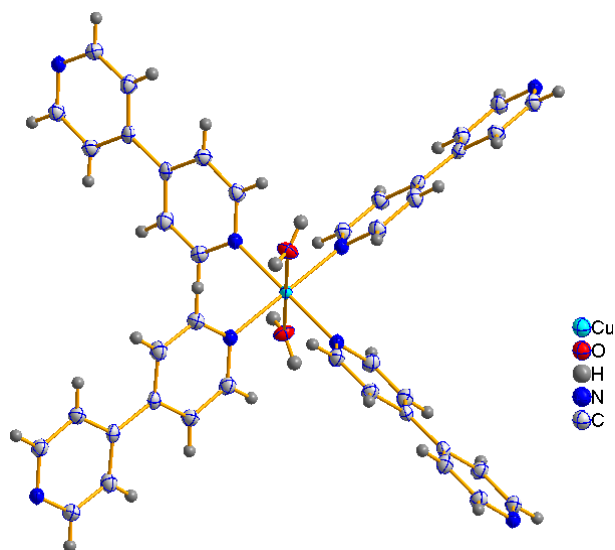
Figure 5.34 Coordination environment of copper in **CuMo–5** and **CuNb–4**.

Bond	Bond Length(Å)	S_{ij}	Bond	Bond Length(Å)	S_{ij}
Mo1–(F/O)1x4	1.877(6)	1.083	Cu1–O4x2	2.333(8)	0.179
Mo1–(F/O)2	1.942(11)	0.700	Cu1–N1x4	2.052(6)	0.458
Mo1–(F/O)3	1.927(12)	0.728			
		ΣMo1=5.76			ΣCu1=2.19

Table 5.10 Selected bond lengths and BVS for **CuMo–5.**

Bond	Bond Length(Å)	S_{ij}	Bond	Bond Length(Å)	S_{ij}
Nb1–(F/O)1x4	1.932(2)	0.873	Cu1–O4x2	2.341(4)	0.167
Nb1–(F/O)2	1.960(4)	0.785	Cu1–N1x4	2.048(3)	0.463
Nb1–(F/O)3	1.907(6)	0.904			
		ΣNb1=5.18			ΣCu1=2.19

Table 5.11 Selected bond lengths and BVS for **CuNb–4**.
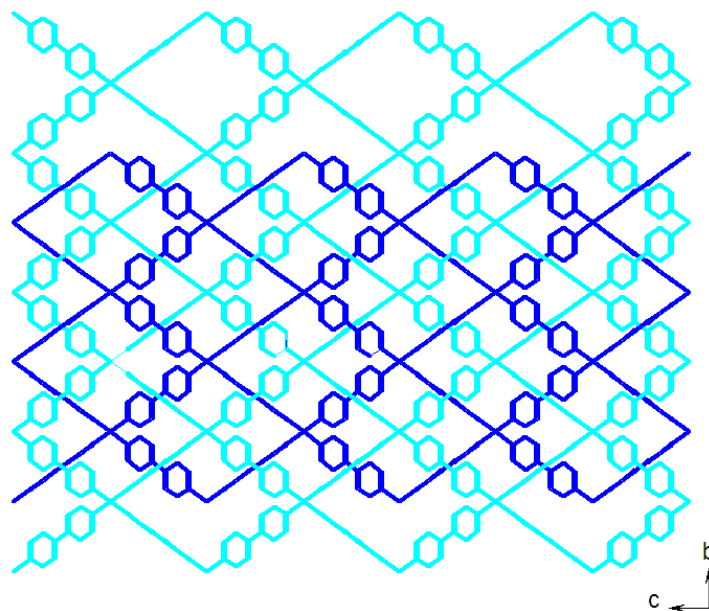
Figure 5.35. Schematic of the two interpenetrated Cu–bipy sublattices in **CuMo–5** and **CuNb–4**.
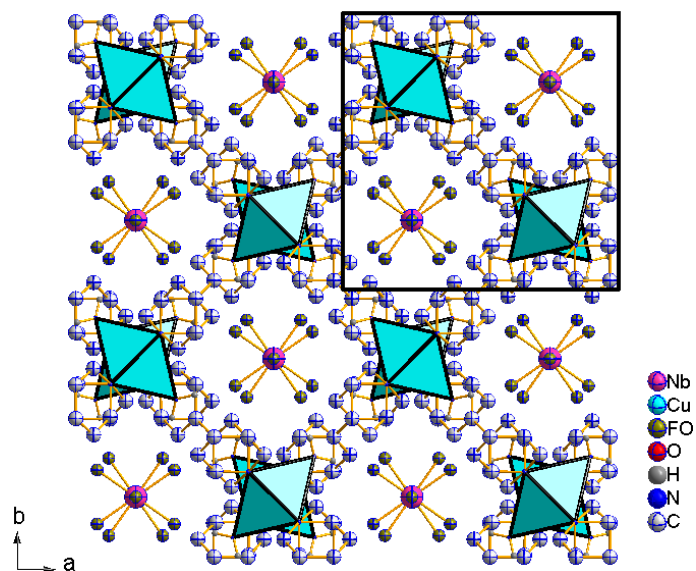
Figure 5.36 Crystal packing of **CuNb–4** viewed down the *c* axis. Nb–centred octahedra occupying the channels are drawn as ball–and–stick. H atoms excluded for clarity.

5.4.3 (Nb₂O₅/MoO₃,CuO)/HF/4,4'–bipyridyl System

The 'composition–space' diagram for the $(Nb_2O_5/MoO_3,CuO)/HF/4,4'$–dipyridyl reactant system (see Figure 5.37) shows a high mole fraction of 4,4'–dipyridyl region producing poorly crystalline products which were not characterised. The single crystals of **CuMo–5** and **CuNb–4** were found in the crystallisation region of higher mole fraction of HF, which helps to completely dissolve the metal oxides to react with the organo amine. The crystallisation field contains well crystalline deep blue crystals of **CuMo–5** and **CuNb–4** with a small amount of unreacted metal oxides. Changing the ratio of hydrofluoric acid and water content, while keeping the other reactants and conditions as constant was also carried out, but only **CuMo–5** and **CuNb–4** were formed. The pure phase was synthesised based on the experimental procedure, as discussed in Appendix–III.
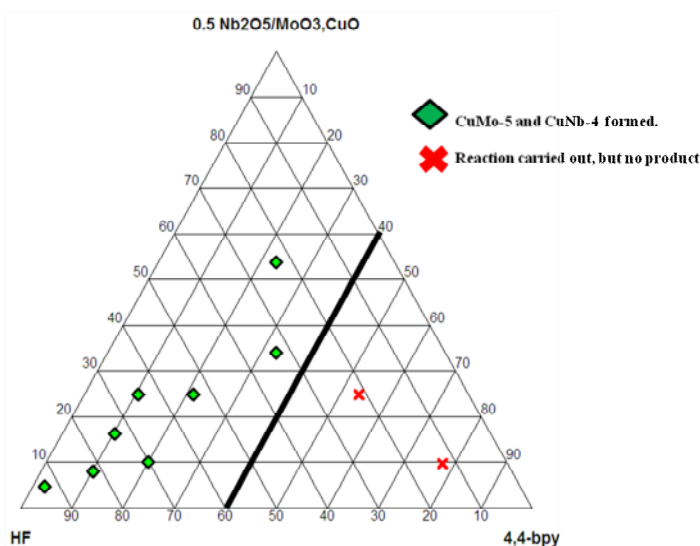
Figure 5.37 'Composition–space' diagram of $(Nb_2O_5/MoO_3,CuO)/HF/4,4'$–bipyridyl.

Heated under Ar, **CuMo–5** undergoes a weight loss occurring between 125°C to 375°C (see Figure 5.38). This is thought to be owing to the loss of organic template and water molecules from the material. The pure phase shows a weight loss of 57%, which corresponds to the removal of 4,4'–bipyridyl (51.5%) and the water (5.5%) molecule coordinated to copper. The final product at 500°C is largely amorphous.
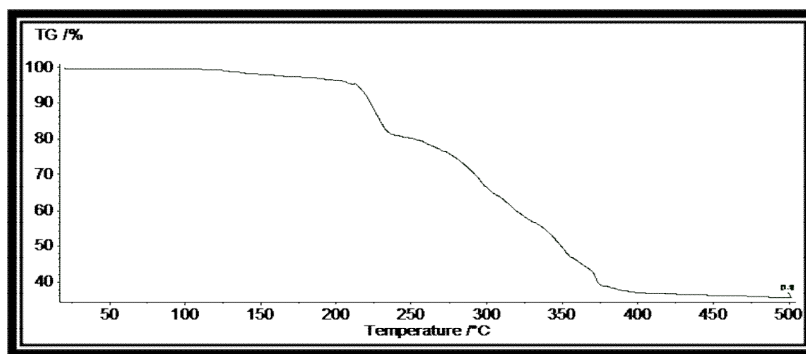
Figure 5.38 TGA of **CuMo–5**

Heated under Ar, **CuNb–4** undergoes a weight loss occurring between 125°C to 375°C (see Figure 5.39). This is thought to be owing to the loss of organic template and water molecules from the material. The pure phase shows a weight loss of 57%, which corresponds to the removal of 4,4'–bipyridyl (51%) and the water (6%) molecule coordinated to copper. The final product at 500°C is largely amorphous.
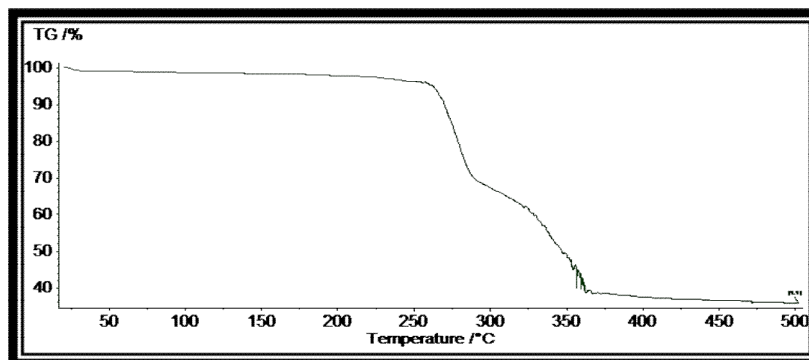
Figure 5.39 TGA of **CuNb–4**

The Magnetic susceptibility data for **CuNb–4** fit very well to a Curie–Weiss law in the range of 2–300 K (see Figure 5.40). The linear plot of $1/\chi_p$ versus T suggests paramagnetic interactions with a small negative Weiss constant ($\theta_{esd}=-2.59$ K) (see Figure 5.40). The experimental value of C=0.41 cm^{3}mol^{-1}K ($\mu_{eff}=1.83$ μB) obtained from the Curie–Weiss plot, is consistent with one isolated spin ½ Cu^{2+} centre per formula unit (C=0.38 cm^{3}mol^{-1}K, $\mu_{eff}=1.73$ μB).

191
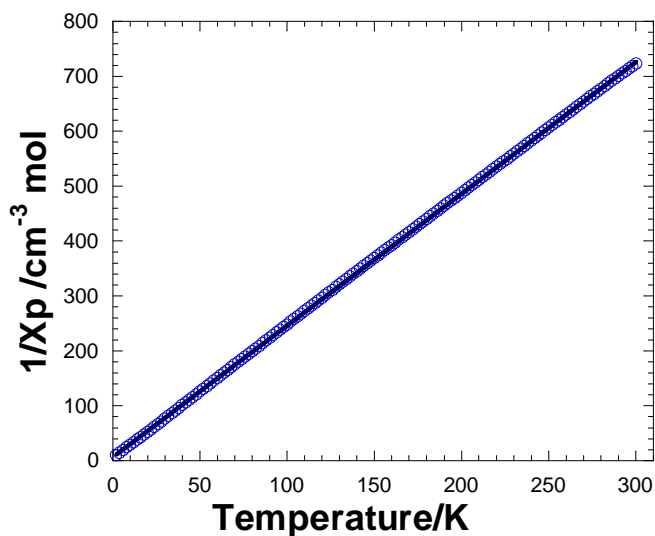
Figure 5.40 $1/\chi_p$ versus T for **CuNb–4**.

5.5 Summary

This preliminary search for novel mixed transition metal oxyfluorides incorporating units based on the first–order Jahn–Teller distorted Cu^{2+} and the second order Jahn–Teller distorted Nb^{5+}/Mo^{6+} cation yields nine new compounds which display a variety of monomers, **CuMo–1**, chains, **CuMo–2**, **CuMo–3**, **CuMo–4**, **CuNb–1**, **CuNb–2** and **CuNb–3** and layers, **CuMo–5** and **CuNb–4**. The systematic studies were carried out based on 'composition–space' diagrams by varying the reaction composition to map out the crystallisation field within each reactant system. Table 5.12 summarises all the structures in this chapter, their connectivity, oxidation states, geometry of the metal centres and overall dimensionality.

5.6 Publications

The work in this chapter has resulted in the following publication:

1. **Organic-inorganic hybrid chains and layers constructed from copper-amine cations and early transition metal (Nb, Mo) oxyfluoride anions.** T. Mahenthirarajah, Y. Li, and P. Lightfoot, *Dalton Trans.*, **2009**, 3280

Table 5.12 A summary of the molybdenum and niobium oxyfluoride structures in this chapter.

Structures	Compound	Overall dimensio nality	Space group	Geometry of Cu	Geometry of Mo/Nb	Oxidation state of Mo or Nb/Cu	Connecti- vity
1.[Cu(C$_{12}$H$_8$N$_2$)(H$_2$O)$_3$][MoO$_2$F$_4$].H$_2$O	**CuMo–1**	0D	P−1	Square pyramidal	Octahedron	+6/+2	-
2.[Cu(C$_2$H$_4$N$_4$)$_2$][MoO$_2$F$_4$].H$_2$O	**CuMo–2**	1D	P2$_1$/n	(4+2) Octahedron	Octahedron	+6/+2	Cu–F–Cu Cu–F–Mo
3.[Cu(C$_2$H$_4$N$_4$)$_2$][NbOF$_5$].H$_2$O	**CuNb–1**	1D	P2$_1$/n	(4+2) Octahedron	Octahedron	+5/+2	Cu–F/O–Cu Cu–F/O–Nb
4.[Cu(C$_3$H$_4$N$_2$)$_4$][MoO$_2$F$_4$]	**CuMo–3**	1D	C2/c	(4+2) Octahedron	Octahedron	+6/+2	Cu–F/O–Mo
5.[Cu(C$_3$H$_4$N$_2$)$_4$][NbOF$_5$]	**CuNb–2**	1D	C2/c	(4+2) Octahedron	Octahedron	+5/+2	Cu–F/O–Nb
6.[Cu$_2$F$_2$(C$_{10}$H$_9$N$_3$)$_2$][MoO$_2$F$_4$]	**CuMo–4**	1D	C2/m	(4+2) Octahedron	Octahedron	+6/+2	Cu–F–Cu Cu–F/O–Mo
7.[Cu$_2$F$_2$(C$_{10}$H$_9$N$_3$)$_2$][NbOF$_5$]	**CuNb–3**	1D	C2/m	(4+2) Octahedron	Octahedron	+5/+2	Cu–F –Cu Cu–F/O–Nb
8. [Cu(C$_{10}$H$_8$N$_2$)$_2$(H$_2$O)$_2$][MoO$_2$F$_4$]	**CuMo–5**	2D	P4/ncc	(4+2) Octahedron	Octahedron	+6/+2	-
9. [Cu(C$_{10}$H$_8$N$_2$)$_2$(H$_2$O)$_2$][NbOF$_5$]	**CuNb–4**	2D	P4/ncc	(4+2) Octahedron	Octahedron	+5/+2	-

References

1. A. C. Larson and R. B. Von Dreele, *General Structure Analysis System (GSAS)*, Los Alamos National Laboratory Report LAUR, **2004**, 86–748.

2. G. M. Sheldrick, *Acta Crystallogr., Sect. A: Found. Crystallogr.*, **2008**, 64, 112. 20

3. L. J. Farrugia, WinGX, *J. Appl. Crystallogr.*, **1999**, 32, 837.

4. H. Serier, M. Gaudon, A. Demourgues, A. Tressaud, *J. Solid State Chem.*, **2007**, 180, 3485.

5. K. R. Heier, A. J. Norquist, P. Halasyamani, A. Duarte, C. L. Stern, K. R. Poeppelmeier, *Inorg. Chem.*, **1999**, 38, 762.

6. D. Hagrman, J. Zubieta, *Chem. Commun*., **1998**, 2005.

7. J. L. Manson, M. M. Conner, J. A. Schlueter, A. C. McConnell, H. I. Southerland, I. Malfant, T. Lancaster, S. J. Blundell, M. L. Brooks, F. L. Pratt, J. Singleton, R. D. McDonald, C. Lee, M. H. Whangbo, *Chem. Mater.*, **2008**, 20, 7408.

8. M. E. Welk, C. L. Stern, K. R. Poeppelmeier, A. J. Norquist, *Cryst. Growth. Des*., **2007**, 7, 956.

9. P. Halasyamani, M. J. Willis, C. L. Stern, P. M. Lundquist, G. K. Wong and K. R. Poeppelmeier, *Inorg. Chem.*, **1996**, 35, 1367.

10. H. Casellas, A. Pevec, B. Kozlevcar, P. Gamez and J. Reedijk, *Polyhedron*, **2005**, 24, 1549.

11. W. C. Velthuizen, J. G. Haasnoot, A. J. Kinneging, F. J. Rietmeijer, J. Reedijk, *J. Chem. Soc., Chem. Commun*. **1983**, 1366.

12. D. A. Handley, P. B. Hitchcock, T. H. Lee, G. J. Leigh, *Inorg. Chim. Acta*., **2001**, 316, 59.

13. S. Noro, R. Kitaura, M. Kondo, S. Kitagawa, T. Ishii, H. Matsuzaka and M. Yamashita, *J. Am. Chem. Soc.*, **2002**, 2568.

CHAPTER SIX

Structural Characterisation of Hilgardite–like Borates

6.1 Introduction

The hilgardite family of borate halides $M_2B_5O_9X$ (M= Ca, Sr, Ba, Pb, Eu; X=Cl, Br), including hydrates and other derivatives[1] has been of continuing interest over four decades[,2,3,4,5]. This interest is often due to their potential applications for luminescence and NLO properties.[1] Exploration of hilgardite–like borohalides is one of the research interests. SHG intensities of the hilgardites were studied by Plachinda *et al*. the measured values are given in Table 6.1 related to the SHG intensity of the α–quartz (3μm powder) taken as standard.[6]

X		Ca	Sr	Ba	Pb
Cl $I^{2\omega}/I^{2\omega}$ SiO$_2$ (<L> =3-5 μm)		4	7	8	**20**
Br $I^{2\omega}/I^{2\omega}$ SiO$_2$ (<L> =3-5 μm)		5	12	32	**80**

Table 6.1 SHG intensities of powdered $M_2B_5O_9X$ hilgardites.

These data show a distinct increment along the series Ca<Sr<Ba<Pb for the metal centres and Cl<Br for the halide verification. According to the Phillips–van Vechten–Levine–Xue bond theory[7,8,9], the borate network itself is the main contributor to the optical nonlinearities of borates. The relationship between these SHG values and the crystal structure of $M_2B_5O_9X$ hilgardites is very interesting area to explore. In particular, the Pb-containing members of the hilgardite family borate halides exhibit an abnormally large NLO response; this factor has not yet been explained. NLO susceptibility is very sensitive to the type and length of chemical bonds in the crystal structure. In order to understand the underlying crystal–chemical rationale, as an initial step synthesised four compounds of this series and used X-ray powder diffraction (XPD) to verify the purity of each phase. Using only XPD data it is difficult to determine the precise position of lighter atoms such as boron atoms in the presence of very heavy atoms such as Pb, Br. To

overcome these problems, we used neutron powder diffraction (NPD) data, leading to a more precise determination of lighter atom positions, and improved precision on the B-O bond lengths (see Table 6.3 and 6.4); typical precision for $Pb_2B_5O_9Cl$, $Pb_2B_5O_9Br$ and $Sr_2B_5O_9Cl$ on the B–O bond lengths from our NPD is in the range ±0.005–0.010 Å, as compared to ±0.02–0.03 Å for the single crystal X–ray diffraction data from the literature.[10,11] In the case of $Ba_2B_5O_9Cl$, unknown impurities reduced the precision compared to other data (see Table 6.3, Table 6.4 and Table 6.5). The synthesis, Rietveld refinement of NPD data and crystal structures are discussed below.

6.2 Synthesis

The reagents used through out this work were not air sensitive and reactions were carried out by conventional solid state techniques. All reagents were of 99.9% or higher purity.

Synthesis of Hilgardite–like Borate $Pb_2B_5O_9Cl$

Polycrystalline samples of $Pb_2B_5O_9Cl$ were prepared by two steps, because of the strong hygroscopic properties of B_2O_3.[6]

Step–1

$$PbO + 2B_2O_3 \longrightarrow PbB_4O_7$$
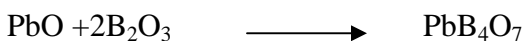
Reactants were ground together according to stoichiometric quantities using an agate motor and pestle. This powder was then pressed into a pellet 13 mm in diameter. The pellets were heat treated at 400°C for 48 hours, and the product quenched to room temperature by removing the alumina boat from the furnace.

Step–2

Once PbB_4O_7 was synthesised with maximum purity, the following reaction was carried out.

$$PbO + 2PbCl_2 + 5PbB_4O_7 \longrightarrow 4Pb_2B_5O_9Cl$$

Stoichiometric quantities of the reactants were ground well and pressed into pellets. These pellets were heated to 750°C for 2 hours in an alumina boat inside a box furnace in the presence of air. The reaction in air was quenched to room temperature by removing from the box furnace.

Synthesis of Hilgardite–like Borate $Pb_2B_5O_9Br$

Polycrystalline samples of $Pb_2B_5O_9Br$ were prepared by two steps, as mentioned in the synthesis procedure of $Pb_2B_5O_9Cl$.

Step–1

$$PbO + 2B_2O_3 \longrightarrow PbB_4O_7$$

Step–2

Once PbB_4O_7 was synthsised with maximum purity, the following reaction was carried out.

$$PbO + 2PbBr_2 + 5PbB_4O_7 \longrightarrow 4Pb_2B_5O_9Br$$

Synthesis of Hilgardite–like Borate $Sr_2B_5O_9Cl$

Polycrystalline $Sr_2B_5O_9Cl$ was synthesised by heating a ground stoichiometric mixture of analytical reagent grade $SrCO_3$ (99.99%), $SrCl_2$ (99.99%) and H_3BO_3 (99.9%). The solid state reaction involved in this case is :
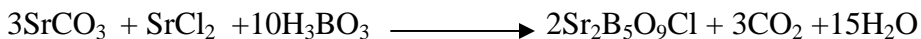
$$3SrCO_3 + SrCl_2 + 10H_3BO_3 \longrightarrow 2Sr_2B_5O_9Cl + 3CO_2 + 15H_2O$$

The reagents were ground at room temperature between heatings. The starting materials were mixed thoroughly in appropriate stoichiometric ratio and pressed into pellets. Pellets were placed in an alumina boat and heated at 300°C for 15 hours in the box furnace. The reaction mixture was the heated for up to 3 hours at 650°C with further heating at 750°C for 90 minutes with intermittent grindings. Finally the reaction was quenched to room temperature.

Synthesis of Hilgardite–like Borate $Ba_2B_5O_9Cl$

Polycrystalline $Ba_2B_5O_9Cl$ was synthesised by heating a ground stoichiometric mixture of analytical reagent grade $BaCO_3$ (99.99%), $BaCl_2$ (99.99%) and H_3BO_3 (99.9%). The following solid state reaction was used to synthesise $Ba_2B_5O_9Cl$.
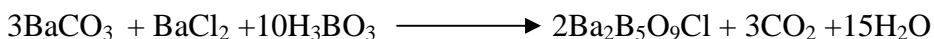
$$3BaCO_3 + BaCl_2 + 10H_3BO_3 \longrightarrow 2Ba_2B_5O_9Cl + 3CO_2 + 15H_2O$$

The reagents were ground at room temperature between heatings. The starting materials were mixed thoroughly in appropriate stoichiometric ratio and pressed into pellets. Pellets were placed in an alumina boat and heated at 800°C for 4 hours in the box furnace with subsequent heating as pellets at 900°C for successive periods of 8 hours with intermittent grindings. Finally the reaction was quenched to room temperature.

6.3 Characterisation

All the samples were measured on a Stoe X–ray powder diffractometer transmitting copper radiation at 1.5406 Å, via a curved germanium monochromator with a 2Ө range from 5 to 100°. These data were collected 15 hours to ensure the best quality pattern for subsequent studies.

For $Pb_2B_5O_9Cl$ the NPD was carried out on the GEM instrument at the ISIS facility, Rutherford Appleton Laboratory, UK. The ISIS neutron source operates in the time–of–flight (energy dispersive mode) so that data are analysed as a function of d-spacing.

The NPD experiment on $Sr_2B_5O_9Cl$, $Pb_2B_5O_9Br$ and $Ba_2B_5O_9Cl$ were performed on the D2B high-resolution two–axis diffractometer at The ILL, Grenoble. The patterns were recorded in the 2θ range of 10-160˚ at a wavelength of 1.594 Å. The resulting crystallographic data and structure refinement details for $Pb_2B_5O_9Cl$, $Pb_2B_5O_9Br$, $Sr_2B_5O_9Cl$ and $Ba_2B_5O_9Cl$ are listed in Tables 6.2 and salient bond lengths and angles in Table 6.3 to 6.7.

Rietveld refinements of NPD data were performed with the GSAS program suite[12] using the atomic co–ordinates determined by single crystal solution of $Pb_2B_5O_9Br$[10] as a starting point. Instrumental parameters (background, zero–point, peak profile coefficients) and structural parameters (unit cell, atomic co–ordinates, thermal parameters) were refined. A close final fit to the observed data was achieved (see Figure 6.1, 6.2, 6.3 and 6.4; Rwp and Rp values of fit given in Table 6.2).

Tables 6.2 Crystallographic data for $Pb_2B_5O_9Cl$, $Pb_2B_5O_9Br$, $Sr_2B_5O_9Cl$ and $Ba_2B_5O_9Cl$

Formula	$Pb_2B_5O_9Cl$	$Pb_2B_5O_9Br$	$Sr_2B_5O_9Cl$	$Ba_2B_5O_9Cl$
Instrument	GEM (ISIS)	D2B(ILL)	D2B(ILL)	D2B(ILL)
Temperature	293(2)	293(2)	293(2)	293(2)
Crystal system	Orthorhombic	Orthorhombic	Orthorhombic	Orthorhombic
Space group	*Pnn2* (34)	*Pnn2* (34)	*Pnn2* (34)	*Pnn2* (34)
a(Å)	11.3808(3)	11.4504(2)	11.3153(5)	11.5827(8)
b(Å)	11.3842(3)	11.5022(2)	11.3838(5)	11.6278(7)
c(Å)	6.5634(1)	6.5398(9)	6.4945(2)	6.6800(4)
Volume(Å^3)	850.35(3)	861.32(3)	836.57(7)	899.66(11)
Z	4	4	4	4
Density(calculated) (mg/m^3)	5.061	5.339	3.245	3.752
Refinement method and software	Rietveld refinement GSAS[12]	Rietveld refinement GSAS[12]	Rietveld refinement GSAS[12]	Rietveld refinement GSAS[12]
Number of parameters	136	69	100	57
Goodness–of–fit	6.38	1.96	1.85	6.32
R_p	Bank 5 0.0258 Bank 6 0.0163	0.0292	0.0315	0.0634
R_{wp}	Bank 5 0.0237 Bank 6 0.0187	0.0366	0.0388	0.0887

6.4 Results and Discussion

6.4.1 Rietveld Refinement of Hilagardite–like Borates
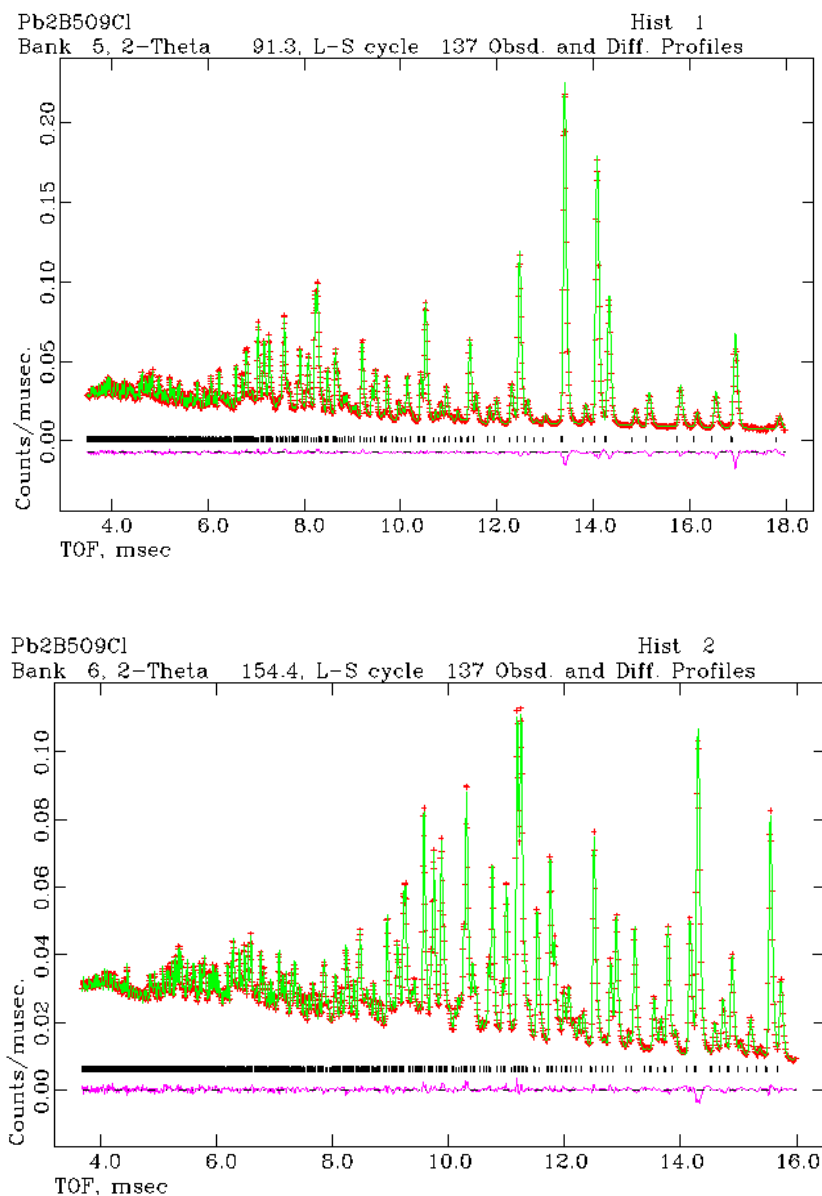
Figure 6.1 Rietveld refinements of hilgardite–like borate $Pb_2B_5O_9Cl$. Observed data red, calculated profile green, difference profile purple.
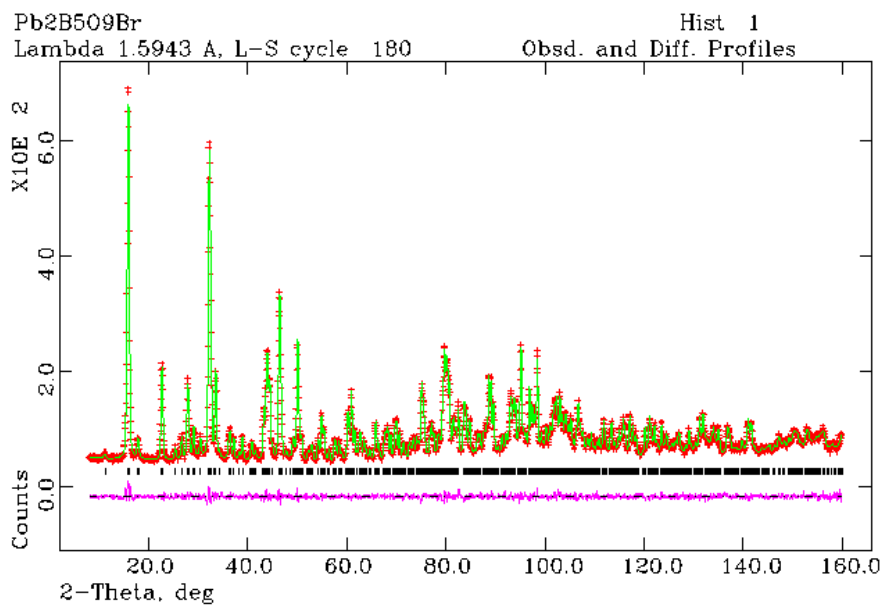
Figure 6.2 Rietveld refinement of hilgardite–like borate $Pb_2B_5O_9Br$. Observed data red, calculated profile green, difference profile purple.
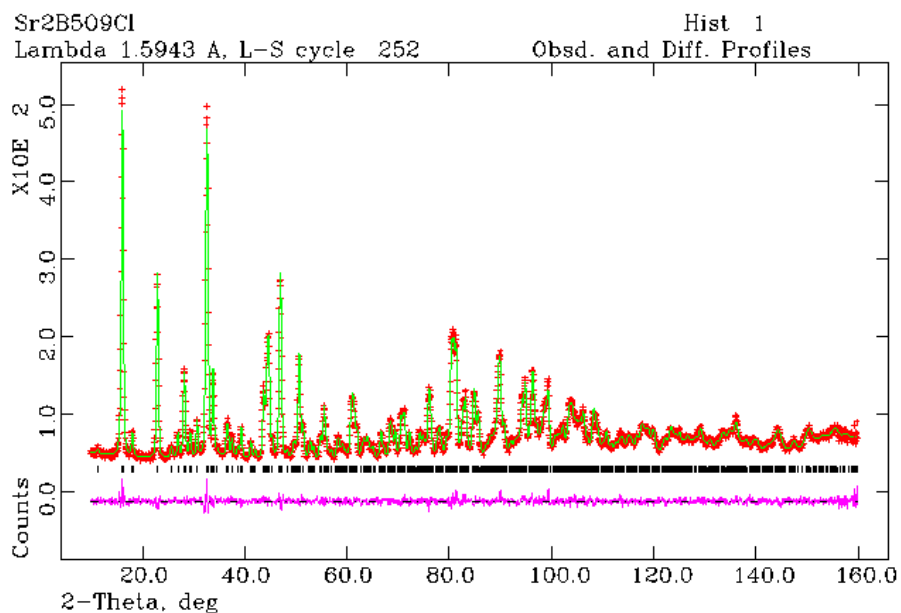
Figure 6.3 Rietveld refinement of hilgardite–like borate $Sr_2B_5O_9Cl$. Observed data red, calculated profile green, difference profile purple.
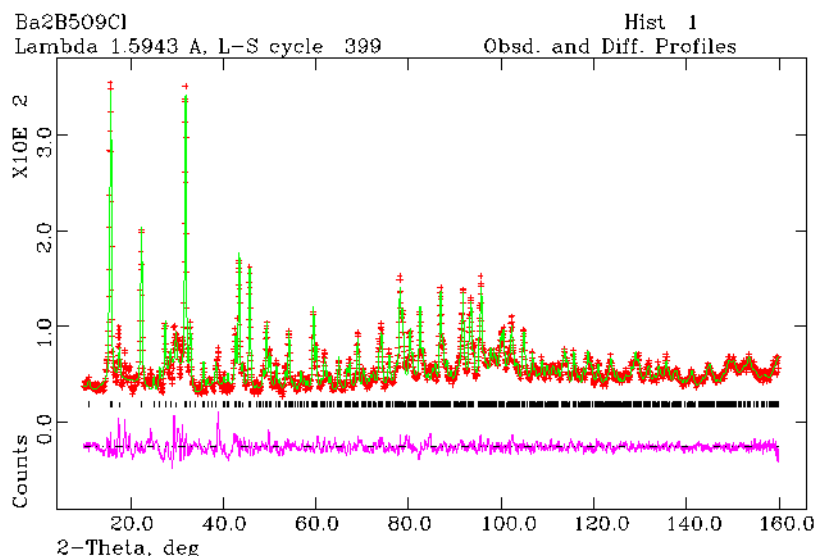
Figure 6.4 Rietveld refinement of hilgardite–like borate $Ba_2B_5O_9Cl$. Observed data red, calculated profile green, difference profile purple.

6.4.2 Structures of Hilagardite–like Borates

$Pb_2B_5O_9Cl$, $Pb_2B_5O_9Br$, $Sr_2B_5O_9Cl$ and $Ba_2B_5O_9Cl$ crystallise in the non-centrosymmetric orthorhombic space group, Pnn2. From the crystallographic data (see Table 6.2), the unit cell parameters are close to a tetragonal unit cell. However, there is no crystallographically imposed four–fold symmetry in the crystal structure.

The crystal structure of hilgardite is an open three–dimensional borate framework, with FBB of pentaborate polyanion $[B_5O_{12}]^{9-}$ (see Figure 6.5), containing two trigonal planar borates and three tetrahedral borates. It is formed by two six-membered alternate boron–oxygen rings which are perpendicular to each other, joined through a common tetrahedral boron atom. The trigonal borates are in *cis* configuration with respect to central tetrahedral borate.

The pentaborate polyanions form a chain parallel to the *c* axis by sharing two tetrahedral corners with another two borate tetrahedra in adjacent polyanions. The polyanion chain repeating unit contains three tetrahedral borates, parallel to the *c* axis (see Figure 6.6).

203

This is a common feature to all hilgardite family materials. The distances between this repeating unit is 6.563(6) Å for $Pb_2B_5O_9Cl$; 6.540(8) Å for $Pb_2B_5O_9Br$; 6.50(1) Å for $Sr_2B_5O_9Cl$ and 6.68(3) Å for $Ba_2B_5O_9Cl$.

In each borate chain, corners are shared with four adjacent chains, tetrahedral corners of one chain are shared with trigonal corners of the other to form a 3–dimensional framework, as shown in Figure 6.7, the molecular formula is $[B_5O_{12}]^{9-} = [B_5O_6O_{6/2}]^{3-}$ The overall stoichiometry of the borate framework is therefore $[B_5O_9]^{3-}$. According to Becker[13], the ordered arrangement of the polar distorted trigonal borate along one direction can significantly contribute to the optical non linearity of borate materials. There are two crystallographically different trigonal borates, almost perpendicular to each other, which are oriented parallel to *ac* and *bc* planes in the framework (see Figure 6.7). However, the calculations by Plachinda *et al.*[6] for polar anisotropy of the components in the borate framework based on the Phillips–van Vechten–Levine–Xue bond theory could not explain the observed high optical non–linearity of the lead containing hilgardite members. The crystallographic data from NPD suggest no significant or systematic change in the borate framework in $Pb_2B_5O_9Cl$, $Pb_2B_5O_9Br$, $Sr_2B_5O_9Cl$ and $Ba_2B_5O_9Cl$ (see Table 6.3, 6.4 and 6.5).
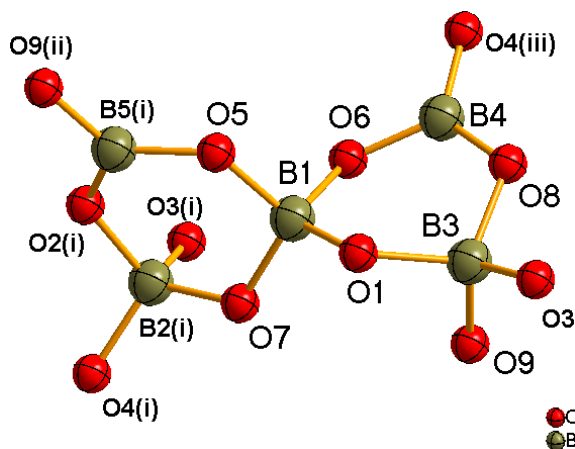
Figure 6.5 FBB of pentaborate polyanion $[B_5O_{12}]^{9-}$.
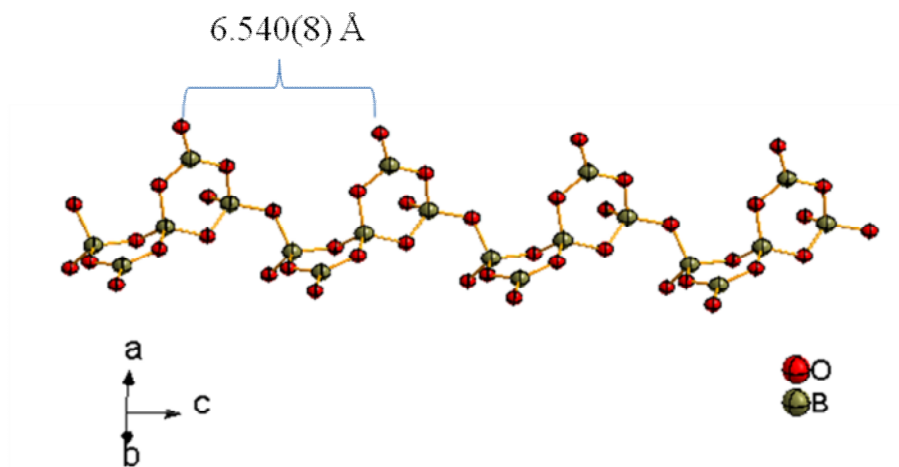
Figure 6.6 The single borate chain with repeating unit in $Pb_2B_5O_9Br$.

The resulting borate framework has channels parallel to the *ac* plane. Cations and halide ions are situated in the channels (see Figure 6.8), forming a metal oxyhalide 3–D network, as shown in Figure 6.10.
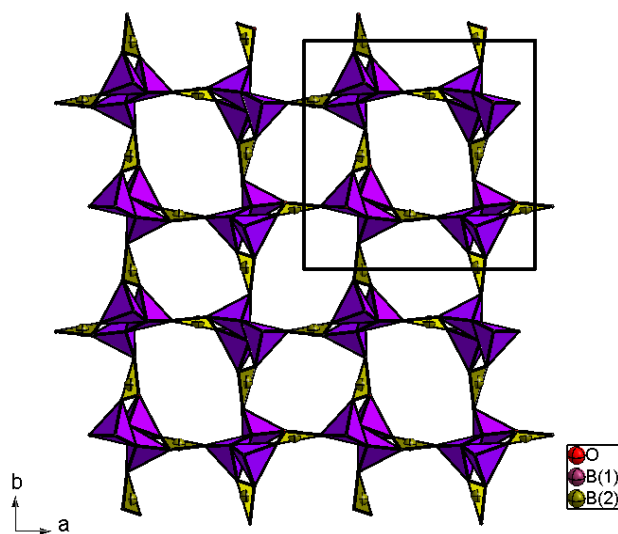
Figure 6.7 3–dimensional borate framework; different colour of polyhedra representing trigonal and tetrahedral borate.
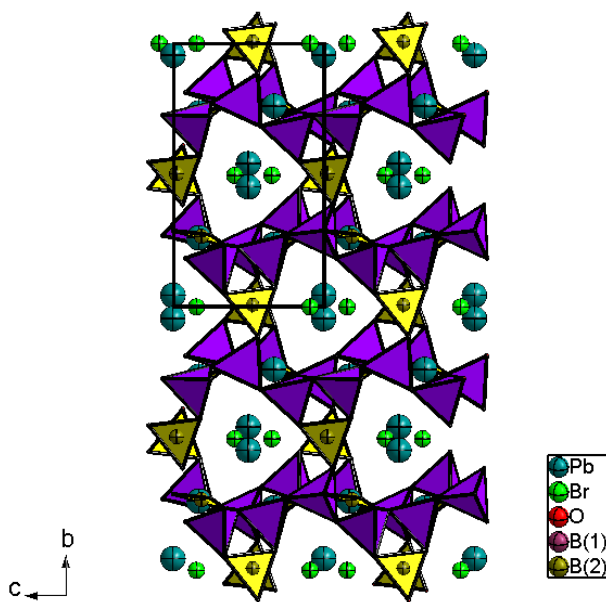
Figure 6.8 The open channels filled with Pb^{2+} and Br^{-} ions in $Pb_2B_5O_9Br$, different colour of polyhedra representing trigonal and tetrahedral borate.

The crystal structures of $Sr_2B_5O_9Cl$ and $Ba_2B_5O_9Cl$ contain two crystallographically independent cations; Sr1, Ba1 and Sr2, Ba2 exhibit slightly distorted pentagonal bipyramidal and hexagonal bipyramidal geometries respectively. The crystal structures of $Pb_2B_5O_9Cl$ and $Pb_2B_5O_9Br$ contain two crystallographically different Pb^{2+}, exhibiting distorted hexagonal bipyramidal geometry. The coordination environments of both cations contain six oxygen atoms in the equatorial position and two chlorine/bromine atoms at the vertices (see Figure 6.9). The BVS calculations (see Table 6.6 and 6.7) show some "underbonded" atoms in the coordination sphere of Pb^{2+}, allowing exclusion of O6 from the coordination sphere of Pb1. In the case of Pb2, it can be described as a hexagonal bipyramid capped by an oxygen atom. Therefore the susceptibility contribution will be subtly different from Pb1 and Pb2. Both the Pb1 and Pb2 are shifted from the equatorial position due to the effect of stereochemically active lone pairs[14], of which we could not determine the positions based on NPD data. It is believed that a significant contribution towards the SHG response is from these active lone pairs on Pb^{2+}.
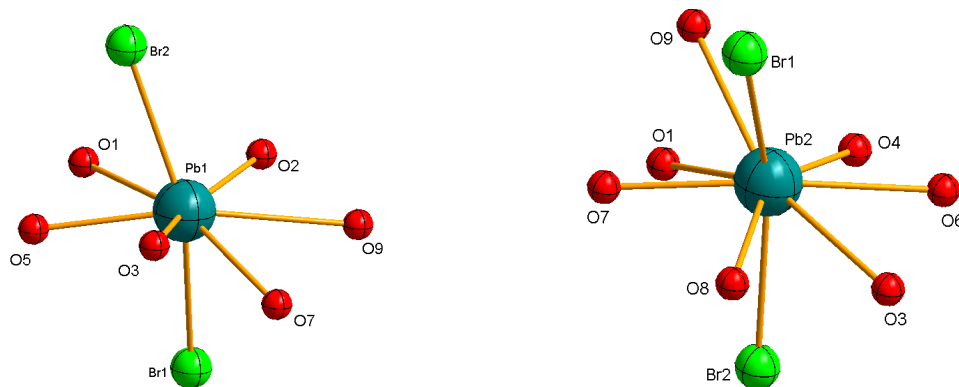
Figure 6.9 The coordination environment of crystallographically different Pb^{2+} in $Pb_2B_5O_9Br$.
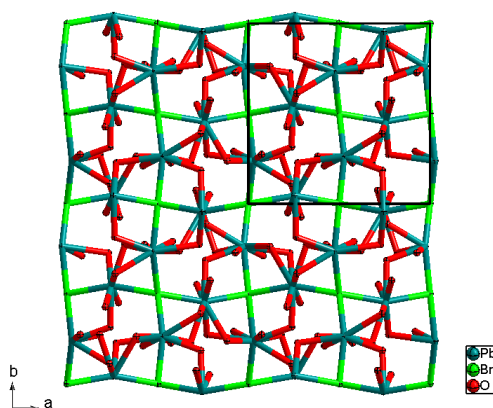
Figure 6.10 The Pb^{2+} cations forming a 3–D network in $Pb_2B_5O_9Br$ represented by a wire model. Boron atoms have been omitted for clarity.

Bond	$Pb_2B_5O_9Br$	$Pb_2B_5O_9Cl$	$Sr_2B_5O_9Cl$	$Ba_2B_5O_9Cl$
B1–O1	1.461(8)	1.461(5)	1.40(1)	1.52(3)
B1–O5	1.511(9)	1.472(5)	1.49(1)	1.44(2)
B1–O6	1.470(8	1.456(5)	1.503(9)	1.42(2)
B1–O7	1.452(8)	1.463(5)	1.49(1)	1.45(3)
B2–O2	1.488(8)	1.484(5)	1.498(9)	1.46(2)
B2–O3	1.511(8)	1.497(5)	1.46(1)	1.56(2)
B2–O4	1.436(8)	1.449(6)	1.45(1)	1.41(3)
B2–O7	1.463(9)	1.446(6)	1.46(1)	1.54(3)

B3–O1	1.450(9)	1.493(6)	1.47(1)	1.50(3)
B3–O3	1.450(7)	1.456(5)	1.46(1)	1.45(2)
B3–O8	1.535(8)	1.497(5)	1.48(1)	1.51(2)
B3–O9	1.477(8)	1.465 (5)	1.50 (1)	1.60 (3)
B4–O4	1.375(8)	1.342(6)	1.378(9)	1.33(2)
B4–O6	1.368(8)	1.351(5)	1.39(1)	1.45(3)
B4–O8	1.336(8)	1.393(5)	1.34(1)	1.40(3)
B5–O2	1.346(9)	1.361(6)	1.33(1)	1.27(3)
B5–O5	1.369(8)	1.389(6)	1.34(1)	1.38(3)
B5–O9	1.400(8)	1.364(5)	1.39(1)	1.37(3)

Table 6.3 Comparison of B–O bond lengths

O–B–O	$Pb_2B_5O_9Cl$	$Pb_2B_5O_9Br$	$Sr_2B_5O_9Cl$	$Ba_2B_5O_9Cl$
O1–B1–O5	103.9(3)	104.2(5)	105.2(7)	100.2(2)
O1–B1–O6	112.4(3)	112.3(5)	114.0(6)	117.1(2)
O1–B1–O7	112.9(3)	112.1(5)	114.5(6)	110.4(2)
O5–B1–O6	109.5(3)	108.1(5)	107.2(6)	108.3(2)
O5–B1–O7	109.5(3)	110.4(5)	110.0(6)	112.8(2)
O6–B1–O7	108.4(3)	109.6(5)	105.7(6)	107.9(2)
O2–B2–O3	109.8(3)	108.4(5)	110.1(6)	107.9(2)
O2–B2–O4	110.5(3)	110.5(5)	108.9(6)	109.9(2)
O2–B2–O7	109.4(3)	110.5(6)	110.0(7)	109.9(2)
O3–B2–O4	105.3(3)	106.0(5)	107.2(6)	113.2(2)
O3–B2–O7	108.3(3)	107.5(5)	110.3(7)	100.5(2)
O4–B2–O7	113.4(4)	113.8(5)	110.3(7)	114.9(2)
O1–B3–O3	113.7(3)	113.7(6)	112.3(7)	118.1(2)
O1–B3–O8	110.9(3)	111.0(5)	111.6(6)	113.8(2)
O1–B3–O9	102.8(3)	104.8(5)	101.5(6)	107.4(2)
O3–B3–O8	104.9(3)	104.5(5)	104.3(6)	103.2(2)
O3–B3–O9	114.6(3)	115.1(5)	117.5(7)	112.7(2)
O8–B3–O9	110.1(3)	107.7(5)	109.9(6)	100.2(2)
O4–B4–O6	116.6(4)	115.1(5)	112.6(6)	116.9(2)
O4–B4–O8	123.9(3)	125.5(6)	125.4(7)	127.4(2)
O6–B4–O8	119.4(3)	119.4(5)	121.8(6)	115.5(1)
O2–B5–O5	118.2(3)	123.2(6)	121.3(7)	119.7(2)
O2–B5–O9	119.5(4)	117.8(6)	116.3(7)	120.5(2)
O5–B5–O9	122.3(4)	118.8(5)	122.3(7)	119.5(2)

Table 6.4 Comparison of O–B–O bond angles

	M			O	M-O Bond length(Å)			
Pb	**Pb**	**Sr**	**Ba**	**O**	**Pb₂B₅O₉Cl**	**Pb₂B₅O₉Br**	**Sr₂B₅O₉Cl**	**Ba₂B₅O₉Cl**
Pb1	Pb1	Sr1	Ba1	O1	2.577(5)	2.685(7)	2.67(1)	2.71(3)
Pb1	Pb1	Sr1	Ba1	O2	2.530(5)	2.530(8)	2.50(1)	2.68(4)
Pb1	Pb1	Sr1	Ba1	O3	2.672(6)	2.659(8)	2.65(1)	2.79(3)
Pb1	Pb1	Sr1	Ba1	O5	2.497(5)	2.514(8)	2.55(1)	2.69(4)
Pb1	Pb1	Sr1	Ba1	O6	3.097(5)	3.077(7)	3.07(1)	3.08(3)
Pb1	Pb1	Sr1	Ba1	O7	2.826(6)	2.781(9)	2.63(1)	2.64(4)
Pb1	Pb1	Sr1	Ba1	O9	3.015(5)	2.969(7)	2.80(1)	3.09(3)
Pb2	Pb2	Sr2	Ba2	O1	2.683(5)	2.642(8)	2.65(1)	2.77(3)
Pb2	Pb2	Sr2	Ba2	O2	2.920(5)	3.009(7)	2.90(1)	2.87(3)
Pb2	Pb2	Sr2	Ba2	O4	2.842(5)	2.835(8)	2.71(1)	2.84(3)
Pb2	Pb2	Sr2	Ba2	O6	2.696(5)	2.733(8)	2.55(1)	2.53(4)
Pb2	Pb2	Sr2	Ba2	O7	2.524(5)	2.484(9)	2.52(1)	2.82(3)
Pb2	Pb2	Sr2	Ba2	O8	2.502(5)	2.570(8)	2.62(1)	2.77(3)
Pb2	Pb2	Sr2	Ba2	O9	2.869(5)	2.863(8)	2.82(1)	3.04(3)

Table 6.5 Comparison of M–O bond distances.

Bond	**Bond Length(Å)**	**S_ij**	**Bond**	**Bond Length(Å)**	**S_ij**
Pb1–O1	2.577(5)	0.285	Pb2–O1	2.683(5)	0.214
Pb1–O2	2.530(5)	0.323	Pb2–O2	2.920(5)	0.113
Pb1–O3	2.672(6)	0.220	Pb2–O4	2.842(5)	0.139
Pb1–O5	2.497(5)	0.353	Pb2–O6	2.696(5)	0.206
Pb1–O6	3.097(5)	0.070	Pb2–O7	2.524(5)	0.328
Pb1–O7	2.826(6)	0.145	Pb2–O8	2.502(5)	0.349
Pb1–O9	3.015(5)	0.087	Pb2–O9	2.869(5)	0.129
Pb1–Cl1	3.015(3)	0.270	Pb2–Cl1	3.078(3)	0.227
Pb1–Cl2	2.961(3)	0.312	Pb2–Cl2	2.981(2)	0.296
		ΣPb1=2.07			**ΣPb2=2.00**

Table 6.6 Selected bond lengths and BVS of Pb₂B₅O₉Cl

Bond	Bond Length(Å)	S_{ij}	Bond	Bond Length(Å)	S_{ij}
Pb1–O1	2.685(7)	0.213	Pb2–O1	2.642(8)	0.239
Pb1–O2	2.530(8)	0.323	Pb2–O2	3.009(7)	0.089
Pb1–O3	2.659(8)	0.228	Pb2–O4	2.835(8)	0.142
Pb1–O5	2.514(8)	0.337	Pb2–O6	2.733(8)	0.187
Pb1–O6	3.077(7)	0.074	Pb2–O7	2.484(9)	0.366
Pb1–O7	2.781(9)	0.164	Pb2–O8	2.570(8)	0.290
Pb1–O9	2.969(7)	0.099	Pb2–O9	2.863(8)	0.131
Pb1–Br1	3.046(5)	0.372	Pb2–Br1	3.150(6)	0.281
Pb1–Br2	3.029(6)	0.389	Pb2–Br2	3.027(4)	0.391
		ΣPb1=2.20			ΣPb2=2.12

Table 6.7 Selected bond lengths and BVS of $Pb_2B_5O_9Br$.

6.5 Conclusions

The four members of the hilgardites ($Pb_2B_5O_9Cl$, $Pb_2B_5O_9Br$, $Sr_2B_5O_9Cl$ and $Ba_2B_5O_9Cl$) were synthesised using conventional solid state techniques to investigate any structural relationship with SHG. The NPD data provided more precise determination of the position of boron; typical precision for $Pb_2B_5O_9Cl$, $Pb_2B_5O_9Br$ and $Sr_2B_5O_9Cl$ on the B-O bond lengths from our NPD is in the range ±0.005–0.010 Å, as compared to ±0.02–0.03 Å for the single crystal X–ray diffraction data from the literature. Nevertheless, crystallographic data from NPD suggested no significant or systematic change in the borate framework (comparison of B–O bond lengths). Therefore the most significant contribution to SHG in the Pb–containing hilgardites appeared to be an effect of stereochemically active lone pairs of Pb^{2+}.

6.6 Publications

The work in this chapter has resulted in the following publication.

Lead–strontium borate halides with hilgardite–type structure and their SHG properties, B. V. Egorova, A. V. Olenev, P. S. Berdonosov, A. N. Kuznetsov, S.Yu. Stefanovich, V. A. Dolgikh, T. Mahenthirarajah, P. Lightfoot, *J. Solid State Chem*., **2008**, 181, 1891.

References

1. J. Barbier, *Solid State Sci*., **2007**, 9, 344.

2. S. Ghose, C. Wan, *Amer. Miner.*, **1979**, 64, 187.

3. S. Menchetti, C. Sabelli, R. Trosti-Ferroni, *Acta Cryst*., **1982**, B38, 2987.

4. E. L. Belokoneva, T. A. Korchemkina, O.V. Dimitrova, S. Yu. Stefanovich, *Cryst. Rep*., **2000**, 45, 744.

5. E. L. Belokoneva, S. Yu. Stefanovich, M. A. Erilov, O.V. Dimitrova, N. N. Mochenova, *Cryst. Rep*., **2008**, 53, 228.

6. P. A. Plachinda, V. A. Dolgikh, S. Y. Stefanovich, P. S. Berdonosov, *Solid State Sci*., **2005**, 7, 1194.

7. J. C. Phillips, *Rev. Modern Phys*., **1970**, 42, 3.

8. J. A. Van Vechten, *Phys. Rev*., **1969**, 182, 3.

9. B. F. Levine, *J. Chem. Phys*., **1973**, 59, 3.

10. E. L. Belokoneva, A. G. Al-Ama, S. Yu. Stefanovich, P. A. Plachinda, *Cryst. Rep*., **2007**, 52, 795.

11. P. J. Hay, W. R. Wadt, *J. Chem. Phys*., **1985**, 82, 284.

12. A. C. Larson and R. B. Von Dreele, *General Structure Analysis System (GSAS)*, Los Alamos National Laboratory Report LAUR, **2004**, 86–748.

13. P. Becker, *Adv. Mater*. **1998**, 10, 979.

14. E. L. Belokoneva,Y. U. Kabalov, O.V. Dimitriev, S. Yu. Stefanovich, *Cryst. Rep*., **2003**, 48, 44.

CHAPTER SEVEN

7.1 General Summary and Conclusions

One of the initial interests of this work was to synthesise materials with combined properties such as magnetic properties and NLO properties using solvothermal techniques. Polar octahedral building units were successfully synthesised together with unpaired spin systems; the magnetic properties of those materials were studied with more interest. The acentric oxyfluorides $[VOF_2(H_2O)(ligand)_2]^{3-}$, $[VOF_5]^{3-}$, $[VOF_5]^{2-}$, $[NbOF_5]^{2-}$ and $[MoO_2F_4]^{2-}$ were crystallised into a host of new mixed metal materials that combine the octahedral oxyfluoride anions with late transition metal cations (see Chapters 3 and 4). In the anion, the metal cation forms a short bond to the oxygen, which leaves a long trans metal fluoride bond, resulting in a distortion of the cation from the centre of the octahedron. Bond valence calculations were performed to quantify the residual negative charge on each ligand. In all cases, the long metal *trans* fluoride bond is weak and highly nucleophilic. However, the majority of the samples contained polar octahedral building units packed with an inversion centre and therefore were not SHG active.

Vanadium and copper was the first bimetallic system explored and this proved to be the most fruitful for the number of novel building units and their variety of structural architectures. Initially the solvent system was examined as the main variable at 160°C. Mixed solvent systems such as pyridine, derivatives of pyridine and ethylene glycol were used with water, which improved the crystallinity as well as enabling the formation of single crystals. This synthetic route was successful and provided several materials which were fully characterised through single crystal X–ray diffraction and magnetic data analysis.

Manipulation of the structure directing amine and the mixed solvent content produced a novel 'superoctahedral' building unit which formed a 3–D network (**CuV–13**). Methylammonium plays a major role in the construction of the $[V_7F_6O_{30}]^{14-}$ by forming hydrogen bonding interactions with the three neighbouring $[VOF_5]^{3-}$ units of the

'superoctahedra'. **CuV–3** and **CuV–4** incorporating face–sharing dimeric vanadium oxyfluoride unit has been synthesised in two polymorphs. The major differences lie in *inter*–chain interactions mediated by hydrogen bonding through the dimethylamine counter cation, which in turn dictates the overall packing. Organic molecules are also found as a ligand bound directly to the vanadium oxyfluoride as a terminal group in **V–1**, **V–2**, **V–3**, **V–4** and **V–5**. In the presence of the copper cation, mostly the organoamine bound to copper (**CuV–3**, **CuV–4**, **CuV–5**, **CuV–6**, **CuV–7**, **CuV–8**, **CuV–9**, **CuV–10**, **CuV–11**, **CuV–12**, **CuV–13**, **CuMo–1**, **CuMo–3**, **CuMo–4**, **CuNb–2** and **CuNb–3**). In **CuV–8**, the copper centre contains two different nitorgen donor ligands, pyridine and ethylenediamine. However, in **CuV–1**, different organoamines, pyridine and imidazole are selectively bound to copper and vanadium respectively. The most common role of the organoamine compound is as a charge–compensating template in **CuV–1**, **CuV–2**, **CuV–3**, **CuV–4**, **CuV–7**, **CuV–13**, **V–6** and **V–7**. The organoamine acts as a ligand bound to a copper cation as a linker in **CuMo–2**, **CuMo–5**, **CuNb–1** and **CuNb–4**. Various organoamines were incorporated into the vanadium/molybdenum/niobium oxyfluoride system.

The final variable is the stoichiometry of the reactants, which was investigated based on 'composition–space' diagrams. This produced two novel 1–D chains (**CuV–9** and **CuV–10**) and a 2–D layer (**CuV–11**) material and helped to establish the diversity of products that can be synthesised solvothermally. Materials that were obtained as pure samples were examined using SQUID for interesting magnetic properties, TGA, microanalysis and fluorine analysis using a fluoride ion-selective electrode.

To establish trends in periodicity upon the products, niobium and molybdenum were investigated together with copper. It became clear that a number of novel structures could be synthesised, such as monomers, 1–D chains (**CuMo–2**, **CuMo–3**, **CuMo–4**, **CuNb–1**, **CuNb–2** and **CuNb–3**) and 2–D interpenetrated networks (**CuMo–5** and **CuNb–4**) and they were also characterised for their magnetic properties. The effect of changing the stoichiometry of the reactants was investigated based on 'composition–space' diagrams and the crystallisation fields were successfully mapped out.

As a part of our initial aim, Pb–containing members of the hilgardite family of borate halides were investigated simultaneously. $M_2B_5O_9X$ (M=Ca, Sr, Ba, Pb; X=Cl, Br) exhibit an abnormally large non-linear optical response. In order to establish any underlying crystal–chemical rationale, these phases were synthesised using conventional solid state techniques and with detailed crystallographic characterisation of the representative members of this series, $Pb_2B_5O_9Cl$, $Pb_2B_5O_9Br$, $Sr_2B_5O_9Cl$ and $Ba_2B_5O_9Cl$, using NPD. However, the crystallographic results suggest no significant or systematic change in the nature of the borate sublattice between these four members of the hilgardite family. It is concluded that the enhanced SHG response in Pb–containing hilgardites is due to the presence of the polarisable nature of Pb^{2+}, in particular the presence of a stereochemically active lone pair.

Overall this research produced the following materials which are of the greatest interest:

- An unusual hybrid 3–D framework solid with novel building units forming a doubly interpenetrated cubic lattice, which has been shown to have antiferromagnetic interactions.[1]

- Vanadium oxyfluoride chains incorporating covalently bound copper coordination complexes,[2] which contain interesting structural features. Some of them show interesting magnetic properties.

- A synthetic route based on 'composition-space' diagrams of the 2,2'–dipyridyl amine system produced three novel extended structures displaying magnetic properties.

- Organic–inorganic hybrid chains and layers constructed from copper-amine cations and niobium or molybdenum oxyfluorides, which reflect the influences of the organo amine ligands.[3]

- The hilgardite family of borate halides and their SHG properties.[4]

7.2 Opportunities for Further Research

Systematic synthetic studies were carried out based on 'composition–space' diagrams by varying the reaction composition to map out the crystallisation field within each reactant system. There are still vast solvothermal reaction domains remaining to be explored, such as pH, temperature, *etc*., and it may be anticipated that further novel structural features will be discovered in similar systems using parallel processing hydrothermal technique, in due course leading to novel physical properties.

It could be interesting to investigate further, based on a 'composition–space' diagram, the HF/pyridine/dimethylamine system using niobium or molybdenum instead of vanadium as discussed in section 4.6.2.1. Also, changing the secondary metal to nickel in the **CuV–13** system and investigation of the structural and property changes.

The key factors which govern the nature of the vanadium oxyfluoride units produced in the reactions, and also mode of linkage into chain fragments or other extended moieties, can only be determined with a considerable amount of further experimentation.

Further investigation is required in the magnetic analysis of **CuV–9**. Significantly higher fields, above 5000 Oe are required to confirm the presence of ferromagnetism.

References

1. T. Mahenthirarajah and P. Lightfoot, *Chem. Commun.,* **2008***, 1401-1403.

2. T. Mahenthirarajah, Y. Li, and P. Lightfoot, *Inorg. Chem.*, **2008**, *47*, 9097.

3. T. Mahenthirarajah, Y. Li, and P. Lightfoot, *Dalton Trans*., **2009**, 3280.

4. B. V. Egorova, A. V. Olenev, P. S. Berdonosov, A. N. Kuznetsov, S.Yu. Stefanovich, V. A. Dolgikh, T. Mahenthirarajah, P. Lightfoot, *J. Solid State Chem*., **2008**, 181, 1891.

Appendix–I

V–F–Cu

Compound	Overall dimensionality	Space group	Geometry of Cu	Geometry of V	Oxidation state of V / Cu
1.[pyH]$_2$[Cu(py)$_4$(VOF$_5$)$_2$]	0D	C2/c	(4+2) Octahedron	Octahedron	+5/+2
2. Cu(py)$_4$VOF$_4$	1D	C222$_1$	(4+2) Octahedron	Square pyramidal	+5/+2
3.[Cu(py)$_4$VOF$_4$][Cu(py)$_4$(H$_2$O)VOF$_4$].H$_2$O	1D	P2$_1$/m	(4+2) Octahedron	Square pyramidal	+4/+2

V–O–Cu

Compound	Overall dimensionality	Space group	Geometry of Cu	Geometry of V	Oxidation state of V / Cu
1.[{Cu$_2$(tpyprz)}$_2$V$_4$O$_{12}$]	2D	P2$_1$/c	Tetrahedron	Tetrahedron	+5/+1
2. [Cu$_3$(tpytrz)$_2$ (H$_2$O)$_2$V$_8$O$_{23}$].3H$_2$O	3D	Pbcn	(4+2) Octahedron	Tetrahedron	+5/+2
3. [{Cu(H$_2$O)(terpy)}V$_2$O$_6$]	0D	P2$_1$/n	(4+1) Square pyramidal	Tetrahedron	+5/+2

4. [{Cu(ttbterby)}V$_2$O$_6$]	0D	P2$_1$/c	(4+1) Square pyramidal	Tetrahedron	+5/+2
5. [C$_2$H$_5$)$_4$N]$_4$[Cu$_2$V$_8$O$_{24}$]	0D	P2$_1$/n	Square planar	Tetrahedron	+5,+4/+2
6. [{Cu(1,2−pn)$_2$}$_7${V$_{16}$O$_{38}$(H$_2$O)}$_2$].4H$_2$O	3D	P2$_1$/n	(4+2) Octahedron	Square pyramidal	+5,+4/+2
7. [Cu$_3$(triazolate)$_2$V$_4$O$_{12}$]	3D	P−1	Octahedron Square pyramidal	Tetrahedron	+5/+2
8. [Cu$_2$(tpyrpyz)$_2$V$_4$O$_{12}$]	1D	P−1	Octahedron	Tetrahedron	+5/+2
9. [Cu$_2$(pyrazine)V$_4$O$_{12}$]	3D	P−1	(4+1) Square pyramidal	Tetrahedron	+5/+2
10. [Cu(1,10–Phen)(H$_2$O)V$_2$O$_6$]	1D	P−1	(4+1) Square pyramidal	Tetrahedron	+5/+2
11. [Cu(bipy)]$_4$V$_4$O$_{12}$.2H$_2$O	3D	Cc	"T" shaped	Tetrahedron	+4/+1
12. [(en)$_2$Cu[V$_6$O$_{14}$]	2D	P2$_1$/n	(4+2) Octahedron	Square pyramidal Tetrahedron	+5,+4/+2
13. [(en)$_2$Cu]$_2$[V$_{10}$O$_{25}$]	2D	P−1	(4+2) Octahedron	Square pyramidal Tetrahedron	+5,+4/+2

14. [Cu(2,2'–bpy)]$_2$[V$_{12}$O$_{32}$]	2D	C2/m	(4+2) Octahedron	Square pyramidal Tetrahedron	+5/+2
15. [Cu(en)$_2$V$_6$O$_{14}$]	2D	P2$_1$/n	(4+2) Octahedron	Square pyramidal Tetrahedron	+5,+4/+2
16. [Cu(phen)V$_4$O$_{10}$	2D	P2$_1$/m	(4+1) Square pyramidal	Square pyramidal Tetrahedron	+5,+4/+2
17. β-[Cu(2,2'–bpy)V$_2$O$_6$]	1D	C2/c	(4+1) Square pyramidal	Square pyramidal Tetrahedron	+5/+2
18. β−[Cu(tpy)V$_2$O$_6$]	1D	P2$_1$/c	(4+1) Square pyramidal	Square pyramidal Tetrahedron	+5/+2
19. [Cu(4,4'–dpa)VO$_3$]	2D	P1	Trigonal planar Tetrahedron	Tetrahedron	+5/+1
20. [{Cu(phen)$_2$}$_4$V$_{10}$O$_{29}$].6H$_2$O	0D	P2$_1$/n	(4+1) Square pyramidal	Tetrahedron	+5/+2
21. [Cu(2,2'–bpy)V$_4$O$_{10.5}$]	2D	P−1	(4+1) Square pyramidal	Square pyramidal Tetrahedron	+5,+4/+2
22. [Cu(terpy)V$_2$O$_6$]	2D	Pbca	(4+2) Octahedron	Tetrahedron	+5/+2
23. [Cu$_2$(H$_2$O)$_2$(OH)$_2$(phen)$_2$] [Cu$_2$(OH)$_2$(phen)$_2$ (V$_4$O$_{12}$)].6H$_2$O	1D	P−1	(4+1) Square pyramidal	Tetrahedron	+5/+2

24. [Cu(eda)(V$_2$O$_6$)]	1D	P2$_1$/n	Square planar	Tetrahedron	+5/+2
25. [Cu(2,2'–dpy)V$_2$O$_6$]	1D	P−1	(4+1) Square pyramidal	Tetrahedron	+5/+2
26. [Cu(2,2'–dpy)$_2$V$_2$O$_6$]	1D	P2$_1$/a	Square pyramidal	Tetrahedron	+5/+2
27. [Cu(2,2'–bpy)V$_2$O$_6$]	1D	P2$_1$/c	Square pyramidal	Tetrahedron	+5/+2
28. [Cu$_4$(bpp)$_4$V$_4$O$_{12}$].3H$_2$O	3D	P2/c	Tetrahedron Trigonal planar	Tetrahedron	+5/+1
29. [Cu(bbi)$_2$V$_{10}$O$_{26}$][Cu(bbi)]$_2$.H$_2$O	3D	I222	(4+2) Octahedron Linear	Tetrahedron Tetragonal pyramid	+5,+4/+2,+1
30. [Cu$_2$(bisterpy)V$_4$O$_{12}$].2H$_2$O	2D	P−1	(4+1) Square pyramidal	Tetrahedron	+5/+2
31. [Cu$_2$(bisterpy)V$_4$F$_2$O$_{11}$]	2D	P−1	(4+1) Square pyramidal	Tetrahedron	+5/+2
32. [Cu$_2$ (2,2'–bpy)$_2$V$_4$O$_{12}$]	2D	P−1	(4+1) Square pyramidal	Tetrahedron	+5/+2
33. [Cu(4,4'–bpy)V$_4$O$_{10}$]	2D	P2$_1$/c	Trigonal planar	Tetragonal pyramid	+5,+4.5/+1

Appendix–II

Atomic co–ordinates of Vanadium Oxyfluorides

Atom	X	Y	Z	U_{iso}
Cu1	1.00000	0	1.00000	0.0367(5)
V1	0.6823(1)	−0.0258(2)	1.0791(1)	0.0365(5)
F1	0.6061(4)	0.0449(5)	1.1938(4)	0.046(1)
F2	0.6800(4)	−0.2065(5)	1.1487(4)	0.053(1)
O1	0.6288(4)	−0.0719(7)	0.9632(4)	0.041(2)
O2	0.8150(4)	−0.0057(6)	1.0736(5)	0.044(2)
N1	0.6595(5)	0.2069(7)	1.0400(5)	0.033(2)
N2	0.9440(5)	0.1024(8)	0.8668(5)	0.036(2)
N3	0.9312(6)	0.2520(8)	0.7276(5)	0.044(2)
N4	0.9675(5)	−0.1975(7)	0.9306(5)	0.034(2)
N5	0.9931(5)	−0.3910(8)	0.8304(5)	0.044(2)
C1	0.6989(5)	0.3083(8)	1.1104(5)	0.042(2)
C2	0.6915(5)	0.4585(8)	1.0903(5)	0.041(2)
C3	0.6446(7)	0.506(1)	0.9949(8)	0.047(2)
C4	0.6028(7)	0.406(1)	0.9248(7)	0.044(2)
C5	0.6097(7)	0.256(1)	0.9472(6)	0.038(2)
C6	0.8326(8)	0.113(1)	0.8295(7)	0.049(3)
C7	0.8259(8)	0.210(1)	0.7420(8)	0.050(3)
C8	0.9992(7)	0.1857(9)	0.8022(7)	0.037(2)
C9	0.9006(6)	−0.3114(9)	0.9603(7)	0.038(2)
C10	0.9174(7)	−0.431(1)	0.8988(7)	0.045(2)
C11	1.0216(6)	−0.243(1)	0.8518(7)	0.039(2)

Table 1 Atomic co–ordinates for **CuV–1**

Atom	X	Y	Z	U_{iso}
V1	1/2	0.18305(5)	3/4	0.0171(2)
F1	0.46952(9)	0.1528(1)	0.5191(2)	0.0214(3)
O1	1/2	−0.0262(2)	3/4	0.0219(5)
O2	1/2	0.3340(2)	3/4	0.0227(5)
N1	0.6321(1)	0.1641(2)	0.6988(2)	0.0189(4)
C1	0.6605(2)	0.0790(2)	0.5892(3)	0.0201(5)

C2	0.7459(2)	0.0624(2)	0.5638(3)	0.0231(5)
C3	0.8072(2)	0.1332(2)	0.6513(3)	0.0253(6)
C31	0.8999(2)	0.1141(3)	0.6303(4)	0.0382(7)
C4	0.7770(2)	0.2226(3)	0.7632(3)	0.0258(6)
C5	0.6909(2)	0.2347(2)	0.7821(3)	0.0227(5)

Table 2 Atomic co–ordinates for **V–1**

Atom	X	Y	Z	U_{iso}
V1	0	0.18401(8)	1/4	0.0272(3)
F1	−0.0219(2)	0.1527(2)	0.4751(3)	0.0303(6)
O1	0	-0.0232(4)	1/4	0.0305(9)
O2	0	0.3361(3)	1/4	0.033(1)
N1	0.1612(3)	0.1610(3)	0.3045(4)	0.0278(8)
C1	0.2010(3)	0.0857(4)	0.4248(5)	0.0313(9)
C2	0.3048(2)	0.0713(3)	0.4581(4)	0.034(1)
C3	0.3713(2)	0.1330(3)	0.3643(4)	0.035(1)
C4	0.3317(3)	0.2099(4)	0.2389(5)	0.036(1)
C5	0.2269(3)	0.2216(4)	0.2135(5)	0.0305(9)

Table 3 Atomic co–ordinates for **V–2**

Atom	X	Y	Z	U_{iso}
Cu1	0	0	0	0.0305(6)
V1	0.2636(2)	0.4803(2)	−0.2210(1)	0.0325(6)
O1	0.063(1)	0.6184(9)	−0.1657(5)	0.049(2)
O2	0.5399(8)	0.2996(7)	−0.2853(5)	0.022(1)
O3	0.132(1)	0.1351(8)	0.0370(5)	0.032(1)
F1	0.1272(8)	0.3680(7)	−0.2830(4)	0.041(1)
F2	0.3733(7)	0.2575(7)	−0.0874(4)	0.039(1)
F3	0.2279(8)	0.6512(6)	−0.3766(4)	0.040(1)
F4	0.4567(8)	0.5618(7)	−0.1776(4)	0.043(1)
N1	−0.312(2)	0.1831(8)	0.0525(5)	0.026(1)
N2	−0.0732(9)	0.1660(9)	−0.1793(5)	0.027(1)
N3	0.206(1)	1.2641(9)	−0.4786(5)	0.032(2)
N4	0.3586(9)	1.2836(9)	−0.6609(5)	0.031(2)
N11	0.446(1)	1.0528(9)	−0.7568(5)	0.035(2)

N31	0.130(1)	1.0235(9)	−0.3915(6)	0.039(2)
N41	0.304(1)	1.5023(9)	−0.5591(5)	0.034(2)
C1	0.361(1)	1.1218(9)	−0.6674(7)	0.035(2)
C2	0.279(1)	1.029(1)	−0.5757(6)	0.032(2)
C3	0.210(1)	1.100(1)	−0.4834(7)	0.031(2)
C4	0.292(1)	1.354(1)	−0.5671(7)	0.038(2)

Table 4 Atomic co–ordinates for **CuV–2**

Atom	X	Y	Z	U_{iso}
V1	0.60804(3)	0.04145(3)	0.56693(2)	0.0130(1)
F1	0.4901(1)	0.0353(1)	0.65025(7)	0.0186(3)
O1	0.5144(1)	0.0993(1)	0.48673(8)	0.0112(3)
O2	0.7126(2)	0.1326(1)	0.60031(9)	0.0189(4)
N1	0.7581(2)	−0.0207(1)	0.4846(1)	0.0122(4)
N2	0.7096(2)	−0.0927(1)	0.6316(1)	0.0129(4)
C1	0.7820(2)	0.0274(2)	0.4121(1)	0.0156(5)
C2	0.8851(2)	−0.0061(1)	0.3614(1)	0.0182(5)
C3	0.9647(2)	−0.0916(1)	0.3860(1)	0.0183(5)
C4	0.9404(2)	−0.1420(2)	0.4605(1)	0.0159(5)
C5	0.8363(2)	−0.1043(2)	0.5090(1)	0.0127(4)
C6	0.8048(2)	−0.1480(2)	0.5914(1)	0.0123(4)
C7	0.8667(2)	−0.2375(2)	0.6264(1)	0.0163(5)
C8	0.8293(2)	−0.2716(2)	0.7044(1)	0.0167(5)
C9	0.7328(2)	−0.2136(2)	0.7460(1)	0.0160(5)
C10	0.6759(2)	−0.1246(2)	0.7081(1)	0.0153(5)

Table 5 Atomic co–ordinates for **V–3**

Atom	X	Y	Z	U_{iso}
V1	0.3234(1)	0.3485(1)	0.3694(1)	0.0290(4)
F1	0.4335(4)	0.1726(4)	0.3307(4)	0.0349(9)
O2	0.3978(4)	0.4738(5)	0.5827(4)	0.0244(9)
O1	0.1167(5)	0.2487(5)	0.3280(5)	0.033(1)
N1	0.2447(6)	0.5720(6)	0.3383(5)	0.028(1)
N2	0.3203(5)	0.3056(6)	0.1152(5)	0.024(1)
C1	0.1994(7)	0.7021(8)	0.4531(7)	0.033(1)

C2	0.1473(5)	0.8393(5)	0.4252(5)	0.033(1)
C3	0.1416(5)	0.8495(5)	0.2801(5)	0.032(1)
C4	0.1869(7)	0.7131(8)	0.1568(7)	0.032(1)
C5	0.2355(7)	0.5756(7)	0.1926(7)	0.027(1)
C6	0.2782(7)	0.4312(7)	0.0723(6)	0.027(1)
C7	0.2728(7)	0.4244(7)	−0.0832(6)	0.026(1)
C8	0.2195(7)	0.5625(8)	−0.1198(7)	0.033(1)
C9	0.1771(7)	0.6993(8)	−0.0058(7)	0.031(1)
C10	0.3179(7)	0.2779(7)	−0.1967(7)	0.026(1)
C11	0.3628(7)	0.1511(8)	−0.1503(7)	0.032(1)
C12	0.3609(7)	0.1680(7)	0.0054(7)	0.029(1)

Table 6 Atomic co–ordinates for **V–4**

Atom	X	Y	Z	U_{iso}
V1	0.89920(9)	0.10768(5)	0.55633(3)	0.0277(3)
F1	0.8620(3)	0.0018(2)	0.4546(1)	0.0220(5)
F2	0.6678(3)	0.1779(2)	0.5369(1)	0.0318(6)
O1	0.9879(3)	0.1720(2)	0.6400(1)	0.0252(6)
N1	1.0325(4)	0.2505(3)	0.4882(2)	0.0235(7)
N2	0.7575(4)	−0.0322(3)	0.6211(1)	0.0213(7)
C1	1.2244(5)	0.2735(3)	0.4963(2)	0.0271(8)
C2	1.3141(6)	0.3702(3)	0.4581(2)	0.0297(9)
C3	1.2041(6)	0.4469(3)	0.4094(2)	0.0331(9)
C31	1.2955(5)	0.5520(3)	0.3653(2)	0.050(1)
C4	1.0059(5)	0.4236(3)	0.4018(2)	0.0347(9)
C5	0.9254(5)	0.3269(3)	0.4422(2)	0.0292(9)
C6	0.8593(6)	−0.0959(3)	0.6772(2)	0.0297(9)
C7	0.7748(6)	−0.1822(4)	0.7243(2)	0.038(1)
C8	0.5759(6)	−0.2066(3)	0.7162(2)	0.036(1)
C81	0.4794(9)	−0.3035(4)	0.7649(3)	0.063(2)
C9	0.4718(5)	−0.1397(4)	0.6602(2)	0.0290(8)
C10	0.5653(5)	−0.0553(3)	0.6138(2)	0.0228(8)

Table 7 Atomic co–ordinates for **V–5**

Atom	X	Y	Z	U$_{iso}$
V1	0.7919(1)	0.05982(9)	0.09830(8)	0.0286(4)
F1	0.5967(3)	0.2017(3)	−0.0236(3)	0.0330(7)
F2	0.9044(4)	0.2548(3)	0.0874(3)	0.0364(7)
F3	0.9590(3)	0.0817(3)	−0.1307(3)	0.0306(6)
O1	0.7426(5)	−0.1568(5)	0.0489(4)	0.0344(8)
O2	0.6747(5)	0.0287(4)	0.2688(4)	0.0393(8)
N1	0.7279(5)	0.3554(5)	−0.3247(4)	0.0314(9)
C11	0.7509(8)	0.0900(6)	−0.3978(6)	0.041(1)
C1	0.7520(6)	0.2789(6)	−0.4413(5)	0.033(1)
C2	0.7769(7)	0.3795(7)	−0.5894(6)	0.043(1)
C3	0.7728(8)	0.5527(7)	−0.6136(6)	0.047(1)
C4	0.7484(7)	0.6268(7)	−0.4922(6)	0.045(1)
C5	0.7256(7)	0.5250(6)	−0.3451(6)	0.038(1)
C51	0.7013(9)	0.5891(7)	−0.2026(6)	0.053(2)

Table 8 Atomic co–ordinates for **V–6**

Atom	X	Y	Z	U$_{iso}$
V1	−0.2982(1)	−0.00151(8)	0.13134(9)	0.0121(5)
F1	−0.4698(4)	−0.1064(3)	−0.1005(3)	0.0129(7)
F2	−0.1180(4)	−0.1420(3)	0.0853(4)	0.0180(7)
F3	−0.4517(4)	−0.1663(3)	0.1908(3)	0.0159(7)
O1	−0.1982(5)	0.1493(4)	0.0063(4)	0.0153(8)
O2	−0.1881(5)	0.0944(4)	0.3026(4)	0.0197(9)
N1	0.3007(5)	0.3115(4)	0.5829(5)	0.0128(9)
C1	0.2960(7)	0.4659(6)	0.6303(6)	0.018(1)
C11	0.3425(8)	0.5276(6)	0.8054(6)	0.021(1)
C2	0.2513(8)	0.5568(6)	0.5201(7)	0.020(1)
C3	0.2119(7)	0.4886(6)	0.3604(6)	0.018(1)
C31	0.1690(8)	0.5884(7)	0.2381(7)	0.027(1)
C4	0.2203(7)	0.3289(6)	0.3163(6)	0.019(1)
C5	0.2639(7)	0.2388(5)	0.4303(6)	0.017(1)
C51	0.2734(7)	0.0672(6)	0.3936(6)	0.018(1)

Table 9 Atomic co–ordinates for **V–7**

Atom	X	Y	Z	U$_{iso}$
V1	0.92360(7)	0.1756(1)	−0.69919(5)	0.061(1)
Cu1	1.00000	0	−1/2	0.058(1)
F1	0.9003(2)	0.3489(4)	−0.6574(2)	0.070(1)
F2	0.9607(2)	0.1091(3)	−0.6051(2)	0.062(1)
F3	1.00000	0.0394(5)	−3/4	0.060(2)
F4	0.9377(2)	0.2598(3)	−0.7961(2)	0.063(1)
O1	0.8291(3)	0.1064(5)	−0.7068(2)	0.066(2)
N1	0.8941(3)	0.0895(5)	−0.4485(3)	0.060(2)
N2	1.0744(3)	0.1654(5)	−0.4718(3)	0.060(2)
N3	1.00000	0.5166(8)	−3/4	0.073(2)
C1	0.8533(4)	0.2001(7)	−0.4762(3)	0.064(2)
C2	0.7862(4)	0.2639(7)	−0.4397(3)	0.067(2)
C3	0.7575(4)	0.2133(7)	−0.3721(3)	0.069(2)
C4	0.7985(4)	0.0987(7)	−0.3443(3)	0.067(2)
C5	0.8666(4)	0.0392(7)	−0.3833(3)	0.066(2)
C6	1.0640(4)	0.2895(6)	−0.5035(4)	0.065(2)
C7	1.1063(4)	0.4026(7)	−0.4765(4)	0.075(2)
C8	1.09650	0.48720	−0.49820	0.080(2)
C9	1.1636(4)	0.3918(8)	−0.4171(4)	0.074(2)
C10	1.1756(4)	0.2632(7)	−0.3867(4)	0.065(2)
C11	1.1305(4)	0.1540(6)	−0.4147(4)	0.095(3)

Table 10 Atomic co–ordinates for **CuV–3**

Atom	X	Y	Z	U$_{iso}$
Cu1	1/2	1.00000	1/2	0.0285(4)
Cu2	1/2	1/2	1.00000	0.0313(4)
V1	0.6947(2)	0.7289(1)	0.6254(1)	0.0283(4)
V2	0.4251(2)	0.6314(1)	0.7274(1)	0.0292(4)
F1	0.8264(7)	0.6754(4)	0.4858(4)	0.038(1)
F2	0.5975(6)	0.8548(4)	0.5757(4)	0.035(1)
F3	0.4946(6)	0.7556(4)	0.7556(4)	0.034(1)
F4	0.7064(7)	0.5886(4)	0.6657(4)	0.035(1)
F5	0.4955(6)	0.6752(4)	0.5860(4)	0.031(1)
F6	0.4447(7)	0.4980(4)	0.6713(4)	0.039(1)
F7	0.4606(7)	0.5732(5)	0.8509(4)	0.042(1)
O1	0.8171(9)	0.7610(6)	0.6731(6)	0.043(2)
O2	0.2305(8)	0.6835(5)	0.7680(5)	0.038(2)
N1	0.5194(9)	0.9112(6)	0.3722(6)	0.031(2)

N2	0.7360(9)	1.0090(6)	0.4290(6)	0.031(2)
N3	0.684(1)	0.3803(6)	0.9084(6)	0.037(2)
N4	0.672(1)	0.5758(6)	0.9920(6)	0.037(2)
N5	0.765(1)	0.4896(7)	0.4390(8)	0.052(2)
C1	0.526(1)	0.8107(7)	0.3773(8)	0.037(2)
C2	0.518(2)	0.7540(9)	0.296(1)	0.053(3)
C3	0.510(2)	0.799(1)	0.207(1)	0.060(3)
C4	0.508(2)	0.9016(9)	0.1992(9)	0.055(3)
C5	0.516(1)	0.9541(8)	0.2836(8)	0.044(2)
C6	0.866(1)	0.9310(8)	0.4308(7)	0.036(2)
C7	1.027(1)	0.9388(8)	0.3888(8)	0.041(2)
C8	1.0556(1)	1.0258(8)	0.3404(8)	0.042(2)
C9	0.922(1)	1.1054(9)	0.340(1)	0.052(3)
C10	0.768(1)	1.0929(8)	0.3838(9)	0.041(2)
C11	0.738(2)	0.2925(9)	0.950(1)	0.052(3)
C12	0.877(2)	0.217(1)	0.895(1)	0.073(4)
C13	0.967(2)	0.234(2)	0.789(1)	0.084(5)
C14	0.908(2)	0.315(1)	0.747(1)	0.057(3)
C15	0.768(1)	0.3887(9)	0.8058(8)	0.045(2)
C16	0.745(1)	0.5671(7)	1.0632(8)	0.036(2)
C17	0.867(1)	0.6149(9)	1.0552(8)	0.042(2)
C18	0.914(1)	0.6737(9)	0.9740(9)	0.046(2)
C19	0.838(1)	0.681(1)	0.9017(9)	0.050(3)
C20	0.719(2)	0.634(1)	0.9104(8)	0.051(3)
C21	0.901(2)	0.484(1)	0.343(1)	0.058(3)
C22	0.791(1)	0.395(1)	0.495(1)	0.057(3)

Table 11 Atomic co–ordinates for **CuV–4**

Atom	X	Y	Z	U_{iso}
Cu1	1/2	−1/2	0	0.0248(7)
V1	1/2	−1/2	−1/4	0.0685(1)
F1	1/2	−1/2	−0.1401(4)	0.030(1)
F2	0.644(2)	−0.356(2)	−1/4	0.043(6)
F21	1/2	−0.294(3)	−1/4	0.054(7)
F22	0.583(2)	−0.314(2)	−0.2475(7)	0.054(5)
N1	0.4151(5)	−0.2903(5)	0	0.025(1)
C1	0.3853(5)	−0.2195(5)	−0.0672(3)	0.032(1)
C2	0.3273(6)	−0.0781(5)	−0.0689(3)	0.039(1)

C3	0.2970(8)	−0.0061(6)	0	0.035(2)
C4	0.302(2)	−0.008(1)	−0.1505(8)	0.053(3)

Table 12 Atomic co–ordinates for **CuV–5**

Atom	X	Y	Z	U_{iso}
Cu1	0	0	1/2	0.0378(8)
V1	0	0	1/4	0.064(1)
F1	0	0	0.3602(3)	0.043(1)
F2	−0.1772(9)	0	1/4	0.107(5)
N1	−0.1845(4)	0.0647(4)	1/2	0.039(1)
C3	−0.4346(5)	0.1619(6)	1/2	0.053(2)
C1	−0.2471(4)	0.0882(5)	0.4334(3)	0.059(2)
C4	−0.5693(6)	0.2140(7)	1/2	0.064(2)
C2	−0.3708(4)	0.1344(5)	0.4327(3)	0.065(2)
O1	−0.5000(4)	0.5000(5)	0.2500(3)	0.33(3)
O2	−0.3804(4)	0.1703(5)	0.2206(3)	0.32(1)

Table 13 Atomic co–ordinates for **CuV–6**

Atom	X	Y	Z	U_{iso}
Cu1	1.00000	0	0	0.0152(2)
V1	0.65205(4)	0.03209(5)	0.04208(4)	0.0127(2)
F1	0.6549(2)	−0.1027(2)	0.1496(1)	0.0181(4)
F2	0.6992(2)	0.1567(2)	0.1609(1)	0.0191(4)
F3	0.6123(2)	0.1831(2)	−0.0546(1)	0.0184(4)
F4	0.4643(2)	0.0725(2)	0.0671(1)	0.0170(4)
O1	0.7812(2)	−0.0066(2)	0.0117(2)	0.0197(5)
N1	1.0190(2)	0.1686(3)	0.0900(2)	0.0184(6)
N2	1.0065(3)	0.3082(3)	0.2206(2)	0.0274(7)
N3	0.9614(2)	0.1146(3)	−0.1342(2)	0.0171(5)
N4	0.9831(3)	0.2558(3)	−0.2604(2)	0.0214(6)
N5	0.7124(3)	0.5760(3)	0.1335(2)	0.0266(7)
N6	0.6730(3)	0.4172(3)	0.0174(2)	0.0243(6)
C1	0.9940(3)	0.1827(4)	0.1865(3)	0.0252(7)
C2	1.0410(4)	0.3808(4)	0.1420(3)	0.0311(8)
C3	1.0491(4)	0.2950(4)	0.0620(3)	0.0301(8)

C4	1.0409(3)	0.1663(3)	−0.1875(2)	0.0182(6)
C5	0.8596(3)	0.2622(3)	−0.2551(3)	0.0244(7)
C6	0.8467(3)	0.1743(3)	−0.1765(3)	0.0211(7)
C7	0.7177(3)	0.4457(4)	0.1208(3)	0.0236(7)
C8	0.6618(4)	0.6329(4)	0.0344(3)	0.0331(9)
C9	0.6380(4)	0.5332(4)	−0.0376(3)	0.0331(9)

Table 14 Atomic co–ordinates for **CuV–7**

Atom	X	Y	Z	U_{iso}
Cu1	0.32139(7)	0.08938(7)	0.25267(6)	0.0178(2)
V1	0.6465(1)	0.29285(9)	0.06754(9)	0.0186(3)
V2	0.3488(1)	0.32916(9)	0.07223(8)	0.0144(3)
O1	0.6976(4)	0.4146(4)	0.0207(4)	0.024(1)
O2	0.6565(5)	0.3002(4)	0.1866(4)	0.029(1)
O3	0.4902(4)	0.2676(4)	0.0304(3)	0.023(1)
O4	0.7381(4)	0.1725(4)	0.0250(4)	0.022(1)
O5	0.2982(4)	0.2552(4)	0.1679(3)	0.022(1)
O6	0.3708(4)	0.4662(4)	0.1024(3)	0.021(1)
N1	0.3287(6)	−0.0256(5)	0.1437(4)	0.022(1)
N2	0.5059(5)	0.0840(4)	0.2435(4)	0.018(1)
N3	0.1370(5)	0.0601(4)	0.2625(4)	0.017(1)
N4	0.3217(5)	0.1793(4)	0.3795(4)	0.019(1)
C1	0.4484(6)	−0.0186(7)	0.0952(5)	0.023(2)
C2	0.5434(6)	−0.0060(6)	0.1739(5)	0.025(2)
C3	0.0937(6)	−0.0166(6)	0.3276(6)	0.023(2)
C4	−0.0285(7)	−0.0499(6)	0.3305(5)	0.024(2)
C5	−0.1084(6)	−0.0016(7)	0.2658(5)	0.027(2)
C6	−0.0637(7)	0.0767(7)	0.1978(6)	0.034(2)
C7	0.0589(6)	0.1057(7)	0.1986(5)	0.025(2)
C8	0.3921(7)	0.1514(6)	0.4561(6)	0.027(2)
C9	0.3837(8)	0.2116(7)	0.5442(6)	0.032(2)
C10	0.3003(8)	0.3011(7)	0.5520(7)	0.036(2)
C11	0.2309(7)	0.3306(7)	0.4755(7)	0.031(2)
C12	0.2419(7)	0.2671(6)	0.3896(6)	0.026(2)

Table 15 Atomic co–ordinates for **CuV–8**

Atom	X	Y	Z	U_{iso}
Cu1	0.4490(1)	0.03014(9)	0.65337(9)	0.0239(3)
V1	0.8803(1)	−0.1760(1)	0.5942(1)	0.0219(4)
F1	0.4158(5)	−0.1207(5)	0.5640(4)	0.0262(9)
O1	1.0130(6)	−0.3546(6)	0.6812(5)	0.030(1)
O2	1.00000	0	1/2	0.043(2)
O3	0.7143(6)	−0.1502(6)	0.7348(5)	0.027(1)
O4	0.8027(6)	−0.2024(6)	0.4569(5)	0.024(1)
N1	0.2914(7)	−0.0761(6)	0.8608(6)	0.019(1)
N2	0.5009(7)	0.2018(6)	0.7141(6)	0.019(1)
N3	0.3160(7)	0.1145(6)	0.9701(6)	0.022(1)
C1	0.2176(8)	−0.2105(8)	0.8792(7)	0.022(1)
C2	0.1086(9)	−0.2974(9)	1.0191(8)	0.028(2)
C3	0.0660(9)	−0.2430(9)	1.1465(8)	0.027(2)
C4	0.1385(8)	−0.1087(8)	1.1281(8)	0.024(1)
C5	0.2510(8)	−0.0264(7)	0.9836(7)	0.020(1)
C6	0.6155(8)	0.3119(8)	0.6045(7)	0.021(1)
C7	0.6502(9)	0.4460(8)	0.6232(8)	0.029(2)
C8	0.5574(9)	0.4767(8)	0.7587(8)	0.028(2)
C9	0.4476(9)	0.3643(8)	0.8738(8)	0.024(1)
C10	0.4228(9)	0.2271(8)	0.8482(8)	0.023(1)

Table 16 Atomic co–ordinates for **CuV–9**

Atom	X	Y	Z	U_{iso}
Cu1	0.1804(2)	0.3693(2)	0.39775(9)	0.0226(5)
Cu2	0.6520(2)	0.3794(2)	0.09975(9)	0.0220(5)
V1	-0.0054(3)	0.2257(3)	0.2438(1)	0.0203(6)
V2	0.4976(3)	0.2212(3)	0.2489(1)	0.0209(6)
F1	0.072(1)	0.1892(9)	0.3557(4)	0.026(2)
F2	0.075(1)	0.4229(9)	0.2955(4)	0.025(2)
F3	0.250(1)	0.2326(9)	0.2062(4)	0.026(2)
F4	0.435(1)	0.3151(9)	0.3472(4)	0.026(2)
F5	0.754(1)	0.2648(9)	0.2878(4)	0.023(2)
F6	0.541(1)	0.4227(9)	0.2009(4)	0.027(2)
F7	0.579(1)	0.1915(9)	0.1350(5)	0.027(2)
F8	0.931(1)	0.3326(9)	0.1513(4)	0.026(2)
O1	−0.049(1)	0.065(1)	0.2139(6)	0.025(2)
O2	0.492(1)	0.058(1)	0.2712(5)	0.027(2)
N1	0.275(2)	0.561(1)	0.4252(6)	0.025(3)

N2	0.184(2)	0.314(1)	0.5116(6)	0.025(3)
N3	0.230(2)	0.547(1)	0.5649(6)	0.027(3)
N4	0.706(2)	0.312(1)	−0.0112(7)	0.027(3)
N5	0.702(2)	0.581(1)	0.0767(6)	0.024(3)
N6	0.816(2)	0.538(1)	−0.0546(6)	0.024(3)
C1	0.335(1)	0.640(1)	0.3609(6)	0.026(3)
C2	0.382(1)	0.778(1)	0.3672(6)	0.029(3)
C3	0.375(2)	0.850(2)	0.4446(8)	0.030(3)
C4	0.326(2)	0.770(2)	0.5093(8)	0.026(3)
C5	0.277(1)	0.626(2)	0.4973(8)	0.024(3)
C6	0.200(1)	0.409(2)	0.5748(7)	0.021(3)
C7	0.187(2)	0.362(2)	0.6550(7)	0.024(3)
C8	0.154(2)	0.220(2)	0.6671(8)	0.028(3)
C9	0.132(2)	0.122(2)	0.6012(8)	0.029(3)
C10	0.153(2)	0.171(2)	0.5250(9)	0.032(3)
C11	0.680(1)	0.171(1)	−0.0299(5)	0.020(3)
C12	0.722(1)	0.107(1)	−0.1026(5)	0.028(3)
C13	0.797(2)	0.195(2)	−0.1605(8)	0.025(3)
C14	0.827(2)	0.337(2)	−0.1455(8)	0.028(3)
C15	0.781(2)	0.395(2)	−0.0693(7)	0.023(3)
C16	0.782(2)	0.629(2)	0.0094(7)	0.026(3)
C17	0.835(2)	0.769(2)	0.0009(8)	0.025(3)
C18	0.804(2)	0.870(2)	0.0618(8)	0.028(3)
C19	0.709(2)	0.820(2)	0.1312(8)	0.027(3)
C20	0.664(2)	0.680(2)	0.1358(8)	0.023(3)

Table 17 Atomic co–ordinates for **CuV–10**

Atom	X	Y	Z	U_{iso}
Cu1	0.62651(8)	0.17630(5)	0.19169(6)	0.0083(2)
V1	0.8154(1)	−0.06586(7)	0.38154(8)	0.0068(2)
V2	0.3264(1)	−0.09795(7)	0.41782(8)	0.0067(2)
V3	0.2298(1)	−0.05041(8)	0.10140(8)	0.0081(2)
O1	0.7901(5)	−0.2263(3)	0.3395(4)	0.0124(7)
O2	0.5794(5)	−0.0452(3)	0.4269(3)	0.0102(7)
O3	0.9033(5)	0.0316(3)	0.5662(3)	0.0112(7)
O4	0.7477(5)	0.0112(3)	0.2434(3)	0.0090(7)
O5	0.3404(5)	−0.2349(3)	0.4831(4)	0.0139(8)
O6	0.2222(5)	−0.1426(3)	0.2388(3)	0.0098(7)
O7	0	0	0	0.015(1)

O9	0.3803(5)	0.0859(3)	0.1756(4)	0.0133(8)
O8	0.3211(5)	−0.1419(3)	0.0070(4)	0.0161(8)
N1	0.4787(6)	0.3275(4)	0.1216(4)	0.0109(9)
N2	0.8698(6)	0.2967(4)	0.2709(4)	0.0095(8)
N3	0.7003(6)	0.4883(4)	0.2878(4)	0.0107(9)
C1	0.3125(7)	0.2967(5)	0.0108(5)	0.012(1)
C2	0.1902(7)	0.3914(5)	−0.0411(5)	0.015(1)
C3	0.2358(7)	0.5236(5)	0.0235(5)	0.012(1)
C4	0.4038(7)	0.5555(5)	0.1348(5)	0.013(1)
C5	0.5254(7)	0.4543(5)	0.1801(5)	0.011(1)
C6	0.8742(7)	0.4286(4)	0.3061(5)	0.007(1)
C7	1.0479(8)	0.5102(5)	0.3640(5)	0.015(1)
C8	1.2222(7)	0.4549(5)	0.3815(5)	0.012(1)
C9	1.2201(7)	0.3182(5)	0.3413(5)	0.014(1)
C10	1.0425(7)	0.2441(5)	0.2879(5)	0.010(1)

Table 18 Atomic co–ordinates for **CuV–11**

Atom	X	Y	Z	U_{iso}
Cu1	−0.20767(6	1.2591(1)	0.0758(1)	0.0619(6)
Cu2	−0.13048(5	0.76181(9)	0.07836(8)	0.0322(4)
Cu3	−0.45955(5	0.75006(8)	0.75852(9)	0.0351(4)
V1	−0.17823(7	1.1011(1)	0.2410(1)	0.0352(5)
V2	−0.10706(8	0.9286(1)	0.2297(1)	0.0390(6)
V3	−0.15337(7	0.5828(1)	−0.0720(1	0.0325(5)
V4	−0.24205(7	0.4296(1)	−0.0664(1	0.0343(5)
V5	−0.48882(8	0.5939(2)	0.5956(1)	0.0507(7)
V6	−0.4325(1)	0.9238(1)	0.9008(1)	0.0712(9)
O1	−0.1284(5)	1.1642(9)	0.2676(8)	0.111(5)
O2	−0.1969(4)	1.1608(6)	0.1751(6)	0.096(5)
O3	−0.2230(6)	1.0912(7)	0.3309(7)	0.135(7)
O4	−0.1352(8)	1.0247(8)	0.2063(7)	0.179(9)
O5	−0.0385(3)	0.9349(6)	0.2308(5)	0.054(3)
O6	−0.1176(3)	0.8644(6)	0.1592(4)	0.050(2)
O7	−0.1536(3)	0.6674(5)	−0.0177(4	0.039(2)
O8	−0.1016(3)	0.5282(5)	−0.0526(5	0.049(2)
O9	−0.1430(3)	0.6084(5)	−0.1759(4	0.036(2)
O10	−0.2195(3)	0.5300(5)	−0.0448(5	0.041(2)
O11	−0.3106(3)	0.4272(5)	−0.0492(5	0.046(2)
O12	−0.2185(3)	0.3635(7)	−0.0110(7	0.089(4)

O13	−0.4511(9)	0.5971(8)	0.5061(6)	0.19(1)
O14	−0.5378(6)	0.665(1)	0.5649(9)	0.129(5)
O15	−0.4738(4)	0.6537(5)	0.6633(4)	0.058(3)
O16	−0.4495(3)	0.8504(4)	0.8444(5)	0.035(2)
O17	−0.3607(6)	0.9322(8)	0.8801(7)	0.107(5)
O18	−0.4662(6)	1.0161(6)	0.8707(6)	0.118(5)
N1	−0.1345(4)	1.3128(8)	0.0959(7)	0.062(4)
N2	−0.2537(4)	1.3227(7)	0.1654(8)	0.064(4)
N3	−0.1634(4)	1.1895(8)	−0.0116(6	0.058(4)
N4	−0.2809(4)	1.2023(8)	0.0566(8)	0.071(4)
N5	−0.0580(4)	0.7068(6)	0.0975(5)	0.032(2)
N6	−0.2037(3)	0.8177(6)	0.0597(6)	0.038(2)
N7	−0.1746(3)	0.6942(6)	0.1672(5)	0.036(2)
N8	−0.0847(3)	0.8244(6)	−0.0140(5	0.030(2)
N9	−0.5034(3)	0.6802(5)	0.8469(5)	0.028(2)
N10	−0.4138(3)	0.8145(5)	0.6681(6)	0.038(3)
N11	−0.5325(3)	0.8064(5)	0.7404(5)	0.031(2)
N12	−0.3853(4)	0.6946(6)	0.7765(6)	0.037(2)
C1	−0.1303(5)	1.3917(9)	0.0965(9)	0.058(4)
C55	−0.5358(4)	0.8875(6)	0.7361(7)	0.037(3)
C30	−0.2044(4)	0.8984(7)	0.0566(6)	0.027(2)
C20	−0.3009(6)	1.1436(9)	0.1069(9)	0.062(4)
C50	−0.3681(5)	0.8582(7)	0.6802(9)	0.049(3)
C56	−0.3630(5)	0.6366(7)	0.7259(8)	0.048(3)
C26	−0.2496(4)	0.7779(7)	0.0446(7)	0.035(3)
C24	0.0090(4)	0.6002(8)	0.0678(7)	0.040(3)
C57	−0.3135(5)	0.5929(7)	0.7395(7)	0.040(3)
C19	−0.3488(8)	1.1001(9)	0.0908(8)	0.077(5)
C23	0.0370(5)	0.6221(8)	0.1292(7)	0.042(3)
C25	−0.0383(4)	0.6457(7)	0.0543(6)	0.032(3)
C29	−0.2504(5)	0.9389(8)	0.0385(7)	0.044(3)
C27	−0.2979(4)	0.8151(8)	0.0275(7)	0.044(3)
C22	0.0163(4)	0.6883(8)	0.1741(7)	0.040(3)
C28	−0.2983(5)	0.8988(8)	0.0231(7)	0.041(3)
C40	−0.1004(4)	0.8210(7)	-0.0865(6)	0.034(3)
C38	−0.0210(5)	0.9061(7)	−0.1414(8	0.043(3)
C53	−0.6291(5)	0.8851(8)	0.6981(7)	0.044(3)
C36	−0.0378(4)	0.8672(7)	−0.0054(6	0.031(3)
C46	−0.4311(5)	0.8197(7)	0.5971(9)	0.053(4)
C59	−0.3128(5)	0.6690(8)	0.8581(8)	0.046(3)
C37	−0.0061(5)	0.9091(7)	−0.0669(7	0.039(3)
C39	−0.0694(5)	0.8649(7)	−0.1497(8	0.044(3)
C43	−0.5588(4)	0.5824(7)	0.9681(7)	0.036(3)

C42	−0.5367(5)	0.5538(6)	0.8946(8)	0.045(3)
C51	−0.5785(5)	0.7648(8)	0.7220(7)	0.040(3)
C5	−0.0908(5)	1.272(1)	0.1157(8)	0.059(4)
C54	−0.5829(5)	0.9261(8)	0.7181(7)	0.046(3)
C58	−0.2893(5)	0.6104(7)	0.8031(8)	0.044(3)
C41	−0.5107(4)	0.6038(7)	0.8350(7)	0.032(3)
C44	−0.5510(5)	0.6625(8)	0.9787(8)	0.051(4)
C48	−0.3545(6)	0.9046(8)	0.546(1)	0.062(4)
C34	−0.2185(5)	0.6761(8)	0.3011(7)	0.043(3)
C47	−0.4022(5)	0.8632(7)	0.5349(9)	0.052(4)
C45	−0.5235(5)	0.7097(6)	0.9196(8)	0.055(4)
C35	−0.1935(5)	0.7226(8)	0.2409(7)	0.041(3)
C11	−0.1501(5)	1.2162(9)	−0.0860(9	0.057(4)
C52	−0.6258(4)	0.8019(8)	0.7044(7)	0.041(3)
C21	−0.0305(4)	0.7274(8)	0.1574(7)	0.043(3)
C33	−0.2260(4)	0.5974(8)	0.2904(8)	0.044(3)
C60	−0.3603(5)	0.7098(7)	0.8384(9)	0.046(3)
C10	−0.2382(5)	1.3262(8)	0.236(1)	0.059(4)
C32	−0.2071(7)	0.5664(9)	0.2182(9)	0.077(5)
C49	−0.3373(6)	0.9036(8)	0.619(1)	0.070(5)
C7	−0.3329(5)	1.4080(9)	0.214(1)	0.078(6)
C4	−0.0425(5)	1.307(1)	0.1377(8)	0.060(4)
C31	−0.1813(7)	0.6127(9)	0.1578(8)	0.072(5)
C8	−0.3148(6)	1.4112(9)	0.286(1)	0.079(6)
C3	−0.0388(5)	1.389(1)	0.1391(8)	0.064(5)
C15	−0.1472(5)	1.1131(9)	0.0038(9)	0.066(5)
C6	−0.2990(5)	1.3655(9)	0.155(1)	0.082(6)
C18	−0.3758(5)	1.1169(9)	0.0286(9)	0.062(4)
C14	−0.1191(5)	1.068(1)	−0.0557(8	0.060(4)
C2	−0.0851(5)	1.433(1)	0.1180(8)	0.067(5)
C12	−0.1199(5)	1.174(1)	−0.1455(9	0.066(5)
C13	−0.1044(6)	1.095(1)	−0.1325(9	0.071(5)
C9	−0.2661(5)	1.3701(8)	0.297(1)	0.064(4)
C16	−0.3076(6)	1.218(1)	−0.007(1)	0.105(8)
C17	−0.3536(6)	1.178(1)	−0.020(1)	0.101(8)

Table 19 Atomic co–ordinates for **CuV–12**

Atom	X	Y	Z	U_{iso}
Cu1	3/4	¼	1/4	0.0101(3)
V1	0.51443(5)	¼	1/4	0.0161(3)
V2	1/4	¼	1/4	0.0268(6)
F1	0.49363(9)	0.36291(8)	0.24372(8)	0.0234(4)
F2	0.3678(2)	¼	1/4	0.0292(8)
O1	0.6141(2)	¼	1/4	0.0174(7)
N1	3/4	0.3373(1)	0.1627(1)	0.0127(6)
N2	0.3812(1)	0.3812(1)	0.1188(1)	0.0167(8)
C1	0.6933(1)	0.3376(1)	0.1044(1)	0.0159(5)
C2	0.6923(1)	0.3955(1)	0.0432(1)	0.0174(5)
C3	3/4	0.4568(1)	0.0432(1)	0.0169(7)
C4	0.4325(2)	0.4325(2)	0.0675(2)	0.029(1)

Table 20 Atomic co–ordinates for **CuV–13**

Atom	X	Y	Z	U_{iso}
Zn1	0.25000	0.25000	0.25000	0.0061(2)
V1	0.00000	0.50000	0.00000	0.0054(3)
F1	0.0886(4)	0.75000	0.00000	0.0081(6)
F2	0.2002(2)	0.4529(2)	0.1263(1)	0.0088(3)
O1	−0.0459(4)	0.25000	0.3116(2)	0.0109(6)

Table 21 Atomic co–ordinates for **V–8**

Atomic co–ordinates of Molybdenum and Niobium Oxyfluorides

Atom	X	Y	Z	U_{iso}
Mo1	0.2328(1)	0.45309(9)	0.73203(7)	0.0157(4)
Cu1	0.2704(1)	0.1805(1)	0.33145(9)	0.0163(4)
F1	0.1001(8)	0.4257(7)	0.5757(5)	0.024(1)
F2	0.3502(9)	0.6558(6)	0.7114(5)	0.026(1)
F3	0.1343(9)	0.2388(6)	0.6958(5)	0.027(1)
F4	0.4347(8)	0.4169(6)	0.6240(4)	0.021(1)
O1	0.389(1)	0.4718(8)	0.8405(6)	0.027(2)
O2	0.049(1)	0.4810(8)	0.7962(6)	0.030(2)
O3	−0.029(1)	0.0650(9)	0.3566(8)	0.030(2)
O4	0.249(1)	0.3770(8)	0.3875(6)	0.017(2)
O5	0.394(1)	0.1792(8)	0.4739(6)	0.018(2)
O6	0.225(1)	0.7520(9)	0.5434(7)	0.023(2)
N1	0.232(1)	0.1953(9)	0.1743(7)	0.017(2)
N2	0.307(1)	−0.0099(8)	0.2595(7)	0.014(2)
C1	0.196(1)	0.301(1)	0.1346(8)	0.019(2)
C2	0.180(1)	0.297(1)	0.0196(9)	0.020(2)
C3	0.199(1)	0.179(1)	−0.0536(9)	0.024(2)
C4	0.230(1)	0.065(1)	−0.0152(8)	0.017(2)
C5	0.251(1)	0.077(1)	0.1008(8)	0.016(2)
C6	0.289(1)	−0.030(1)	0.1470(8)	0.018(2)
C7	0.313(1)	−0.155(1)	0.0779(9)	0.021(2)
C8	0.292(1)	−0.170(1)	−0.0392(9)	0.026(2)
C9	0.252(1)	−0.064(1)	−0.0835(9)	0.028(3)
C10	0.350(1)	−0.261(1)	0.1270(9)	0.021(2)
C11	0.371(1)	−0.234(1)	0.2415(9)	0.022(2)
C12	0.346(2)	−0.108(1)	0.3020(9)	0.026(2)

Table 22 Atomic co–ordinates for **CuMo–1**

Atom	X	Y	Z	U_{iso}
Mo1	−0.26651(5)	0.25681(3)	0.14647(3)	0.0197(2)
Cu2	1/2	0	0	0.0115(2)
Cu1	0	0	0	0.0112(2)
F1	−0.2756(4)	0.3398(2)	0.0366(2)	0.0275(6)
F2	−0.2018(5)	0.1454(2)	0.2421(2)	0.0412(8)

F3	0.0128(4)	0.2607(2)	0.1354(2)	0.0290(6)
F4	−0.2438(3)	0.1160(2)	0.0613(2)	0.0181(5)
O1	−0.2586(4)	0.3714(3)	0.2209(2)	0.0230(7)
O2	−0.5058(4)	0.2264(3)	0.1518(2)	0.0256(7)
O3	0.2328(5)	0.2227(3)	0.2994(3)	0.0245(8)
N1	0.1611(4)	−0.0130(3)	0.1156(2)	0.0125(7)
N2	0.3541(4)	−0.0114(3)	0.1145(2)	0.0122(7)
N3	0.2704(5)	−0.0234(3)	0.2570(2)	0.0136(7)
N4	0.2737(5)	−0.0306(3)	0.3546(2)	0.0233(8)
N5	0.1490(4)	0.1310(3)	−0.0393(2)	0.0122(7)
N6	0.3418(4)	0.1328(3)	−0.0422(2)	0.0113(7)
N7	0.2354(4)	0.3023(3)	−0.0657(2)	0.0139(7)
N8	0.2178(5)	0.4199(3)	−0.0813(3)	0.0277(9)
C1	0.4163(6)	−0.0165(3)	0.2002(3)	0.0153(8)
C2	0.1150(5)	−0.0197(3)	0.2017(3)	0.0129(8)
C3	0.3904(5)	0.2374(3)	−0.0589(3)	0.0129(8)
C4	0.0885(6)	0.2334(3)	−0.0539(3)	0.0152(8)

Table 23 Atomic co–ordinates for **CuMo–2**

Atom	X	Y	Z	U_{iso}
Mo1	0.05906(1)	0.26778(3)	0.45086(3)	0.0175(2)
Mo2	1/4	¾	1/2	0.0235(2)
Cu1	0.15741(2)	0.50261(4)	0.48443(4)	0.0192(2)
Cu2	0	0	1/2	0.0253(2)
F1	0.0368(1)	0.3498(3)	0.5179(2)	0.0499(9)
F2	0.1178(1)	0.2302(2)	0.5841(2)	0.0306(7)
F3	0.0948(1)	0.1786(3)	0.4135(3)	0.070(1)
F4	0.1031(1)	0.3782(2)	0.4649(2)	0.0321(7)
O4	0.1031(1)	0.3782(2)	0.4649(2)	0.0321(7)
F5	0.0317(1)	0.1454(2)	0.4726(2)	0.0343(8)
O5	0.0317(1)	0.1454(2)	0.4726(2)	0.0343(8)
F6	0.2030(1)	0.7731(2)	0.3760(2)	0.0358(8)
O6	0.2030(1)	0.7731(2)	0.3760(2)	0.0358(8)
F7	0.2848(1)	0.6574(3)	0.4647(2)	0.0446(9
O7	0.2848(1)	0.6574(3)	0.4647(2)	0.0446(9
F8	0.2110(1)	0.6346(2)	0.4995(2)	0.0295(7)
O8	0.2110(1)	0.6346(2)	0.4995(2)	0.0295(7)
O1	0.0117(1)	0.2997(3)	0.3470(2)	0.0418(9)
N1	0.1910(1)	0.4085(3)	0.4370(2)	0.0219(8)

N1A	0.1784(2)	0.3102(3)	0.4062(3)	0.035(1)
N2	0.1279(1)	0.6020(3)	0.5372(2)	0.0191(7)
N2A	0.1444(1)	0.6978(3)	0.5696(3)	0.0312(9)
N3	0.1111(1)	0.5507(3)	0.3546(2)	0.0212(8)
N3A	0.1228(1)	0.6254(3)	0.3120(2)	0.0235(8)
N4	0.2033(1)	0.4513(3)	0.6135(3)	0.0233(8)
N4A	0.1947(1)	0.3698(3)	0.6539(2)	0.0233(8)
N5	−0.0611(1)	0.0119(3)	0.3744(3)	0.0248(9)
N5A	−0.0984(1)	−0.0578(3)	0.3405(3)	0.0280(9)
N6	0.0299(1)	−0.0910(3)	0.4434(3)	0.0270(9)
N6A	0.0202(1)	−0.1932(3)	0.4220(3)	0.0270(9)
C1	0.2094(2)	0.2697(4)	0.3784(4)	0.044(2)
C2	0.2419(2)	0.3457(5)	0.3938(4)	0.046(2)
C3	0.2307(2)	0.4306(4)	0.4308(3)	0.025(1)
C4	0.1234(2)	0.7358(4)	0.6187(4)	0.035(1)
C5	0.0928(1)	0.6578(3)	0.6153(2)	0.036(1)
C6	0.0959(1)	0.5764(3)	0.5638(2)	0.0205(9)
C7	0.0894(2)	0.6327(4)	0.2238(3)	0.025(1)
C8	0.0532(2)	0.5583(4)	0.2061(3)	0.027(1)
C9	0.0685(2)	0.5089(4)	0.2899(3)	0.025(1)
C10	0.2293(2)	0.3611(4)	0.7420(3)	0.027(1)
C11	0.2622(2)	0.4403(4)	0.7608(3)	0.032(1)
C12	0.2443(2)	0.4974(4)	0.6783(3)	0.027(1)
C13	−0.0693(2)	0.0739(4)	0.3049(3)	0.027(1)
C14	−0.1136(2)	0.0439(4)	0.2248(3)	0.033(1)
C15	−0.1298(2)	−0.0423(4)	0.2527(3)	0.032(1)
C16	0.0421(2)	−0.2283(4)	0.3748(4)	0.032(1)
C17	0.0660(2)	−0.1440(5)	0.3671(4)	0.047(2)
C18	0.0573(2)	−0.0602(4)	0.4096(4)	0.034(1)

Table 24 Atomic co–ordinates for **CuMo–3**

Atom	X	Y	Z	U_{iso}
Mo1	1/2	0	0	0.0374(4)
Cu1	0.32670(9)	0	0.4115(1)	0.0160(3)
F1	0.6556(5)	0	0.2595(6)	0.022(1)
F2	0.3438(5)	0	0.0968(6)	0.021(1)
F3	1/2	0.1105(3)	0	0.033(1)
F4	1/2	0.0717(2)	1/2	0.0203(9)
O1	0.6556(5)	0	0.2595(6)	0.022(1)

O2	0.3438(5)	0	0.0968(6)	0.021(1)
N1	0.1668(5)	0.0837(2)	0.3260(6)	0.0158(9)
N2	−0.046(1)	0	0.240(3)	0.101(6)
C1	0.2173(6)	0.1578(3)	0.3315(9)	0.026(1)
C2	0.1208(6)	0.2206(3)	0.2738(8)	0.027(1)
C3	−0.0378(6)	0.2086(3)	0.2059(8)	0.023(1)
C4	−0.0910(6)	0.1346(4)	0.200(1)	0.045(2)
C5	0.0137(7)	0.0743(3)	0.258(1)	0.036(2)

Table 25 Atomic co–ordinates for **CuMo–4**

Atom	X	Y	Z	U_{iso}
Mo1	1/4	¼	0.1848(1)	0.0333(7)
Cu1	3/4	¼	1/4	0.0189(7)
F1	0.3480(5)	0.1150(5)	0.1901(4)	0.038(1)
O1	0.3480(5)	0.1150(5)	0.1901(4)	0.038(1)
F2	1/4	¼	0.0617(7)	0.037(3)
O2	1/4	¼	0.0617(7)	0.037(3)
F3	1/4	¼	0.3070(8)	0.033(3)
O3	1/4	¼	0.3070(8)	0.033(3)
O4	0.8967(5)	0.1033(5)	1/4	0.026(2)
N1	0.6590(5)	0.1573(6)	0.1586(4)	0.019(1)
C1	0.6575(7)	0.0384(7)	0.1581(5)	0.025(2)
C2	0.5980(7)	−0.0266(7)	0.0967(5)	0.023(2)
C3	0.5325(7)	0.0330(7)	0.0337(5)	0.023(2)
C4	0.5331(7)	0.1550(7)	0.0365(5)	0.026(2)
C5	0.5966(8)	0.2156(8)	0.0985(5)	0.028(2)

Table 26 Atomic co–ordinates for **CuMo–5**

Atom	X	Y	Z	U_{iso}
Nb1	−0.24805(7)	−0.25231(4)	1.14127(3)	0.0313(2)
Cu2	1/2	0	1.00000	0.0229(3)
Cu1	0	0	1.00000	0.0213(3)
F1	−0.2791(5)	−0.3461(3)	1.0343(2)	0.0471(9)
F5	−0.2534(5)	−0.3848(3)	1.2166(2)	0.0395(9)
O5	−0.2534(5)	−0.3848(3)	1.2166(2)	0.0395(9)

F3	−0.1900(7)	−0.1609(3)	1.2461(3)	0.078(2)
F4	−0.5107(5)	−0.2369(3)	1.1573(4)	0.064(1)
F2	0.0199(5)	−0.2697(3)	1.1304(3)	0.054(1)
F6	−0.2487(5)	−0.1199(3)	1.0651(2)	0.0354(8)
O6	−0.2487(5)	−0.1199(3)	1.0651(2)	0.0354(8)
O1	0.2405(7)	−0.2275(3)	1.3029(3)	0.044(1)
N1	0.1581(6)	0.0118(3)	1.1139(3)	0.0217(9)
N2	0.3514(6)	0.0109(3)	1.1140(3)	0.0215(9)
N3	0.2614(6)	0.0194(3)	1.2538(3)	0.023(1)
N4	0.2588(7)	0.0231(4)	1.3492(3)	0.037(1)
N5	0.1497(6)	−0.1298(3)	0.9591(3)	0.0227(9)
N6	0.3431(6)	−0.1336(3)	0.9604(3)	0.024(1)
N7	0.2351(7)	−0.3014(3)	0.9342(3)	0.028(1)
N8	0.2160(8)	−0.4183(3)	0.9190(4)	0.049(2)
C1	0.1091(8)	0.0172(4)	1.1988(4)	0.027(1)
C2	0.4105(5)	0.0154(3)	1.1982(3)	0.026(1)
C3	0.0883(5)	−0.2317(3)	0.9431(3)	0.026(1)
C4	0.3902(8)	−0.2388(4)	0.9442(4)	0.025(1)

Table 27 Atomic co–ordinates for **CuNb–1**

Atom	X	Y	Z	U_{iso}
Nb1	0	½	0	0.0417(2)
Cu1	−1/4	¾	0	0.0424(3)
F1	−0.1131(3)	0.6185(2)	−0.0035(2)	0.0522(8)
O1	−0.1131(3)	0.6185(2)	−0.0035(2)	0.0522(8)
F2	−0.0217(3)	0.4811(2)	0.1243(2)	0.0615(8)
F3	0.1515(3)	0.5850(3)	0.0360(2)	0.077(1)
N1	−0.2728(4)	0.7134(3)	0.1280(2)	0.0423(9)
N2	−0.2018(4)	0.6383(3)	0.1737(2)	0.051(1)
N3	−0.0970(4)	0.8425(3)	0.0493(2)	0.0398(9)
N4	−0.1075(4)	0.9385(3)	0.0797(3)	0.053(1)
C1	−0.2232(6)	0.6310(5)	0.2579(3)	0.064(2)
C2	−0.3120(6)	0.7054(5)	0.2705(3)	0.065(2)
C3	−0.3402(5)	0.7572(4)	0.1866(3)	0.056(1)
C4	0.0093(4)	0.9751(3)	0.1176(3)	0.059(2)
C5	0.0965(4)	0.8991(3)	0.1101(3)	0.075(2)
C6	0.0271(5)	0.8186(4)	0.0675(3)	0.050(1)

Table 28 Atomic co–ordinates for **CuNb–2**

Atom	X	Y	Z	U_{iso}
Nb1	0	0	1/2	0.0245(4)
Cu1	−0.17213(9)	0	−0.0781(1)	0.0177(4)
F2	−0.1613(5)	0	0.2414(6)	0.026(1)
O2	−0.1613(5)	0	0.2414(6)	0.026(1)
F3	0.1591(5)	0	0.3983(6)	0.029(1)
O3	0.1591(5)	0	0.3983(6)	0.029(1)
F1	0	0.1119(3)	1/2	0.041(1)
F4	0	0.0719(3)	0	0.024(1)
N1	−0.3296(5)	0.0837(3)	−0.1679(6)	0.019(1)
N2	−0.5416(9)	0	−0.232(1)	0.042(2)
C4	−0.5839(5)	0.1364(4)	−0.2906(8)	0.027(2)
C1	−0.2797(6)	0.1580(3)	−0.1680(8)	0.026(1)
C5	−0.4818(6)	0.0732(3)	−0.2289(8)	0.022(1)
C3	−0.5315(6)	0.2095(3)	−0.2905(8)	0.026(1)
C2	−0.3738(6)	0.2211(3)	−0.2271(8)	0.027(1)

Table 29 Atomic co–ordinates for **CuNb–3**

Atom	X	Y	Z	U_{iso}
Nb1	1/4	¼	0.18766(5)	0.0249(3)
Cu1	3/4	¼	1/4	0.0158(4)
F1	0.3477(2)	0.1105(2)	0.1915(2)	0.0344(6)
O1	0.3477(2)	0.1105(2)	0.1915(2)	0.0344(6)
F2	1/4	¼	0.3128(3)	0.025(1)
O2	1/4	¼	0.3128(3)	0.025(1)
F3	1/4	¼	0.0659(3)	0.038(1)
O3	1/4	¼	0.0659(3)	0.038(1)
O4	0.8960(2)	0.1040(2)	1/4	0.0257(8)
N1	0.6583(2)	0.1592(2)	0.3415(2)	0.0200(6)
C1	0.7139(3)	0.0964(3)	0.4014(2)	0.0237(7)
C2	0.6557(3)	0.0316(3)	0.4630(2)	0.0252(8)
C3	0.5331(3)	0.0329(3)	0.4663(2)	0.0196(7)
C4	0.4748(2)	0.0973(2)	0.4032(2)	0.0233(7)
C5	0.5400(2)	0.1582(2)	0.3423(2)	0.0232(7)

Table 30 Atomic co–ordinates for **CuNb–4**

Atomic co–ordinates of Hilgardite–like Borates

Atom	X	Y	Z	U_{iso}
Pb1	0.2560(4)	0.0443(4)	0.0058(7)	0.0094(6)
Pb2	0.0272(4)	0.2372(4)	−0.6645(7)	0.0094(6)
Br1	0.0000(0)	0.0000(0)	−0.904(1)	0.023(2)
Br2	0.0000(0)	0.0000(0)	−0.650(2)	0.023(2)
O1	0.2377(6)	0.3146(6)	−0.5768(9)	0.0037(5)
O2	0.2112(6)	0.4258(6)	−0.173(1)	0.0037(5)
O3	0.2721(5)	0.2266(6)	−0.245(1)	0.0037(5)
O4	0.0729(5)	0.2738(7)	−0.2433(9)	0.0037(5)
O5	0.2844(6)	0.4496(5)	−0.834(1)	0.0037(5)
O6	0.3818(5)	0.2629(5)	−0.834(1)	0.0037(5)
O7	0.1809(6)	0.2716(6)	−0.924(1)	0.0037(5)
O8	0.4188(5)	0.2099(6)	−0.4953(9)	0.0037(5)
O9	0.2342(6)	0.1125(6)	−0.5580(8)	0.0037(5)
B1	0.2700(5)	0.3206(5)	−0.7925(9)	0.0035(6)
B2	0.1804(5)	0.3008(5)	−0.1421(9)	0.0035(6)
B3	0.2867(5)	0.2173(5)	−0.4641(9)	0.0035(6)
B4	0.4585(4)	0.2319(5)	−0.6834(9)	0.0035(6)
B5	0.2500(7)	0.4934(5)	−0.0189(9)	0.0035(6)

Table 31 Atomic co–ordinates of $Pb_2B_5O_9Br$

Atom	X	Y	Z	U_{iso}
Pb1	0.2523(3)	0.0397(3)	0.0001(4)	0.0075(3)
Pb2	0.0218(2)	0.2405(2)	−0.6674(5)	0.0075(3)
Cl1	0.0000(0)	0.0000(0)	−0.8782(7)	0.0051(4)
Cl2	0.0000(0)	0.5000(0)	−0.6187(6)	0.0051(4)
O1	0.2387(3)	0.3184(4)	−0.5814(6)	0.0060(2)
O2	0.2126(4)	0.4272(3)	−0.1731(7)	0.0060(2)
O3	0.2717(3)	0.2256(4)	−0.2463(7)	0.0060(2)
O4	0.0720(4)	0.2784(4)	−0.2474(6)	0.0060(2)
O5	0.2863(4)	0.4481(3)	−0.8392(6)	0.0060(2)
O6	0.3808(4)	0.2605(3)	−0.8375(6)	0.0060(2)
O7	0.1803(4)	0.2739(4)	−0.9302(6)	0.0060(2)
O8	0.4192(3)	0.2104(4)	−0.4935(6)	0.0060(2)
O9	0.2321(4)	0.1157(4)	−0.5613(6)	0.0060(2)

B1	0.2712(3)	0.3220(3)	−0.7966(5)	0.0025(2)
B2	0.1816(3)	0.3015(3)	−0.1453(5)	0.0025(2)
B3	0.2889(3)	0.2173(3)	−0.4657(5)	0.0025(2)
B4	0.4588(3)	0.2306(3)	−0.6913(5)	0.0025(2)
B5	0.2538(3)	0.4988(3)	−0.0232(6)	0.0025(2)

Table 32 Atomic co–ordinates of $Pb_2B_5O_9Cl$

Atom	X	Y	Z	U_{iso}
Sr1	0.2511(8)	0.0456(6)	0.009(1)	0.013(1)
Sr2	0.0272(7)	0.2408(6)	−0.656(1)	0.013(1)
Cl1	0.0000(0)	0.0000(0)	−0.856(2)	0.023(1)
Cl2	0.0000(0)	0.5000(0)	−0.600(2)	0.023(1)
O1	0.2444(7)	0.3153(7)	−0.583(1)	0.0075(6)
O2	0.2131(7)	0.4229(7)	−0.177(1)	0.0075(6)
O3	0.2807(6)	0.2239(7)	−0.250(1)	0.0075(6)
O4	0.0789(6)	0.2651(7)	−0.251(1)	0.0075(6)
O5	0.2804(7)	0.4495(6)	−0.841(1)	0.0075(6)
O6	0.3867(7)	0.2656(6)	−0.850(1)	0.0075(6)
O7	0.1824(8)	0.2647(7)	−0.930(1)	0.0075(6)
O8	0.4232(7)	0.2051(8)	−0.503(1)	0.0075(6)
O9	0.2345(8)	0.1118(8)	−0.577(1)	0.0075(6)
B1	0.2711(6)	0.3211(6)	−0.794(1)	0.0046(6)
B2	0.1889(6)	0.2937(6)	−0.150(1)	0.0046(6)
B3	0.2947(6)	0.2135(6)	−0.472(1)	0.0046(6)
B4	0.4629(5)	0.2360(6)	−0.690(1)	0.0046(6)
B5	0.2516(7)	0.4929(6)	−0.027(1)	0.0046(6)

Table 33 Atomic co–ordinates of $Sr_2B_5O_9Cl$

Atom	X	Y	Z	U_{iso}
Ba1	0.250(2)	0.043(2)	0.004(4)	0.004(3)
Ba2	0.014(2)	0.229(2)	−0.644(4)	0.004(3)
Cl1	0.0000(0)	0.0000(0)	−0.887(4)	0.020(3)
Cl2	0.0000(0)	0.5000(0)	−0.617(3)	0.020(3)
O1	0.2334(17)	0.316(2)	−0.591(3)	0.001(1)
O2	0.208(2)	0.424(2)	−0.160(4)	0.001(1)

O3	0.2775(2)	0.232(2)	−0.250(3)	0.001(1)
O4	0.071(2)	0.283(2)	−0.242(3)	0.001(1)
O5	0.287(2)	0.434(2)	−0.847(3)	0.001(1)
O6	0.380(2)	0.257(2)	−0.846(3)	0.001(1)
O7	0.187(2)	0.259(2)	−0.933(3)	0.001(1)
O8	0.412(2)	0.204(2)	−0.502(3)	0.001(1)
O9	0.236(2)	0.102(2)	−0.547(3)	0.001(1)
B1	0.274(2)	0.313(2)	−0.807(3)	0.002(2)
B2	0.178(1)	0.302(2)	−0.150(3)	0.002(2)
B3	0.285(2)	0.222(2)	−0.466(3)	0.002(2)
B4	0.460(1)	0.221(2)	−0.692(3)	0.002(2)
B5	0.249(2)	0.486(1)	−0.020(3)	0.002(2)

Table 34 Atomic co–ordinates of $Ba_2B_5O_9Cl$

Appendix–III

Synthesis of Vanadium Oxyfluoride Materials

CuV–1 was formed by reacting CuO, V_2O_5, HF, H_2O, imidazole and pyridine in the ratio 5:2:50:600:10:500, followed by heating at 160˚C for 24 hours. Initially 0.100 g (0.5×10^{-3} mol) of V_2O_5 was weighed into a 27 mL Teflon–lined stainless steel autoclave and dissolved with 0.2 mL (0.9×10^{-2} mol) of 48% HF at room temperature for 5 minutes. To the resultant solution, 10 mL (0.12 mol) of pyridine, 0.2 g (0.3×10^{-2} mol) of imidazole, 0.3 mL (0.16×10^{-1} mol) of water and finally 0.1 g (1.25×10^{-3} mol) of CuO was added and stirred well until fully dissolved. The reaction vessel was sealed and heated to 160˚C for 24 hours, and then cooled to room temperature over an additional 24 hours. Blue crystals were recovered by vacuum filtration. Purity of the phase was confirmed by elemental analysis, together with comparison of observed and simulated powder X–ray diffraction patterns. Elemental and crystallographic analyses are in good agreement with the structural formula of **CuV–1**: Calcd: C, 36.06%; H, 3.005%; N, 19.12%, measured: C, 35.82%; H, 3.18%; N, 18.68%.

V–1 and **V–2** were obtained under similar synthetic conditions. V_2O_5, HF, H_2O and 4–methylpyridine/pyridine were added in the ratio 1:25:15:50 and heated at 160˚C for a day. CuO was also used as a starting material of this reaction; it was not incorporated into the crystal structure and in the absence of a copper source a similar product was produced. 0.200 g (0.1×10^{-2} mol) of V_2O_5 was weighed into a 27 mL Teflon–lined stainless steel autoclave and dissolved with 0.5 mL (0.025 mol) of 48% HF at room temperature for 5 minutes. To the resultant solution, 5 mL of 4–methylpyridine/pyridine, and finally 0.3 mL (0.01 mol) of water was added and stirred well until fully dissolved. The reaction vessel was sealed and heated to 160˚C for a day, and then cooled to room temperature over an additional 24 hours. The crystals were recovered by vacuum filtration. Purity of the phase was confirmed by elemental analysis, together with

comparison of observed and simulated powder X–ray diffraction patterns. Elemental and crystallographic analyses are in good agreement with the structural formula of **V–1**: Calcd: C, 46.61%; H, 5.22%; N, 9.05%, measured: C, 46.30%; H, 5.19%; N, 8.95% and **V–2**: Calcd: C, 42.72%; H, 4.30%; N, 9.96%, measured: C, 42.28%; H, 4.85%; N, 10.39%.

CuV–2 was synthesised from CuO, V_2O_5, HF, H_2O, 2,4,6–triaminopyrimidine and pyridine in the ratio 5:1:50:500:5:25, followed by heating at 160˚C for 24 hours. Initially 0.100 g (0.5×10^{-3} mol) of V_2O_5 was weighed into a 27 mL Teflon–lined stainless steel autoclave and dissolved with 0.5 mL (0.025 mol) of 48% HF at room temperature for 5 minutes. To the resultant solution, 1 mL (0.01 mol) of pyridine, 0.2 g (0.1×10^{-2} mol) of 2,4,6-triaminopyrimidine, 5 mL (0.28 mol) of water and finally 0.1 g (0.1×10^{-2} mol) of CuO was added and stirred well until fully dissolved. The reaction vessel was sealed and heated to 160˚C for a day, and then cooled to room temperature over an additional 24 hours. Cyan blue crystals were recovered by vacuum filtration. Purity of the phase was confirmed by elemental analysis, together with comparison of observed and simulated powder X–ray diffraction patterns. Elemental and crystallographic analyses are in good agreement with the structural formula **CuV–2**: Calcd: C, 12.95%; H, 4.62%; N, 26.43%, measured: C, 12.38%; H, 4.73%; N, 26.04%.

V–3 and **V–4** were obtained under similar reaction conditions by reacting V_2O_5, 2,2'–bipyridyl/1,10–phenanthroline, HF and H_2O, in the ratio 1:2:20:1000, followed by heating at 160˚C for 24 hours. Initially 0.100 g (0.5×10^{-3} mol) of V_2O_5 was weighed into a 27 mL Teflon–lined stainless steel autoclave and dissolved with 0.2 mL (0.9×10^{-2} mol) of 48% HF at room temperature for 5 minutes. Finally 0.2 g (0.1×10^{-2} mol) of 2,2'–bipyridyl/0.17 g (0.1×10^{-2} mol) of 1,10–phenanthroline and 10 mL (0.6 mol) of water was added and stirred well until fully dissolved. The reaction vessel was sealed and heated to 160˚C for a day, and then cooled to room temperature over an additional 24 hours. The

product was recovered, filtered off, washed with water and dried at 60˚C in air to give deep yellow/orange crystals. Purity of phase was confirmed by elemental analysis, together with comparison of observed and simulated powder X–ray diffraction patterns. Elemental and crystallographic analysis are in good agreement with the structural formula **V–3**: Calcd: C, 46.53%; H, 3.12%; N, 10.84%, F, 7.36% measured: C, 46.85%; H, 3.08%; N, 10.61%; F, 7.68%; and **V–4**: Calcd: C, 50.54%; H, 2.82%; N, 9.82%, measured: C, 49.77%; H, 2.69%; N, 9.71%.

V–5 was prepared from a 1:30:30:20 approximate ratio of V_2O_5 HF, H_2O and 4–methylpyridine, heated at 160˚C for 24 hours. The autoclave was then cooled in air, the mixture filtered and washed with distilled water and the product air-dried. Initially 0.100 g (0.5×10^{-3} mol) of V_2O_5 was weighed into a 27 mL Teflon–lined stainless steel autoclave and dissolve with 0.3 mL (0.15×10^{-1} mol) of 48% HF at room temperature for 5 minutes. Finally 0.3 mL (0.1×10^{-1} mol) of water and 5 mL (0.5×10^{-1} mol) of 4–methylpyridine were added and stirred well until fully dissolved. The reaction vessel was sealed and heated to 160˚C for a day, and then cooled to room temperature over an additional 24 hours. Blue crystals were recovered by vacuum filtration. Purity of the phase was confirmed by elemental analysis, together with comparison of observed and simulated powder X–ray diffraction patterns. Elemental and crystallographic analyses are in good agreement with the structural formula **V–5**: Calcd: C, 49.49%; H, 4.80%; N, 9.61%, measured: C, 49.45%; H, 5.33%; N, 10.00%.

V–6 was prepared from a 1:30:30:20 approximate ratio of V_2O_5 HF, H_2O and 2,6–lutidine heated at 160˚C for 24 hours. The autoclave was then cooled in air, the mixture filtered and washed with distilled water and the product air-dried. Initially 0.05 g (0.25×10^{-3} mol) of V_2O_5 was weighed into a 27 mL Teflon–lined stainless steel autoclave and dissolved with 0.3 mL (0.15×10^{-1} mol) of 48% HF at room temperature for 5 minutes. Finally 0.3 mL (0.1×10^{-1} mol) of water and 5 mL (0.5×10^{-1} mol) of 2,6–lutidine

were added and stirred well until fully dissolved. The reaction vessel was sealed and heated to 160°C for a day, and then cooled to room temperature over an additional 24 hours. Blue crystals were recovered by vacuum filtration. Purity of the phase was confirmed by elemental analysis, together with comparison of observed and simulated powder X–ray diffraction patterns. Elemental and crystallographic analyses are in good agreement with the structural formula **V–6**: Calcd: C, 33.61%; H, 4.83%; N, 5.60%, measured: C, 33.48%; H, 4.59%; N, 5.51%.

V–7 was prepared from a 1:20:20:60 approximate ratio of V_2O_5 HF, H_2O and pyridine, heated at 160°C for 24 hours. The autoclave was then cooled in air, the mixture filtered and washed with distilled water and the product air–dried. Initially 0.200 g (0.1×10^{-2} mol) of V_2O_5 was weighed into a 27 mL Teflon–lined stainless steel autoclave and dissolved with 0.5 mL (0.2×10^{-1} mol) of 48% HF at room temperature for 5 minutes. Finally 0.5 mL (0.28×10^{-1} mol) of water and 5 mL (0.6×10^{-1} mol) of pyridine were added and stirred well until fully dissolved. The reaction vessel was sealed and heated to 160°C for a day, and then cooled to room temperature over an additional 24 hours. Blue crystals were recovered by vacuum filtration. Purity of the phase was confirmed by elemental analysis, together with comparison of observed and simulated powder X–ray diffraction patterns. Elemental and crystallographic analyses are in good agreement with the structural formula **V–7**: Calcd: C, 36.51%; H, 4.97%; N, 5.32%, measured: C, 36.08%; H, 5.00%; N, 5.12%.

Single crystals of **CuV–3** and **CuV–4** were prepared from a 1:20:1:50:20 approximate ratio of V_2O_5 HF, CuO, pyridine, and H_2O in the presence of organoamine and heated at 160°C for 24 hours. The autoclave was then cooled in air, the mixture filtered and washed with distilled water and the product air–dried. Initially 0.200 g (1.09×10^{-3} mol) of V_2O_5 was weighed into a 27 mL Teflon–lined stainless steel autoclave and dissolved with 0.5 mL (2.89×10^{-2} mol) of 48% HF at room temperature for 5min. To the resultant solution, 5

mL (6.18×10^{-2} mol) of pyridine, 0.15 g (2.26×10^{-3} mol) of trimethylamine-N-oxide, 0.5 mL (2.77×10^{-2} mol) of water and finally 0.1 g (1.25×10^{-3} mol) of CuO was added and stirred well until fully dissolved. The preparation of single crystals of **CuV–4** followed the same reaction conditions as **CuV–3**, but dimethylamine, 0.5 mL (1.10×10^{-2} mol) was used instead of trimethylamine-N–oxide. In each case, the reaction vessel was sealed and heated to 160˚C for 24 hours, and then cooled to room temperature over a day. Crystals were recovered by vacuum filtration. Phase purity was ascertained by elemental analysis (CHN), together with comparison of observed and simulated powder X–ray diffraction patterns. Elemental and crystallographic analyses are in reasonable agreement with the structural formula. for **CuV–3**: Calcd: C, 38.09%; H, 4.04%; N, 10.10%, measured: C, 37.59%; H, 3.77%; N, 9.57%, revealing that the template had broken down *in situ*; for **CuV–4** : Calcd: C, 38.09%; H, 4.04%; N, 10.10%, measured: C, 37.50%; H, 4.49%; N 9.98%. However, the single crystals of **CuV–3** and **CuV–4** are decomposable in air at room temperature within a few days.

Single crystals of **CuV–5** and **CuV–6** were synthesised under similar conditions with a 1:30:50:30:1 with approximate ratio of V_2O_5, HF, 3–methylpyridine/4–methylpyridine, H_2O and CuO. Initially 0.200g (1.09×10^{-3} mol) of V_2O_5 was weighed into a 27 mL Teflon–lined stainless steel autoclave and dissolved with 0.5 mL (2.89×10^{-2} mol) of 48% HF at room temperature for 5 minutes. To the resultant solution, 5 mL (5.37×10^{-2} mol) of 3–methylpyridine, for **CuV–5** or 4–methylpyridine, for **CuV–6**, 0.5 mL (2.77×10^{-2} mol) of water and finally 0.1 g (1.25×10^{-3} mol) of CuO was added and stirred well until fully dissolved. The reaction vessels were sealed and heated to 160˚C for 24 hours, and then cooled to room temperature over a day. Crystals were recovered by vacuum filtration. Phase purity was ascertained by elemental analysis (CHN), together with comparison of observed and simulated powder X–ray diffraction patterns. Elemental and crystallographic analyses are in reasonable agreement with the structural formula **CuV–5**: Calcd: C, 48.2%; H, 4.05%; N 9.38%; F, 18.98%, measured: C, 47.70%; H, 4.41%; N

9.38%; F, 18.56%. Compared to single crystals of **CuV–5**, **CuV–6** deteriorated in air at room temperature within a few days.

Single crystals of **CuV–7** were prepared from a 1:30:50:30:1 approximate ratio of V_2O_5, CuO, HF, H_2O, 3–methylpyridine, and imidazole. Initially 0.100 g (0.54×10^{-3} mol) of V_2O_5 , 0.1 g (1.25×10^{-3} mol) of CuO, 0.3 mL (1.73×10^{-2} mol) of 48% HF, 0.3 mL (1.662×10^{-2} mol) of water, 10 mL (12.36×10^{-2} mol) of 3-methylpyridine and 0.200 g (2.93×10^{-2} mol) of imidazole were added and stirred well until fully dissolved. The reaction vessels were sealed and heated to 160°C for 24 hours, and then cooled to room temperature over a day. Crystals were recovered by vacuum filtration. A major product of **CuV–7** was found, with an uncharacterised poorly crystalline phase.

CuV–8 was synthesised from a 4:5:120:120:500:130 approximate ratio of V_2O_5, CuO, HF, H_2O, pyridine, and ethylenediamine. Initially 0.200 g (1.09×10^{-3} mol) of V_2O_5 was weighed into a 27 mL Teflon-lined stainless steel autoclave and dissolved with 0.5 mL (2.89×10^{-2} mol) of 48% HF at room temperature for 5 minutes. To the resultant solution 0.1g (1.25×10^{-3} mol) of CuO, 0.5mL (2.77×10^{-2} mol) of water, 10 mL (1.23×10^{-1} mol) of pyridine and 0.2 mL (3.3×10^{-2} mol) of ethylenediamine were added and stirred well until fully dissolved. The reaction vessel was sealed and heated to 160°C for 24 hours, and then cooled to room temperature over a day. Crystals were recovered by vacuum filtration. The product **CuV–8** was found together with a poorly crystalline unknown phase.

CuV–9 was prepared from a 10:1:200:200 approximate ratio of V_2O_5, CuO, HF and 2,2–dipyridylamine in the presence of water as solvent. Initially 0.100 g (0.54×10^{-3} mol) of V_2O_5 was weighed into a 27 mL Teflon–lined stainless steel autoclave and dissolved with 0.2 mL (1.15×10^{-2} mol) of 48% HF at room temperature for 5 minutes. To the resultant solution 0.05 g (0.062×10^{-3} mol) of CuO and 0.2 g (1.16×10^{-2} mol) of 2,2'–dipyridylamine and finally 10 mL (5.54×10^{-1} mol) of water added and stirred well until

fully dissolved. The reaction vessel was sealed and heated to 160˚C for 48 hours, and then cooled to room temperature over a day. The product was filtered off, washed with water and dried at 60˚C in air to give green crystals. Purity of phase was confirmed by elemental analysis, together with comparison of observed and simulated powder X–ray diffraction patterns. Elemental and crystallographic analyses are in good agreement with the structural formula **CuV–9** Calcd: C, 33.02%; H, 2.49%; N 11.55%; F, 5.25%, measured: C, 32.94%; H, 2.28%; N 11.25%; F, 5.19%.

CuV–10 was prepared from a 5:1:125:10 approximate ratio of V_2O_5, CuO, HF and 2,2'–dipyridylamine in the presence of water as solvent. Initially 0.08 g (0.43×10^{-3} mol) of V_2O_5 was weighed into a 27 mL Teflon–lined stainless steel autoclave and dissolved with 0.2 mL (1.15×10^{-2} mol) of 48% HF at room temperature for 5 minutes. To the resultant solution 0.1 g (0.12×10^{-3} mol) of CuO and 0.15 g (0.88×10^{-3} mol) of 2,2'–dipyridylamine and finally 4 mL (2.2×10^{-1} mol) of water added and stirred well until fully dissolved. The reaction vessel was sealed and heated to 160˚C for 2 days, and then cooled to room temperature over an additional 24 hours. The product was filtered off, washed with water and dried at 60˚C in air to give green crystals. Purity of phase was confirmed by elemental analysis, together with comparison of observed and simulated powder X–ray diffraction patterns. Elemental and crystallographic analyses are in good agreement with the structural formula **CuV–10** Calcd: C, 31.80%; H, 2.40%; N 11.13%; F, 20.12%, measured: C, 31.61%; H, 2.27%; N 10.89%; F, 19.78%.

CuV–11 was prepared from a 4:40:5:1:200 approximate ratio of V_2O_5 HF, CuO, 2,2'–dipyridylamine and H_2O. Initially 0.2 g (1.1×10^{-3} mol) of V_2O_5 was weighed into a 27 mL Teflon–lined stainless steel autoclave and dissolved with 0.2 mL (0.1×10^{-1} mol) of 48% HF at room temperature for 5 minutes. Then 0.05 g (3.0×10^{-4} mol) of 2,2'–dipyridylamine and 0.1 g (1.25×10^{-3} mol) of CuO and finally 10 mL (0.5 mol) of water were added and stirred well until fully dissolved. The reaction vessel was sealed and

heated to 160˚C for 24 hours, and then cooled to room temperature over an additional 24 hours. The product was filtered off, washed with water and dried at 60˚C in air to give deep green crystals. Purity of phase was confirmed by elemental analysis, together with comparison of observed and simulated powder X–ray diffraction patterns. Elemental and crystallographic analyses are in good agreement with the structural formula **CuV–11**: Calcd: C, 22.94%; H, 1.73%; N, 8.03%, measured: C, 22.68%; H, 1.63%; N, 7.91%.

CuV–12 was prepared from a 4:100:5:100:200:250 approximate ratio of V_2O_5, HF, CuO, H_2O, methylamine and pyridine. Initially 0.200 g (1.1×10^{-3} mol) of V_2O_5 was weighed into a 27 mL Teflon–lined stainless steel autoclave and dissolved with 0.5 mL (0.25×10^{-1} mol) of 48% HF at room temperature for 5 minutes. Then 0.5 mL (2.8×10^{-2} mol) of water, 1.5 mL (4.8×10^{-2} mol) of methylamine, 0.1 g (0.12×10^{-3} mol) of CuO and finally 5 mL (6.3×10^{-2} mol) of pyridine were added and stirred well until fully dissolved. The reaction vessel was sealed and heated to 160˚C for 24 hours, and then cooled to room temperature over an additional 24 hours. Blue crystals together with an uncharacterised powder phase were recovered by vacuum filtration. The product was decomposable in air at room temperature after a few days.

Single crystals of **CuV–13** were synthesised by a hydrothermal method. Initially 0.200 g (1.09×10^{-3} mol) of V_2O_5 was weighed into a 27 mL Teflon–lined stainless steel autoclave and dissolved with 0.5 mL (2.89×10^{-2} mol) of 48% HF at room temperature for 5minutes. To the resultant solution, 5 mL (6.18×10^{-2} mol) of pyridine, 0.15 mL (2.26×10^{-3} mol) of dimethylamine, 0.5 mL (2.77×10^{-2} mol) of water and finally 0.1 g (1.25×10^{-3} mol) of CuO was added and stirred well until fully dissolved. The reaction vessel was sealed and heated to 160˚C for 24 hours, and then cooled to room temperature over an additional 24 hours. Blue colour cubic crystals were recovered by vacuum filtration. Purity of phase was confirmed by elemental analysis, together with comparison of observed and simulated powder X–ray diffraction patterns. Elemental and crystallographic analyses are

in good agreement with the structural formula **CuV–13**: Calcd: C, 33.76%; H, 4.49%; N 11.58%; F, 20.66%; measured: C, 33.22%; H, 4.38%; N, 11.68%; F, 21.39%.

V–8 was formed by reacting ZnO, V_2O_5, HF and ethylene glycol in the ratio 2:1:60:65. 0.2 g (2.5×10^{-3} mol) of ZnO and 0.25 g (1.4×10^{-3} mol) of V_2O_5 were dissolved in 1.5 mL (7.5×10^{-2} mol) of HF and finally 5 mL (8.02×10^{-2} mol) of ethylene glycol added as solvent. The reaction vessel was sealed and heated to 160˚C for 24 hours, and then cooled to room temperature over an additional 24 hours. The product was filtered off and washed with distilled water and dried at 60˚C in air to give deep green crystals. Elemental and crystallographic analyses are in good agreement with the structural formula **V–8**: Calcd: H, 1.61%; measured: H, 1.68%.

Synthesis of Niobium/Molybdenum Oxyfluoride Materials

CuMo–1 was formed by reacting CuO, MoO_3, HF, H_2O and 1,10–phenanthroline in the ratio 2:1:40:800:1. Initially 0.100 g (6.9×10^{-4} mol) of MoO_3 was weighed into a 27 mL Teflon–lined stainless steel autoclave and dissolved with 0.5 mL (2.89×10^{-2} mol) of 48% HF at room temperature for 5 minutes. To the resultant solution, 0.1 g of 1,10–phenanthroline (5.55×10^{-4} mol), 10 mL (5.54×10^{-1} mol) of water and finally 0.1 g (1.25×10^{-3} mol) of CuO was added and stirred well until fully dissolved. The reaction vessel was sealed and heated to 160°C for 24 hours, and then cooled to room temperature over an additional 24 hours. The product was filtered with water and dried at 60°C in air. Phase purity was ascertained by elemental analysis (CHN), together with Rietveld refinement of powder X–ray diffraction pattern using the single crystal X–ray diffraction model. Elemental and crystallographic analyses are in good agreement with the structural formula. For **CuMo–1**: Calcd: C, 27.70%; H, 3.08%; N, 5.39%, measured: C, 27.54%; H, 2.92%; N, 5.16%.

CuMo–2 and **CuNb–1** were formed by reacting CuO, MoO_3/Nb_2O_5, HF, H_2O and 1–amino–1,3,4–triazole in the ratio 2:2/1:2:1000:4. Initially 0.200 g (1.38×10^{-3} mol) of MoO_3 for **CuMo–2** and 0.200 g (7.52×10^{-4} mol) of Nb_2O_5 for **CuNb-1** was weighed into a 27 mL Teflon–lined stainless steel autoclave and dissolved with 0.5 mL (2.89×10^{-2} mol) of 48% HF at room temperature for 5 minutes. To the resultant solution, 0.2 g of 1–amino–1,3,4–triazole (2.37×10^{-3} mol),10 mL (5.54×10^{-1} mol) of water and finally 0.1 g (1.25×10^{-3} mol) of CuO was added and stirred well until fully dissolved. The reaction vessel was sealed and heated to 160°C for 24 hours, and then cooled to room temperature over an additional 24 hours. The product was filtered with water and dried at 60°C in air. Phase purity was ascertained by elemental analysis (CHN), together with Rietveld refinement of powder X–ray diffraction pattern using the single crystal X–ray diffraction model. Elemental and crystallographic analyses are in good agreement with the structural

formula. For **CuMo-2**: Calcd: C, 10.59%; H, 2.21%; N, 24.68%; F, 16.74% measured: C, 10.60%; H, 1.72%; N, 23.86%; F, 16.65% for **CuNb-1**: Calcd: C, 10.66%; H, 2.23%; N, 24.86%; F, 20.94% measured: C, 10.71%; H, 1.76%; N, 24.12%; F, 20.38%

CuMo–3 and **CuNb–2** were formed by reacting CuO, MoO_3/Nb_2O_5, HF, H_2O and pyrazole in the ratio 2:2/1:2:1000:4. Initially 0.200 g (1.38×10^{-3} mol) of MoO_3 for **CuMo–3** and 0.200 g (7.52×10^{-4} mol) of Nb_2O_5 for **CuNb–2** was weighed into a 27 mL Teflon–lined stainless steel autoclave and dissolved with 0.5 mL (2.89×10^{-2} mol) of 48% HF at room temperature for 5 minutes. To the resultant solution, 0.2 g of pyrazole (2.93×10^{-3} mol),10 mL (5.54×10^{-1} mol) of water and finally 0.1 g (1.25×10^{-3} mol) of CuO was added and stirred well until fully dissolved. The reaction vessel was sealed and heated to 160°C for 24 hours, and then cooled to room temperature over an additional 24 hours. The product was filtered with water and dried at 60°C in air. Purity of the phase was confirmed by elemental analysis, together with comparison of observed and simulated powder X–ray diffraction patterns. Elemental and crystallographic analyses are in good agreement with the structural formula. For **CuMo-3**: Calcd: C, 26.70%; H, 2.98%; N, 20.75%; F, 14.08% measured: C, 26.68%; H, 2.71%; N, 20.37%; F, 14.29%, for **CuNb-2**: Calcd: C, 26.79%; H, 2.99%; N, 20.77%; F, 17.59% measured: C, 27.01%; H, 2.75%; N, 20.23%; F, 17.85%.

CuMo–4 and **CuNb–3** were formed by reacting CuO, MoO_3/Nb_2O_5, HF, H_2O and 2,2–dipyridylamine in the ratio 2:2/1:2:1000:2. Initially 0.200 g (1.38×10^{-3} mol) of MoO_3 for **CuMo–4** and 0.200 g (7.52×10^{-4} mol) of Nb_2O_5 for **CuNb–3** was weighed into a 27 mL Teflon–lined stainless steel autoclave and dissolved with 0.5 mL (2.89×10^{-2} mol) of 48% HF at room temperature for 5 minutes. To the resultant solution, 0.2 g of 2,2'–dipyridylamine (1.16×10^{-3} mol),10 mL (5.54×10^{-1} mol) of water and finally 0.1 g (1.25×10^{-3} mol) of CuO was added and stirred well until fully dissolved. The reaction vessel was sealed and heated to 160°C for 24 hours, and then cooled to room temperature

over an additional 24 hours. The product was filtered with water and dried at 60˚C in air. Purity of phase was confirmed by elemental analysis, together with comparison of observed and simulated powder X–ray diffraction patterns. Elemental and crystallographic analyses are in good agreement with the structural formula. For **CuMo–4**: Calcd: C, 33.77%; H, 2.55%; N, 11.80%; F, 16.01% measured: C, 33.86%; H, 2.12%; N, 11.51%; F, 18.71%, for **CuNb–3**: Calcd: C, 33.79%; H, 2.58%; N, 11.83%; F, 15.93%, measured: C, 33.67%; H, 2.45%; N, 11.49%; F, 18.22%.

CuMo–5 and **CuNb–4** were formed by reacting CuO, MoO_3/Nb_2O_5, HF, H_2O and 4,4'–bipyridyl in the ratio 2:2/1:2:1000:2. Initially 0.200 g (1.38×10^{-3} mol) of MoO_3 for **CuMo–5** and 0.200 g (7.52×10^{-4} mol) of Nb_2O_5 for **CuNb–4** was weighed into a 27 mL Teflon–lined stainless steel autoclave and dissolved with 0.5 mL (2.89×10^{-2} mol) of 48% HF at room temperature for 5 minutes. To the resultant solution, 0.2 g (1.28×10^{-3} mol) of 4,4'–bipyridyl, 10 mL (5.54×10^{-1} mol) of water and finally 0.1 g (1.25×10^{-3} mol) of CuO was added and stirred well until fully dissolved. The reaction vessel was sealed and heated to 160˚C for 24 hours, and then cooled to room temperature over an additional 24 hours. The product was filtered with water and dried at 60˚C in air. Phase purity was ascertained by elemental analysis (CHN), together with Rietveld refinement of powder X–ray diffraction pattern using the single crystal X–ray diffraction model. Elemental and crystallographic analyses are in good agreement with the structural formula. For **CuMo–5**: Calcd: C, 39.00%; H, 3.21%; N, 9.01%; F, 12.34% measured: C, 38.34%; H, 3.04%; N, 8.55%; F, 11.78%; for **CuNb–4**: Calcd: C, 39.03%; H, 3.27%; N, 9.09%; F, 15.42% measured: C, 38.58%; H, 3.16%; N, 8.78%; F, 14.44%.